Adaptive Control of Self-Excited Systems with Application to a Gas Turbine Combustor

by

Juan Augusto Paredes Salazar

A dissertation submitted in partial fulfillment
of the requirements for the degree of
Doctor of Philosophy
(Aerospace Engineering)
in The University of Michigan
2023

Doctoral Committee:

Professor Dennis S. Bernstein, Chair
Associate Professor Kira Barton
Associate Professor Mirko Gamba
Professor Anouck Girard

Juan Augusto Paredes Salazar
jparedes@umich.edu
ORCID iD: 0000-0001-7486-1231

DEDICATION

First, I would like to help professor Dennis S. Bernstein for being a wonderful advisor. His guidance, fruitful discussions and support have made me into a better researcher and engineer, and I will be forever grateful for the trust he has placed in me.

I would also like to thank my parents, brothers and family for the support they have provided me throughout my entire career. I will always keep the advice and lessons I have received from them close to my heart.

Finally, I would like to thank my colleagues, mentors and friends from the University of Michigan for making my time in Ann Arbor a thoroughly enjoyable one. The irreplaceable memories I have made with you will accompany for the rest of my days.

ACKNOWLEDGMENTS

This research was supported by NSF grant CMMI 1634709. The author thanks Arthur Yang for his assistance in the development of the mixed-integer optimization algorithm in Chapter 3, John Spencer for his assistance with the experiments in Chapter 4, and Rahul Ramesh for his assistance with the experiments in Chapter 5.

TABLE OF CONTENTS

CHAPTER

LIST OF FIGURES

FIGURE

LIST OF TABLES

TABLE

LIST OF ACRONYMS

A/D analog-to-digital

CPA continuous, piecewise-affine

CT continuous-time

D/A digital-to-analog

DISCo dual independent swirl combustor

DT discrete-time

DTL discrete-time Lur'e

DTLI DTL identification

EKF extended Kalman filter

ESC extremum seeking control

FTDDTL filtered time-delay DTL

LMI linear matrix inequality

MIO-ID mixed-integer-optimisation identification

PSD power spectral density

QSRCAC quasi-static RCAC

PWC^1 piecewise-continuously differentiable

RCAC retrospective cost adaptive control

RLS recursive least squares

RMS root-mean-square

SES self-excited system

SISO single-input, single-output

TISO two-input, two-output

TITO two-input, two-output

SNR signal-to-noise ratio

ZOH zero-order-hold

ABSTRACT

A self-excited system (SES) has the property that constant inputs produce oscillatory outputs. SES arise in biochemical systems, aeroelasticity, and combustion. In particular, gas-turbine combustors are SES since a constant fuel rate yields thermoacoustic oscillations. This behavior arises due to the interaction between combustion and acoustics, and it can result in performance degradation and failure.

In practice, the dynamics of a thermoacoustic system may change due to varying operating conditions as well as hardware and environmental changes. With this motivation, the present work applies adaptive control to thermoacoustic systems. Although first-principles models capture the physics of these systems, model-based control methods require details that may be impossible to obtain in practice due to unpredictable changes in the hardware and environment. To address these challenges, this dissertation applies retrospective cost adaptive control (RCAC) to thermoacoustic systems under extremely limited modeling information and actuator limitations.

The first part of the dissertation analyzes discrete-time Lur'e systems that are self-excited in the sense that 1) for all initial conditions the response is bounded, and 2) for almost all initial conditions, the response is nonconvergent. These models capture the behavior of SES, and they are reminiscent of thermoacoustic systems in the sense that the acoustic dynamics are typically linear and the combustion/heat dynamics are nonlinear. The main contribution of this section is a proof that, under specific assumptions on the linear dynamics and feedback nonlinearity, discrete-time Lur'e systems are self-excited.

The second part of the dissertation develops a system identification method based on discrete-time, self-excited Lur'e models. The main contribution of this section is the application of mixed-integer optimization to automating the selection of parameters needed for the identification procedure. This method is applied to illustrative examples as well as to experimental data from the Dual Independent Swirl Combustor (DISCo), which is a gas-turbine model combustor.

The third part of the dissertation applies RCAC to a Rijke-tube experiment, which is an SES due to the interaction between the heat source and the acoustics dynamics. The main contribution of this section is the demonstration of a design methodology wherein an initial set of hyperparameters required by RCAC is determined by a rudimentary model fit using open-loop data from a single experimental scenario. Using the single, fixed choice of hyperparameters, adaptive control

experiments show that RCAC achieves an oscillation suppression greater than 45 dB over a range of operating conditions. Further tests are performed to examine the effect of modified hyperparameters on the time it takes for the adaptive controller to suppress oscillations, the performance and robustness of the frozen-gain adaptive controller, the ability of the adaptive controller to readapt under changes in working conditions, the stability of the adaptive controller under changes in its gain, and the effect of the relative degree of the closed-loop target model on the level of suppression. The experimental scenarios are designed to test the robustness of the adaptive controller under off-nominal perturbations that reflect real-world conditions.

The final part of the dissertation applies RCAC to DISCo; this application differs fundamentally from the Rijke-tube experiment due to significantly more complex physics as well as constraints on the bandwidth of the control actuation. In particular, the control inputs to DISCo are air-injection inputs with 5-Hz bandwidth, which is significantly below the oscillation frequencies of DISCo, the lowest of which is approximately 274 Hz. The main contribution of this section is the development and demonstration of an extension of RCAC that accounts for the actuator bandwidth limitation; this extension is called quasi-static RCAC (QSRCAC). Using modeling information given by the pressure RMS and combustor exit-temperature maps versus inner and outer swirler air mass-flow rate, QSRCAC uses an extended Kalman filter to estimate the gradient of the effect of the actuation on the performance variables. QSRCAC is then applied to DISCo in a multi-input, multi-output setting, with two input signals corresponding to inner and outer swirler air-injection valves, and two output signals given by pressure and temperature sensors. For experimental testing, DISCo uses methane as fuel and is operated at atmospheric pressure (1 atm) and constant power, with a constant fuel mass-flow rate of 0.4 g/s, while maintaining the equivalence ratio between 0.6 and 1.1 to prevent flameout. Experimental results show that QSRCAC achieves an oscillation suppression of 28 dB while reaching a specified exit temperature corresponding to a desired flame length.

CHAPTER 1

Introduction

1.1 Background and Motivation

A self-excited system (SES) has the property that constant inputs produce oscillatory outputs. These oscillations arise from a combination of destabilizing and stabilizing effects. Roughly speaking, destabilization causes the response to grow from the vicinity of an equilibrium, whereas, far from the equilibrium, the effective feedback gain decreases, leading to oscillations [1]. Self-excited systems arise in biochemical systems [2, 3], aeroelasticity [4–6], and combustion [7, 8]. Overviews of SES are given in [9, 10]. As in the case of a wind turbine, whose blades spin in response to the ambient wind flow, self-excited dynamics can be extremely useful. In other cases, however, SES dynamics may be undesirable, as demonstrated by the destruction of the Tacoma-Narrows bridge [11]. Hence, a typical control objective for SES is suppression of the oscillations, and SES provide motivation for developing new techniques for modeling and control [12–17].

A particular type of SES are thermoacoustic systems, which are self-oscillating due to the fact that a constant input (fuel rate in gas-turbine combustors, for example) yields an asymptotically oscillatory acoustic response. This behavior arises from the interaction between combustion and acoustics, resulting in thermoacoustic oscillations. One of the earliest studied systems that demonstrated this phenomenon was the Rijke tube, whose physics have been extensively analyzed, with the original work by Rijke [18] and subsequent work of Lord Rayleigh [19]. In particular, Rayleigh showed that, under certain conditions involving heat and geometry, thermoacoustic oscillations arise from the feedback interaction of the expansion and compression of the air and the heat flux. In thermoacoustic oscillations, the positive feedback between the acoustic field of the system and the unsteady rate of heat release from combustion creates pressure waves whose amplitude increases until it is limited by nonlinear effects. Extensive research has been devoted to modeling thermoacoustic oscillations [1, 20–26].

Gas turbine combustors are typical thermoacoustic systems in aerospace applications and a primary source of power generation in aircraft propulsion. While traditional diffusion approaches, such as rich-quench-lean combustion [27, 28] produce highly stable and flashback-free operation of the combustor, these fail to meet evolving emission regulations, especially NOx [29], which motivates the adoption of lean combustion by the industry. Lean combustion however is prone to thermoacoustic oscillations. The underlying mechanism responsible for these instabilities is a combination of of convective and acoustic dynamics, each supported by and coupled to the dynamics of the turbulent and vortical flowfield, the acoustic properties of the combustor, and the interaction of the chemistry with the turbulent and acoustic fields [30–33]. All of these effects may be present in a given configuration, although their onset depends on the conditions of operation, and, as operation is shifted among operating points, one or more of these instability mechanisms may develop. These instabilities cause large-amplitude pressure oscillations of the flowfield, which may result in flameout, thermal cycling, thermal NOx growth, structural fatigue, and combustion efficiency reduction, which can negatively impact the performance and structural integrity of the turbomachinery. Redesigning the hardware of the combustors, such as the fuel and air injectors or the combustor geometry, and placing acoustic dampers, has been proposed to prevent or reduce these oscillations [34–37]. However, as mentioned in [38], these methods only work effectively within a range of operation, and design modifications usually result in high costs and time-consuming activities. This motivates the development of feedback control laws for thermoacoustic oscillation mitigation in gas turbine combustors [39–45]. As mentioned in [12], model-based controllers require detailed modeling information about the system in order to achieve closed-loop stability and robustness, and, while model-based controllers may suffer loss of performance due to uncertainty or changes in operating conditions, adaptive controllers can achieve suppression over a wide range of operating conditions. Hence, a data-driven, adaptive controller that requires minimal modeling information is desirable.

The objective of this dissertation is thus the development of a digital adaptive controller for suppressing thermoacoustic oscillations; in particular, restorspective cost adaptive control (RCAC) is applied to thermoacoustic systems under extremely limited modeling infromation and actuator limitations. A crucial aspect of data-driven algorithms is the selection of hyperparameters [46–49], which motivates the development of a model-based methodology for selecting adaptive controller hyperparameters. The models used for hyperparameter selection are constructed to approximate the behavior of the studied system without relying on overly complex mechanisms [50]. Hence, a model structure that exhibits self-excited oscillations is developed to abstract key properties.

1.2 Dissertation Outline

The dissertation is organized in two sections. the first section provides a study of self-excited oscillations using discrete-time Lur'e models (Chapters 2 and 3), and the second section develops a model-based hyperparameter selection methodology for adaptive control implementation on systems exhibiting thermoacoustic oscillations (Chapters 4 and 5). Figure 1.1 provides an outline dependence diagram, in which the dependencies between chapters are shown. A summary of each chapter is provided next.

Chapter 2

This chapter analyzes the self-excited dynamics of discrete-time Lur'e models with affinely constrained, piecewise-C^1 feedback nonlinearities. The Lur'e model is chosen as a candidate model structure due to its ability to exhibit self-oscillation and because it is reminiscent of thermoacoustic systems in the sense that acoustic dynamics are typically linear and the combustion/heat dynamics are nonlinear. Discrete-time models are considered in support of system identification, which is covered in Chapter 3. The main result provides sufficient conditions under which a discrete-time Lur'e model is self-excited in the sense that its response is 1) bounded for all initial conditions, and 2) nonconvergent for almost all initial conditions. The content of this chapter is based on [51,52].

Chapter 3

In this chapter, nonlinear identification of self-excited systems is considered using a modified version of the Lur'e model structure introduced in Chapter 2. To facilitate identification, the nonlinear feedback function is assumed to be continuous and piecewise affine, and thus piecewise-C^1. The main contribution is a technique that uses least-squares optimization to estimate the coefficients of the linear dynamics and the slope vector of the nonlinearity, as well as mixed-integer optimization to estimate the order of the linear dynamics and the breakpoints of the nonlinear function. This method is applied to illustrative examples as wel as to experimental data from the Dual Independent Swirl Combustor (DISCo), which is a gas-turbine model combustor. The successful application of this identification technique validates the choice of the Lur'e model structure for modelling self-excited systems. The content of this chapter is based on [53,54] and represents joint research with Y. Yang.

Chapter 4

This chapter introduces an adaptive suppression algorithm to reduce the thermoacoustic oscillations in a Rijke-tube experiment. Retrospective cost adaptive control (RCAC) is introduced in this chapter and implemented in a digital controller to modulate the Rijke-tube experiment oscillations. The main contribution of this chapter is the development of a design methodology wherein an initial set of hyperparameters required by RCAC is determined by using a rudimentary model fit using open-loop data from a single experimental scenario. The model structure is constructed using the self-excitation properties abstracted in Chapter 2 and validated in Chapter 3. Using the single, fixed choice of hyperparameters, adaptive control experiments show that RCAC achieves an oscillation suppression greater than 45 dB over a range of operating conditions. Further tests are performed to examine the effect of modified hyperparameters on the time it takes for the adaptive controller to suppress oscillations, the performance and robustness of the frozen-gain adaptive controller, the ability of the adaptive controller to readapt under changes in working conditions, the stability of the adaptive controller under changes in its gain, and the effect of the relative degree of the closed-loop target model on the level of suppression. The experimental scenarios are designed to test the robustness of the adaptive controller under off-nominal perturbations that reflect real-world conditions. The content of this chapter is based on [55, 56].

Chapter 5

This chapter applies RCAC to DISCo; this application differs fundamentally from the Rijke-tube experiment due to significantly more complex physics as well as constraints on the bandwidth of the control actuation. In particular, the control inputs to DISCo are air-injection inputs with 5-Hz bandwidth, which is significantly below the oscillation frequencies of DISCo, the lowest of which is approximately 274 Hz. The main contribution of this section is the development and demonstration of an extension of RCAC that accounts for the actuator bandwidth limitation; this extension is called quasi-static RCAC (QSRCAC). Using modeling information given by the pressure RMS and combustor exit-temperature maps versus inner and outer swirler air mass-flow rate, QSRCAC uses an extended Kalman filter to estimate the gradient of the effect of the actuation on the performance variables. QSRCAC is then applied to DISCo in a multi-input, multi-output setting, with two input signals corresponding to inner and outer swirler air-injection valves, and two output signals given by pressure and temperature sensors. For experimental testing, DISCo uses methane as fuel and is operated at atmospheric pressure (1 atm) and constant power, with a constant fuel mass-flow rate of 0.4 g/s, while maintaining the equivalence ratio between 0.6 and 1.1 to prevent flameout. Experimental results show that QSRCAC achieves an oscillation suppression of 28 dB while reaching a specified exit temperature corresponding to a desired flame length. The content of this chapter is based on [57, 58].

Nomenclature and Terminology for the Dissertation. $\mathbb{R} \triangleq (-\infty, \infty)$, $\mathbb{N} \triangleq \{1, 2, \ldots\}$, $\mathbb{N}_0 \triangleq \{0, 1, 2, \ldots\}$, $\mathbb{C}$ denotes the complex numbers. $\|\cdot\|$ denotes the Euclidean norm on $\mathbb{C}^n$, and $\mathbf{z} \in \mathbb{C}$ denotes the Z-transform variable. Positive-definite and positive-semidefinite matrices are assumed to be symmetric. For $A \in \mathbb{R}^{n\times m}$, $\|A\|$ denotes the maximum singular value of A, and $\mathrm{vec}\, A \in \mathbb{R}^{nm}$ is the vector formed by stacking the columns of A, such that vec^{-1} satisfies $A = \mathrm{vec}^{-1}(\mathrm{vec}\, A)$.

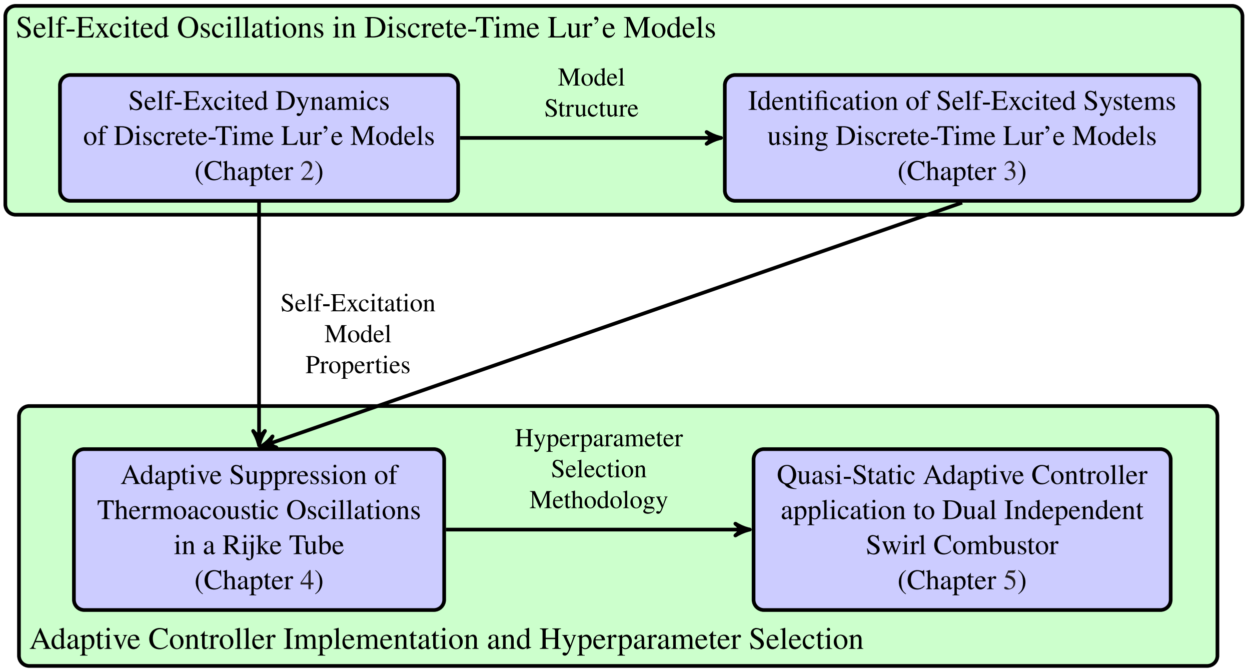

Figure 1.1: Dissertation outline dependence diagram.

CHAPTER 2

Self-Excited Dynamics of Discrete-Time Lur'e Models

A self-excited system (SES) has the property that its response to a constant input is bounded and nonconvergent. Although an undamped oscillator as well as some linear systems with time delay are self-excited, these systems lack structural robustness in the sense that arbitrarily small perturbations of the dynamics can lead to either a convergent (damped) or divergent (unbounded) response. Structurally robust SES's are thus nonlinear. A Lur'e model consists of linear dynamics with memoryless nonlinear feedback [59]. Many SES are modeled by Lur'e models that have unstable equilibria and bounded response. The ability of Lur'e models to exhibit self-oscillation has been widely studied [10, 60–65]. A classical example is the Lur'e model of a Rijke tube, in which acoustic waves interact through feedback with the flame dynamics to produce thermoacoustic oscillations [1, 8].

Self-excited oscillations in continuous-time Lur'e models have been studied in [66–70]. In particular, using the bounded real lemma, continuous-time Lur'e models with superlinear feedback and minimum-phase linear dynamics with relative degree 1 or 2 are shown in [68] to possess bounded solutions. Related results are given in [69] based on dissipativity theory as well as in [70] using Lyapunov methods.

In contrast to [66–70], this chapter focuses on discrete-time, self-excited Lur'e models, with the property that, for all constant inputs, the response is 1) bounded for all initial conditions, and 2) nonconvergent for almost all initial conditions. The main contribution of this study is the derivation of sufficient conditions for this behavior to arise in Lur'e models with a specific class of nonlinear feedback functions. The analogous property for continuous-time Lur'e models is not addressed in the literature.

It is important to stress the distinctions between continuous-time and discrete-time Lur'e models that exhibit self-excited behavior. In particular, since superlinear feedback has unbounded gain, the linear dynamics of a continuous-time Lur'e model must be high-gain stable. From a root locus perspective, this means that the linear dynamics must be minimum phase, the relative degree cannot exceed 2, and, when the relative degree is 2, the root locus center must lie in the open left half plane. These conditions, which are invoked in [68] for continuous-time dynamics, do not imply high-gain stability for discrete-time systems with strictly proper linear dynamics. As discussed in [71], bounded response of a discrete-time Lur'e model with superlinear feedback requires positive-real, and thus relative-degree-zero, linear dynamics. Superlinear feedback is thus incompatible with discrete-time Lur'e models of SES.

The main objective of this chapter is to prove that a class of discrete-time Lur'e models with *affinely constrained* feedback are self-excited in the sense that 1) all trajectories are bounded and 2) the set of initial conditions for which the state trajectory is convergent has measure zero. Although an affinely constrained function need not be bounded or even sector-bounded, it must have linear growth, thus ruling out superlinear nonlinearities, as necessitated by the fact that discrete-time strictly proper linear systems are not high-gain stable. By bounding the feedback gain, the linear-growth assumption enables self-oscillating discrete-time Lur'e models with unbounded feedback nonlinearities. As a benefit of this setting, the linear discrete-time dynamics of the Lur'e model need not be minimum phase, which is assumed in [68] for continuous-time systems.

An additional novel feature of the discrete-time Lur'e model considered in this chapter is the structural assumption that the linear dynamics possess a zero at 1. This assumption, which places a washout filter in the loop, blocks the DC component arising from the constant exogenous input to the system and ensures that the nonlinear closed-loop system have a unique equilibrium for each constant, exogenous input. Most importantly, this property prevents the Lur'e model from having an additional equilibrium with a nontrivial domain of attraction.

Theorem 2.2.6 provides conditions under which the set of initial conditions for which the trajectories of the Lur'e model are convergent has measure zero, and this is the main contribution of this chapter. This result is applicable to discrete-time Lur'e models with piecewise-C^1 (piecewise-continuously differentiable (PWC^1)) nonlinearities for which the Jacobian of the closed-loop dynamics may be singular on a set of measure zero. The need to consider PWC^1 nonlinearities is motivated by their role in nonlinear system identification [54, 72–74]. Under the stronger assumptions of C^1 nonlinearities and everywhere-nonsingular Jacobian, Theorem 2 in [75] is applicable. Theorem 2.2.6 thus extends Theorem 2 in [75] to the case where the nonlinearity is PWC^1 (and thus not necessarily C^1) and the Jacobian of the closed-loop dynamics may be singular on a set of measure zero.

The contents of this chapter are as follows. Section 2.1 introduces the discrete-time Lur'e model, which involves asymptotically stable linear dynamics in feedback with a memoryless nonlinearity, and analyzes its equilibrium properties. Section 2.2 defines affinely constrained nonlinearities and provides sufficient conditions under which the discrete-time Lur'e model possesses a bounded, nonconvergent response for almost all initial conditions. In particular, Theorem 2.2.9 provides a sufficient condition for the Lur'e model to be self-excited. Theorem 2.2.9 depends on Theorem 2.2.6, which provides conditions under which the set of initial conditions for which the state trajectory converges has measure zero. In the case where the feedback nonlinearity is C^1 and the Jacobian of the closed-loop dynamics is nonsingular at all points, Theorem 2.2.6 follows from Theorem 2 in [75]. The case where the feedback nonlinearity is only PWC^1 is required for system identification as considered in Chapter 3, where the identified feedback nonlinearity is constructed to be piecewise affine. Section 2.3 presents numerical examples that illustrate the conditions for self-excitation presented in Section 2.2. Finally, Section 2.4 presentd conclusions to this chapter. Figure 2.1 shows the dependencies of the results in this chapter.

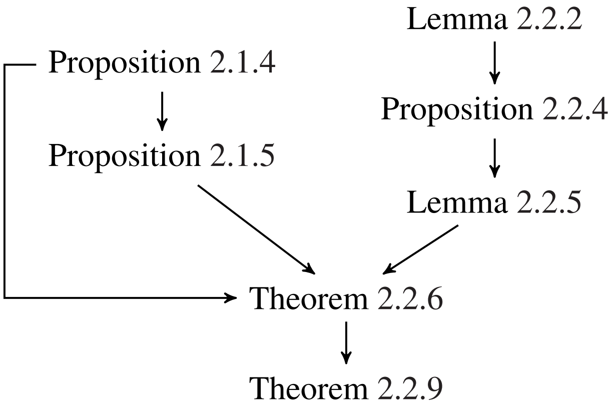

Figure 2.1: Result dependencies.

Nomenclature and Terminology for this Chapter. For $\mathcal{G} \subseteq \mathbb{R}^n$, $\mathrm{acc}(\mathcal{G})$ denotes the set of accumulation points of $\mathcal{G}$ (Definition 2.2.1). For $\mathcal{G} \subseteq \mathbb{R}^n$, $\dim(\mathcal{G})$ denotes the dimension of $\mathcal{G}$, and, for (Lebesgue) measurable $\mathcal{G} \subseteq \mathbb{R}^n$, $\mu(\mathcal{G})$ denotes the measure of $\mathcal{G}$. For $x \in \mathbb{R}^n$ and $\varepsilon > 0$, $\mathbb{B}_\varepsilon(x)$ denotes the open ball of radius ε centered at x. For $A \in \mathbb{R}^{n\times n}$, $\mathrm{spr}(A)$ denotes the spectral radius of A, and, if A is positive definite, then $\lambda_{\min}(A)$ denotes the eigenvalue of A of minimum magnitude and $\lambda_{\max}(A)$ denotes the eigenvalue of A of maximum magnitude. The terminology "$\lim_{k\to\infty} \alpha_k$ exists" implies that the indicated limit is finite.

2.1 Analysis of the Lur'e Model

Let $G(\mathbf{z}) = C(\mathbf{z}I - A)^{-1}B$ be a strictly proper, discrete-time single-input, single-output (SISO) transfer function with nth-order minimal realization (A, B, C) and state $x_k \in \mathbb{R}^n$ at step k, let $\psi\colon \mathbb{R} \to \mathbb{R}$, and let $u \in \mathbb{R}$. Then, for all $k \geq 0$, the discrete-time Lur'e (DTL) model in Fig. 2.2 has the closed-loop dynamics

$$x_{k+1} = Ax_k + B(\psi(y_k) + u), \tag{2.1}$$

$$y_k = Cx_k, \tag{2.2}$$

and thus

$$y_k = CA^k x_0 + \sum_{i=0}^{k-1} CA^{k-1-i} B(\psi(y_i) + u). \tag{2.3}$$

Note that (2.1), (2.2) can be written as

$$x_{k+1} = f(x_k), \tag{2.4}$$

where $f(x) \overset{\triangle}{=} Ax + B(\psi(Cx) + u)$. Henceforth, we assume that $n \geq 2$.

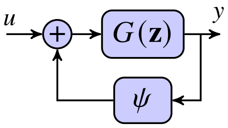

Figure 2.2: Discrete-time Lur'e (DTL) model.

Definition 2.1.1 (2.1), (2.2) *is self-excited if, for all* $u \in \mathbb{R}$, *the following statements hold:*

i) *For all* $x_0 \in \mathbb{R}^n$, $(x_k)_{k=1}^{\infty}$ *is bounded.*

ii) *For almost all* $x_0 \in \mathbb{R}^n$, $\lim_{k\to\infty} x_k$ *does not exist.*

Note that *ii*) holds if and only if $\{x_0 \in \mathbb{R}^n \colon \lim_{k\to\infty} x_k \text{ exists}\}$ has measure zero. The following result concerns the measure of the set of initial conditions for which the output converges.

Proposition 2.1.2 *Assume that* $\operatorname{spr}(A) < 1$, *and, for all* $u \in \mathbb{R}$, $\{x_0 \in \mathbb{R}^n \colon \lim_{k\to\infty} x_k \text{ exists}\}$ *has measure zero. Then,* $\{x_0 \in \mathbb{R}^n \colon \lim_{k\to\infty} y_k \text{ exists}\}$ *has measure zero.*

Proof: Suppose that $X_0 \overset{\triangle}{=} \{x_0 \in \mathbb{R}^n \colon \lim_{k\to\infty} y_k \text{ exists}\}$ has positive measure. For all $x_0 \in X_0$, $\lim_{k\to\infty}(\psi(y_k) + u)$ exists, and thus, since $\operatorname{spr}(A) < 1$, it follows from (2.1) and input-to-state stability for linear time-invariant discrete-time systems [76, Example 3.4] that, for all $x_0 \in X_0$, $\lim_{k\to\infty} x_k$ exists, which is a contradiction. □

Definition 2.1.3 $x \in \mathbb{R}^n$ *is an equilibrium of* (2.1), (2.2) *if* x *is a fixed point of* f, *that is,*

$$x = Ax + B(\psi(Cx) + u). \tag{2.5}$$

When $I - A$ is nonsingular, define

$$x_{\mathrm{e}} \overset{\triangle}{=} (I - A)^{-1} B u \tag{2.6}$$

and note that

$$C x_{\mathrm{e}} = G(1) u. \tag{2.7}$$

The following result establishes useful properties of G and ψ.

Proposition 2.1.4 *Assume that $I - A$ is nonsingular. Then, the following statements hold:*

- *i)* *$x \in \mathbb{R}^n$ is an equilibrium of* (2.1), (2.2) *if and only if*

$$x = (I - A)^{-1} B(\psi(Cx) + u). \tag{2.8}$$

- *ii)* *If $x \in \mathbb{R}^n$ is an equilibrium of* (2.1), (2.2)*, then the following statements hold:*
  - *a)* $Cx = G(1)(\psi(Cx) + u)$.
  - *b)* $\psi(Cx) = -u$ *if and only if* $x = 0$.
  - *c)* *If* $G(1) = 0$*, then* $Cx = 0$ *and* $x = (I - A)^{-1} B(\psi(0) + u)$ *is the unique equilibrium of* (2.1), (2.2).
  - *d)* *If* $Cx = 0$*, then either* $G(1) = 0$ *or* $u = -\psi(0)$.
  - *e)* *If* $\psi(Cx) = 0$*, then* $x = x_{\mathrm{e}}$.
- *iii)* *The following statements are equivalent:*
  - *a)* x_{e} *is an equilibrium of* (2.1), (2.2).
  - *b)* $\psi(Cx_{\mathrm{e}}) = 0$.
  - *c)* $\psi(G(1)u) = 0$.
- *iv)* *Assume that* $G(1) \neq 0$. *Then, the following statements are equivalent:*
  - *a)* x_{e} *is an equilibrium of* (2.1), (2.2).
  - *b)* $\psi(Cx_{\mathrm{e}}) = 0$.
  - *c)* $u \in \frac{1}{G(1)} \psi^{-1}(\{0\})$.
- *v)* *Assume that* $G(1) = 0$. *Then, the following statements are equivalent:*
  - *a)* $\psi(0) = 0$.
  - *b)* x_{e} *is an equilibrium of* (2.1), (2.2).
  - *c)* x_{e} *is the unique equilibrium of* (2.1), (2.2).

Proof: To prove *i)*, note that, since $I - A$ is nonsingular, it follows that (2.5) and (2.8) are equivalent.

To prove *ii)a)*, note that *i)* implies $Cx = C(I - A)^{-1}B(\psi(Cx) + u) = G(1)(\psi(Cx) + u)$.

To prove necessity in *ii)b)*, note that (2.8) implies $x = 0$. To prove sufficiency in *ii)b)*, note that (2.8) implies $B(\psi(Cx) + u) = 0$. Since B is nonzero, it follows that $\psi(Cx) = -u$.

To prove *ii)c)*, note that, since $G(1) = 0$, it follows that *ii)a)* implies $Cx = G(1)(\psi(Cx)+u) = 0$. Furthermore, since $I - A$ is nonsingular, (2.8) implies that $x = (I - A)^{-1}B(\psi(0) + u)$ is the unique equilibrium of (2.1), (2.2).

To prove *ii)d)*, note that, since $Cx = 0$, it follows from *ii)a)* that $G(1)(\psi(0) + u) = 0$, which implies that either $G(1) = 0$ or $u = -\psi(0)$.

To prove *ii)e)*, note that, since $\psi(Cx) = 0$, (2.6) and (2.8) imply $x = x_{\rm e}$.

To prove *iii)*, note that (2.7) implies *iii)b)* $\Longleftrightarrow$ *iii)c)*. Next, we show that *iii)a)* $\Longrightarrow$ *iii)b)* and *iii)b)* $\Longrightarrow$ *iii)a)*. To prove *iii)a)* $\Longrightarrow$ *iii)b)*, note that (2.8) implies $x_{\rm e} = (I - A)^{-1}B(\psi(Cx_{\rm e}) + u) = (I - A)^{-1}Bu$, which implies $\psi(Cx_{\rm e}) = 0$. To prove *iii)b)* $\Longrightarrow$ *iii)a)*, note that $x_{\rm e} = (I - A)^{-1}Bu = (I - A)^{-1}B(\psi(Cx_{\rm e}) + u)$. Hence, *i)* implies $x_{\rm e}$ is an equilibrium.

iv) follows from *iii)* in the case $G(1) \neq 0$.

To prove *v)*, we show *v)c)* $\Longrightarrow$ *v)b)* $\Longrightarrow$ *v)a)* $\Longrightarrow$ *v)c)*. *v)c)* $\Longrightarrow$ *v)b)* is immediate. Next, since $G(1) = 0$, *iv)* implies $Cx_{\rm e} = G(1)u = 0$. Hence, *iii)* with $Cx_{\rm e} = 0$ implies *v)b)* $\Longrightarrow$ *v)a)*. Finally, since $G(1) = 0$, *ii) c)* implies that $x = (I - A)^{-1}B(\psi(0) + u)$ is the unique equilibrium of (2.1), (2.2). In the case $\psi(0) = 0$, $x = (I - A)^{-1}Bu = x_{\rm e}$ is the unique equilibrium of (2.1), (2.2), and thus *v)a)* $\Longrightarrow$ *v)c)*. □

Note that the converse of Proposition 2.1.4*ii)e)* is true and is given by *iii)*. In the following result, the first statement implies that every convergent state trajectory of (2.1), (2.2) converges to an equilibrium solution. Under stronger conditions, the second statement implies that every convergent state trajectory of (2.1), (2.2) converges to the unique equilibrium solution given by (2.6).

Proposition 2.1.5 *Assume that $I - A$ is nonsingular and ψ is continuous. Then, the following statements hold:*

i) If $x_\infty \stackrel{\triangle}{=} \lim_{k\to\infty} x_k$ exists, then x_∞ is an equilibrium of (2.1), (2.2).

ii) Assume that $G(1) = 0$ and $\psi(0) = 0$. Then, the following statements hold:
  a) If $x_\infty \stackrel{\triangle}{=} \lim_{k\to\infty} x_k$ exists, then $x_\infty = x_{\rm e}$.
  b) $\{x_0\colon \lim_{k\to\infty} x_k$ exists$\} = \{x_0\colon \lim_{k\to\infty} x_k = x_{\rm e}\}$.

Proof: To prove *i)*, note that, since ψ is continuous, it follows that f is continuous. Hence, (2.4) implies that $x_\infty = \lim_{k\to\infty} x_k = \lim_{k\to\infty} f(x_k) = f(x_\infty)$.

To prove *ii)a)*, note that *i)* implies that x_∞ is an equilibrium of (2.1), (2.2). Since $G(1) = 0$ and $\psi(0) = 0$, Proposition 2.1.4*v)* implies that $x_{\rm e}$ is the unique equilibrium of (2.1), (2.2). Hence, $x_\infty = x_{\rm e}$.

To prove $ii)b)$, note that "$\subseteq$" follows from $ii)a)$. Finally, "$\supseteq$" is immediate. $\square$

2.2 Self-Excited Dynamics of the Lur'e Model

This section presents sufficient conditions under which the Lur'e model (2.1), (2.2) with an affinely constrained nonlinearity is self-excited.

2.2.1 Preliminary Results

Definition 2.2.1 *Let $\mathcal{B} \subseteq \mathbb{R}^n$. Then, $z \in \mathcal{B}$ is an isolated point of $\mathcal{B}$ if there exists $\varepsilon > 0$ such that $\mathbb{B}_\varepsilon(z) \cap (\mathcal{B}\backslash\{z\}) = \varnothing$. Furthermore, $z \in \mathbb{R}^n$ is an accumulation point of $\mathcal{B}$ if, for all $\varepsilon > 0$, $\mathbb{B}_\varepsilon(z) \cap (\mathcal{B}\backslash\{z\}) \neq \varnothing$. The set of accumulation points of $\mathcal{B}$ is denoted by* $\mathrm{acc}(\mathcal{B})$*, and the set of isolated points of $\mathcal{B}$ is denoted by* $\mathrm{iso}(\mathcal{B})$.

It can be seen that $z \in \mathrm{acc}(\mathcal{B})$ if and only if there exists $(x_i)_{i=1}^\infty \subseteq \mathcal{B}\backslash\{z\}$ such that $\lim_{i\to\infty} x_i = z$. Note that $z \in \mathrm{acc}(\mathcal{B})$ need not be an element of $\mathcal{B}$. In fact, $\mathrm{cl}(\mathcal{B})\backslash\mathcal{B} \subseteq \mathrm{cl}(\mathcal{B})\backslash\mathrm{iso}(\mathcal{B}) = \mathrm{acc}(\mathcal{B})$, and thus $\mathrm{acc}(\mathcal{B}) = \varnothing$ if and only if $\mathcal{B} = \mathrm{iso}(\mathcal{B})$.

Lemma 2.2.2 *Let $\mathcal{A} \subseteq \mathbb{R}$, assume that $\mathrm{acc}(\mathcal{A}) = \varnothing$, and define $\mathcal{B} \overset{\triangle}{=} \{x \in \mathbb{R}^n \colon Cx \in \mathcal{A}\}$. Then, the following statements hold:*

$i)$ $\mathcal{B}$ has measure zero.

$ii)$ $\mathcal{B}$ is closed.

Proof: Both statements are true when $\mathcal{A}$ is empty; hence assume that $\mathcal{A}$ is not empty. To prove $i)$, note that $\mathcal{B}$ is the union of hyperplanes, each of which has measure zero. Since $\mathrm{acc}(\mathcal{A}) = \varnothing$, $\mathcal{A}$ is countable, and thus $\mathcal{B}$ is a countable union of sets, each with measure zero. Therefore, $\mathcal{B}$ has measure zero. To prove $ii)$, note that, since $\mathrm{acc}(\mathcal{A}) = \varnothing$, it follows that $\mathcal{A} = \mathrm{iso}(\mathcal{A})$, and thus $\mathcal{A}$ is closed. Hence, $\mathcal{B}$ is closed. $\square$

2.2.2 Piecewise-C^1 Functions

Definition 2.2.3 *ψ is piecewise continuously differentiable (PWC^1) if the following conditions hold:*

$i)$ ψ is continuous.

$ii)$ Define $\mathcal{R} \overset{\triangle}{=} \{y \in \mathbb{R} \colon \psi'(y)$ exists and ψ' is continuous at $y\}$. Then, $\mathcal{S} \overset{\triangle}{=} \mathbb{R}\backslash\mathcal{R}$ has no accumulation points.

iii) For all $y \in \mathcal{S}$, $\lim_{t\uparrow 0} \psi'(y+t)$ *and* $\lim_{t\downarrow 0} \psi'(y+t)$ *exist.*

Note that, if ψ is C^1, then $\mathcal{S} = \varnothing$.

As an example, consider $\psi(y) = y^2 \sin(1/y)$ for $y \neq 0$ and $\psi(0) = 0$. Then, $\psi'(y) = 2y\sin(1/y) - \cos(1/y)$ for $y \neq 0$ and $\psi'(0) = 0$. Hence, $\mathcal{R} = \mathbb{R}\backslash\{0\}$ and $\mathcal{S} = \{0\}$. However, neither $\lim_{t\uparrow 0} \psi'(t)$ nor $\lim_{t\downarrow 0} \psi'(t)$ exists, and thus ψ is not PWC^1.

It can be shown that, if $\psi'(y)$, $\lim_{t\uparrow 0} \psi'(y+t)$, and $\lim_{t\downarrow 0} \psi'(y+t)$ exist, then $\psi'(y) = \lim_{t\uparrow 0} \psi'(y+t) = \lim_{t\downarrow 0} \psi'(y+t)$, and thus ψ' is continuous at y. Therefore, if ψ is PWC^1 and $y \in \mathcal{S}$, then $\psi'(y)$ does not exist. Furthermore, *ii*) holds if and only if each bounded subset of $\mathbb{R}$ contains a finite number of elements of $\mathcal{S}$.

Assume that ψ is PWC^1. Then, define $\mathcal{D} \triangleq \{x \in \mathbb{R}^n \colon Cx \in \mathcal{R}\}$ and $\mathcal{E} \triangleq \{x \in \mathbb{R}^n \colon Cx \in \mathcal{S}\} = \mathbb{R}^n\backslash\mathcal{D}$ so that $\mathcal{R} = C\mathcal{D}$ and $\mathcal{S} = C\mathcal{E}$. If $x \in \mathcal{D}$, then $f'(x) = A + \psi'(Cx)BC$. Note that, in the case where $G(1) = 0$, $f'(x_{\mathrm{e}}) = f'(0) = A + \psi'(0)BC$. Finally, define

$$\mathcal{D}_0 \triangleq \{x \in \mathcal{D} \colon f'(x) \text{ is singular}\} \tag{2.9}$$

and

$$\mathcal{R}_0 \triangleq C\mathcal{D}_0. \tag{2.10}$$

It thus follows that

$$\mathcal{R}_0 = \{y \in \mathcal{R} \colon A + \psi'(y)BC \text{ is singular}\} \subseteq \mathcal{R}. \tag{2.11}$$

Proposition 2.2.4 *Assume that* ψ *is* PWC^1 *and* $\mathrm{acc}(\mathcal{R}_0) = \varnothing$. *Then,* $\mathcal{D}_0$ *and* $\mathcal{E}$ *are closed and have measure zero.*

Proof: Write

$$\mathcal{D}_0 = \bigcup_{y \in \mathcal{R}_0} \{x \in \mathbb{R}^n \colon Cx = y\},$$
$$\mathcal{E} = \bigcup_{y \in \mathcal{S}} \{x \in \mathbb{R}^n \colon Cx = y\}.$$

Since $\mathrm{acc}(\mathcal{R}_0) = \mathrm{acc}(\mathcal{S}) = \varnothing$, *i*) and *ii*) of Lemma 2.2.2 imply that $\mathcal{D}_0$ and $\mathcal{E}$ are closed and have measure zero. □

Next, define $f^1 \triangleq f$ and, for all $k \geq 1$, $f^{k+1} \triangleq f \circ f^k$. Furthermore, for all $\mathcal{M} \subseteq \mathbb{R}^n$, define $f^{-1}(\mathcal{M}) \triangleq \{x \in \mathbb{R}^n \colon f(x) \in \mathcal{M}\}$ and, for all $k \geq 1$, $f^{-k-1}(\mathcal{M}) \triangleq f^{-1}(f^{-k}(\mathcal{M}))$.

Lemma 2.2.5 *Assume that* ψ *is* PWC^1 *and* $\mathrm{acc}(\mathcal{R}_0) = \varnothing$, *and let* $\mathcal{M} \subset \mathbb{R}^n$ *have measure zero. Then, for all* $k \geq 1$, $\mu(f^{-k}(\mathcal{M})) = 0$.

Proof: Proposition 2.2.4 implies that $\mathcal{D}_0$ and $\mathcal{E}$ are closed, and thus $\mathcal{U} \overset{\triangle}{=} \mathbb{R}^n \backslash (\mathcal{D}_0 \cup \mathcal{E})$ is open. Next, since $\mathcal{U} \cap (\mathcal{D}_0 \cup \mathcal{E}) = \varnothing$, it follows that f is C^1 on $\mathcal{U}$ and $f'(x)$ is nonsingular for all $x \in \mathcal{U}$. The inverse function theorem thus implies that, for all $x \in \mathcal{U}$, there exists an open neighborhood $U_x \subseteq \mathcal{U}$ of x and $V_x \subset \mathbb{R}^n$ of $f(x)$ such that $V_x = f(U_x)$, f is bijective on U_x, and f^{-1} is C^1 on V_x [77, Theorem 9.17], which implies that, for all $x \in \mathcal{U}$, $f\colon U_x \to V_x$ is a C^1 diffeomorphism. Note that $\cup_{x\in\mathcal{U}} U_x$ is an open covering of $\mathcal{U}$ and $\mathbb{R}^n$ is a Lindelöf space [78, p. 96]. Hence, there exists a countable subset $\mathcal{J} \subset \mathcal{U}$ such that $\mathcal{U} \subseteq \cup_{x\in\mathcal{J}} U_x$ and thus, for all $x \in \mathcal{J}$, $f\colon U_x \to V_x$ is a C^1 diffeomorphism.

Next, let $\mathcal{P} \subset \mathbb{R}^n$ be a measurable set such that $\mu(\mathcal{P}) > 0$. Then, since $\mu(\mathcal{D}_0) = \mu(\mathcal{E}) = 0$ and $\mathcal{D}_0$, $\mathcal{E}$, and $\mathcal{U}$ are disjoint,

$$\mu(\mathcal{P}) = \mu(\mathcal{P} \cap \mathcal{D}_0) + \mu(\mathcal{P} \cap \mathcal{E}) + \sum_{x\in\mathcal{J}} \mu(\mathcal{P} \cap \mathcal{U}_x) = \sum_{x\in\mathcal{J}} \mu(\mathcal{P} \cap \mathcal{U}_x),$$

which implies that there exists $\chi \in \mathcal{J}$ such that $\mu(\mathcal{P} \cap U_\chi) > 0$. Since, for all $x \in U_\chi$, $f'(x)$ exists, the change of variables theorem implies

$$\mu(f(\mathcal{P} \cap U_\chi)) = \int_{f(\mathcal{P}\cap\mathcal{U}_\chi)} d\mu(y) = \int_{\mathcal{P}\cap\mathcal{U}_\chi} |\det f'(x)| d\mu(x) > 0.$$

Hence, $\mu(f(\mathcal{P})) > 0$.

Next, suppose $\mu(f^{-1}(\mathcal{M})) > 0$. Since $f(f^{-1}(\mathcal{M})) \subseteq \mathcal{M}$, it follows that

$$0 < \mu(f(f^{-1}(\mathcal{M}))) \le \mu(\mathcal{M}) = 0,$$

which is a contradiction. Hence, $\mu(f^{-1}(\mathcal{M})) = 0$. Finally, induction implies that, for all $k \geq 1$, $\mu(f^{-k}(\mathcal{M})) = 0$. □

The following theorem, which is the central result of this chapter, provides sufficient conditions under which the set of initial conditions for which the state trajectory of (2.1), (2.2) converges has measure zero.

Theorem 2.2.6 *Assume that* $I - A$ *is nonsingular,* $G(1) = 0$, $\psi(0) = 0$, ψ *is PWC*^{1}, $\psi'(0)$ *exists,* $\operatorname{acc}(\mathcal{R}_0) = \varnothing$, $\operatorname{spr}(f'(x_\mathrm{e})) > 1$, *and* $f'(x_\mathrm{e})$ *is nonsingular. Then,* $\mu(\{x_0\colon \lim_{k\to\infty} x_k \text{ exists}\}) = 0$.

Proof: Proposition 2.1.4v) implies that x_e is a fixed point of f. Since $\operatorname{spr}(f'(x_\mathrm{e})) > 1$, define $\mathcal{X} \overset{\triangle}{=} x_\mathrm{e} + \mathcal{Y}$, where $\mathcal{Y}$ is the proper subspace of $\mathbb{R}^n$ spanned by the generalized eigenvectors associated with the eigenvalues of $f'(x_\mathrm{e})$ whose magnitude is less than or equal to 1.

Since $f'(x_\mathrm{e})$ is nonsingular, the inverse function theorem implies that there exist open neighborhoods $U \subset \mathbb{R}^n$ of $x_\mathrm{e} \in U$ and $V \subset \mathbb{R}^n$ of $f(x_\mathrm{e})$ such that $V = f(U)$, f is bijective on U, and f^{-1} is continuously differentiable on V [77, Theorem 9.17]. Then, the stable manifold theorem (Theorem

III.7 in [79, pp. 65, 66]) implies that there exist a local f-invariant C^1 embedded disk $\mathcal{W} \subset \mathbb{R}^n$ and a ball $\mathcal{B}_{x_\mathrm{e}}$ around x_e in an adapted norm such that $\mathcal{W}$ is tangent to $\mathcal{X}$ at x_e, $f(\mathcal{W}) \cap \mathcal{B}_{x_\mathrm{e}} \subset \mathcal{W}$, $\mathcal{W}_{x_\mathrm{e}} \triangleq \cap_{p=0}^{\infty} f^{-p}(\mathcal{B}_{x_\mathrm{e}}) \subset \mathcal{W}$, and, since $\mathrm{spr}(f'(x_\mathrm{e})) > 1$, $\mathcal{W}$ has codimension of at least 1, and thus $\mu(\mathcal{W}) = 0$. Furthermore, since $\mathcal{W}_{x_\mathrm{e}} \subset \mathcal{W}$, $\mu(\mathcal{W}_{x_\mathrm{e}}) = 0$.

Next, let $\chi_0 \in \{x_0\colon \lim_{k\to\infty} x_k = x_\mathrm{e}\}$, and note that there exists $k_1 \geq 1$ such that, for all $k \geq k_1$, $f^k(\chi_0) \in \mathcal{B}_{x_\mathrm{e}}$, which in turn implies that $f^{k_1}(\chi_0) \in \mathcal{W}_{x_\mathrm{e}}$. This, in turn, implies that $\chi_0 \in \cup_{k=0}^{\infty} f^{-k}(\mathcal{W}_{x_\mathrm{e}})$, and thus $\{x_0\colon \lim_{k\to\infty} x_k = x_\mathrm{e}\} \subseteq \cup_{k=0}^{\infty} f^{-k}(\mathcal{W}_{x_\mathrm{e}})$. Hence, since $\mu(\mathcal{W}_{x_\mathrm{e}}) = 0$, Lemma 2.2.5 implies that

$$\begin{aligned}\mu(\{x_0\colon \lim_{k\to\infty} x_k = x_\mathrm{e}\}) &\leq \mu\left(\bigcup_{k=0}^{\infty} f^{-k}(\mathcal{W}_{x_\mathrm{e}})\right)\\ &= \sum_{k=0}^{\infty} \mu(f^{-k}(\mathcal{W}_{x_\mathrm{e}})) = 0,\end{aligned}$$

which, with Proposition 2.1.5*ii*)*b*), implies that

$$\mu(\{x_0\colon \lim_{k\to\infty} x_k \text{ exists}\}) = 0. \qquad \square$$

2.2.3 Boundedness of Solutions of the Lur'e Model

The following definition will be used to obtain conditions for the boundedness of solutions of (2.1), (2.2).

Definition 2.2.7 *ψ is affinely constrained if there exist $\alpha_\mathrm{l}, \alpha_\mathrm{h}, s_\mathrm{l}, s_\mathrm{h} \in \mathbb{R}$ and $\rho > 0$ such that $s_\mathrm{l} < s_\mathrm{h}$ and such that, for all $y \leq s_\mathrm{l}$, $|\psi(y) - \alpha_\mathrm{l} y| < \rho$ and, for all $y \geq s_\mathrm{h}$, $|\psi(y) - \alpha_\mathrm{h} y| < \rho$. Furthermore, ψ is affinely constrained by $(\alpha_\mathrm{l}, \alpha_\mathrm{h})$.*

Example 2.2.8 *This example illustrates Definition 2.2.7. Let $\gamma, \zeta, \eta, \mu, s_\mathrm{l}, s_\mathrm{h} \in \mathbb{R}$, where $\mu \neq 0$, $s_\mathrm{l} < 0 < s_\mathrm{h}$, let $\psi(y) = g(y) + h(\gamma y)$, where $g, h\colon \mathbb{R} \to \mathbb{R}$ are given by*

$$g(y) \triangleq \zeta \tanh(y)\sin(\eta y) + \frac{y}{\sqrt{2\pi}\mu^3} e^{\frac{-y^2}{2\mu^2}}, \tag{2.12}$$

$$h(y) \triangleq \begin{cases} s_\mathrm{l}^2 + 2s_\mathrm{l}(y - s_\mathrm{l}), & y \leq s_\mathrm{l},\\ y^2, & y \in (s_\mathrm{l}, s_\mathrm{h}),\\ s_\mathrm{h}^2 + 2s_\mathrm{h}(y - s_\mathrm{h}), & y \geq s_\mathrm{h}.\end{cases} \tag{2.13}$$

Since $\lim_{|y|\to\infty} g(y) = 0$ it follows that ψ is affinely constrained by $(2\gamma s_\mathrm{l}, 2\gamma s_\mathrm{h})$. Fig. 2.3 shows $\psi(y)$ for all $y \in [-3, 3]$ when $\gamma = 4$, $\zeta = 3$, $\eta = 20$, $\mu = 0.125$, $s_\mathrm{l} = -1$, $s_\mathrm{h} = 1.5$. In this case, ψ is *affinely constrained by* $(-8, 12)$.

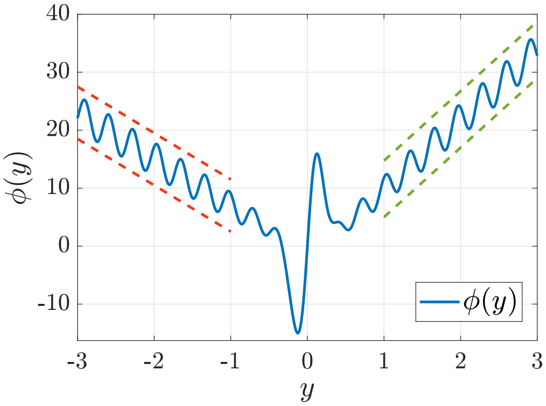

Figure 2.3: Plot of $\psi(y) = g(y) + h(\gamma y)$, where g and h are given by (2.12) and (2.13), and $\gamma = 4, \zeta = 3, \eta = 20, \mu = 0.125, s_{\rm l} = -1, s_{\rm h} = 1.5$. In this case, ψ is affinely constrained by $(\alpha_{\rm l}, \alpha_{\rm h})$, where $\alpha_{\rm l} = 2\gamma s_{\rm l} = -8$ is the slope of the red, dashed line segments, and $\alpha_{\rm h} = 2\gamma s_{\rm h} = 12$ is the slope of the green, dashed line segments.

The following result provides sufficient condition under which (2.1), (2.2) is self-excited.

Theorem 2.2.9 *Assume that* $I - A$ *is nonsingular,* A *is asymptotically stable,* $G(1) = 0$, ψ *is continuous, and* $\psi(0) = 0$, *let* $\alpha_{\rm l}, \alpha_{\rm h} \in \mathbb{R}$, *assume that* ψ *is affinely constrained by* $(\alpha_{\rm l}, \alpha_{\rm h})$, *assume that* $A_{\rm l} \overset{\triangle}{=} A + \alpha_{\rm l}BC$ *and* $A_{\rm h} \overset{\triangle}{=} A + \alpha_{\rm h}BC$ *are asymptotically stable, and assume that there exists a positive-definite matrix* $P \in \mathbb{R}^{n\times n}$ *such that* $P - A^{\mathsf{T}}PA$, $P - A_{\rm l}^{\mathsf{T}}PA_{\rm l}$, *and* $P - A_{\rm h}^{\mathsf{T}}PA_{\rm h}$ *are positive definite. Then, the following statements hold:*

i) *For all* $x_0 \in \mathbb{R}^n$, $(x_k)_{k=1}^{\infty}$ *is bounded.*

ii) *Assume that* ψ *is PWC*^{1} *and differentiable at 0,* $\operatorname{acc}(\mathcal{R}_0) = \varnothing$, $\operatorname{spr}(f'(x_{\rm e})) > 1$, *and* $f'(x_{\rm e})$ *is nonsingular. Then,* (2.1), (2.2) *is self-excited.*

Proof: To prove *i*), let $s_{\rm l}, s_{\rm h} \in \mathbb{R}$ and $\rho > 0$ be such that $s_{\rm l} < s_{\rm h}$ and such that, for all $y \in (-\infty, s_{\rm l}]$, $|\psi(y) - \alpha_{\rm l}y| < \rho$ and, for all $y \in [s_{\rm h}, \infty)$, $|\psi(y) - \alpha_{\rm h}y| < \rho$. For all $k \geq 0$, (2.1) can be rewritten as

$$x_{k+1} = \begin{cases} (A + \alpha_{\rm l}BC)x_k & \\ \quad +B(\psi(Cx_k) - \alpha_{\rm l}Cx_k + u), & Cx_k \leq s_{\rm l}, \\ Ax_k + B(\psi(Cx_k) + u), & Cx_k \in (s_{\rm l}, s_{\rm h}), \\ (A + \alpha_{\rm h}BC)x_k & \\ \quad +B(\psi(Cx_k) - \alpha_{\rm h}Cx_k + u), & Cx_k \geq s_{\rm h}. \end{cases} \tag{2.14}$$

Furthermore, defining

$$A_k \triangleq \begin{cases} A_{\mathrm{l}}, & Cx_k \le s_{\mathrm{l}}, \\ A, & Cx_k \in (s_{\mathrm{l}}, s_{\mathrm{h}}), \\ A_{\mathrm{h}}, & Cx_k \ge s_{\mathrm{h}}, \end{cases}$$

$$\nu_k \triangleq \begin{cases} \psi(Cx_k) - \alpha_{\mathrm{l}} Cx_k + u, & Cx_k \le s_{\mathrm{l}}, \\ \psi(Cx_k) + u, & Cx_k \in (s_{\mathrm{l}}, s_{\mathrm{h}}), \\ \psi(Cx_k) - \alpha_{\mathrm{h}} Cx_k + u, & Cx_k \ge s_{\mathrm{h}}, \end{cases}$$

(2.14) can be written as

$$x_{k+1} = A_k x_k + B\nu_k. \tag{2.15}$$

Since ψ is continuous and affinely constrained by $(\alpha_{\mathrm{l}}, \alpha_{\mathrm{h}})$, it follows that $(\nu_k)_{k=0}^{\infty}$ is bounded. Next, define the positive-definite matrices

$$Q_{\mathrm{l}} \triangleq P - A_{\mathrm{l}}^{\mathsf{T}} P A_{\mathrm{l}}, \quad Q \triangleq P - A^{\mathsf{T}} P A, \quad Q_{\mathrm{h}} \triangleq P - A_{\mathrm{h}}^{\mathsf{T}} P A_{\mathrm{h}},$$

and $V\colon \mathbb{R}^n \to \mathbb{R}$ such that, for all $x \in \mathbb{R}^n$, $V(x) \triangleq x^{\mathsf{T}} P x$. Then, for all $k \ge 0$, (2.15) implies

$$\begin{aligned} &V(x_{k+1}) - V(x_k) \\ &= \begin{cases} -x_k^{\mathsf{T}} Q_{\mathrm{l}} x_k + 2x_k^{\mathsf{T}} A_{\mathrm{l}}^{\mathsf{T}} PB\nu_k + \nu_k^{\mathsf{T}} B^{\mathsf{T}} PB\nu_k, & Cx_k \le s_{\mathrm{l}}, \\ -x_k^{\mathsf{T}} Q x_k + 2x_k^{\mathsf{T}} A^{\mathsf{T}} PB\nu_k + \nu_k^{\mathsf{T}} B^{\mathsf{T}} PB\nu_k, & Cx_k \in (s_{\mathrm{l}}, s_{\mathrm{h}}), \\ -x_k^{\mathsf{T}} Q_{\mathrm{h}} x_k + 2x_k^{\mathsf{T}} A_{\mathrm{h}}^{\mathsf{T}} PB\nu_k + \nu_k^{\mathsf{T}} B^{\mathsf{T}} PB\nu_k, & Cx_k \ge s_{\mathrm{h}}. \end{cases} \end{aligned}$$

Hence, for all $k \ge 0$,

$$V(x_{k+1}) - V(x_k) \le -\gamma(\|x_k\|) + \zeta(\|\nu_k\|),$$

where $\gamma\colon [0,\infty) \to [0,\infty)$ and $\zeta\colon [0,\infty) \to [0,\infty)$ are defined by

$$\gamma(r) \triangleq \tfrac{1}{2} \min(\{\lambda_{\min}(Q_{\mathrm{l}}),\ \lambda_{\min}(Q),\ \lambda_{\min}(Q_{\mathrm{h}})\}) r^2,$$

$$\begin{aligned} \zeta(r) \triangleq \Bigg[&\max \left\{ \tfrac{2|A_{\mathrm{l}}^{\mathsf{T}} PB|^2}{\lambda_{\min}(Q_{\mathrm{l}})}, \tfrac{2|A^{\mathsf{T}} PB|^2}{\lambda_{\min}(Q)}, \tfrac{2|A_{\mathrm{h}}^{\mathsf{T}} PB|^2}{\lambda_{\min}(Q_{\mathrm{h}})} \right\} \\ &+ |B^{\mathsf{T}} PB|^2 \Bigg] r^2. \end{aligned}$$

Since, for all $x \in \mathbb{R}^n$, $\lambda_{\min}(P)\|x\|_2^2 \le V(x) \le \lambda_{\max}(P)\|x\|_2^2$, γ and ζ are continuous and strictly increasing, $\gamma(0) = \zeta(0) = 0$, and $\zeta(r) \to \infty$ as $r \to \infty$, Lemma 3.5 of [76] implies that (2.15) with input v is input-to-state stable. Since $(v_k)_{k=0}^{\infty}$ is bounded, it follows that, for all $x_0 \in \mathbb{R}^n$, $(x_k)_{k=1}^{\infty}$ is bounded.

Finally, *ii*) follows from *i*) and Theorem 2.2.6. □

Note that Theorem 2.2.9 assumes that the linear matrix inequality (linear matrix inequality (LMI))

$$\begin{bmatrix} P & 0 & 0 & 0 \\ 0 & P - A^{\mathsf{T}}PA & 0 & 0 \\ 0 & 0 & P - A_{\mathrm{l}}^{\mathsf{T}}PA_{\mathrm{l}} & 0 \\ 0 & 0 & 0 & P - A_{\mathrm{h}}^{\mathsf{T}}PA_{\mathrm{h}} \end{bmatrix} > 0 \tag{2.16}$$

is feasible, that is, there exists $P \in \mathbb{R}^{n\times n}$ such that the $4n \times 4n$ matrix in (2.16) is positive definite. The following result provides sufficient conditions under which (2.16) is satisfied.

Proposition 2.2.10 *Assume that* $\|A\| < 1$, $\|A_{\mathrm{l}}\| < 1$, *and* $\|A_{\mathrm{h}}\| < 1$. *Then,* (2.16) *is satisfied with* $P = I$.

Proof: Since $\|A\| < 1$, $\|A_{\mathrm{l}}\| < 1$, and $\|A_{\mathrm{h}}\| < 1$, it follows that

$$I - A^{\mathsf{T}}A > 0, \quad I - A_{\mathrm{l}}^{\mathsf{T}}A_{\mathrm{l}} > 0, \quad I - A_{\mathrm{h}}^{\mathsf{T}}A_{\mathrm{h}} > 0,$$

which, in turn, implies that (2.16) is satisfied with $P = I$. □

The following is a corollary of Theorem 2.2.9*ii*) when ψ is bounded.

Corollary 2.2.11 *Assume that* $I - A$ *is nonsingular,* $G(1) = 0$, *and* $\psi(0) = 0$. *Furthermore, assume that A is asymptotically stable,* ψ *is PWC*^{1}*, differentiable at 0, and bounded,* $\mathrm{acc}(\mathcal{R}_0) = \varnothing$, $\mathrm{spr}(f'(x_{\mathrm{e}})) > 1$, *and* $f'(x_{\mathrm{e}})$ *is nonsingular. Then,* (2.1), (2.2) *is self-excited.*

2.3 Numerical examples

Although the conditions of Theorem 2.2.9 and Corollary 2.2.11 are not necessary, the numerical examples in this section show that, when some of these conditions are not met, the response of (2.1), (2.2) may yield a convergent or divergent response for a nonnegligible set of initial conditions. Examples 2.3.1 to 2.3.4 concern cases in which some of these conditions are not met. Table 2.1 summarizes these examples and their objectives. In these examples, the feasibility of the LMI in (2.16) is determined by using the Matlab function *feasp*, which is also used to compute a feasible solution when it exists.

Table 2.1: Summary of Numerical Examples

Example	Nonlinearity type	Objective
2.3.1	Bounded, C^1	Shows that Corollary 2.2.11 is false if $G(1) = 0$ is omitted
2.3.2	Unbounded, C^1, affinely constrained by (α, α)	Shows that Theorem 2.2.9 is false if either $\mathrm{spr}(A + \alpha BC) < 1$ or $\mathrm{spr}(f'(x_e)) > 1$ is omitted
2.3.3	Unbounded, PWC^1, affinely constrained by (α_l, α_h)	Shows that Theorem 2.2.9 is false if either $\mathrm{spr}(A + \alpha_l BC) < 1$ or $\mathrm{spr}(A + \alpha_h BC) < 1$ is omitted
2.3.4	Unbounded, PWC^1, affinely constrained by (α_l, α_h)	Shows that Theorem 2.2.9 is false if the feasibility of (2.16) is omitted

Example 2.3.1 *This example shows that Corollary 2.2.11 is false if the assumption that* $G(1) = 0$ *is omitted. Let* $u = 5$, $\psi(y) = \tanh(y)$, *and* $G(\mathbf{z}) = -1/(\mathbf{z}^2 - \mathbf{z} + 0.5)$ *with minimal realization*

$$A = \begin{bmatrix} 1 & -0.5 \\ 1 & 0 \end{bmatrix},\ B = \begin{bmatrix} 1 \\ 0 \end{bmatrix},\ C = \begin{bmatrix} 0 & -1 \end{bmatrix}.$$

Note that ψ *is* C^1, *bounded, and* $\psi(0) = 0$. *Root-locus properties imply that* $A + \psi'(y)BC$ *is singular if and only if* $\psi'(y) = -0.5$. *Since, for all* $y \in \mathbb{R}$, $\psi'(y) = \mathrm{sech}^2(y) \in [0, 1]$, *it follows that* $A + \psi'(y)BC$ *is nonsingular, and thus* $\mathrm{acc}(\mathcal{R}_0) = \varnothing$. *Furthermore,* $I - A$ *is nonsingular,* A *is asymptotically stable, and* $\mathrm{spr}(f'(x_e)) > 1$. *Since* $G(1) \neq 0$, *it follows that the assumptions of Corollary 2.2.11 are not satisfied. Accordingly, Fig. 2.4 shows that, for the indicated initial states, the response of* (2.1), (2.2) *converges.*

Next, let $G(\mathbf{z}) = -(\mathbf{z} - 1)/(\mathbf{z}^2 - \mathbf{z} + 0.5)$ *with minimal realization*

$$A = \begin{bmatrix} 1 & -0.5 \\ 1 & 0 \end{bmatrix},\ B = \begin{bmatrix} 1 \\ 0 \end{bmatrix},\ C = \begin{bmatrix} 1 & -1 \end{bmatrix}.$$

Root-locus properties imply that $A + \psi'(y)BC$ *is singular if and only if* $\psi'(y) = -0.5$. *Since, for all* $y \in \mathbb{R}$, $\psi'(y) = \mathrm{sech}^2(y) \in [0, 1]$, *it follows that* $A + \psi'(y)BC$ *is nonsingular, that is,* $\mathcal{R}_0 = \varnothing$. *Furthermore,* $I - A$ *is nonsingular,* A *is asymptotically stable, and* $\mathrm{spr}(f'(x_e)) > 1$. *Since* $G(1) = 0$, *all of the assumptions of Corollary 2.2.11 are satisfied. Accordingly, Fig. 2.5 shows that, for the indicated initial states except the equilibrium, the response of* (2.1), (2.2) *does not converge and is bounded.* ◇

Example 2.3.2 *This example shows that Theorem 2.2.9 is false if either* $\mathrm{spr}(A + \alpha BC) < 1$ *or* $\mathrm{spr}(f'(x_e)) > 1$ *is omitted. Let* $u = 5$, α, $\beta \in \mathbb{R}$, *where* $\beta \neq 0$, $\psi(y) = \alpha y + \beta \sin(y)$, *and*

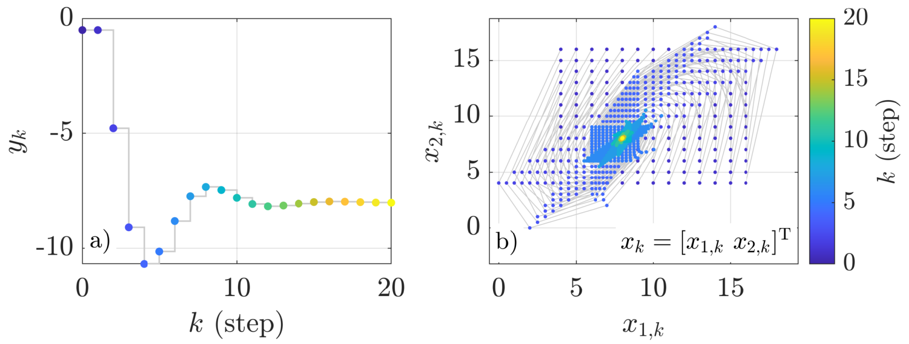

Figure 2.4: Example 2.3.1: Response of (2.1), (2.2) for $G(\mathbf{z}) = \frac{-1}{\mathbf{z}^2-\mathbf{z}+0.5}$, $u = 5$, and $\psi(y) = \tanh(y)$. For all $k \in [0, 20]$, *a)* shows y_k for $x_0 = [0.5\ \ 0.5]^{\mathsf{T}}$. For all $k \in [0, 20]$, *b)* shows x_k for all $x_0 \in \{4, 5, \ldots, 16\} \times \{4, 5, \ldots, 16\}$. The gray lines follow the trajectory from each initial state. Note that all state trajectories converge to $x = [8\ \ 8]^{\mathsf{T}}$, which is an asymptotically stable equilibrium.

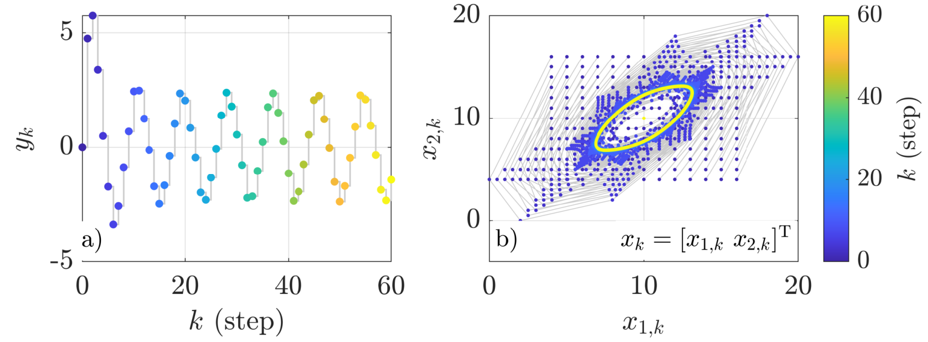

Figure 2.5: Example 2.3.1: Response of (2.1), (2.2) for $G(\mathbf{z}) = \frac{-(\mathbf{z}-1)}{\mathbf{z}^2-\mathbf{z}+0.5}$, $u = 5$, and $\psi(y) = \tanh(y)$. For all $k \in [0, 60]$, *a)* shows y_k for $x_0 = [0.5\ \ 0.5]^{\mathsf{T}}$. For all $k \in [0, 60]$, *b)* shows x_k for all $x_0 \in \{4, 5, \ldots, 16\} \times \{4, 5, \ldots, 16\}$. The gray lines follow the trajectory from each initial state. Note that each state trajectory is bounded and does not converge, except for the state trajectory for $x_0 = [10\ \ 10]^{\mathsf{T}} = x_{\mathrm{e}}$, which is an unstable equilibrium.

$G(\mathbf{z}) = (\mathbf{z} - 1)/(\mathbf{z}^2 - \mathbf{z} + 0.5)$ *with minimal realization*

$$A = \begin{bmatrix} 1 & -0.5 \\ 1 & 0 \end{bmatrix}, \ B = \begin{bmatrix} 1 \\ 0 \end{bmatrix}, \ C = \begin{bmatrix} 1 & -1 \end{bmatrix}.$$

Note that ψ *is* C^1 *and affinely constrained by* (α, α) *since, for all* $y \in \mathbb{R}$, $|\psi(y) - \alpha y| = |\beta \sin(y)| \leq |\beta|$. *Next, root-locus properties imply that* $A + \psi'(y)BC$ *is singular if and only if* $\psi'(y) = -0.5$ *Then, since* $\psi'(y) = \alpha + \beta\cos(y)$, $\mathcal{R}_0 = \{y \in \mathbb{R}\colon \cos(y) = (-0.5 - \alpha)/\beta\}$ *is countable and thus* $\operatorname{acc}(\mathcal{R}_0) = \varnothing$. *Furthermore,* $I - A$ *is nonsingular,* A *is asymptotically stable,* $G(1) = 0$, *and* $\psi(0) = 0$.

In particular, for $\alpha = 0.25$ *and* $\beta = 0.05$, *it follows that* $\operatorname{spr}(A + \alpha BC) < 1$ *and* $\operatorname{spr}(f'(x_{\mathrm{e}})) < 1$.

Hence, the assumptions of Theorem 2.2.9 are not satisfied. Accordingly, Fig. 2.6 shows that, for the indicated initial states, the response of (2.1), (2.2) *converges.*

Furthermore, for $\alpha = 0.75$ *and* $\beta = 0.5$, *it follows that* $\operatorname{spr}(A + \alpha BC) > 1$ *and* $\operatorname{spr}(f'(x_\mathrm{e})) > 1$. *Hence, the assumptions of Theorem 2.2.9 are not satisfied. Accordingly, Fig. 2.7 shows that, for the indicated initial states except the equilibrium, the response of* (2.1), (2.2) *diverges.*

Finally, for $\alpha = 0.25$ *and* $\beta = 0.5$, *it follows that* $\operatorname{spr}(A + \alpha BC) < 1$ *and* $\operatorname{spr}(f'(x_\mathrm{e})) > 1$. *Furthermore,* (2.16) *is feasible with*

$$P = \begin{bmatrix} 2.24 & -1.32 \\ -1.32 & 1.62 \end{bmatrix}.$$

Hence, the assumptions of Theorem 2.2.9 are satisfied. Accordingly, Fig. 2.8 shows that, for the indicated initial states except the equilibrium, the response of (2.1), (2.2) *does not converge and is bounded.* ◇

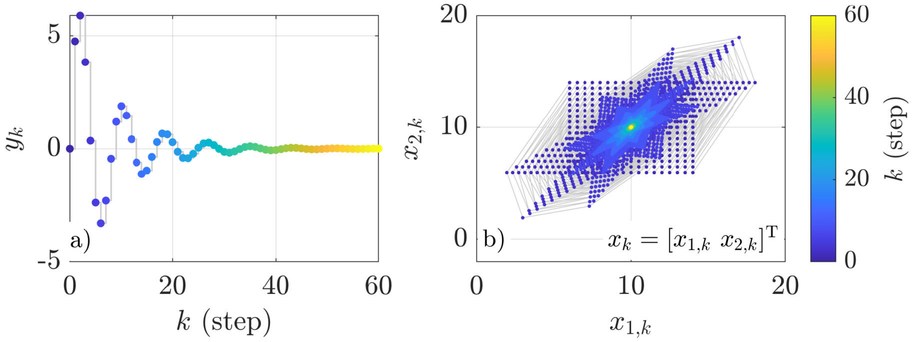

Figure 2.6: Example 2.3.2: Response of (2.1), (2.2) for $G(\mathbf{z}) = (\mathbf{z} - 1)/(\mathbf{z}^2 - \mathbf{z} + 0.5)$, $u = 5$, $\psi(y) = \alpha y + \beta \sin(y)$, and $\alpha = 0.25$, $\beta = 0.05$. For all $k \in [0, 60]$, *a)* shows y_k for $x_0 = [0.5\ \ 0.5]^\mathsf{T}$. For all $k \in [0, 60]$, *b)* shows x_k for all $x_0 \in \{6, 6.5, \ldots, 14\} \times \{6, 6.5, \ldots, 14\}$. The gray lines follow the trajectory from each initial state. Note that all state trajectories converge to $x = [10\ \ 10]^\mathsf{T}$, which is an asymptotically stable equilibrium.

Example 2.3.3 *This example shows that Theorem 2.2.9 is false if either* $\operatorname{spr}(A + \alpha_\mathrm{l} BC) < 1$ *or* $\operatorname{spr}(A + \alpha_\mathrm{h} BC) < 1$ *is omitted.* *Let* $u = 5$, *let* $\mu, s_\mathrm{l}, s_\mathrm{h} \in \mathbb{R}$, *where* $\mu \neq 0$, $s_\mathrm{l} < 0 < s_\mathrm{h}$, *let*

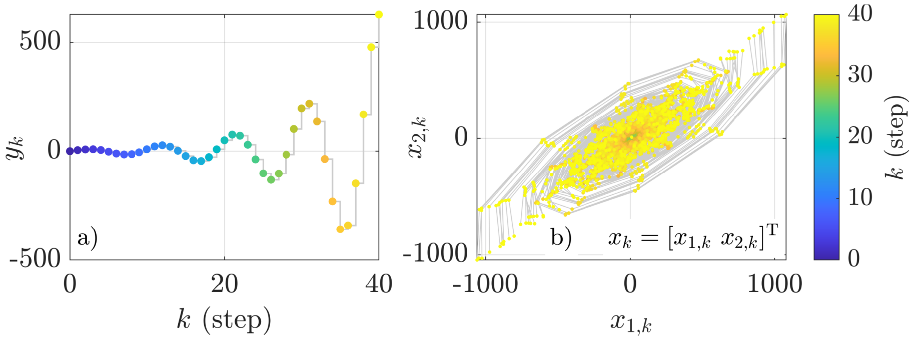

Figure 2.7: Example 2.3.2: Response of (2.1), (2.2) for $G(\mathbf{z}) = (\mathbf{z} - 1)/(\mathbf{z}^2 - \mathbf{z} + 0.5)$, $u = 5$, $\psi(y) = \alpha y + \beta \sin(y)$, and $\alpha = 0.75$, $\beta = 0.5$. For all $k \in [0, 40]$, *a*) shows y_k for $x_0 = [0.5\ \ 0.5]^{\mathsf{T}}$. For all $k \in [0, 40]$, *b*) shows x_k for all $x_0 \in \{6, 6.5, \ldots, 14\} \times \{6, 6.5, \ldots, 14\}$. The gray lines follow the trajectory from each initial state. Note that all state trajectories diverge, except for the state trajectory with $x_0 = [10\ \ 10]^{\mathsf{T}} = x_{\mathrm{e}}$, which is an unstable equilibrium.

$\psi(y) = g(y) + h(y)$*, where* $g, h\colon \mathbb{R} \to \mathbb{R}$ *are given by*

$$g(y) \overset{\triangle}{=} \frac{y}{\sqrt{2\pi}\mu^3} e^{\frac{-y^2}{2\mu^2}}, \tag{2.17}$$

$$h(y) \overset{\triangle}{=} \begin{cases} s_{\mathrm{l}}^2 + s_{\mathrm{l}}(y - s_{\mathrm{l}}), & y \le s_{\mathrm{l}}, \\ y^2, & y \in (s_{\mathrm{l}}, s_{\mathrm{h}}), \\ s_{\mathrm{h}}^2 + s_{\mathrm{h}}(y - s_{\mathrm{h}}), & y \ge s_{\mathrm{h}}, \end{cases} \tag{2.18}$$

and let $G(\mathbf{z}) = \frac{\mathbf{z}(\mathbf{z}-1)}{\mathbf{z}^3 - 0.5\mathbf{z}^2 + 0.25}$ *with minimal realization*

$$A = \begin{bmatrix} 0.5 & 0 & -0.25 \\ 1 & 0 & 0 \\ 0 & 1 & 0 \end{bmatrix}, \quad B = \begin{bmatrix} 1 \\ 0 \\ 0 \end{bmatrix}, \quad C = \begin{bmatrix} 1 & -1 & 0 \end{bmatrix}.$$

Note that ψ *is not* C^1 *but it is* PWC^1 *with* $\mathcal{S} = \{s_{\mathrm{l}}, s_{\mathrm{h}}\}$ *and, since* $\lim_{|y| \to \infty} g(y) = 0$, ψ *is affinely constrained by* $(s_{\mathrm{l}}, s_{\mathrm{h}})$*. Next, since* $G(0) = 0$*, root-locus properties imply that, for all* $y \in \mathcal{R}$, $A + \psi'(y)BC$ *is nonsingular, and thus* $\mathrm{acc}(\mathcal{R}_0) = \varnothing$*. Furthermore,* $I - A$ *is nonsingular,* A *is asymptotically stable,* $G(1) = 0$*, and* $\psi(0) = 0$.

In particular, for $\mu = 0.5$, $s_{\mathrm{l}} = -2$*, and* $s_{\mathrm{h}} = 0.2$*, it follows that* $\mathrm{spr}(A + s_{\mathrm{l}}BC) > 1$, $\mathrm{spr}(A + s_{\mathrm{h}}BC) < 1$*, and, since* $\psi'(0) = g'(0) = 3.19$, $\mathrm{spr}(f'(x_{\mathrm{e}})) > 1$*. Hence, the assumptions of Theorem 2.2.9 are not satisfied. Accordingly, Fig. 2.9 shows that, for some initial states, the response of* (2.1), (2.2) *is unbounded.*

Furthermore, for $\mu = 0.5$, $s_{\mathrm{l}} = -0.4$*, and* $s_{\mathrm{h}} = 0.2$*, it follows that* $\mathrm{spr}(A + s_{\mathrm{l}}BC) < 1$,

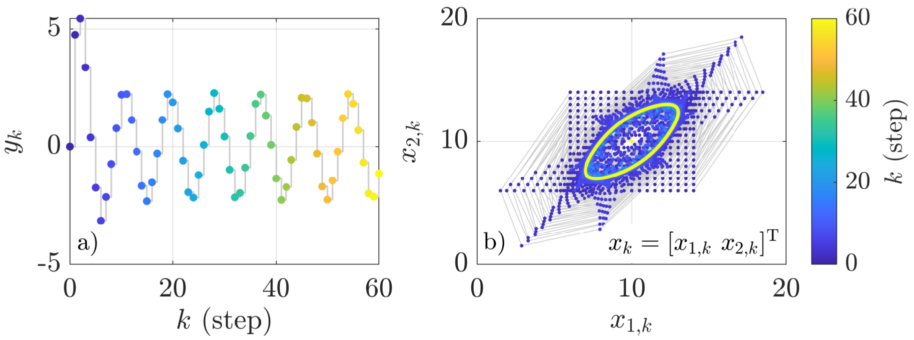

Figure 2.8: Example 2.3.2: Response of (2.1), (2.2) for $G(\mathbf{z}) = (\mathbf{z} - 1)/(\mathbf{z}^2 - \mathbf{z} + 0.5)$, $u = 5$, $\psi(y) = \alpha y + \beta \sin(y)$, and $\alpha = 0.25$, $\beta = 0.5$. For all $k \in [0, 60]$, *a*) shows y_k for $x_0 = [0.5\ \ 0.5]^{\mathsf{T}}$. For all $k \in [0, 60]$, *b*) shows x_k for all $x_0 \in \{6, 6.5, \ldots, 14\} \times \{6, 6.5, \ldots, 14\}$. The gray lines follow the trajectory from each initial state. Note that each state trajectory is bounded and does not converge, except for the state trajectory for $x_0 = [10\ \ 10]^{\mathsf{T}} = x_{\mathrm{e}}$, which is an unstable equilibrium.

$\mathrm{spr}(A + s_{\mathrm{h}}BC) < 1$, *and, since* $\psi'(0) = 3.19$, $\mathrm{spr}(f'(x_{\mathrm{e}})) > 1$. *Furthermore,* (2.16) *is feasible with*

$$P = \begin{bmatrix} 105.65 & -20.67 & -7.47 \\ -20.67 & 68.99 & -6.21 \\ -7.47 & -6.21 & 34.77 \end{bmatrix}.$$

Hence, the assumptions of Theorem 2.2.9 are satisfied. Accordingly, Fig. 2.9 shows that, for the indicated initial states, the response of (2.1), (2.2) *is bounded and does not converge.* ◇

Example 2.3.4 *This example shows that Theorem 2.2.9 is false if the assumption that* (2.16) *is feasible is omitted. Let* $u = 5$, *let* γ, μ, η, s_{l}, $s_{\mathrm{h}} \in \mathbb{R}$, *where* μ, η *are nonzero and* $s_{\mathrm{l}} < 0 < s_{\mathrm{h}}$, *let* ψ *be given by*

$$\psi(y) = \begin{cases} s_{\mathrm{l}}(s_{\mathrm{l}}^2 + \gamma) + 3s_{\mathrm{l}}^2(y - s_{\mathrm{l}}) + \mu \sin(\eta(y - s_{\mathrm{l}})), & y \le s_{\mathrm{l}}, \\ y^3 + \gamma y, & y \in (s_{\mathrm{l}}, s_{\mathrm{h}}), \\ s_{\mathrm{l}}(s_{\mathrm{h}}^2 + \gamma) + 3s_{\mathrm{h}}^2(y - s_{\mathrm{h}}) + \mu \sin(\eta(y - s_{\mathrm{h}})), & y \ge s_{\mathrm{h}}, \end{cases} \tag{2.19}$$

and let

$$G(\mathbf{z}) = \frac{\mathbf{z}^3 - 1.1\mathbf{z}^2 + 0.88\mathbf{z} - 0.78}{\mathbf{z}^4 + 0.1\mathbf{z}^3 + 0.77\mathbf{z}^2 - 10^{-3}\mathbf{z} - 7.8 \cdot 10^{-3}} \tag{2.20}$$

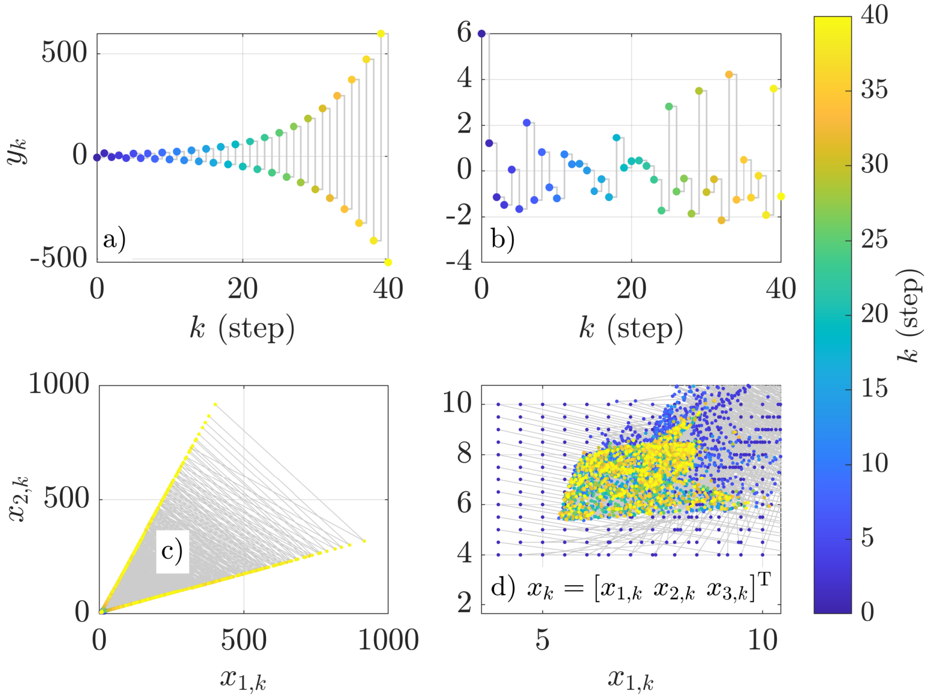

Figure 2.9: Example 2.3.3: Response of (2.1), (2.2) for $G(\mathbf{z}) = \frac{\mathbf{z}(\mathbf{z}-1)}{\mathbf{z}^3-0.5\mathbf{z}^2+0.25}$, $u = 5$, $\psi(y) = g(y) + h(y)$, where g and h are given by (2.17) and (2.18), and $\mu = 0.5$, $s_{\mathrm{l}} = -2$, $s_{\mathrm{h}} = 0.2$. For all $k \in [0, 40]$, *a*) shows y_k for $x_0 = [4\ \ 10\ \ 0]^{\mathsf{T}}$. For all $k \in [0, 40]$, *b*) shows y_k for $x_0 = [10\ \ 4\ \ 0]^{\mathsf{T}}$. For all $k \in [0, 40]$, *c*) shows x_k for all $x_0 \in \{4, 5, \ldots, 10\} \times \{4, 5, \ldots, 10\} \times \{0\}$. *d*) is a magnified version of *c*). The gray lines follow the trajectory from each initial state. Note that, while some state trajectories remain bounded, the response of (2.1), (2.2) is unbounded for some initial states.

with minimal realization

$$A = \begin{bmatrix} -0.1 & -0.77 & 10^{-3} & 7.8\cdot 10^{-3} \\ 1 & 0 & 0 & 0 \\ 0 & 1 & 0 & 0 \\ 0 & 0 & 1 & 0 \end{bmatrix}, \ B = \begin{bmatrix} 1 \\ 0 \\ 0 \\ 0 \end{bmatrix},$$

$$C = \begin{bmatrix} 1 & -1.1 & 0.88 & -0.78 \end{bmatrix}.$$

Note that ψ *is not* C^1 *but it is* PWC^1 *with* $\mathcal{S} = \{s_{\mathrm{l}}, s_{\mathrm{h}}\}$, *for all* $y \le s_{\mathrm{l}}$, $|\psi(y) - 3s_{\mathrm{l}}^2 y| = |\mu \sin(\eta(y - s_{\mathrm{l}})) - 2s_{\mathrm{l}}^3| \le |\mu| + 2|s_{\mathrm{l}}|^3$, *and, for all* $y \ge s_{\mathrm{h}}$, $|\psi(y) - 3s_{\mathrm{h}}^2 y| = |\mu \sin(\eta(y - s_{\mathrm{l}})) - 2s_{\mathrm{h}}^3| \le |\mu| + 2|s_{\mathrm{h}}|^3$. *Hence,* ψ *is affinely constrained by* $(3s_{\mathrm{l}}^2, 3s_{\mathrm{h}}^2)$. *Next, root-locus properties imply that* $A + \psi'(y)BC$

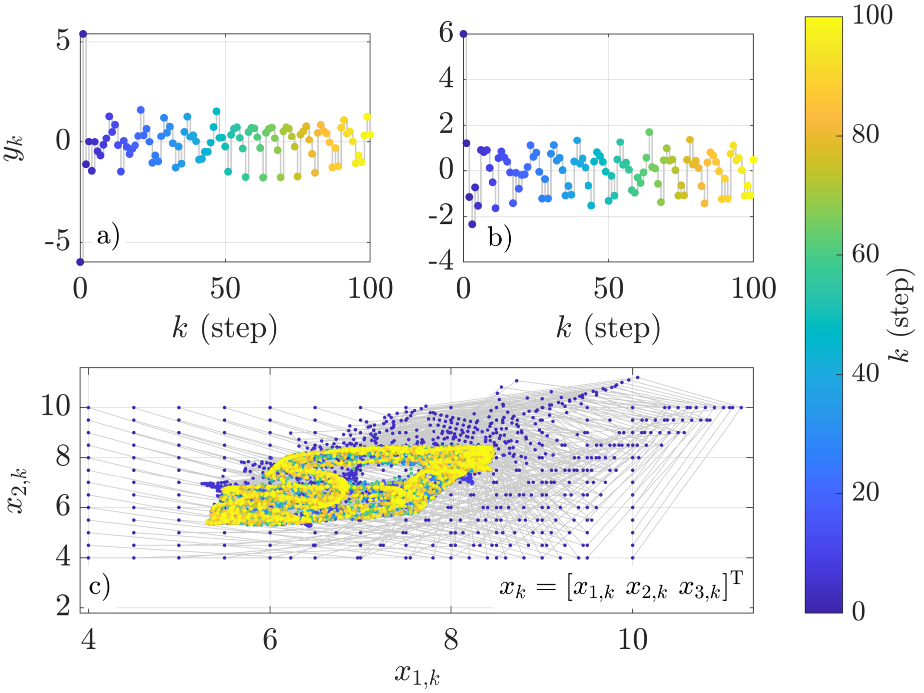

Figure 2.10: Example 2.3.3: Response of (2.1), (2.2) for $G(\mathbf{z}) = \frac{\mathbf{z}(\mathbf{z}-1)}{\mathbf{z}^3-0.5\mathbf{z}^2+0.25}$, $u = 5$, $\psi(y) = g(y) + h(y)$, where g and h are given by (2.17) and (2.18), and $\mu = 0.5$, $s_{\rm l} = -0.4$, $s_{\rm h} = 0.2$. For all $k \in [0, 100]$, *a)* shows y_k for $x_0 = [4\ \ 10\ \ 0]^{\rm T}$. For all $k \in [0, 100]$, *b)* shows y_k for $x_0 = [10\ \ 4\ \ 0]^{\rm T}$. For all $k \in [0, 100]$, *c)* shows x_k for all $x_0 \in \{4, 5, \ldots, 10\} \times \{4, 5, \ldots, 10\} \times \{0\}$. The gray lines follow the trajectory from each initial state. Note that each state trajectory is bounded and does not converge.

is singular if and only if $\psi'(y) = 0.01$. *For all* $y \in \mathcal{R}$, ψ' *is given by*

$$\psi'(y) = \begin{cases} 3s_{\rm l}^2 + \mu\eta\cos(\eta(y - s_{\rm l})), & y < s_{\rm l}, \\ 3y^2 + \gamma, & y \in (s_{\rm l}, s_{\rm h}), \\ 3s_{\rm h}^2 + \mu\eta\cos(\eta(y - s_{\rm h})), & y > s_{\rm h}, \end{cases}$$

which implies that

$$\begin{aligned} \mathcal{R}_0 \subset & \{-\sqrt{|0.01 - \gamma|/3}, \sqrt{|0.01 - \gamma|/3}\} \\ & \cup \{y \in \mathcal{R}\colon\ y < s_{\rm l} \text{ and } 0.01 - 3s_{\rm l}^2 = \mu\eta\cos(\eta(y - s_{\rm l}))\} \\ & \cup \{y \in \mathcal{R}\colon\ y > s_{\rm h} \text{ and } 0.01 - 3s_{\rm h}^2 = \mu\eta\cos(\eta(y - s_{\rm h}))\}, \end{aligned}$$

which in turn implies that $\mathcal{R}_0$ *is countable and thus* $\operatorname{acc}(\mathcal{R}_0) = \varnothing$. *Furthermore,* $I - A$ *is nonsingular,* A *is asymptotically stable,* $G(1) = 0$, *and* $\psi(0) = 0$.

In particular, for $\gamma = 1.5$, $\mu = 0.1$, $\eta = 40$, $s_{\rm l} = -0.29$, $s_{\rm h} = 0.62$, *it follows that* $\operatorname{spr}(A + 3s_{\rm l}^2 BC) <$

1, $\mathrm{spr}(A+3s_\mathrm{h}^2BC) < 1$, *and* $\mathrm{spr}(f'(x_\mathrm{e})) > 1$. *However,* (2.16) *in infeasible. Hence, the assumptions of Theorem 2.2.9 are not satisfied. Accordingly, Fig. 2.11 shows that the response of* (2.1), (2.2) *is unbounded for some initial states.*

Furthermore, for $\gamma = 1.5$, $\mu = 0.1$, $\eta = 40$, $s_\mathrm{l} = -0.29$, $s_\mathrm{h} = 0.29$, *it follows that* $\mathrm{spr}(A + 3s_\mathrm{l}^2BC) < 1$, $\mathrm{spr}(A + 3s_\mathrm{h}^2BC) < 1$, *and* $\mathrm{spr}(f'(x_\mathrm{e})) > 1$. *Furthermore,* (2.16) *is feasible with*

$$P = \begin{bmatrix} 2.34 & -1.05\cdot 10^{-1} & 1.14 & -1.13\cdot 10^{-1} \\ -1.04\cdot 10^{-1} & 1.74 & -1.07\cdot 10^{-1} & 6.35\cdot 10^{-1} \\ 1.14 & -1.07\cdot 10^{-1} & 1.21 & -3.58\cdot 10^{-2} \\ -1.13\cdot 10^{-1} & 6.35\cdot 10^{-1} & -3.58\cdot 10^{-2} & 6.10\cdot 10^{-1} \end{bmatrix}.$$

Hence, the assumptions of Theorem 2.2.9 are satisfied. Accordingly, Fig. 2.12 shows that, for the indicated initial states, the response of (2.1), (2.2) *is bounded and does not converge.* ◇

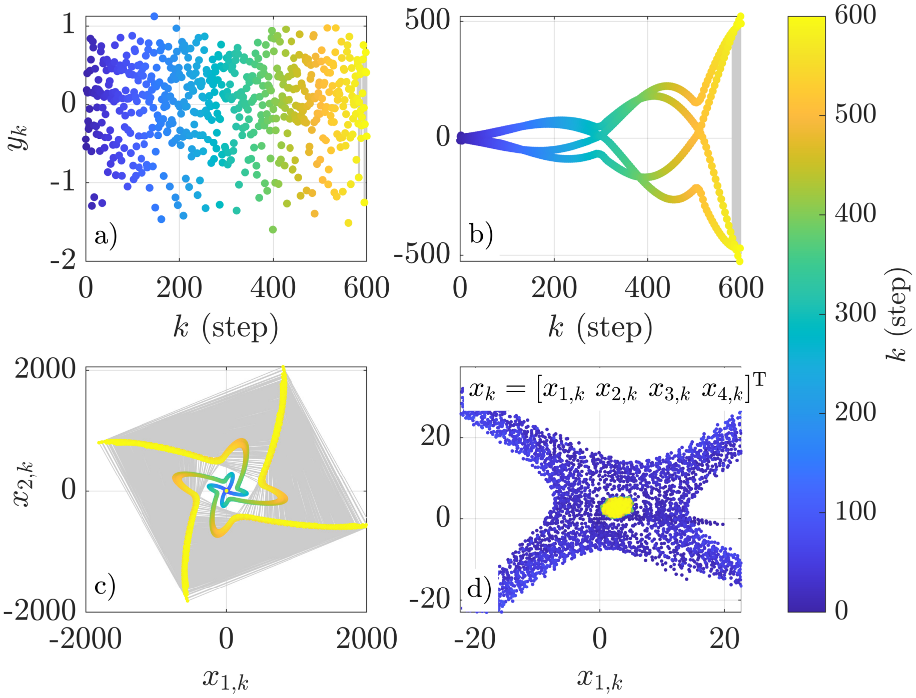

Figure 2.11: Example 2.3.4: Response of (2.1), (2.2) for G given by (2.20), $u = 5$, ψ is given by (2.19), and $\gamma = 1.5$, $\mu = 0.1$, $\eta = 40$, $s_\mathrm{l} = -0.29$, $s_\mathrm{h} = 0.62$. For all $k \in [0, 600]$, *a*) shows y_k for $x_0 = [2\ \ 4\ \ 4\ \ 2]^\mathsf{T}$. For all $k \in [0, 600]$, *b*) shows y_k for $x_0 = [-2\ \ 4\ \ -4\ \ 2]^\mathsf{T}$. For all $k \in [0, 600]$, *c*) shows x_k for all $x_0 \in \{-4, -3, \ldots, 4\} \times \{4\} \times \{-4, -3, \ldots, 4\} \times \{2\}$. *d*) is a magnified version of *c*). For all $k \in [580, 600]$, the gray lines follow the trajectory from each initial state. Note that, while some state trajectories remain bounded, the response of (2.1), (2.2) is unbounded for some initial states.

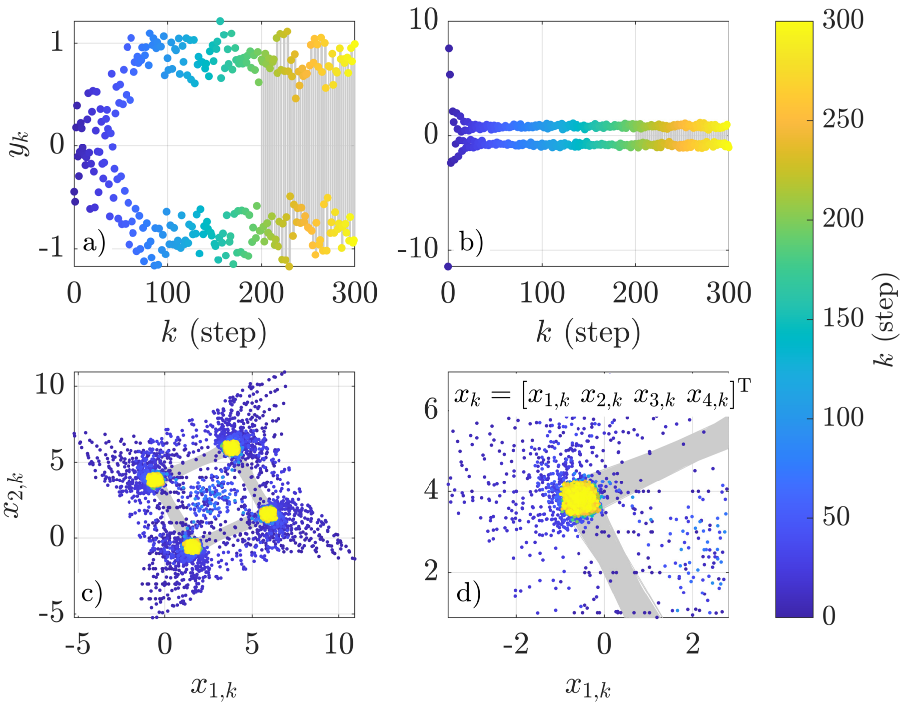

Figure 2.12: Example 2.3.4: Response of (2.1), (2.2) for G given by (2.20), $u = 5$, ψ is given by (2.19), and $\gamma = 1.5$, $\mu = 0.1$, $\eta = 40$, $s_{\mathrm{l}} = -0.29$, $s_{\mathrm{h}} = 0.29$. For all $k \in [0, 300]$, *a*) shows y_k for $x_0 = [2\ \ 4\ \ 4\ \ 2]^{\mathrm{T}}$. For all $k \in [0, 300]$, *b*) shows y_k for $x_0 = [-2\ \ 4\ \ -4\ \ 2]^{\mathrm{T}}$. For all $k \in [0, 300]$, *c*) shows x_k for all $x_0 \in \{-4, -3, \ldots, 4\} \times \{4\} \times \{-4, -3, \ldots, 4\} \times \{2\}$. *d*) is a magnified version of *c*). For all $k \in [200, 300]$, the gray lines follow the trajectory from each initial state. Note that each state trajectory is bounded and does not converge.

2.4 Conclusions

This chapter considered discrete-time Lur'e models whose response is self-excited in the sense that it is 1) bounded for all initial conditions, and 2) nonconvergent for almost all initial conditions. These models involve asymptotically stable linear dynamics with a washout filter connected in feedback with a piecewise-C^1 affinely constrained nonlinearity. The model structure properties derived in this chapter will be validated via system identification in Chapter 3 and used to construct a SES model in Chapter 4.

CHAPTER 3

Identification of Self-Excited Systems Using Discrete-Time Lur'e Models

As shown in Chapter 2, a Lur'e model exhibits self-excited behavior when the linear dynamics are asymptotically stable, the nonlinear feedback function is sigmoidal, and the loop gain is sufficiently high. In effect, high loop gain renders the zero equilibrium unstable, driving the state to the saturation region, where the system operates as an open-loop system driven by a step input. A washout filter (an asymptotically stable transfer function with a zero at 1 and thus zero asymptotic step response) drives the state of the open-loop asymptotically stable dynamics back into the linear region, which yields an oscillatory response. This chapter applies nonlinear system identification to construct a Lur'e model for SES. This approach does not assume or require that the SES possess a Lur'e structure; rather, the goal is to estimate a linear model G and a nonlinear feedback function ψ that, when combined into a Lur'e model, capture the nonconvergent behavior of the SES. For example, although the van der Pol oscillator is a Lur'e model with a 2-input, 1-output nonlinear feedback function, the present chapter uses a Lur'e model with a 1-input, 1-output nonlinear feedback function for system identification.

For nonlinear system identification, the present chapter applies a variation of the technique in [72]. As in [72], the nonlinear feedback function is parameterized as a continuous, piecewise-affine (CPA) function, a type of PWC[1] function where the slope of each segment is estimated for a given partition of the domain of the CPA function. Although the domain of ψ is known from data, the number and locations of the breakpoints of the CPA function were determined in [53] by trial and error. In this chapter, mixed-integer optimization is used to automate and optimize a subset of the parameters needed for the identified Lur'e model, while using least-squares optimization to estimate the remaining parameters. By encompassing both continuous and discrete variables, the present chapter shows that mixed integer optimization [80, 81] is advantageous for identifying Lur'e models with a CPA nonlinear feedback function. Mixed integer optimisation has been used for system identification in [82–85].

Since the objective of this chapter is to identify self-excited systems, the input is assumed to be constant. However, the approach of the present chapter does not require knowledge of the constant input, and thus measurements of only the output are needed. Numerical examples show that measurements of the self-excited response of the system, including the transient and asymptotic response for systems that are asymptotically periodic, is sufficient for identifying a Lur'e model that reproduces the asymptotic waveform and, in many cases, the shape of the nonlinearity as well.

The contents of this chapter are as follows. Section 3.1 introduces the filtered time-delayed DTL (FTDDTL) system as a special case of the DTL system. Section 3.2 introduces the discrete-time Lur'e identification (DTLI) model, which has the form of the FTDDTL, as well as the parameterization of the CPA function used to approximate the nonlinear feedback function. Section 3.3 presents the nonlinear least-squares technique used for identifying SES using the DTLI model, which is an modification of the technique presented in [53]. Section 3.4 presents the mixed-integer optimization framework used in this chapter for identifying SES using the DTLI model. Section 3.5 presents resents the results obtained from applying the proposed identification technique on numerical and experimental data, including experimental data obtained from a gas turbine combustor. Finally, Section 3.6 presents conclusions to this chapter.

Nomenclature and Terminology for this Chapter. $\|A\|_{\rm F}$ is the Frobenius norm of A. $1_{n\times m} \in \mathbb{R}^{n\times m}$ is a matrix whose entries are all ones.

3.1 Filtered Time-Delayed DTL System

In this section we consider a special case of the DTL system structure. In particular, the *filtered time-delayed DTL* (FTDDTL) system shown in Figure 3.1 includes a transfer function G, a time delay $G_{\rm d}$, a washout filter $G_{\rm f}$, and a nonlinear feedback function ψ. Under suitable assumptions, it is shown in [51] that this structure gives rises to self-excited oscillations.

The nth-order, asymptotically stable, strictly proper transfer function G has the form

$$G(\mathbf{q}) = \frac{\mathcal{B}(\mathbf{q})}{\mathcal{A}(\mathbf{q})} = \frac{b_1\mathbf{q}^{-1} + \cdots + b_n\mathbf{q}^{-n}}{1 + a_1\mathbf{q}^{-1} + \cdots + a_n\mathbf{q}^{-n}}, \tag{3.1}$$

where $\mathbf{q}$ is the forward-shift operator (used in place of the Z-transform variable in order to include both the free and forced response), the time delay $G_{\rm d}$ is given by

$$G_{\rm d}(\mathbf{q}) = \mathbf{q}^{-d}, \tag{3.2}$$

where d is a nonnegative integer, the washout filter $G_{\rm f}$ is given by

$$G_{\rm f}(\mathbf{q}) = \frac{\mathbf{q}-1}{\mathbf{q}} = 1 - \mathbf{q}^{-1}, \tag{3.3}$$

and the nonlinear feedback function $\psi\colon \mathbb{R} \to \mathbb{R}$ satisfies

$$v_k = \psi(z_k). \tag{3.4}$$

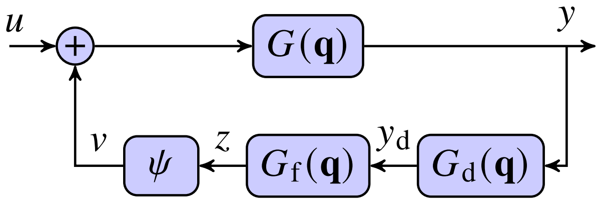

Figure 3.1: Filtered time-delayed discrete-time Lur'e (FTDDTL) system with input u, asymptotically stable plant $G(\mathbf{q})$, time delay $G_{\mathrm{d}}(\mathbf{q})$, washout filter $G_{\mathrm{f}}(\mathbf{q})$, and nonlinear feedback function ψ.

Using $y_k = G(\mathbf{q})(u_k + v_k)$, it follows that

$$\mathcal{A}(\mathbf{q})y_k = \mathcal{B}(\mathbf{q})(\psi(z_k)) + u_k), \tag{3.5}$$

and thus, for all $k \geq n + d + 1$,

$$\begin{aligned} y_k =& (1 - \mathcal{A}(\mathbf{q}))y_k + \mathcal{B}(\mathbf{q})(\psi(z_k) + u_k) \\ =& -a_1 y_{k-1} - \cdots - a_n y_{k-n} + b_1\psi(z_{k-1}) + \cdots + b_n\psi(z_{k-n}) + b_1 u_{k-1} + \cdots + b_n u_{k-n}, \end{aligned} \tag{3.6}$$

where

$$z_k = y_{k-d} - y_{k-d-1}, \tag{3.7}$$

is the input of ψ in this chapter, with the initial output values $y_0, \ldots, y_{n+d}$.

3.2 Discrete-Time Lur'e Identification Model

To facilitate identification, we consider the *discrete-time Lur'e identification* (DTLI) model, which has the form of the FTDDTL. The DTLI model, which is shown in Figure 3.2, incorporates the $\hat{n}$th-order, asymptotically stable, strictly proper linear dynamics

$$\hat{G}(\mathbf{q}) = \frac{\hat{\mathcal{B}}(\mathbf{q})}{\hat{\mathcal{A}}(\mathbf{q})} = \frac{\hat{b}_1\mathbf{q}^{-1} + \cdots + \hat{b}_{\hat{n}}\mathbf{q}^{-\hat{n}}}{1 + \hat{a}_1\mathbf{q}^{-1} + \cdots + \hat{a}_{\hat{n}}\mathbf{q}^{-\hat{n}}}, \tag{3.8}$$

the constant input $\hat{u}$, the time delay

$$\hat{G}_{\mathrm{d}}(\mathbf{q}) = \mathbf{q}^{-\hat{d}}, \tag{3.9}$$

where $\hat{d}$ is a nonnegative integer, the washout filter $G_{\rm f}$ given by (3.3), and the nonlinear feedback function $\hat{\psi}\colon \mathbb{R} \to \mathbb{R}$ written as

$$\hat{v}_k = \hat{\psi}(\hat{z}_k). \tag{3.10}$$

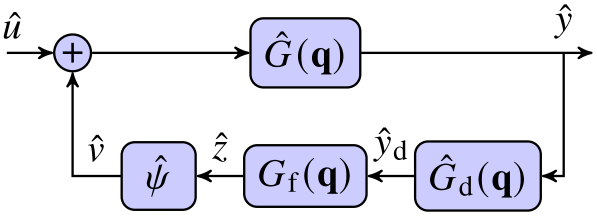

Figure 3.2: Discrete-time Lur'e identification (DTLI) model with constant input $\hat{u}$, asymptotically stable plant $\hat{G}(\mathbf{q})$, time delay $\hat{G}_{\rm d}(\mathbf{q})$, washout filter $G_{\rm f}(\mathbf{q})$, and nonlinear feedback function $\hat{\psi}$. The structure of the DTLI model coincides with the structure of the FTDDTL system.

Using $\hat{y}_k = \hat{G}(\mathbf{q})(\hat{u} + \hat{v}_k)$, it follows that

$$\hat{\mathcal{A}}(\mathbf{q})\hat{y}_k = \hat{\mathcal{B}}(\mathbf{q})(\hat{\psi}(\hat{z}_k) + \hat{u}), \tag{3.11}$$

and thus, for all $k \geq \hat{n} + \hat{d} + 1$,

$$\begin{aligned} \hat{y}_k &= (1 - \hat{\mathcal{A}}(\mathbf{q}))\hat{y}_k + \hat{\mathcal{B}}(\mathbf{q})(\hat{\psi}(\hat{z}_k) + \hat{u}) \\ &= -\hat{a}_1\hat{y}_{k-1} - \cdots - \hat{a}_{\hat{n}}\hat{y}_{k-\hat{n}} + \hat{b}_1\hat{\psi}(\hat{z}_{k-1}) + \cdots + \hat{b}_{\hat{n}}\hat{\psi}(\hat{z}_{k-\hat{n}}) + (\hat{b}_1 + \cdots + \hat{b}_{\hat{n}})\hat{u}, \end{aligned} \tag{3.12}$$

where

$$\hat{z}_k = \hat{y}_{k-\hat{d}} - \hat{y}_{k-\hat{d}-1}. \tag{3.13}$$

Since $\hat{u}$ is not measured in output-only identification and the input to $\hat{G}$ is $\hat{\psi}(\hat{z}_k) + \hat{u}$, the range space of $\hat{\psi}$ can be shifted arbitrarily. Hence, we assume without loss of generality that $\hat{\psi}(0) = 0$.

For system identification, we use a *continuous, piecewise-affine* (CPA) model $\hat{\psi}$ of ψ with the following parameterization. Let $(-\infty, \hat{c}_1], (\hat{c}_1, \hat{c}_2], \ldots, (\hat{c}_{\hat{p}-1}, \hat{c}_{\hat{p}}], (\hat{c}_{\hat{p}}, \infty)$ be a partition of the domain $\mathbb{R}$ of $\hat{\psi}$, and define the vector

$$\hat{c} \triangleq [\hat{c}_1 \ \ \cdots \ \ \hat{c}_{\hat{p}}]^{\mathsf{T}} \in \mathbb{R}^{\hat{p}}. \tag{3.14}$$

Since $\hat{\psi}(0) = 0$, let $\hat{c}_{\hat{r}} = 0$, where $\hat{r} \in [1, \hat{p}]$, and thus $\hat{\psi}(\hat{c}_{\hat{r}}) = \hat{\psi}(0) = 0$. Furthermore, for all

$i \in [1, \hat{p}+1]$, let $\hat{\mu}_i$ denote the slope of $\hat{\psi}$ in the i-th partition interval, and define the slope vector

$$\hat{\mu} \triangleq [\hat{\mu}_1 \ \ \cdots \ \ \hat{\mu}_{\hat{p}+1}]^{\mathsf{T}} \in \mathbb{R}^{\hat{p}+1}. \tag{3.15}$$

Then, for all $\hat{z} \in \mathbb{R}$, $\hat{\psi}$ can be written as

$$\hat{\psi}(\hat{z}) = \hat{\mu}^{\mathsf{T}} \hat{\eta}(\hat{z}), \tag{3.16}$$

where $\hat{\eta}\colon \mathbb{R} \to \mathbb{R}^{\hat{p}+1}$ is given by

$$\hat{\eta}(\hat{z}) \triangleq \begin{cases} \hat{\eta}_1(\hat{z}), & \hat{\delta}(\hat{z}) < \hat{r}+1, \\ \hat{\eta}_2(\hat{z}), & \hat{\delta}(\hat{z}) \geq \hat{r}+1, \end{cases} \tag{3.17}$$

$\hat{\delta}(\hat{z}) \in [1, \hat{p}+1]$ is the index of the partition interval containing $\hat{z}$, and

$$\hat{\eta}_1(\hat{z}) \triangleq [0_{1\times(\hat{\delta}(\hat{z})-1)} \ \ \hat{z} - \hat{c}_{\hat{\delta}(\hat{z})} \ \ \hat{c}_{\hat{\delta}(\hat{z})} - \hat{c}_{\hat{\delta}(\hat{z})+1} \ \ \cdots \ \ \hat{c}_{\hat{r}-1} - \hat{c}_{\hat{r}} \ \ 0_{1\times(\hat{p}+1-\hat{r})}]^{\mathsf{T}}, \tag{3.18}$$

$$\hat{\eta}_2(\hat{z}) \triangleq [0_{1\times\hat{r}} \ \ \hat{c}_{\hat{r}+1} - \hat{c}_{\hat{r}} \ \ \cdots \ \ \hat{c}_{\hat{\delta}(\hat{z})-1} - \hat{c}_{\hat{\delta}(\hat{z})-2} \ \ \hat{z} - \hat{c}_{\hat{\delta}(\hat{z})-1} \ \ 0_{1\times(\hat{p}+1-\hat{\delta}(\hat{z}))}]^{\mathsf{T}}. \tag{3.19}$$

Figure 3.3 illustrates the parameterization of the CPA function $\hat{\psi}$ in terms of $\hat{c}$, $\hat{\mu}$, and $\hat{r}$.

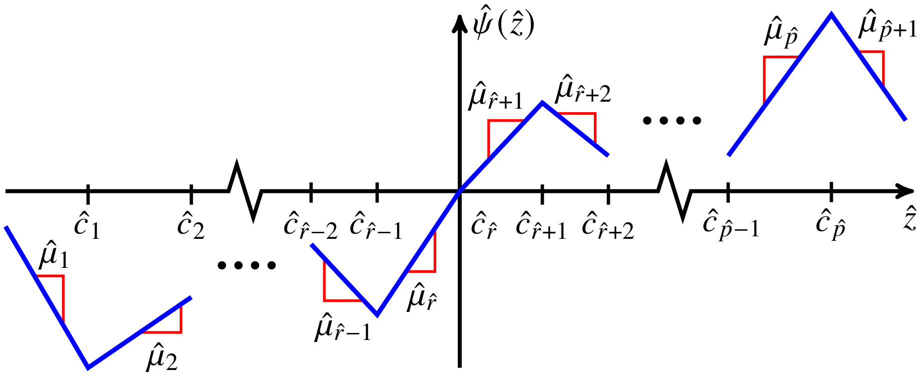

Figure 3.3: Parameterization of the CPA function $\hat{\psi}$. Note that $\hat{c}_{\hat{r}} = 0$ and $\hat{\psi}(\hat{c}_{\hat{r}}) = \hat{\psi}(0) = 0$.

Next, consider DTLI/CPA, which is DTLI with CPA $\hat{\psi}$. It thus follows from (3.12) and (3.16) that

$$\hat{y}_k = -\hat{a}_1 \hat{y}_{k-1} - \cdots - \hat{a}_{\hat{n}} \hat{y}_{k-\hat{n}} + \hat{b}_1 \hat{\mu}^{\mathsf{T}} \hat{\eta}(\hat{z}_{k-1}) + \cdots + \hat{b}_{\hat{n}} \hat{\mu}^{\mathsf{T}} \hat{\eta}(\hat{z}_{k-\hat{n}}) + 1_{1\times\hat{n}} \hat{b} \hat{u}, \tag{3.20}$$

where

$$\hat{a} \triangleq \begin{bmatrix} \hat{a}_1 \\ \vdots \\ \hat{a}_{\hat{n}} \end{bmatrix}, \quad \hat{b} \triangleq \begin{bmatrix} \hat{b}_1 \\ \vdots \\ \hat{b}_{\hat{n}} \end{bmatrix}. \tag{3.21}$$

Then, (3.20) can be written as

$$\hat{y}_k = -\hat{\varphi}_k^{\mathsf{T}} \hat{a} + \hat{\varphi}_{\hat{\eta},k}^{\mathsf{T}} \hat{b} + 1_{1\times\hat{n}} \hat{b}\hat{u} = \hat{\varphi}_k^{\mathsf{T}} \hat{\theta}, \tag{3.22}$$

where

$$\hat{\varphi}_k \triangleq \begin{bmatrix} -\hat{\varphi}_{\hat{y},k} \\ \hat{\varphi}_{\hat{\eta},k} \\ 1 \end{bmatrix} \in \mathbb{R}^{\hat{n}(\hat{p}+2)+1}, \quad \hat{\theta} \triangleq \begin{bmatrix} \hat{a} \\ \mathrm{vec}(\hat{\mu}\hat{b}^{\mathsf{T}}) \\ 1_{1\times\hat{n}}\hat{b}\hat{u} \end{bmatrix} \in \mathbb{R}^{\hat{n}(\hat{p}+2)+1} \tag{3.23}$$

and

$$\hat{\varphi}_{\hat{y},k} \triangleq \begin{bmatrix} \hat{y}_{k-1} \\ \vdots \\ \hat{y}_{k-\hat{n}} \end{bmatrix} \in \mathbb{R}^{\hat{n}}, \quad \hat{\varphi}_{\hat{\eta},k} \triangleq \begin{bmatrix} \hat{\eta}(\hat{z}_{k-1}) \\ \vdots \\ \hat{\eta}(\hat{z}_{k-\hat{n}}) \end{bmatrix} \in \mathbb{R}^{\hat{n}(\hat{p}+1)}. \tag{3.24}$$

3.3 Nonlinear Least-Squares Optimization for System Identification

In this section, we use a technique based on least squares to construct a DTLI/CPA model $\mathcal{M}$ that approximates the response of the self-excited system $\mathcal{S}$. This technique is a variation of the method used in [72]. The objective is to determine a transfer function $\hat{G}$, delay $\hat{d}$, and CPA function $\hat{\psi}$ such that the response of the identified model $\mathcal{M}$ approximates the response of $\mathcal{S}$. This technique requires a choice of $\hat{n}, \hat{d}, \hat{c}, \hat{r}$; these values are then used to obtain parameter estimates $\hat{a}, \hat{b}, \hat{u}, \hat{\mu}$. In the next section, an optimization technique is used to update the parameter estimates $\hat{n}, \hat{d}, \hat{c}, \hat{r}$. In the special case where $\mathcal{S}$ is a FTDDTL system with CPA function ψ, the parameters $\hat{n}, \hat{d}, \hat{c}, \hat{r}, \hat{a}, \hat{b}, \hat{u}, \hat{\mu}$ are estimates of n, d, c, r, a, b, u, μ.

For system identification, we use measurements of y from a data window, which may include portions of the transient and asymptotic response. To define the data window, let $l_{\mathrm{u}} \geq l_{\mathrm{l}} \geq \hat{n} + \hat{d} + 1$, and assume that measurements of y_k are available for all $k \in [l_{\mathrm{l}} - \hat{n} - \hat{d} - 1, l_{\mathrm{u}}]$. The objective is to minimize a cost function involving, for all $k \in [l_{\mathrm{l}}, l_{\mathrm{u}}]$, the difference $y_k - \hat{y}_k$ between the measurement y_k from $\mathcal{S}$ and the output $\hat{y}_k$ of the DTLI/CPA model $\mathcal{M}$, where $\hat{y}_k$ is obtained by propagating (3.20), where, for all $\kappa \in [k - \hat{d} - \hat{n} - 1, k - 1]$, the initial values are given by $\hat{y}_\kappa = y_\kappa$.

Hence, we define the least-squares cost

$$J(\hat{a}, \hat{b}, \hat{u}, \hat{\mu}) \triangleq \|Y - \psi\hat{\theta}\|_2, \tag{3.25}$$

where $\hat{\theta}$ is defined by (3.23),

$$Y \triangleq \begin{bmatrix} y_{l_\mathrm{l}} \\ \vdots \\ y_{l_\mathrm{u}} \end{bmatrix} \in \mathbb{R}^{l_\mathrm{u}-l_\mathrm{l}+1} \tag{3.26}$$

and

$$\psi \triangleq \begin{bmatrix} -\psi_y & \psi_{\hat{\eta}} & 1_{(l_\mathrm{u}-l_\mathrm{l}+1)\times 1} \end{bmatrix} \in \mathbb{R}^{(l_\mathrm{u}-l_\mathrm{l}+1)\times(\hat{n}(\hat{p}+2)+1)}, \tag{3.27}$$

where

$$\psi_y \triangleq \begin{bmatrix} \varphi_{y,l_\mathrm{l}} \\ \vdots \\ \varphi_{y,l_\mathrm{u}} \end{bmatrix} \in \mathbb{R}^{(l_\mathrm{u}-l_\mathrm{l}+1)\times\hat{n}}, \quad \psi_{\hat{\eta}} \triangleq \begin{bmatrix} \varphi_{\hat{\eta},l_\mathrm{l}} \\ \vdots \\ \varphi_{\hat{\eta},l_\mathrm{u}} \end{bmatrix} \in \mathbb{R}^{(l_\mathrm{u}-l_\mathrm{l}+1)\times(\hat{n}(\hat{p}+1))}, \tag{3.28}$$

and, for all $k \in [l_\mathrm{l}, l_\mathrm{u}]$,

$$\varphi_{y,k} \triangleq \begin{bmatrix} y_{k-1} & \cdots & y_{k-\hat{n}} \end{bmatrix} \in \mathbb{R}^{1\times\hat{n}}, \tag{3.29}$$

$$\varphi_{\hat{\eta},k} \triangleq \begin{bmatrix} \hat{\eta}(y_{k-\hat{d}-1} - y_{k-\hat{d}-2}) & \cdots & \hat{\eta}(y_{k-\hat{d}-\hat{n}} - y_{k-\hat{d}-\hat{n}-1}) \end{bmatrix} \in \mathbb{R}^{1\times(\hat{n}(\hat{p}+1))}. \tag{3.30}$$

Since $\hat{\theta}$ defined by (3.23) is a nonlinear function of $\hat{b}, \hat{u}, \hat{\mu}$, we derive an upper bound for J, which is subsequently minimized by means of a two-step process. To do this, let $\hat{\theta}_{\hat{\mu}} \in \mathbb{R}^{\hat{n}(\hat{p}+1)}$ be an approximation of $\mathrm{vec}(\hat{\mu}\hat{b}^\mathsf{T})$ and define

$$\hat{\theta}_{\hat{u}} \triangleq 1_{1\times\hat{n}}\hat{b}\hat{u} \in \mathbb{R}, \tag{3.31}$$

$$\tilde{\theta} \triangleq \begin{bmatrix} \hat{a} \\ \hat{\theta}_{\hat{\mu}} \\ \hat{\theta}_{\hat{u}} \end{bmatrix} \in \mathbb{R}^{\hat{n}(\hat{p}+2)+1}, \tag{3.32}$$

and the cost functions

$$J_1(\tilde{\theta}) \triangleq \|Y - \psi\tilde{\theta}\|_2, \tag{3.33}$$

$$J_2(\hat{\theta}_{\hat{\mu}}, \hat{\mu}, \hat{b}) \triangleq \|\hat{\theta}_{\hat{\mu}} - \mathrm{vec}(\hat{\mu}\hat{b}^\mathsf{T})\|_2. \tag{3.34}$$

Proposition 3.3.1 *Let* $\hat{\theta}_{\hat{\mu}} \in \mathbb{R}^{\hat{n}(\hat{p}+1)}$, *define* $\tilde{\theta}$ *by* (3.32)*, and define* J, J_1, *and* J_2 *by* (3.25)*,* (3.33)*, and* (3.34)*. Then,*

$$J(\hat{a}, \hat{b}, \hat{u}, \hat{\mu}) \le J_1(\tilde{\theta}) + ||\psi_{\hat{\eta}}|| J_2(\hat{\theta}_{\hat{\mu}}, \hat{\mu}, \hat{b}). \tag{3.35}$$

Proof: Note that (3.25) can be written as

$$\begin{aligned} J(\hat{a}, \hat{b}, \hat{u}, \hat{\mu}) &= \|Y - \psi\hat{\theta} + \psi_{\hat{\eta}}\hat{\theta}_{\hat{\mu}} - \psi_{\hat{\eta}}\hat{\theta}_{\hat{\mu}}\|_2 \\ &= \|Y + \psi_y\hat{a} - \psi_{\hat{\eta}}\operatorname{vec}(\hat{\mu}\hat{b}^{\mathsf{T}}) - 1_{(l_{\mathrm{u}}-l_{\mathrm{l}}+1)\times 1}\hat{\theta}_{\hat{u}} + \psi_{\hat{\eta}}\hat{\theta}_{\hat{\mu}} - \psi_{\hat{\eta}}\hat{\theta}_{\hat{\mu}}\|_2 \\ &= \|Y - \psi\tilde{\theta} + \psi_{\hat{\eta}}(\hat{\theta}_{\hat{\mu}} - \operatorname{vec}(\hat{\mu}\hat{b}^{\mathsf{T}}))\|_2, \end{aligned}$$

which implies that

$$\begin{aligned} J(\hat{a}, \hat{b}, \hat{u}, \hat{\mu}) &\le \|Y - \psi\tilde{\theta}\|_2 + \|\psi_{\hat{\eta}}(\hat{\theta}_{\hat{\mu}} - \operatorname{vec}(\hat{\mu}\hat{b}^{\mathsf{T}}))\|_2 \\ &\le \|Y - \psi\tilde{\theta}\|_2 + ||\psi_{\hat{\eta}}|| \|\hat{\theta}_{\hat{\mu}} - \operatorname{vec}(\hat{\mu}\hat{b}^{\mathsf{T}})\|_2 \\ &= J_1(\tilde{\theta}) + ||\psi_{\hat{\eta}}|| J_2(\hat{\theta}_{\hat{\mu}}, \hat{\mu}, \hat{b}). \end{aligned} \qquad \square$$

The upper bound for J given by (3.35) is minimized by sequentially minimizing J_1 and J_2. First, J_1 is minimized to obtain $\tilde{\theta}$, such that

$$\tilde{\theta} = \begin{bmatrix} \hat{a} \\ \hat{\theta}_{\hat{\mu}} \\ \hat{\theta}_{\hat{u}} \end{bmatrix} = \underset{\bar{\theta} \in \mathbb{R}^{\hat{n}(\hat{p}+2)+1}}{\operatorname{argmin}} \; J_1(\bar{\theta}). \tag{3.36}$$

Since J_1 is a linear least-squares function of $\tilde{\theta}$, we use *recursive least squares* (recursive least squares (RLS)) [86] with $P_0 = 10^6$.

Next, using $\hat{\theta}_{\hat{\mu}}$ given by (3.36), we rewrite (3.34) as

$$J_2(\hat{\theta}_{\hat{\mu}}, \hat{\mu}, \hat{b}) = \|\operatorname{vec}^{-1}(\hat{\theta}_{\hat{\mu}}) - \hat{\mu}\hat{b}^{\mathsf{T}}\|_{\mathrm{F}}. \tag{3.37}$$

Then, [87, Fact 11.16.39, p. 906] implies that the rank-1 approximation of $\hat{\mu}\hat{b}^{\mathsf{T}}$ that minimizes J_2 is given by

$$\hat{\mu}\hat{b}^{\mathsf{T}} = ||\operatorname{vec}^{-1}(\hat{\theta}_{\hat{\mu}})|| \psi_{\mathrm{l},1}(\operatorname{vec}^{-1}(\hat{\theta}_{\hat{\mu}}))\psi_{\mathrm{r},1}(\operatorname{vec}^{-1}(\hat{\theta}_{\hat{\mu}}))^{\mathsf{T}}, \tag{3.38}$$

where $\psi_{\mathrm{l},1}(A)$ denotes the first left singular vector of A and $\psi_{\mathrm{r},1}(A)$ denotes the first right singular vector of A. Since $\hat{\mu}$ and $\hat{b}$ are not separately identifiable from (3.38), choosing an arbitrary nonzero scaling parameter $\hat{\beta} \in \mathbb{R}$ and using it to separate (3.38) yields

$$\hat{\mu} = \hat{\beta}\sigma_{\max}(\mathrm{vec}^{-1}(\hat{\theta}_{\hat{\mu}}))\psi_{1,1}(\mathrm{vec}^{-1}(\hat{\theta}_{\hat{\mu}})), \tag{3.39}$$

$$\hat{b} = \frac{1}{\hat{\beta}}\psi_{\mathrm{r},1}(\mathrm{vec}^{-1}(\hat{\theta}_{\hat{\mu}})). \tag{3.40}$$

Finally, if $\hat{\theta}_{\hat{u}}$ given by (3.36) is nonzero, then it follows from (3.31) that $1_{1\times\hat{n}}\hat{b}$ is nonzero, and thus $\hat{u}$ is given by

$$\hat{u} = \frac{\hat{\theta}_{\hat{u}}}{1_{1\times\hat{n}}\hat{b}}. \tag{3.41}$$

Note that $\hat{\beta}$ is unidentifiable, and thus it can be chosen arbitrarily.

3.4 Mixed-Integer Optimization for System Identification

The minimization of (3.25) in Section 3.3 depends on the chosen model parameters $\hat{n}$, $\hat{d}$, $\hat{c}$, and $\hat{r}$. In this section, a mixed-integer approach is used to determine optimal model parameters $\hat{n}$, $\hat{d}$, $\hat{c}$, and $\hat{r}$ such that the output of the identified model $\mathcal{M}$ parameterized by the estimates $\hat{a}, \hat{b}, \hat{u}$, and $\hat{\mu}$ matches the output of $\mathcal{S}$.

In order to constrain the width of the partitions in $\hat{c}$ used to define CPA function ψ, let $\hat{\varepsilon} > 0$ denote the minimum partition width. Furthermore, let $\hat{\lambda}$ be an integer such that $\hat{\lambda}\hat{\varepsilon}$ is the uniform distance between consecutive break points in $\hat{c}$, and let $\hat{\nu}_{\mathrm{n}}$ and $\hat{\nu}_{\mathrm{p}}$ denote the number of negative and positive components in $\hat{c}$, respectively. With this notation, (3.14) can be written as

$$\hat{c} = \hat{\varepsilon}\,[-\hat{\nu}_{\mathrm{n}}\hat{\lambda} \;\; -(\hat{\nu}_{\mathrm{n}}-1)\hat{\lambda} \;\; \cdots \;\; (\hat{\nu}_{\mathrm{p}}-1)\hat{\lambda} \;\; \hat{\nu}_{\mathrm{p}}\hat{\lambda}]^{\mathsf{T}} \in \mathbb{R}^{\hat{\nu}_{\mathrm{n}}+\hat{\nu}_{\mathrm{p}}+1}, \tag{3.42}$$

and thus $\hat{p} = \hat{\nu}_{\mathrm{n}} + \hat{\nu}_{\mathrm{p}} + 1$ and $\hat{r} = \hat{\nu}_{\mathrm{n}} + 1$. Since $\hat{\varepsilon}$ is arbitrarily chosen, note that (3.42) requires estimates of only $\hat{\lambda}$, $\hat{\nu}_{\mathrm{n}}$, and $\hat{\nu}_{\mathrm{p}}$. In this chapter, $\hat{\varepsilon} = 10^{-3}$.

Next, suppose y_k for all $k \in [0, l_{\max}]$ are the measurements available to use for identification, such that $l_{\max} \geq l_{\mathrm{u}}$. Given $\hat{n}, \hat{d}, \hat{\lambda}, \hat{\nu}_{\mathrm{n}}, \hat{\nu}_{\mathrm{p}}$, let $\hat{a}, \hat{b}, \hat{u}, \hat{\mu}$ minimize (3.25), let $l_{\mathrm{MIO,u}} > l_{\mathrm{MIO,l}} \geq \hat{n}+\hat{d}+1$, such that $l_{\mathrm{MIO,u}} \leq l_{\max}$ and let $l_{\mathrm{shift,max}}$ be the maximum time-step shift. Then, we define the cost function

$$J_{\mathrm{MIO}} \overset{\triangle}{=} \|Y_{\mathrm{MIO}} - \hat{Y}_{\mathrm{MIO},l_{\mathrm{shift}}}\|_2, \tag{3.43}$$

where

$$Y_{\mathrm{MIO}} \overset{\triangle}{=} \begin{bmatrix} y_{l_{\mathrm{MIO,l}}} \\ \vdots \\ y_{l_{\mathrm{MIO,u}}} \end{bmatrix} \in \mathbb{R}^{l_{\mathrm{MIO,u}}-l_{\mathrm{MIO,l}}+1}, \tag{3.44}$$

$$\hat{Y}_{\mathrm{MIO},l_{\mathrm{shift}}} \overset{\triangle}{=} \begin{bmatrix} \hat{y}_{l_{\mathrm{MIO,l}}-l_{\mathrm{shift}}} \\ \vdots \\ \hat{y}_{l_{\mathrm{MIO,u}}-l_{\mathrm{shift}}} \end{bmatrix} \in \mathbb{R}^{l_{\mathrm{MIO,u}}-l_{\mathrm{MIO,l}}+1}, \tag{3.45}$$

$$l_{\mathrm{shift}} \overset{\triangle}{=} \operatorname*{argmin}_{l_{\mathrm{shift}}\in[0,l_{\mathrm{shift,max}}]} \|Y_{\mathrm{MIO}} - \hat{Y}_{\mathrm{MIO},l_{\mathrm{shift}}}\|_2, \tag{3.46}$$

subject to

$$\hat{d} \geq 0, \tag{3.47}$$

$$\hat{n}, \hat{\lambda}, \hat{\nu}_{\mathrm{n}}, \hat{\nu}_{\mathrm{p}} > 0, \tag{3.48}$$

$$\hat{n}, \hat{d}, \hat{\lambda}, \hat{\nu}_{\mathrm{n}}, \hat{\nu}_{\mathrm{p}} \in \mathbb{N}_0. \tag{3.49}$$

Note that J_{MIO} considers shifts of $\hat{y}$ relative to y by up to $l_{\mathrm{shift,max}}$ steps using data y_k for all $k \in [l_{\mathrm{MIO,l}}, l_{\mathrm{MIO,u}}]$, and that (3.25) is computed using y_k for all $k \in [l_{\mathrm{l}}, l_{\mathrm{u}}]$. Figure 3.4 illustrates the data sets used to compute J_{MIO}.

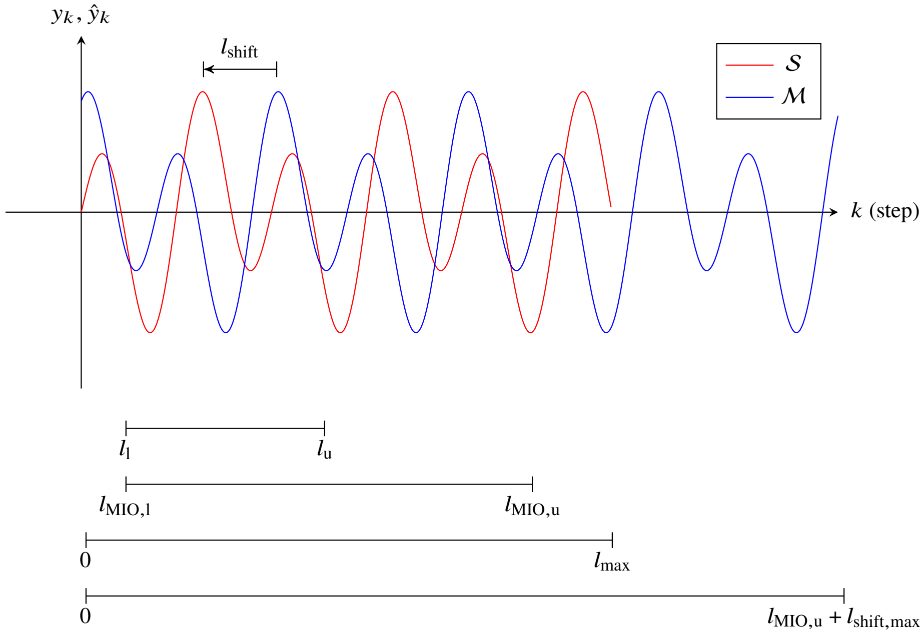

Figure 3.4: Output y_k of system $\mathcal{S}$ for all $k \in [0, l_{\text{max}}]$ available for MIO-ID and output $\hat{y}_k$ of estimated DTLI/CPA model $\mathcal{M}$ for all $k \in [0, l_{\text{MIO,u}} + l_{\text{shift,max}}]$ obtained by propagating (3.12). J in (3.25) is computed using y_k for all $k \in [l_{\text{l}}, l_{\text{u}}]$, and J_{MIO} in (3.43) is computed using y_k for all $k \in [l_{\text{MIO,l}}, l_{\text{MIO,u}}]$. To compute J_{MIO}, the output $\hat{y}$ of $\mathcal{M}$ is shifted by up to $l_{\text{shift,max}} - 1$ steps to minimize the difference between $\hat{y}$ and the output y of $\mathcal{S}$. Note that l_{shift} is the number of shift steps that minimize the difference between y and $\hat{y}$.

To perform *mixed-integer-optimization identification* (MIO-ID), we use an integer optimization algorithm to minimize J_{MIO} over $\hat{n}, \hat{d}, \hat{\lambda}, \hat{\nu}_{\text{n}}$, and $\hat{\nu}_{\text{p}}$. At each iteration, a DTLI/CPA model is estimated along with its associated J_{MIO} cost. Let $\ell \in \mathbb{N}_0$ be an MIO-ID iteration, and let $\hat{n}_\ell, \hat{d}_\ell, \hat{\lambda}_\ell, \hat{\nu}_{\text{n},\ell}, \hat{\nu}_{\text{p},\ell}, \hat{a}_\ell, \hat{b}_\ell, \hat{u}_\ell$, $\hat{\mu}_\ell$ and $J_{\text{MIO},\ell}$ be the DTLI/CPA parameters estimated at the ℓ-th MIO-ID iteration and their associated cost obtained using (3.43). For all $\ell \geq 1$, $\hat{n}_\ell, \hat{d}_\ell, \hat{\lambda}_\ell, \hat{\nu}_{\text{n},\ell}, \hat{\nu}_{\text{p},\ell}$ are determined by a *1-step mixed-integer search* (1SMIS) algorithm with input $J_{\text{MIO},i}, \hat{n}_i, \hat{d}_i, \hat{\lambda}_i, \hat{\nu}_{\text{n},i}, \hat{\nu}_{\text{p},i}$ for all $i \in [0, \ell - 1]$. For $\ell = 0$, the 1SMIS function initializes $\hat{n}_0, \hat{d}_0, \hat{\lambda}_0, \hat{\nu}_{\text{n},0}, \hat{\nu}_{\text{p},0}$ randomly. Then, for all $\ell \in \mathbb{N}_0$, Algorithm 1 shows how $J_{\text{MIO},\ell}$, $\hat{a}_\ell, \hat{b}_\ell, \hat{u}_\ell$, and $\hat{\mu}_\ell$, are computed using $\hat{n}_\ell, \hat{d}_\ell, \hat{\lambda}_\ell, \hat{\nu}_{\text{n},\ell}, \hat{\nu}_{\text{p},\ell}$ as input. Note that $\hat{a}_\ell, \hat{b}_\ell, \hat{u}_\ell$, and $\hat{\mu}_\ell$ are estimated by minimizing (3.25) using the least-squares optimization technique in Section 3.3. The MIO-ID process terminates at step $\ell \geq 1$ when either $J_{\text{MIO},\ell-1} < J_{\text{min}}$ or $\ell > \ell_{\text{max}}$, where J_{min} is a chosen minimal cost function value and ℓ_{max} is the chosen maximum number of optimization iterations. Then, the identified DTLI/CPA model $\mathcal{M}$ is characterized by the estimated parameters

$\hat{n} = \hat{n}_j, \hat{d} = \hat{d}_j, \hat{\lambda} = \hat{\lambda}_j, \hat{\nu}_{\rm n} = \hat{\nu}_{{\rm n},j}, \hat{\nu}_{\rm p} = \hat{\nu}_{{\rm p},j}, \hat{a} = \hat{a}_j, \hat{b} = \hat{b}_j, \hat{u} = \hat{u}_j$, and $\hat{\mu} = \hat{\mu}_j$, where

$$j = \underset{i\in[0,\ell-1]}{\operatorname{argmin}} J_{{\rm MIO},i}. \tag{3.50}$$

The flow chart shown in Figure 3.5 summarizes MIO-ID.

The 1SMIS algorithm, which searches through the $\hat{n}, \hat{d}, \hat{\lambda}, \hat{\nu}_{\rm n}, \hat{\nu}_{\rm p}$ variable space, is a single step of a derivative-free mixed-integer optimization algorithm. To reduce the optimization time, the search space is constrained by setting minimum and maximum feasible values of $\hat{n}, \hat{d}, \hat{\lambda}, \hat{\nu}_{\rm n}$, and $\hat{\nu}_{\rm p}$, which implies that the values of $l_{\rm l}$ and $l_{\rm MIO,l}$ need to be chosen to be greater than the sum of the maximum values set for $\hat{n}$ and $\hat{d}$. In this chapter, the 1SMIS algorithm consists of a single step of a mixed-integer genetic algorithm and is implemented in Matlab by running a single optimization iteration of the `surrogateopt` function. Note that `surrogateopt` chooses the initial values of $\hat{n}, \hat{d}, \hat{\lambda}, \hat{\nu}_{\rm n}$, and $\hat{\nu}_{\rm p}$ based on their corresponding minimum and maximum feasible values.

The choice of certain optimization parameters can determine the resulting identified DTLI/CPA model. In that regard, the following suggestions may improve the identification results:

- Choosing $l_{\rm l}$ and $l_{\rm u}$ to include the transient response of system $\mathcal{S}$.

- In most cases, choosing $l_{\rm l} = l_{\rm MIO,l}$ and $l_{\rm u} = l_{\rm MIO,u}$ will suffice. However, in cases where the oscillatory behavior displayed by the output of system $\mathcal{S}$ is irregular, $l_{\rm l}$ and $l_{\rm u}$ may be chosen to include a representative waveform, while $l_{\rm MIO,l}$ and $l_{\rm MIO,u}$ may be chosen to include more periods of the waveform.

- Increasing the maximum values of $\hat{n}$ and $\hat{d}$ in the case where the output of system $\mathcal{S}$ displays richer frequency content.

- Let z be given by (3.7) with y as the output of system $\mathcal{S}$ and $d = 0$. Then, the maximum values of $\hat{\lambda}$, $\hat{\nu}_{\rm n}$, and $\hat{\nu}_{\rm p}$ can be chosen so that the values of z are within $-\hat{\varepsilon}\hat{\nu}_{\rm n}\hat{\lambda}$ and $\hat{\varepsilon}\hat{\nu}_{\rm p}\hat{\lambda}$.

Algorithm 1 Computation of $J_{\mathrm{MIO},\ell}$

```
**Input:** $\hat{n}_\ell$, $\hat{d}_\ell$, $\hat{\lambda}_\ell$, $\hat{v}_{\mathrm{n},\ell}$, $\hat{v}_{\mathrm{p},\ell}$
**Output:** $J_{\mathrm{MIO},\ell}, \hat{a}_\ell, \hat{b}_\ell, \hat{u}_\ell, \hat{\mu}_\ell$
$\hat{c}_\ell \leftarrow \hat{\varepsilon}\,[-\hat{v}_{\mathrm{n},\ell}\hat{\lambda}_\ell \quad -(\hat{v}_{\mathrm{n},\ell}-1)\hat{\lambda}_\ell \quad \cdots \quad (\hat{v}_{\mathrm{p},\ell}-1)\hat{\lambda}_\ell \quad \hat{v}_{\mathrm{p},\ell}\hat{\lambda}_\ell]^\mathsf{T}$
$\hat{a}_\ell, \hat{b}_\ell, \hat{u}_\ell, \hat{\mu}_\ell \leftarrow \operatorname{argmin}_{a^*,b^*,v^*,\mu^*} J(a^*, b^*, v^*, \mu^*)$
▷ Given $\hat{n}_\ell$, $\hat{d}_\ell$, $\hat{c}_\ell$, and $y_k$ for all $k \in [l_\mathrm{l}, l_\mathrm{u}]$, minimize (3.25) using the least-squares optimization technique in Section 3.3.
$\hat{y} \leftarrow \begin{bmatrix} 0 & \cdots & 0 \end{bmatrix}^\mathsf{T} \in \mathbb{R}^{l_{\mathrm{MIO,u}}+l_{\mathrm{shift,max}}}$
**for** k $\leftarrow \hat{n}_\ell + \hat{d}_\ell + 1$ to $l_{\mathrm{MIO,u}} + l_{\mathrm{shift,max}}$ **do**
    $\hat{y}_k \leftarrow \hat{\varphi}_k^\mathsf{T} \left[\hat{a}_\ell^\mathsf{T} \quad (\mathrm{vec}(\hat{\mu}_\ell \hat{b}_\ell^\mathsf{T}))^\mathsf{T} \quad \hat{u}_\ell 1_{1\times\hat{n}_\ell}\hat{b}_\ell\right]^\mathsf{T}$
**end for**
▷ Simulates DTL model with identified parameters given $\hat{n}_\ell$, $\hat{d}_\ell$, and $\hat{c}_\ell$.
NaNFlag ← isNaN($\hat{y}$)
▷ Determines whether the output of the simulated model yields a NaN response.
$J_{\mathrm{MIO},\ell} \leftarrow \infty$
**if** NaNFlag is true **then**
    **return** $J_{\mathrm{MIO},\ell}, \hat{a}_\ell, \hat{b}_\ell, \hat{u}_\ell, \hat{\mu}_\ell$
**end if**
**for** $j \leftarrow 0$ to $l_{\mathrm{shift}}$ **do**
    $s_{\mathrm{temp}} \leftarrow \sum_{k=l_{\mathrm{MIO,l}}}^{l_{\mathrm{MIO,u}}} \left(y_k - \hat{y}_{k+j}\right)^2$
    **if** $s_{\mathrm{temp}} < J_{\mathrm{MIO},\ell}$ **then**
        $J_{\mathrm{MIO},\ell} \leftarrow s_{\mathrm{temp}}$
    **end if**
**end for**
▷ Local cost function computation with shift to account for the phase shift of the identified model.
**return** $J_{\mathrm{MIO},\ell}, \hat{a}_\ell, \hat{b}_\ell, \hat{u}_\ell, \hat{\mu}_\ell$
```

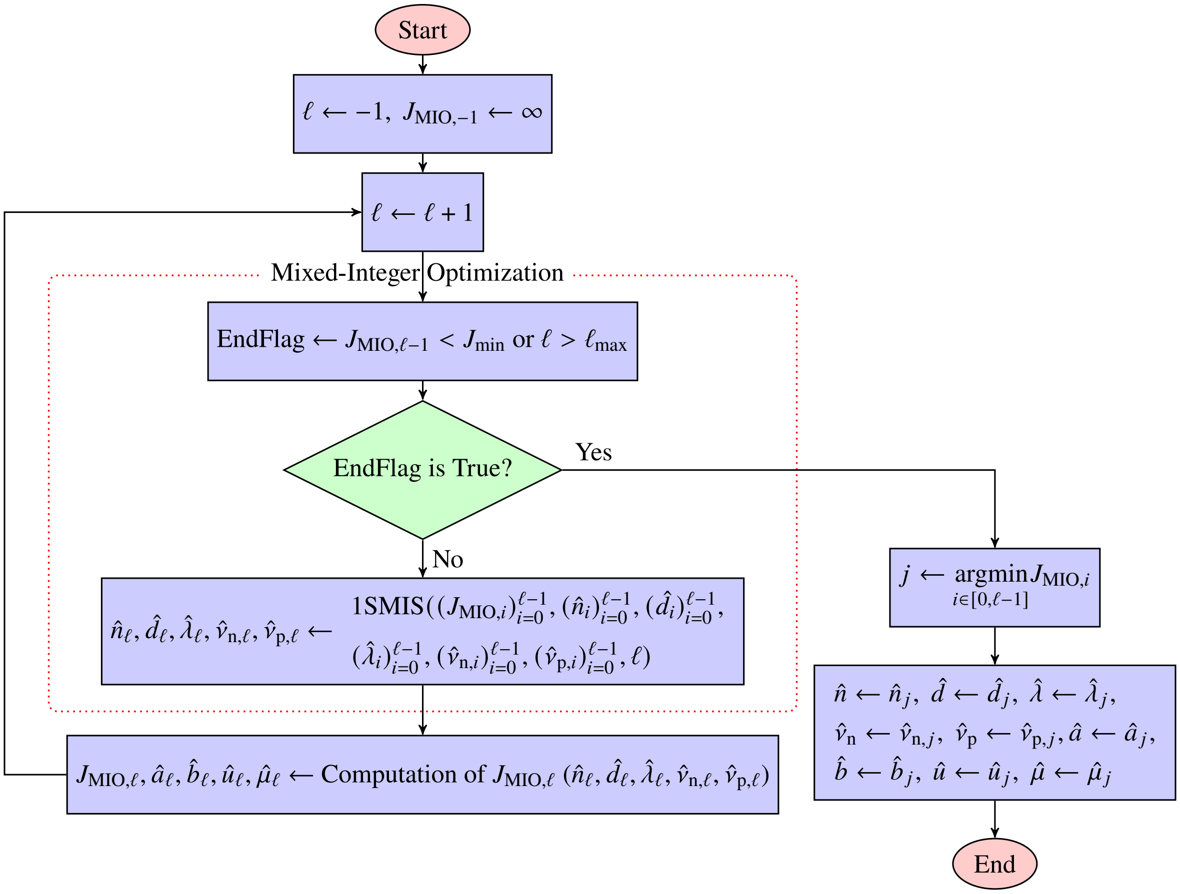

Figure 3.5: Flow chart of mixed-integer-optimization identification (MIO-ID).

3.5 Application of MIO-ID to Numerical and Experimental Data

In this section, we present examples to illustrate the application of MIO-ID to data obtained from numerical simulations from discrete-time and continuous-time systems, and via experiments from sensor data sets. The figures in the following examples provide qualitative evidence of the performance of MIO-ID in producing an estimated model $\mathcal{M}$ whose response approximates that of the studied system $\mathcal{S}$. Table 3.1 summarizes the details of the considered systems.

In the case where $\mathcal{S}$ is a FTDDTL system (Example 3.5.1), the accuracy of MIO-ID is evaluated by comparing the estimates $\hat{G}$ and $\hat{\psi}$ with G and ψ, respectively, and the unidentifiable parameter $\hat{\beta}$ is chosen to minimize the root-mean-square (RMS) fit between ψ and $\hat{\psi}$. Furthermore, the power spectral density (PSD) and the waveforms of the outputs, the nonlinearities, and the frequency responses of the linear dynamics of the studied system $\mathcal{S}$ and the estimated DTLI/CPA model $\mathcal{M}$ are compared.

In the rest of the examples, (Examples 3.5.2, 3.5.3, 3.5.4), since no true nonlinearity is available, the scaling parameter is chosen to be $\hat{\beta} = 1$. Furthermore, the phase portrait of the responses of both the studied system $\mathcal{S}$ and the estimated model $\mathcal{M}$ are displayed to better visualize how the response of $\mathcal{M}$ approximates the limit-cycling behavior of $\mathcal{S}$, in which an estimate of the output derivative is used, such that, for all $k > 1$,

$$\dot{y}_k \triangleq \frac{y_{k+1} - y_{k-1}}{2\tau_{\rm s}}, \tag{3.51}$$

$$\dot{\hat{y}}_k \triangleq \frac{\hat{y}_{k+1} - \hat{y}_{k-1}}{2\tau_{\rm s}}, \tag{3.52}$$

where $\tau_{\rm s}$ denotes the sampling time.

Table 3.1: Summary of Examples of MIO-ID Application

Example	**System Type of $\mathcal{S}$**	**CT or DT**	**$\tau_{\rm s}$ (s)**	**Type of Data**
3.5.1	FTDDTL	DT	–	Numerical
3.5.2	van der Pol Oscillator	CT	0.1	
3.5.3	Lotka-Volterra Model			
3.5.4	Gas-Turbine Combustor Experiment (DISCo)	–	1 / 15000	Experimental

Example 3.5.1: Numerical Data from FTDDTL system

Consider the FTDDTL system $\mathcal{S}$ with $d = 4$,

$$G(\mathbf{q}) = \frac{\mathbf{q} - 0.5}{\mathbf{q}^2 - 1.6\mathbf{q} + 0.8}, \tag{3.53}$$

and the CPA, monotonic, odd ψ shown in Figure 3.6. The domain of ψ is partitioned by $c = \begin{bmatrix} -10 & -9 & \cdots & 9 & 10 \end{bmatrix}^{\rm T}$, and ψ is constructed such that, for all $i \in [1, 21]$, $\psi(c_i) = 18.75 \ \tanh(1.2c_i/2.5)$. To obtain data for identification, y_k is generated by simulating $\mathcal{S}$ subject to $v = 37.5$. For MIO-ID, we let $\hat{n} \in [1, 10]$, $\hat{d} \in [0, 10]$, $\hat{\lambda} \in [1, 2000]$, $\hat{v}_{\rm n} \in [1, 30]$, and $\hat{v}_{\rm p} \in [1, 30]$, with $l_{\rm l} = l_{\rm MIO,l} = 100$, $l_{\rm u} = 500$, and $l_{\rm MIO,u} = 10000$, that is, y_k for all $k \in [100, 500]$ is used for least-squares optimization, and y_k and $\hat{y}_k$ for all $k \in [100, 10000]$ is used to compute $J_{\rm MIO}$.

Figure 3.7 compares the response of the model $\mathcal{M}$ identified using MIO-ID with the response of $\mathcal{S}$. The estimated DTLI/CPA model parameters are

$$\hat{G}(\mathbf{q}) = \frac{1.0002\mathbf{q} - 0.4996}{\mathbf{q}^2 - 1.6000\mathbf{q} + 0.8001}, \tag{3.54}$$

$\hat{d} = 4$, $\hat{u} = 37.46$, $\hat{v}_{\rm n} = 20$, $\hat{v}_{\rm p} = 26$, and $\hat{\psi}$ shown in Figure 3.7. The optimization process required 30.29 s, during which $J_{\rm MIO}$ was computed 263 times. The minimum values of $J_{\rm MIO}$ up to each optimization iteration ℓ are shown in Figure 3.8. Furthermore, the response of the identified model as the number of optimization iterations increase is displayed in Figure 3.9 at three snapshots during MIO-ID, that is, for all $\ell \in \{1, 50, 250\}$.

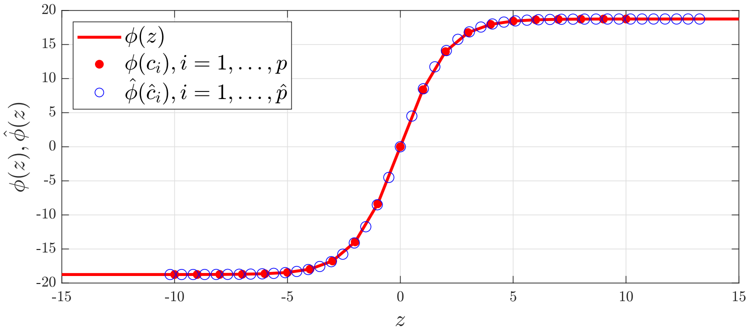

Figure 3.6: Example 3.5.1: Continuous piecewise-affine feedback mapping $\psi(z)$ partitioned by c and the estimated $\hat{\psi}(z)$ partitioned by $\hat{c}$.

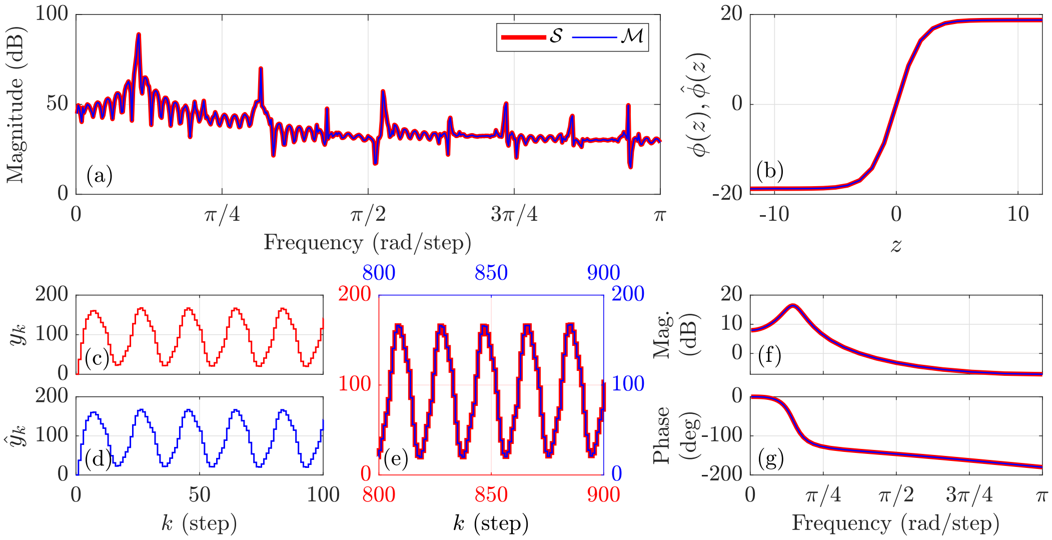

Figure 3.7: Example 3.5.1: MIO-ID of FTDDTL system using noiseless measurements. (a) compares the PSD of the output of $\mathcal{S}$ with the PSD of the output of $\mathcal{M}$. (b) shows ψ of $\mathcal{S}$ and $\hat{\psi}$ of $\mathcal{M}$. (c) shows the output y_k of $\mathcal{S}$ with $v = 37.5$ for all $k \in [0, 100]$. (d) shows the output $\hat{y}_k$ of $\mathcal{M}$ with $\hat{u} = 37.46$. (e) shows the output y_k of $\mathcal{S}$ and the output $\hat{y}_k$ of $\mathcal{M}$ for all $k \in [800, 900]$. (f) and (g) compare the frequency responses G and $\hat{G}$.

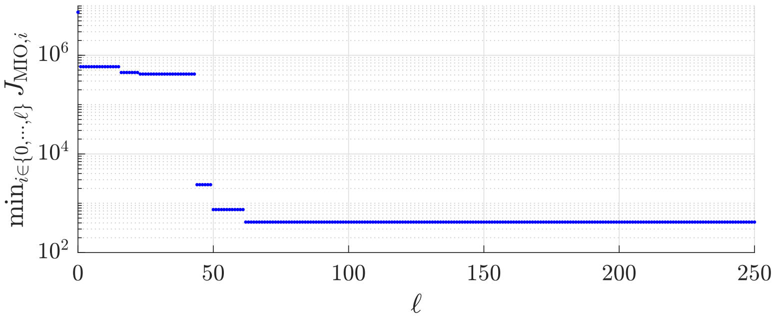

Figure 3.8: Example 3.5.1: Minimal cost $\min\limits_{i\in[0,\ell]} J_{\text{MIO},i}$ up to iteration ℓ used in MIO-ID. The identified model $\mathcal{M}$, whose response is shown in Figure 3.7 is obtained by minimizing (3.43).

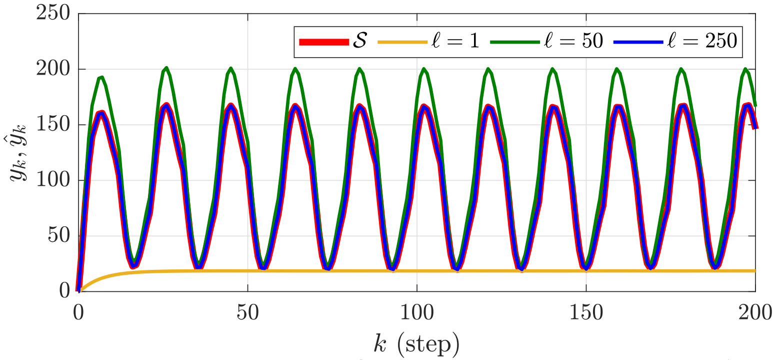

Figure 3.9: Example 3.5.1: Responses of $\mathcal{S}$ and the identified model $\mathcal{M}$ that minimizes J_{MIO} as the number of optimization iterations increases. The responses of $\mathcal{M}$ are displayed for all $\ell \in \{1, 50, 250\}$.

Now, consider the output of $\mathcal{S}$ with sensor noise with standard deviation $\sqrt{1.5}$, which yields an output signal with 30 dB SNR. Figure 3.10 compares the response of the model $\mathcal{M}$ identified using MIO-ID in the presence of noisy measurements with the response of $\mathcal{S}$. The estimated DTLI/CPA model parameters are

$$\hat{G}(\mathbf{q}) = \frac{1.0911\mathbf{q}^2 - 0.1186\mathbf{q} - 0.2134}{\mathbf{q}^3 - 1.2092\mathbf{q}^2 + 0.1745\mathbf{q} + 0.3128}, \tag{3.55}$$

$\hat{d} = 4$, $\hat{u} = 34.345$, $\hat{\nu}_{\text{n}} = 4$, $\hat{\nu}_{\text{p}} = 12$, and $\hat{\psi}$ shown in Figure 3.10. The optimization process required 95.55 s, during which J_{MIO} was computed 767 times.

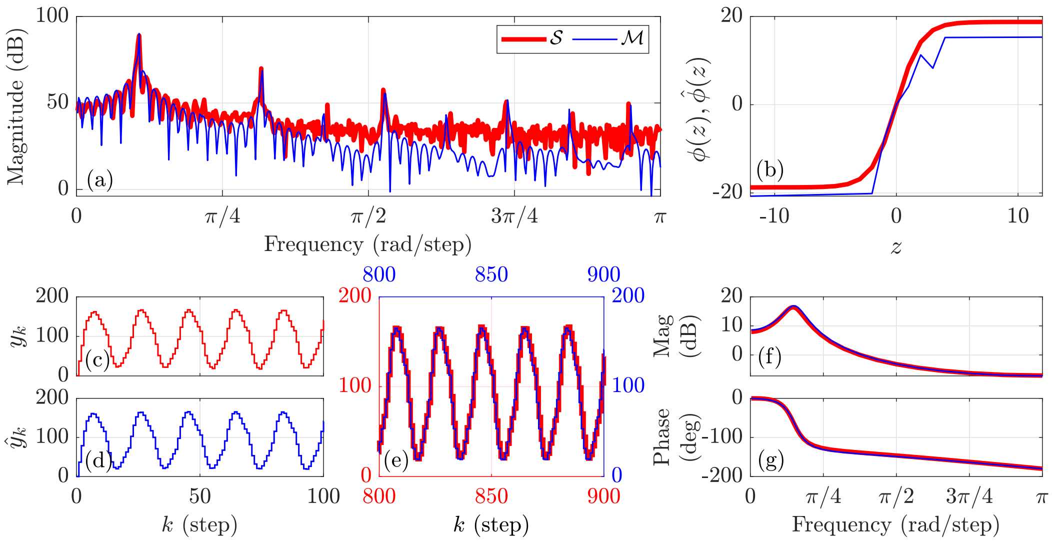

Figure 3.10: Example 3.5.1: MIO-ID of FTDDTL system using noisy measurements. (a) compares the PSD of the output of $\mathcal{S}$ with the PSD of the output of $\mathcal{M}$. (b) shows ψ of $\mathcal{S}$ and $\hat{\psi}$ of $\mathcal{M}$. (c) shows the output y_k of $\mathcal{S}$ with $v = 37.5$ for all $k \in [0, 100]$. (d) shows the output $\hat{y}_k$ of $\mathcal{M}$ with $\hat{u} = 34.345$ for all $k \in [0, 100]$. (e) shows the output y_k of $\mathcal{S}$ and the output $\hat{y}_k$ of $\mathcal{M}$ for all $k \in [800, 900]$. (f) and (g) compare the frequency responses of G and $\hat{G}$.

Figure 3.11 shows the time domain responses of identified models estimated via MIO-ID by fixing $\hat{n}$ and $\hat{d}$, such that $\{\hat{n},\ \hat{d}\} \in \{1, 2, 3\} \times \{2, 3, 4\}$. Note that small changes in $\hat{n}$ and $\hat{d}$ can yield significantly different responses and thus different values of $J_{\rm MIO}$. The complex changes of $J_{\rm MIO}$ over the $\hat{n}, \hat{d}, \hat{\lambda}, \hat{\nu}_1, \hat{\nu}_{\rm p}$ parameter space motivated the use of a genetic algorithm for mixed-integer optimization. Furthermore, note that, in the cases where $\hat{d} = d$ and $\hat{n} > n$, the responses of the identified models are very similar to those of $\mathcal{S}$, which implies that, under appropriate coefficients, higher order linear systems can approximate the response of lower order linear systems. ◇

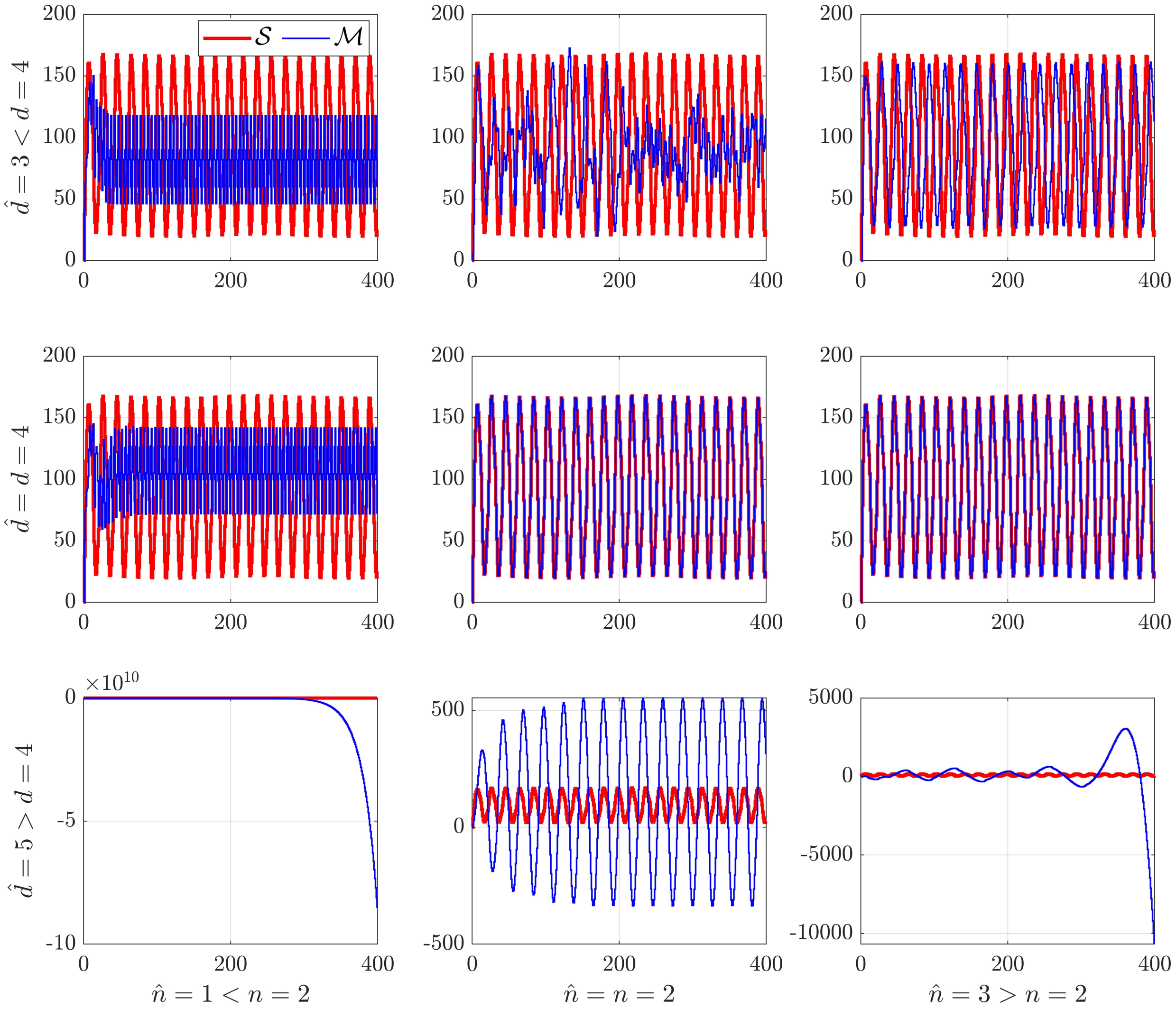

Figure 3.11: Example 3.5.1: MIO-ID of FTDDTL system with fixed $\hat{n}$ and $\hat{d}$, such that $\{\hat{n},\ \hat{d}\} \in \{1, 2, 3\} \times \{2, 3, 4\}$. These plots compare the output $\hat{y}_k$ of the identified model $\mathcal{M}$ with the output y_k of system $\mathcal{S}$ for all $k \in [0, 400]$.

Example 3.5.2: Numerical Data from van der Pol Oscillator

Let $\mathcal{S}$ be the continuous-time van der Pol system, given by

$$\dot{x}(t) = \begin{bmatrix} 0 & 1 \\ -1 & 0 \end{bmatrix} x(t) + \begin{bmatrix} 0 \\ \gamma \end{bmatrix} \psi(x(t)), \tag{3.56}$$

$$y(t) = \begin{bmatrix} 1 & 0 \end{bmatrix} x(t), \tag{3.57}$$

$$\psi(x(t)) = (1 - x_1^2(t))x_2(t), \tag{3.58}$$

where, for all $t \geq 0$, $x(t) = [x_1(t)\ \ x_2(t)]^{\mathsf{T}}$, $y(t) = x_1(t)$, $\gamma = 1$, $x_1(0) = y(0) = 0.1$, and $x_2(0) = 0$. To obtain data for identification, for all $t > 0$, the van der Pol model is simulated using ode45, and the output is sampled with sampling time $\tau_{\rm s} = 0.1$ s. The integration accuracy of ode45 is set so that approximately 160 integration steps are implemented within each sample interval. For identification, we let $\hat{n} \in [1, 20]$, $\hat{d} \in [0, 25]$, $\hat{\lambda} \in [10, 1000]$, $\hat{\nu}_{\rm n} \in [1, 15]$, and $\hat{\nu}_{\rm p} \in [1, 15]$, with $l_{\rm l} = l_{\rm MIO,l} = 500$, $l_{\rm u} = 3000$, and $l_{\rm MIO,u} = 20000$ that is, y_k for all $k \in [500, 3000]$ is used for least-squares optimization, and y_k and $\hat{y}_k$ for all $k \in [500, 20000]$ is used to compute $J_{\rm MIO}$.

Figure 3.12 compares the response of the model $\mathcal{M}$ identified using MIO-ID in the presence of noiseless measurements with the response of $\mathcal{S}$. Figure 3.12 also compares the phase portraits of the continuous-time system $\mathcal{S}$, and the identified model $\mathcal{M}$ using (3.51) and (3.52) to approximate the derivative of the output. The estimated DTLI/CPA model parameters are $\hat{n} = 13$, $\hat{d} = 11$, $\hat{\nu}_{\rm n} = 9$, $\hat{\nu}_{\rm p} = 10$, $\hat{u} = -70.77 \cdot 10^{-4}$, $\hat{G}$ with a frequency response shown in Figure 3.13, and $\hat{\psi}$ shown in Figure 3.13.

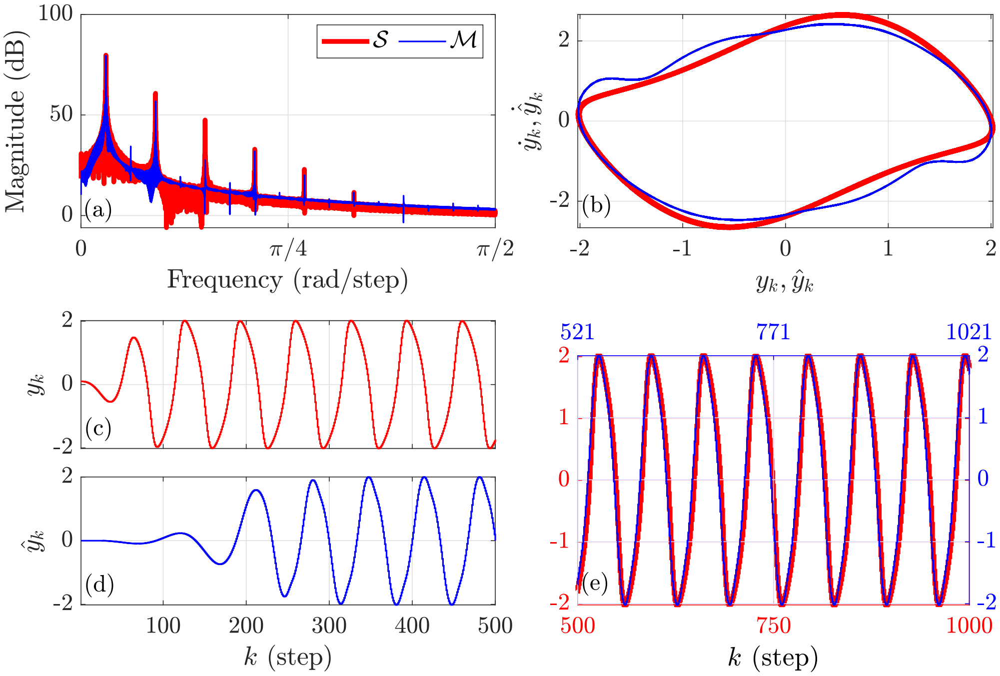

Figure 3.12: Example 3.5.2: MIO-ID of the continuous-time van der Pol oscillator using noiseless measurements. For the sampling time $\tau_{\rm s} = 0.1$ s, (a) compares the PSD of the output of $\mathcal{S}$ with the PSD of the output of $\mathcal{M}$. (b) shows the phase portraits of the response y of the continuous-time van der Pol system $\mathcal{S}$ and the response $\hat{y}$ of the identified model $\mathcal{M}$. The derivatives of the outputs are approximated using (3.51) and (3.52) with $\tau_{\rm s} = 0.1$ s. (c) shows the output y_k of $\mathcal{S}$ for all $k \in [0, 500]$. (d) shows the output $\hat{y}_k$ of $\mathcal{M}$ with $\hat{u} = -70.77 \cdot 10^{-4}$ for all $k \in [0, 500]$. (e) shows the sampled output y_k of $\mathcal{S}$ for all $k \in [500, 1000]$, and the output $\hat{y}_k$ of $\mathcal{M}$ for all $k \in [521, 1021]$.

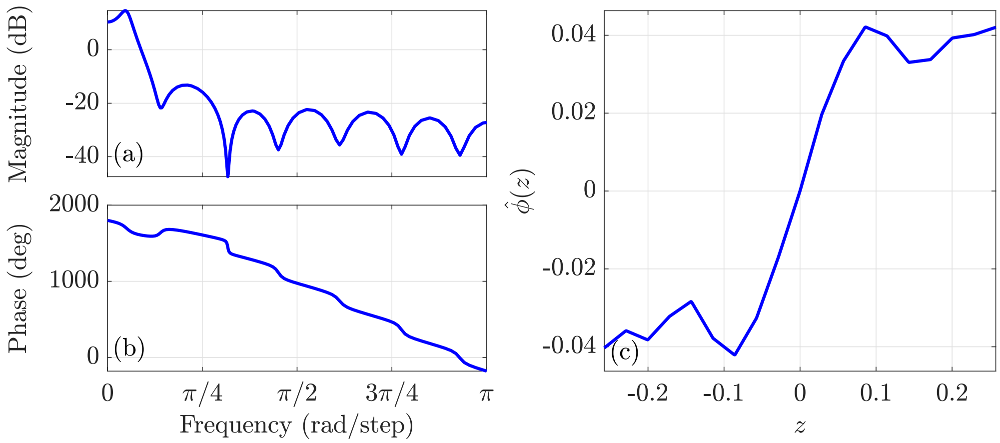

Figure 3.13: Example 3.5.2: MIO-ID of the continuous-time van der Pol oscillator using noiseless measurements. (a) and (b) show the frequency response of $\hat{G}$. (c) shows the estimated nonlinearity $\hat{\psi}$ of $\mathcal{M}$.

Next, consider the output of $\mathcal{S}$ with sensor noise that yields an output signal with 30 dB SNR. Figure 3.14 compares the response of the model $\mathcal{M}$ identified using MIO-ID in the presence of noisy measurements with the response of $\mathcal{S}$. Figure 3.14 also compares the phase portraits of the continuous-time system $\mathcal{S}$, with and without sensor noise, and the identified model $\mathcal{M}$ using (3.51) and (3.52) to approximate the derivative of the output. The estimated DTLI/CPA model parameters are $\hat{n} = 47$, $\hat{d} = 7$, $\hat{\nu}_{\rm n} = 16$, $\hat{\nu}_{\rm p} = 10$, $\hat{u} = -0.4624$, $\hat{G}$ with a frequency response shown in Figure 3.15, and $\hat{\psi}$ shown in Figure 3.15. $\diamond$

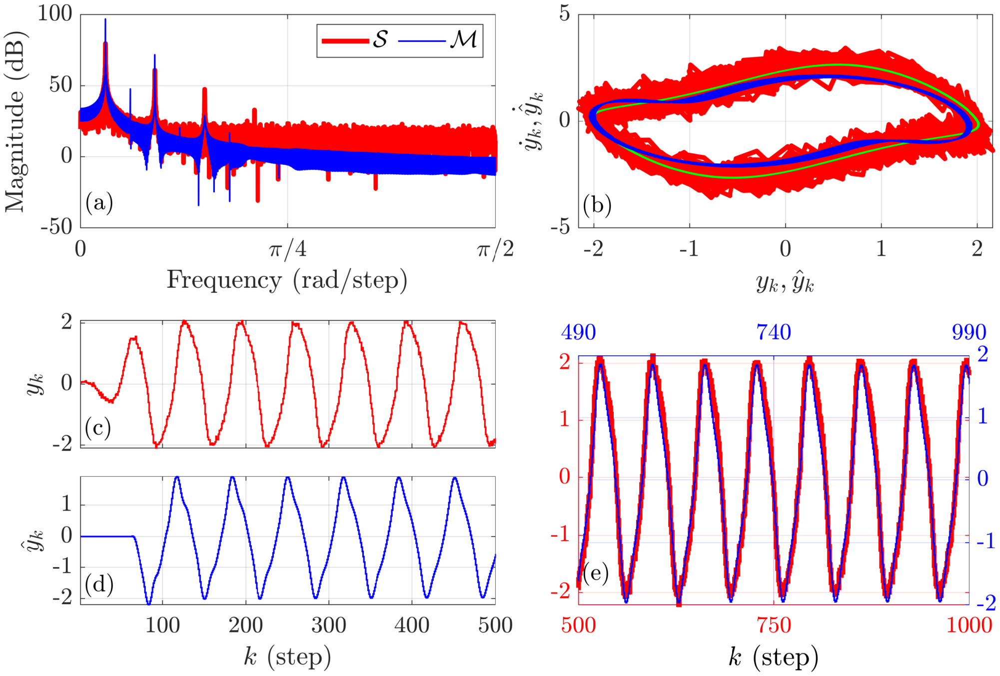

Figure 3.14: Example 3.5.2: MIO-ID of the continuous-time van der Pol oscillator with 30 dB SNR. For the sampling time $\tau_s = 0.1$ s, (a) compares the PSD of the output of $\mathcal{S}$ with the PSD of the output of $\mathcal{M}$. (b) shows the phase portraits of the response y of the continuous-time van der Pol system $\mathcal{S}$ with sensor noise, response of the continuous-time van der Pol system $\mathcal{S}$ without sensor noise in green, and the response $\hat{y}$ of the identified model $\mathcal{M}$. The derivatives of the outputs are approximated using (3.51) and (3.52) with $\tau_s = 0.1$ s. (c) shows the output y_k of $\mathcal{S}$ for all $k \in [0, 500]$. (d) shows the output $\hat{y}_k$ of $\mathcal{M}$ with $\hat{u} = 0.6444$ for all $k \in [0, 500]$. (e) shows the sampled output y_k of $\mathcal{S}$ for all $k \in [500, 1000]$, and the output $\hat{y}_k$ of $\mathcal{M}$ for all $k \in [490, 990]$.

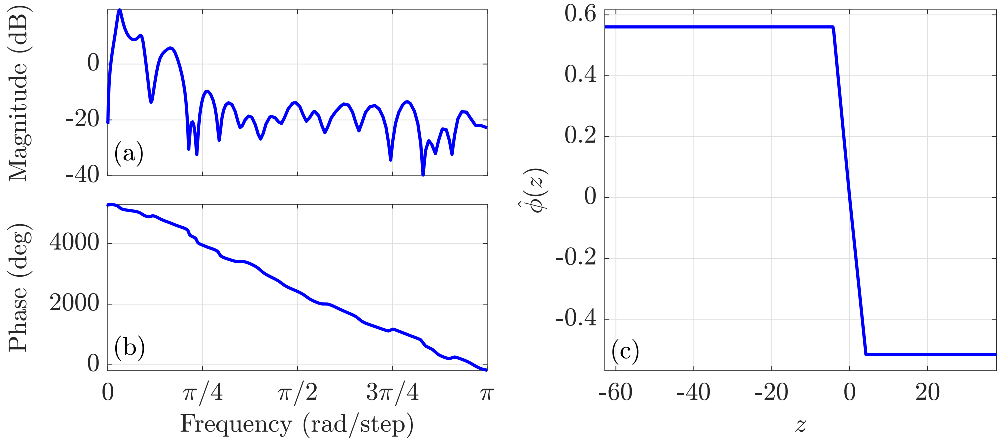

Figure 3.15: Example 3.5.2: MIO-ID of the continuous-time van der Pol oscillator with 30 dB SNR. (a) and (b) show the frequency response of $\hat{G}$. (c) shows the estimated nonlinearity $\hat{\psi}$.

Example 3.5.3: Numerical Data from Lotka-Volterra Model

Let $\mathcal{S}$ be the continuous-time Lotka-Volterra model, given by

$$\dot{x}(t) = \begin{bmatrix} \alpha & 0 \\ 0 & -\gamma \end{bmatrix} x(t) + \begin{bmatrix} -\zeta \\ \xi \end{bmatrix} \psi(x(t)), \tag{3.59}$$

$$y(t) = \begin{bmatrix} 1 & 0 \end{bmatrix} x(t), \tag{3.60}$$

$$\psi(x(t)) = x_1(t)x_2(t), \tag{3.61}$$

where, for all $t \geq 0$, $x(t) = [x_1(t) \ \ x_2(t)]^{\mathsf{T}}$, $y(t) = x_2(t)$, $\alpha = 2/3$, $\gamma = 1$, $\zeta = 4/3$, $\xi = 1$, and $x_1(0) = x_2(0) = y(0) = 1$. To obtain data for identification, for all $t > 0$, the Lotka-Volterra model is simulated using ode45, and the output is sampled with sampling time $\tau_{\mathrm{s}} = 0.1$ s. The integration accuracy of ode45 is set so that approximately 160 integration steps are implemented within each sample interval. For identification, we let $\hat{n} \in [1, 30]$, $\hat{d} \in [0, 30]$, $\hat{\lambda} \in [10, 5000]$, $\hat{\nu}_{\mathrm{n}} \in [1, 10]$, and $\hat{\nu}_{\mathrm{p}} \in [1, 10]$, with $l_{\mathrm{l}} = l_{\mathrm{M,l}} = 100$ and $l_{\mathrm{u}} = l_{\mathrm{M,u}} = 10000$, that is, y_k for all $k \in [100, 10000]$ is used for identification. Figure 3.16 compares the response of the model $\mathcal{M}$, identified using MIO-ID, with the response of $\mathcal{S}$. Figure 3.16 also compares the phase portraits of the continuous-time system $\mathcal{S}$ and the identified model $\mathcal{M}$ using (3.51) and (3.52) to approximate the derivative of the output. The estimated DTLI/CPA model parameters are $\hat{n} = 14$, $\hat{d} = 16$, $\hat{\nu}_{\mathrm{n}} = 7$, $\hat{\nu}_{\mathrm{p}} = 7$, $\hat{u} = 0.258$, $\hat{G}$ with a frequency response shown in Figure 3.17, and $\hat{\psi}$ shown in Figure 3.17.

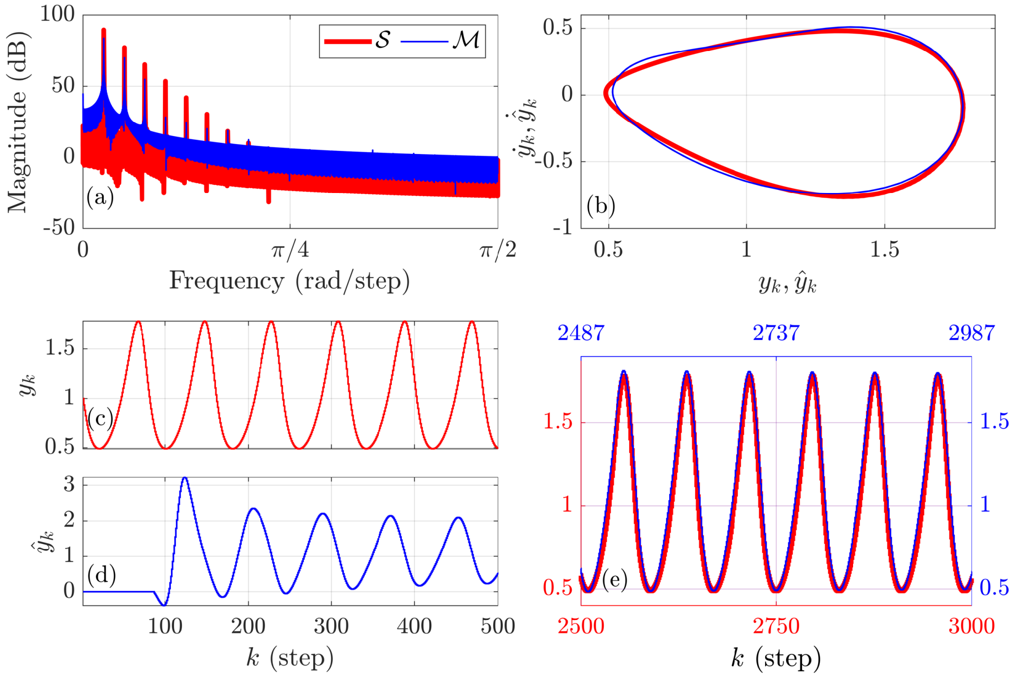

Figure 3.16: Example 3.5.3: MIO-ID of the continuous-time Lotka-Volterra model using noiseless measurements. (a) compares the PSD of the output of $\mathcal{S}$ with sampling time $\tau_\mathrm{s} = 0.1$ s, with the PSD of the output of $\mathcal{M}$. (b) shows the phase portraits of the response y of the continuous-time van der Pol system $\mathcal{S}$ and the response $\hat{y}$ of the identified model $\mathcal{M}$. The derivatives of the outputs are approximated using (3.51) and (3.52) with $\tau_\mathrm{s} = 0.1$ s. (c) shows the output y_k of $\mathcal{S}$ for all $k \in [0, 500]$. (d) shows the output $\hat{y}_k$ of $\mathcal{M}$ with $\hat{u} = 0.258$ for all $k \in [0, 500]$. (e) shows the sampled output y_k of $\mathcal{S}$ for all $k \in [2500, 3000]$, and the output $\hat{y}_k$ of $\mathcal{M}$ for all $k \in [2487, 2987]$.

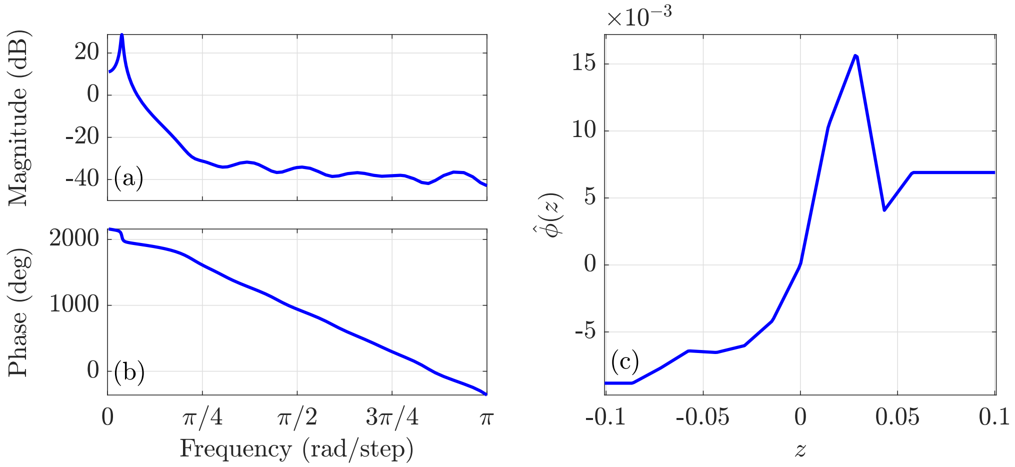

Figure 3.17: Example 3.5.3: MIO-ID of the continuous-time Lotka-Volterra model using noiseless measurements. (a) and (b) show the frequency response of $\hat{G}$. (c) shows the estimated nonlinearity $\hat{\psi}$.

Next, consider the output of $\mathcal{S}$ with sensor noise that yields an output signal with 30 dB SNR.

Figure 3.18 compares the response of the model $\mathcal{M}$ identified using MIO-ID in the presence of noisy measurements with the response of $\mathcal{S}$. Figure 3.18 also compares the phase portraits of the continuous-time system $\mathcal{S}$, with and without sensor noise, and the identified model $\mathcal{M}$ using (3.51) and (3.52) to approximate the derivative of the output. The estimated DTLI/CPA model parameters are $\hat{n} = 48$, $\hat{d} = 25$, $\hat{\nu}_{\rm n} = 7$, $\hat{\nu}_{\rm p} = 12$, $\hat{u} = -3.3042$, $\hat{G}$ with a frequency response shown in Figure 3.19, and $\hat{\psi}$ shown in Figure 3.19. $\diamond$

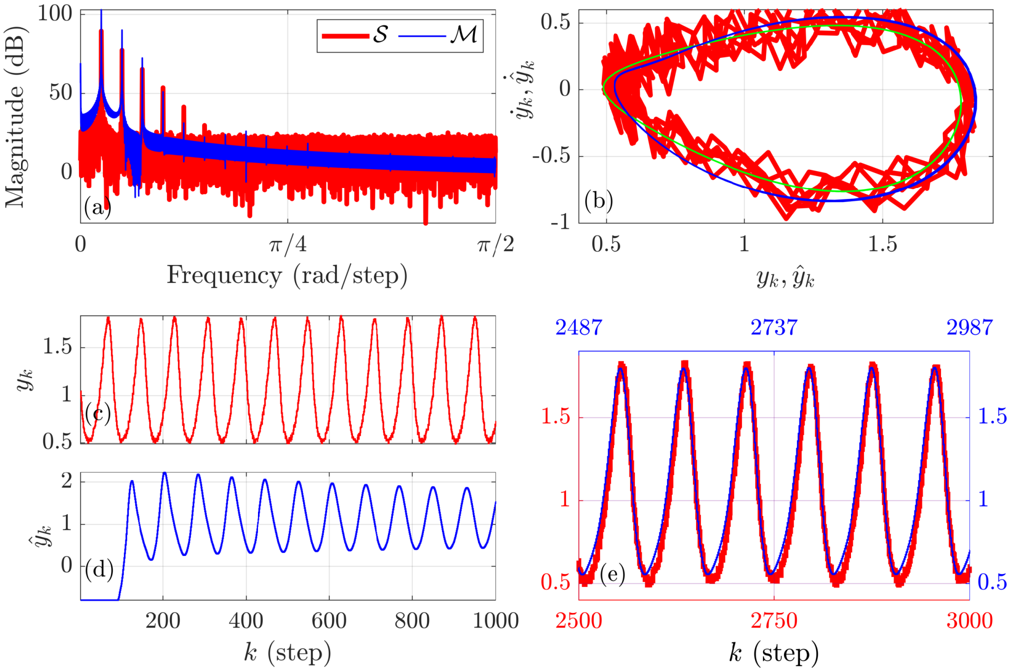

Figure 3.18: Example 3.5.3: MIO-ID of the continuous-time Lotka-Volterra model with 30 dB SNR. (a) compares the PSD of the output of $\mathcal{S}$ with sampling time $\tau_{\rm s} = 0.1$ s, with the PSD of the output of $\mathcal{M}$. (b) shows the phase portraits of the response y of the continuous-time van der Pol system $\mathcal{S}$ with sensor noise, response of the continuous-time Lotka-Volterra model $\mathcal{S}$ without sensor noise in green, and the response $\hat{y}$ of the identified model $\mathcal{M}$. The derivatives of the outputs are approximated using (3.51) and (3.52) with $\tau_{\rm s} = 0.1$ s. (c) shows the output y_k of $\mathcal{S}$ for all $k \in [0, 500]$. (d) shows the output $\hat{y}_k$ of $\mathcal{M}$ with $\hat{u} = 0.258$ for all $k \in [0, 500]$. (e) shows the sampled output y_k of $\mathcal{S}$ for all $k \in [2500, 3000]$, and the output $\hat{y}_k$ of $\mathcal{M}$ for all $k \in [2487, 2987]$.

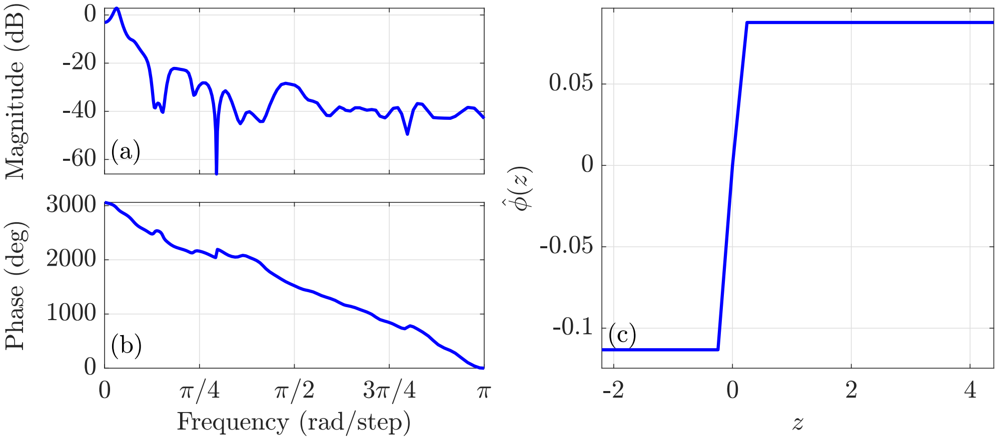

Figure 3.19: Example 3.5.3: MIO-ID of the continuous-time Lotka-Volterra model with 30 dB SNR. (a) and (b) show the frequency response of $\hat{G}$. (c) shows the estimated nonlinearity $\hat{\psi}$.

Example 3.5.4: Experimental Data of Thermoacoustic Oscillations from Gas-Turbine Combustor

In this example, experimental data obtained from a recording of the sound generated by thermoacoustic oscillations during the operation of a gas-turbine combustor is used for identification. Let $\mathcal{S}$ be the Dual Independent Swirl Combustor Facility (DISCo), featured in [88] and in Chapter 5. More information abuot DISCo wil be provided in Chapter 5. The data used for identification was obtained from a microphone (Kulite type MIC-190L) placed in the combustion chamber, as is shown in Figure 3.20, with a sensitivity of 9 Pa/mV, computed after the signal is amplified. The pressure measurements from this sensor were acquired at a sampling rate of 15 kHz. The microphone measurements used for identification are obtained from a run of the DISCo system in which the manipulated mass flow rates are kept constant and are shown in Figure 3.21.

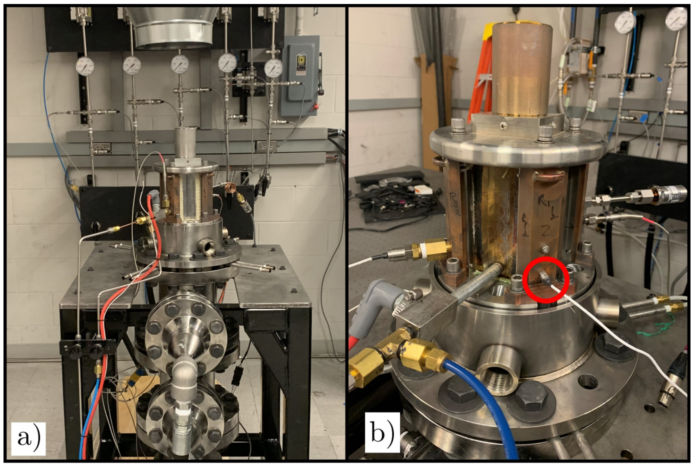

Figure 3.20: Example 3.5.4: DISCo facility. a) Commissioned DISCo facility in atmospheric condition. b) Placement of microphone in the combustion chamber used for pressure data recording.

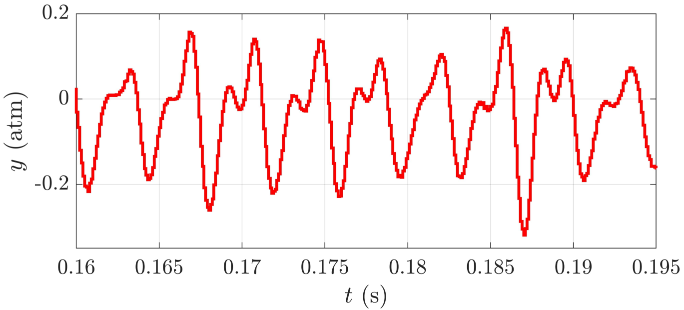

Figure 3.21: Example 3.5.4: Original signal from DISCo combustor

For identification, we let $\hat{n} \in [1, 75]$, $\hat{d} \in [0, 75]$, $\hat{\lambda} \in [1, 20000]$, $\hat{\nu}_{\rm n} \in [1, 30]$, and $\hat{\nu}_{\rm p} \in [1, 30]$, with $l_{\rm l} = 2505$, $l_{\rm u} = 2685$, $l_{\rm MIO,l} = 1000$, and $l_{\rm MIO,u} = 60000$ that is, y_k for all $k \in [2505, 2685]$ is used for least-squares optimization, and y_k and $\hat{y}_k$ for all $k \in [1000, 60000]$ is used to compute $J_{\rm MIO}$. This arrangement was chosen due to the irregularity of the oscillatory behavior displayed by the data. A representative waveform from the available data is chosen to minimize J, and this waveform is used to determine the accuracy of the identified model. Figure 3.22 compares the response of the model identified using MIO-ID with the measurements obtained from the combustor. Furthermore, Figure 3.22 compares the phase portraits of the combustor data (system $\mathcal{S}$) and the identified model $\mathcal{M}$ using (3.51) and (3.52) to approximate the derivative of the output with $\tau_{\rm s} = 1/15000$ s. The estimated DTLI/CPA model parameters are $\hat{n} = 59$, $\hat{d} = 26$, $\hat{\nu}_{\rm n} = 9$, $\hat{\nu}_{\rm p} = 8$, $\hat{u} = 0.7765$, the frequency response of $\hat{G}$ is shown in Figure 3.23, and $\hat{\psi}$ is shown in Figure 3.23. ◇

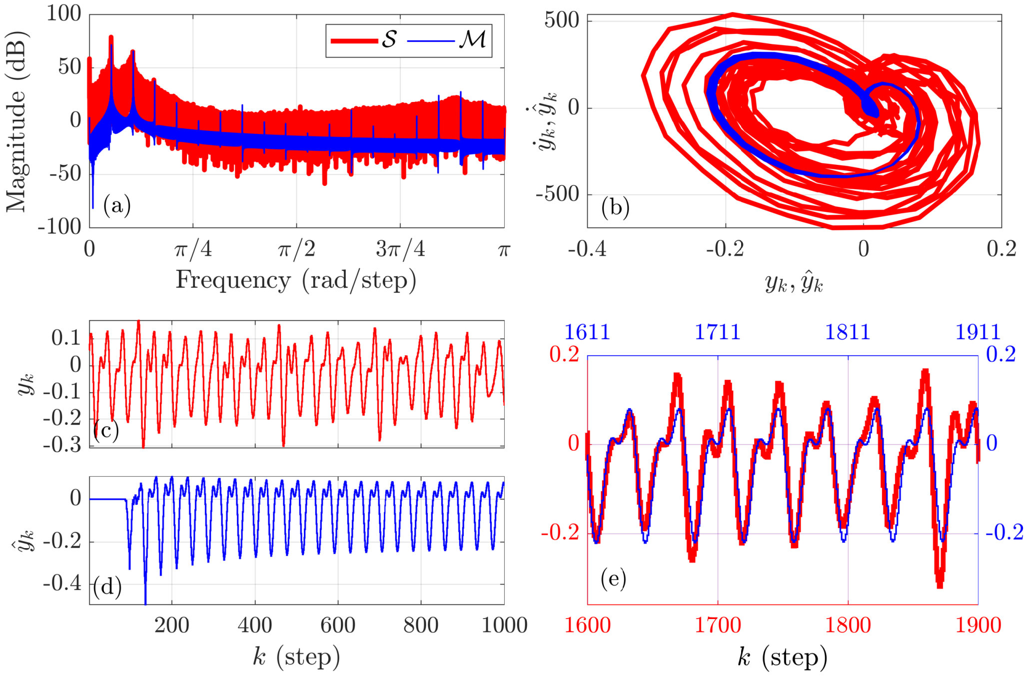

Figure 3.22: Example 3.5.4: MIO-ID using the data from a recording of sound generated by thermoacoustic oscillations during the operation of a gas-turbine combustor. (a) compares the PSD of the sampled output of $\mathcal{S}$ with the PSD of the output of $\mathcal{M}$. (b) shows the estimated phase portraits of the response y of $\mathcal{S}$ and the response $\hat{y}$ of the identified model $\mathcal{M}$. The derivatives of the outputs of $\mathcal{S}$ and $\mathcal{M}$ are approximated using (3.51) and (3.52) with $\tau_{\rm s} = 1/f_{\rm s}$ s and $f_{\rm s} = 15$ kHz. (c) shows the output y_k of $\mathcal{S}$ for all $k \in [0, 1000]$. (d) shows the output $\hat{y}_k$ of $\mathcal{M}$ with $\hat{u} = 0.7765$ for all $k \in [0, 1000]$. (e) shows the output y_k of $\mathcal{S}$ for all $k \in [1600, 1900]$, and the output $\hat{y}_k$ of $\mathcal{M}$ for all $k \in [1611, 1911]$.

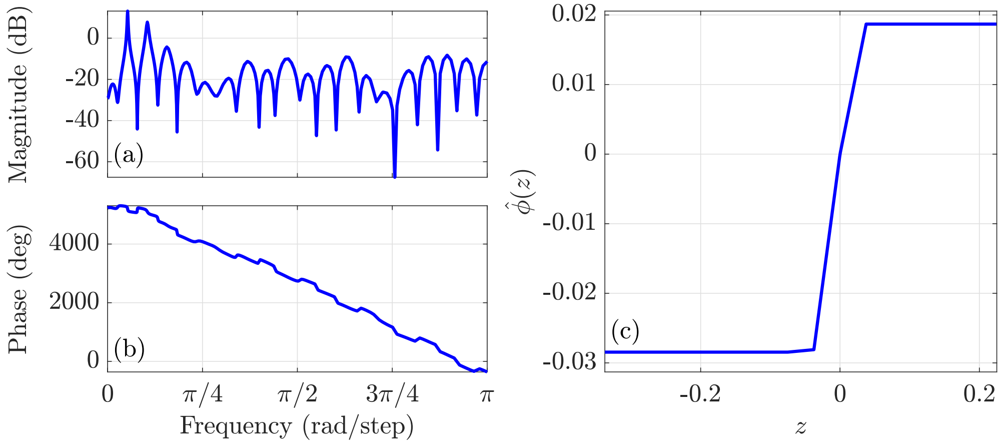

Figure 3.23: Example 3.5.4: MIO-ID using the data from a recording of sound generated by thermoacoustic oscillations during the operation of a gas-turbine combustor. (a) and (b) show the frequency response of linear dynamics $\hat{G}$ of $\mathcal{M}$. (c) shows the estimated nonlinearity $\hat{\psi}$ of $\mathcal{M}$.

3.6 Conclusions

This chapter presented a framework for identifying SES's based on a DTL model. The nonlinear feedback function was chosen to be CPA parameterized by its slope in each interval of a partition of the real line. A mixed-integer optimization approach was used for parameter estimation within the DTLI model as an extension of the technique presented in [53]. This approach allows optimization of the model parameters that were previously chosen manually, thus improving the identification accuracy and reducing the effort required by the user. Numerical examples included both discrete-time and continuous-time systems with noiseless and noisy sampled data. Finally, the MIO-ID was applied to a data set obtained from DISCo, which resulted in a DTLI model that closely reproduced the oscillatory behavior displayed by the combustor. Although the combustor does not have the structure of a DTL model, the system identification technique was able to approximately reproduce the phase-plane dynamics of these systems. The successful implementation of MIO-ID validates the choice of Lur'e models and model properties obtained in Chapter 2. The self-excitation model properties obtained in the previous two chapter will be used to construct a SES model in Chapter 4.

CHAPTER 4

Adaptive Suppression of Thermoacoustic Oscillations in a Rijke Tube

As mentioned in the introduction to this dissertation, a widely studied SES is the Rijke tube, which consists of a cylinder and a heating element. A Rijke tube is a spatially one-dimensional thermoacoustic system that is highly susceptible to thermoacoustic oscillation. Under constant heating, the Rijke tube undergoes self-excited oscillations due to the interaction between the heat source and fluid dynamics. The physics of the Rijke tube have been extensively analyzed, with the original work by Rijke [18] and subsequent work of Lord Rayleigh [19]. In particular, Rayleigh showed that, under certain conditions involving heat and geometry, thermoacoustic oscillations arise from the feedback interaction of the expansion and compression of the air and the heat flux. In thermoacoustic oscillations, the positive feedback between the acoustic field of the system and the unsteady rate of heat release from combustion creates pressure waves whose amplitude increases until it is limited by nonlinear effects. Self-excited pressure oscillations can cause structural vibrations within a combustor, which results in premature component wear and thus reduced lifespan of the combustor, reduced efficiency, and possible system failure [30, 89, 90] [91, pp. 3–26].

A Rijke tube provides an ideal venue for developing and implementing modeling and control techniques for SES. In particular, a laboratory-scale Rijke tube requires only a suitable tube and heating element; for feedback control, a microphone and speaker provide high-authority, high-bandwidth sensing and actuation. All of these components are inexpensive and accessible to classroom demonstrations. Most importantly, control experiments involving a Rijke tube are safe to run since no damage is incurred when the feedback controller inadvertently amplifies the thermoacoustic oscillations. The most expensive component needed for digital feedback control is the processor for controller implementation. For the adaptive control experiments reported in the present work, we use a dSpace Scalexio system; low-power embedded processors are sufficient, however, for implementing fixed-gain control laws.

Extensive research has been devoted to modeling thermoacoustic oscillations [1, 20–26] and suppressing these instabilities using a wide variety of techniques [12, 92, 93]. Experimental applications of various control algorithms are reported; in particular, [94–96] implement phase-shift controllers, [97] implements an LMS controller, [98] implements LQG and H_∞ controllers, [99] implements self-tuning regulators, [100] implements a time-averaged gradient controller, [101] implements an LQG controller and a Nussbaum adaptive controller, [102] implements an adaptive controller based on dynamic compensation, [103] implements a neural-network controller, and [104] proposes a backstepping-based controller. An interesting aspect of these control studies is the fact that, although a Rijke tube is an SES and thus is nonlinear, all of the techniques applied to the Rijke tube in [1, 94–96, 98, 101] are based on linear models and methodologies. These results show that linear controllers are effective for this nonlinear system. Furthermore, as mentioned in [12], while model-based controllers may suffer loss of performance due to uncertainty or changes in operating conditions, adaptive controllers can achieve suppression over a wide range of operating conditions. However, model-based controllers require detailed modeling information about the system in order to achieve closed-loop stability and robustness. To reduce the need for modeling, a data-driven, adaptive controller that requires minimal modeling information is desirable.

The goal of this chapter is to experimentally investigate the modeling requirements, performance, and robustness of retrospective cost adaptive control (RCAC) [105, 106] for suppressing thermoacoustic oscillations in a Rijke tube. The focus of this chapter is on the experimental application of data-driven control. Stability analysis for RCAC is discussed in [107]; however, within the current experimental data-driven context, no theoretical truth model is available. A crucial aspect of the adaptive controller is the selection of hyperparameters, which determine the speed of adaptation, the assumed modeling information, and the controller order. Hence, a hyperparameter selection procedure based on closed-loop numerical simulation is developed in this chapter. For this purpose, a physical model is constructed in this chapter using the insight on SES's gained in Chapters 2 and 3; in particular, a linear feedback model for a Rijke tube is augmented with a nonlinearity in a feedback to yield parameterically stable nonlinear oscillations, as suggested by the results shown in Chapters 2 and 3. After the hyperparameter selection procedure, the adaptive controller is implemented in a physical Rijke tube experiment. The main goal of these experiments is to examine the properties of the controller under various experimental scenarios, including the effect of modified hyperparameters on the time it takes for the adaptive controller to suppress oscillations, the performance and robustness of the frozen-gain adaptive controller, the ability of the adaptive controller to readapt under changes in working conditions, the stability of the adaptive controller under changes in its gain, and the effect of the relative degree of the closed-loop target model on the level of suppression. The experimental scenarios are designed to test the robustness of the adaptive controller under off-nominal perturbations that reflect real-world conditions. The level of suppression of the thermoacoustic oscillations, referred to as oscillation suppression, is used to evaluate the performance of the controller, which is defined to be the ratio of the steady-state open-loop maximum time-domain pressure amplitude to the steady-state closed-loop maximum time-domain pressure amplitude in dB.

The contents of this chapter are as follows. Section 4.1 presents the Rijke-tube physical experimental. Section 4.2 presents an overview of the hyperparameter selection methodology applied to the Rijke-tube experiment. Section 4.3 presents a Rijke-tube model, in which the insight obtained from Chapters 2 and 3 is used to augment the physics-based model proposed in [20, 95]. Section 4.4 presents the parameters used in the Rijke-tube model given in Section 4.3 to obtain a Rijke-tube simulation model. Section 4.5 describes the adaptive control law considered in this chapter for adaptive suppression. Section 4.6 considers the approach under which the discrete-time adaptive controller interacts with continuous-time systems. To determine the initial hyperparameters, Section 4.7 presents numerical examples where the adaptive controller suppresses the thermoacoustic oscillations in the simulation model of the Rijke tube. Section 4.8 presents physical closed-loop Rijke-tube experiments. Finally, Section 4.9 presents conclusions to the chapter.

4.1 Description of the Rijke-tube physical experiment

The Rijke-tube physical experiment is shown in Figure 4.1, where a heating element is placed inside a vertical Pyrex tube whose length is 1.2 m and whose inner cross-sectional area is $4.6 \cdot 10^{-3}$ m^2, similarly to the setup in [1]. The heating element is a coil made from 22-gauge Kanthal wire with a resistance of 22 ohms. The coil is attached by a Kevlar rope to a DC motor, which is used to reposition the coil. A Variac is used as a power supply to control the voltage supplied to the coil. To measure pressure oscillations, a microphone is placed at the top of the tube and connected to a preamplifier. The microphone was calibrated using a sound pressure level meter to convert voltage measurements to pascals (Pa). To provide the control input, a speaker is placed at the bottom of the tube and connected to an amplifier. Note that, since the speaker and microphone are not colocated, the linearized plant dynamics have NMP zeros, as shown in [1]. Consequently, passivity arguments cannot be used to guarantee closed-loop stability.

Pressure oscillations are created within the Rijke-tube physical experiment by supplying voltage to the heating element, as noted by Rijke in [18] and subsequently elucidated by Rayleigh [19, 108]. As explained in [108–110] [111, pp. 232-234], pressure oscillations are created and become self-excited if and only if the heating element is placed in the lower half of the tube and sufficient power is provided to the heating element to overcome the acoustic damping. Furthermore, pressure oscillations are more easily created when the heat source is placed at one quarter of the length of the tube from its bottom and become harder to create as the heat source is moved from this position [108]. The chosen Rijke-tube physical experiment exhibits thermoacoustic oscillations, whose characteristics depend on the vertical position of the heating element and the voltage provided to the heating element, as shown in Figures 4.2 and 4.3.

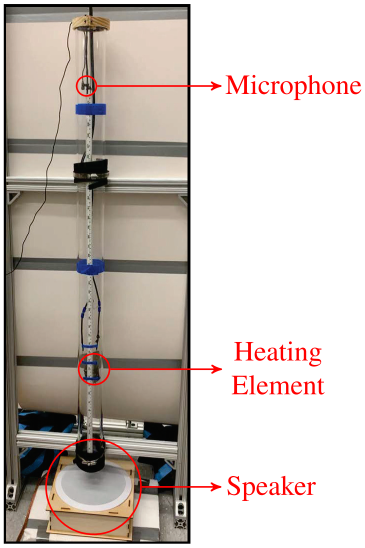

Figure 4.1: Rijke-tube physical experiment. The heating element can be raised or lowered by a DC motor (not shown) to vary the dynamics of the system.

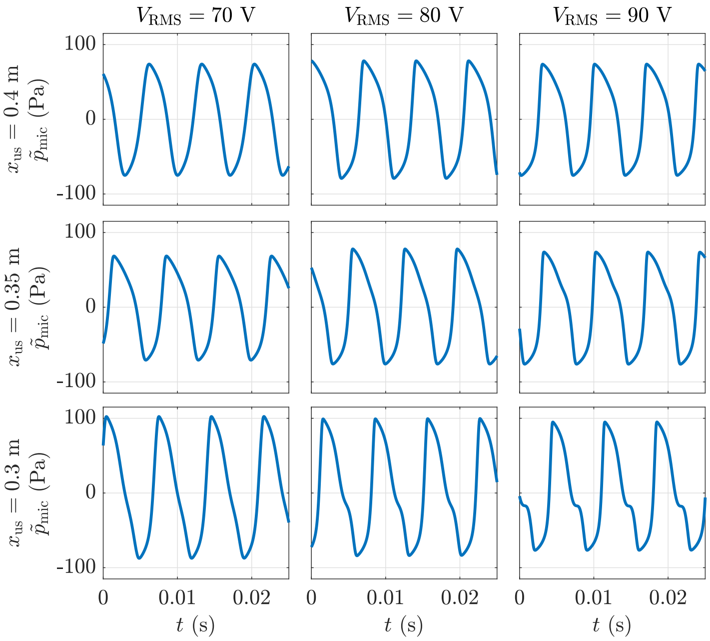

Figure 4.2: Pressure measurements from the open-loop Rijke-tube physical experiment obtained at the coil positions $x_{\mathrm{us}} \in \{0.3, 0.35, 0.4\}$ m and the AC voltage levels $V_{\mathrm{RMS}} \in \{70, 80, 90\}$ V, where x_{us} is the distance of the coil from the bottom of the tube, and V_{RMS} is the root-mean-square (RMS) voltage provided by the Variac.

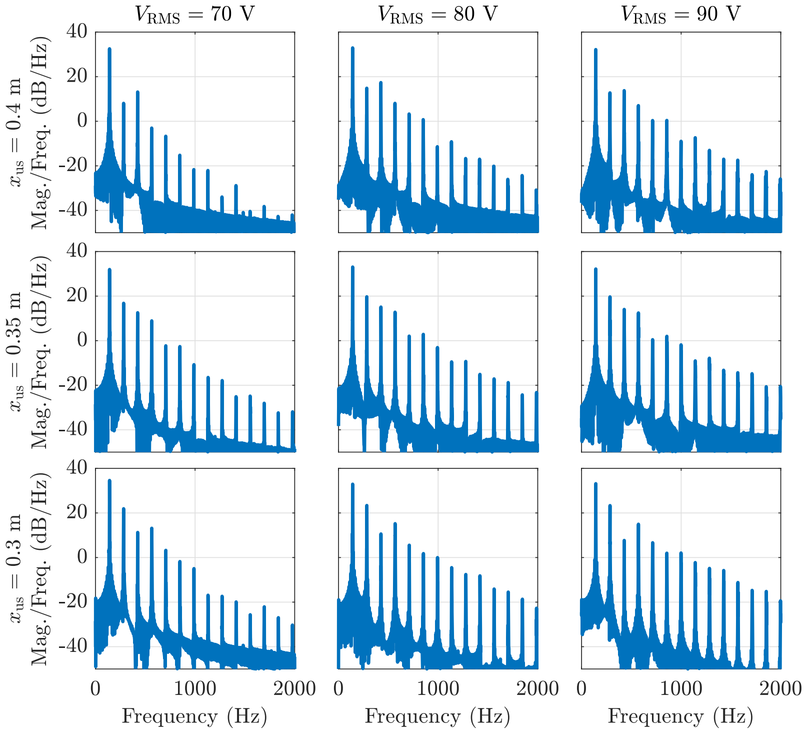

Figure 4.3: Amplitude spectra of the pressure measurements from the open-loop experiment at each setting considered in Figure 4.2.

4.2 Overview of the hyperparameter selection methodology

A hyperparameter selection procedure based on closed-loop numerical simulation is shown in Figure 4.4. First, physical Rijke-tube experiments are conducted in an open-loop configuration (no feedback control) to obtain pressure measurements. Then, a fit procedure is applied, where the parameters of the Rijke-tube model are chosen to capture the frequency and magnitude of the highest peak of the open-loop pressure measurements. This procedure yields a rudimentary simulation model, which is used for adaptive closed-loop numerical simulations to select hyperparameters based on achieved oscillation suppression. The selected hyperparameters are then used in physical closed-loop Rijke-tube experiments. For these experiments, the adaptive controller is implemented on a dSpace Scalexio system to suppress thermoacoustic oscillations generated by the coil heat for various coil positions and voltage levels. Note that the simulation model is used only to select an initial set of hyperparameters for adaptation, and is otherwise not used or needed for feedback control.

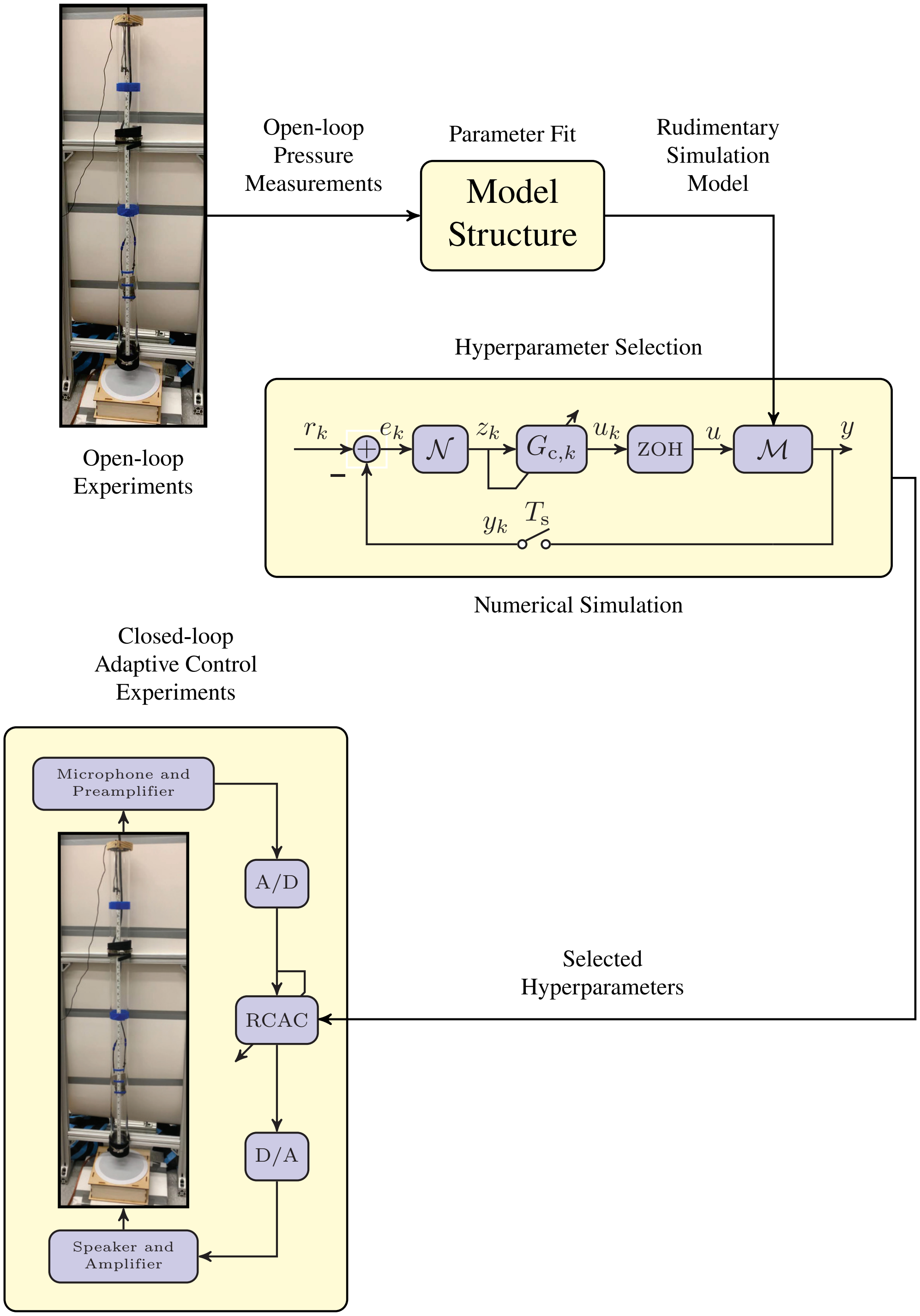

Figure 4.4: Hyperparameter selection procedure. The objective is to select initial hyperparameters by applying the adaptive controller to a rudimentary simulation model of the Rijke-tube physical experiment.

4.3 Physics-based model of the Rijke tube

A schematic of the Rijke-tube physical experiment is shown in Figure 4.5. The tube has length L and cross-sectional area A. The heating element is positioned x_{ds} m below the top of the tube and x_{us} m above the bottom of the tube; note that $L = x_{\mathrm{ds}} + x_{\mathrm{us}}$. The microphone is positioned x_{mic} m above the heating element, and the speaker is placed below the tube. In Figure 4.5, f_1 and g_1 represent the bidirectional acoustic pressure propagation in the upstream portion of the tube, and f_2 and g_2 represent the bidirectional acoustic pressure propagation in the downstream portion of the tube.

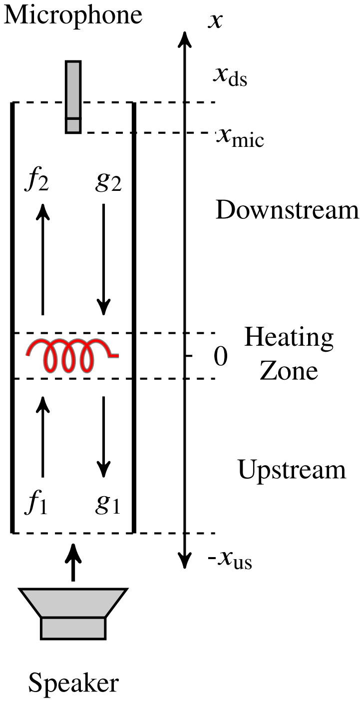

Figure 4.5: Schematic of the Rijke-tube model.

The Rijke-tube model (4.12)–(4.15) is based on the ducted-flame model given in [7] and further developed in [20, 95]. A key difference between the models developed in [7] and [20, 95] is that, in [7], a nonlinearity is added before the linear flame dynamics. This feature is congruent with the insight obtained in Chapters 2 and 3, and is included in (4.12)–(4.15), where the saturation function used in [7] is replaced by a hyperbolic tangent to improve numerical stability. Note that these nonlinearities are distinct from the square-root function used in [1] within the context of a different model. Let $x \in [-x_{\mathrm{us}}, x_{\mathrm{ds}}]$ denote a position within the tube in m, where $x = 0$ m is the position of the heating element in the tube. Let p and v be the airflow pressure and velocity such that

$$p(t,x) \triangleq \begin{cases} \bar{p}_1 + \tilde{p}_1(t,x), & x \in [-x_{\rm us}, 0], \\ \bar{p}_2 + \tilde{p}_2(t,x), & x \in (0, x_{\rm ds}], \end{cases} \tag{4.1}$$

$$v(t,x) \triangleq \begin{cases} \bar{v}_1 + \tilde{v}_1(t,x), & x \in [-x_{\rm us}, 0], \\ \bar{v}_2 + \tilde{v}_2(t,x), & x \in (0, x_{\rm ds}], \end{cases} \tag{4.2}$$

where $\bar{p}_1, \bar{p}_2 > 0$ are the mean airflow pressure in the upstream and downstream portions, respectively, $\bar{v}_1, \bar{v}_2 > 0$ are the mean airflow velocities in the upstream and downstream portions, respectively, and, for all $i \in \{1, 2\}$,

$$\tilde{p}_i(t,x) \triangleq f_i(t - \tfrac{x}{\bar{c}_i}) + g_i(t + \tfrac{x}{\bar{c}_i}), \tag{4.3}$$

$$\tilde{v}_i(t,x) \triangleq \tfrac{1}{\bar{\rho}_i \bar{c}_i}[f_i(t - \tfrac{x}{\bar{c}_i}) - g_i(t + \tfrac{x}{\bar{c}_i})], \tag{4.4}$$

where $\bar{c}_1, \bar{c}_2 > 0$ are the mean wave speeds in the upstream and downstream portions, respectively, and $\bar{\rho}_1, \bar{\rho}_2 > 0$ are the mean air densities in the upstream and downstream portions, respectively. Furthermore, f_1 and g_2 are given by

$$f_1(t) = R_{\rm us} g_1(t - \tau_{\rm us}) + \tilde{p}_{\rm spk}(t - \tfrac{\tau_{\rm us}}{2}), \tag{4.5}$$

$$g_2(t) = R_{\rm ds} f_2(t - \tau_{\rm ds}), \tag{4.6}$$

where $R_{\rm us}, R_{\rm ds} \in \mathbb{R}$ are reflection coefficients, $\tau_{\rm us} \triangleq \frac{2x_{\rm us}}{\bar{c}_1}$, $\tau_{\rm ds} \triangleq \frac{2x_{\rm ds}}{\bar{c}_2}$, and $\tilde{p}_{\rm spk} \in \mathbb{R}$ is the speaker pressure.

Next, the dynamics of the heat release rate perturbations of the coil $\tilde{Q}$ are modeled by

$$b\dot{\tilde{Q}}(t) + \tilde{Q}(t) = a\psi(\tilde{v}_1(t,0)), \tag{4.7}$$

where $a, b \in (0, \infty)$ and $\psi\colon \mathbb{R} \to \mathbb{R}$ is given by

$$\psi(\tilde{v}_1(t,0)) \triangleq \delta \tanh(\eta \tilde{v}_1(t,0)), \tag{4.8}$$

where $\delta, \eta \in (0, \infty)$. Then, define

$$F \triangleq X^{-1} \begin{bmatrix} Y & \begin{matrix} 0 \\ \frac{1}{A\bar{c}_1} \end{matrix} \end{bmatrix} \in \mathbb{R}^{2\times 3},$$

where $X, Y \in \mathbb{R}^{2\times 2}$, and let g_1 and f_2 be given by

$$\begin{bmatrix} g_1(t) \\ f_2(t) \end{bmatrix} = F \begin{bmatrix} f_1(t) \\ g_2(t) \\ \tilde{Q}(t) \end{bmatrix}. \tag{4.9}$$

Since the Mach numbers are assumed to be low [20, 95], it follows from the expressions for X and Y given in the appendix of [7] that

$$X \triangleq \begin{bmatrix} -1 & 1 \\ \frac{1}{\bar{\gamma}-1} & \frac{\bar{c}_2}{\bar{c}_1}\frac{1}{\bar{\gamma}-1} \end{bmatrix}, \quad Y \triangleq \begin{bmatrix} 1 & -1 \\ \frac{1}{\bar{\gamma}-1} & \frac{\bar{c}_2}{\bar{c}_1}\frac{1}{\bar{\gamma}-1} \end{bmatrix}, \tag{4.10}$$

where $\bar{\gamma}$ is the adiabatic ratio of dry air at room temperature. Finally, the acoustic pressure $\tilde{p}_{\text{mic}}$ measured by the microphone is given by

$$\begin{aligned} \tilde{p}_{\text{mic}}(t) \triangleq \tilde{p}_2(t, x_{\text{mic}}) &= f_2(t - \tfrac{x_{\text{mic}}}{\bar{c}_2}) + g_2(t + \tfrac{x_{\text{mic}}}{\bar{c}_2}) \\ &= f_2(t - \tau_{\text{mic}}) + R_{\text{ds}} f_2(t - (\tau_{\text{ds}} - \tau_{\text{mic}})), \end{aligned} \tag{4.11}$$

where $\tau_{\text{mic}} \triangleq \frac{x_{\text{mic}}}{\bar{c}_2}$.

The block diagram in Figure 4.6 summarizes the dynamics of the Rijke-tube model, where the control input $u = \tilde{p}_{\text{spk}}$ is the speaker pressure, and the measurement $y = \tilde{p}_{\text{mic}}$ is the microphone signal. These dynamics can be written as

$$\dot{\tilde{Q}}(t) = -\frac{1}{b}\tilde{Q}(t) + \frac{a}{b}\psi(\tilde{v}_1(t, 0)), \tag{4.12}$$

$$\tilde{v}_1(t, 0) = \frac{1}{\bar{\rho}_1 \bar{c}_1} \begin{bmatrix} 1 & -1 & R_{\text{us}} \end{bmatrix} \begin{bmatrix} \tilde{p}_{\text{spk}}(t - \tau_{\text{us}}/2) \\ g_1(t) \\ g_1(t - \tau_{\text{us}}) \end{bmatrix}, \tag{4.13}$$

$$\begin{bmatrix} g_1(t) \\ f_2(t) \end{bmatrix} = F \begin{bmatrix} 1 & 0 & 0 & 0 \\ 0 & 1 & R_{\text{us}} & 0 \\ 0 & 0 & 0 & R_{\text{ds}} \end{bmatrix} \begin{bmatrix} \tilde{Q}(t) \\ \tilde{p}_{\text{spk}}(t - \tau_{\text{us}}/2) \\ g_1(t - \tau_{\text{us}}) \\ f_2(t - \tau_{\text{ds}}) \end{bmatrix}, \tag{4.14}$$

$$\tilde{p}_{\text{mic}}(t) = \begin{bmatrix} 1 & R_{\text{ds}} \end{bmatrix} \begin{bmatrix} f_2(t - \tau_{\text{mic}}) \\ f_2(t - (\tau_{\text{ds}} - \tau_{\text{mic}})) \end{bmatrix}. \tag{4.15}$$

Note that (4.12)–(4.15) are delay differential equations (DDEs) with state $\tilde{Q}$, input $\tilde{p}_{\text{spk}}$, output $\tilde{p}_{\text{mic}}$, and time varying parameters g_1 and f_2. Furthermore, the placement of the speaker and the microphone relative to the coil result in input and output time delays, as shown in (4.14), (4.15), and Figure 4.6.

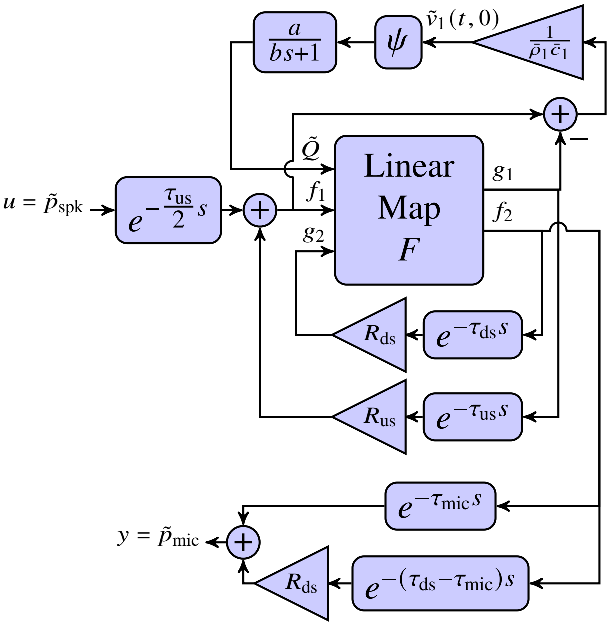

Figure 4.6: Block diagram of the Rijke-tube model. The control input $u = \tilde{p}_{\rm spk}$ is the speaker pressure, and the microphone signal $y = \tilde{p}_{\rm mic}$ is the measurement. This block diagram is executed in Simulink.

4.4 Rijke-tube model parameter fit

The parameters for the Rijke-tube model introduced in Section 4.3 and shown in Figure 4.6 are chosen to emulate the characteristics of the Rijke-tube physical experiment. In particular, with the coil placed 0.4 m above the bottom of the tube and the RMS Variac voltage set to $V_{\rm RMS} = 70$ V, the simulation model captures the amplitude and frequency of the highest magnitude of the spectrum of the pressure measurements obtained from open-loop experiments. The constants $\bar{\rho}_1$ and $\bar{\gamma}$ denote the density and adiabatic ratio of dry air at room temperature, respectively, $\bar{c}_1$ and $\bar{c}_2$ are chosen as in [95], and $x_{\rm us}, x_{\rm ds}$, and $x_{\rm mic}$ are based on the configuration used in open-loop experiments. Hence, $L = 1.2$ m, $x_{\rm us} = 0.4$ m and $x_{\rm ds} = 1.2$ m $- 0.4$ m $= 0.8$ m. Since the microphone is placed approximately 0.1 m below the top of the tube, $x_{\rm mic} = x_{\rm ds} - 0.1$ m $= 0.7$ m. $R_{\rm us}$ and $R_{\rm ds}$ are fixed to values that induce a self-excited response in the model output more easily. Then, a b, δ, and η are manually adjusted to match the pressure measurements obtained from the open-loop experiments. The chosen parameters for the Rijke-tube simulation model are shown in Table 4.1.

Numerical simulations of the simulation model are performed in Simulink using fixed-step integration with step size 10^{-4} s/step.Linear interpolation is used to calculate the delayed values of

$\tilde{p}_{\rm spk}$, g_1, and f_2. For all $t \leq 0$, $\tilde{p}_{\rm spk}(t) = g_1(t) = f_2(t) = 0$. The value of $\tilde{Q}(0)$ is randomly selected and provides the initial disturbance to generate the oscillations.

The open-loop ($u \equiv 0$) response of the simulation model and the experimental data are shown in Figure 4.7. The highest magnitude peaks of the amplitude spectra of the open-loop experiment and the simulation model match at 140 Hz, as shown in Figure 4.7. As can be seen, the magnitude peaks of the amplitude spectrum of the emulation model match only the peaks corresponding to the odd harmonics of the amplitude spectrum of the open-loop experiment. Although this mismatch is inconsistent with the reflection coefficients $R_{\rm us}$ and $R_{\rm ds}$, which model open-open boundary conditions, the predictions of a linear acoustic model are not valid for the emulation model, which is nonlinear. While the emulation model output only roughly matches the data, Subsection 4.8.1 shows that this emulation model is sufficient for hyperparameter tuning.

Table 4.1: Parameters of the Rijke-tube Simulation Model

Parameter	**Value**	**Units**	**Comment**
$\bar{\rho}_1$	1.225	kg/m^3	Based on the Rijke-tube physical experiment
$\bar{\gamma}$	1.4	–	
$\bar{c}_1$	340	m/s	
$\bar{c}_2$	360	m/s	
A	$4.6 \cdot 10^{-3}$	m^2	
L	1.2	m	
$x_{\rm us}$	0.4	m	
$x_{\rm ds}$	$L - x_{\rm us}$	m	
$x_{\rm mic}$	$x_{\rm ds} - 0.1$	m	
$R_{\rm us}$	-0.99	–	Based on open-loop pressure measurements
$R_{\rm ds}$	-0.99	–	
a	375	–	
b	$2 \cdot 10^{-3}$	–	
δ	0.1128	m/s	
η	3.21	–	

4.5 Review of Retrospective Cost Adaptive Control

RCAC is described in detail in [105]. In this section we summarize the main elements of this method.

Consider the strictly proper, discrete-time, input-output controller

$$u_k = \sum_{i=1}^{l_{\rm c}} P_{i,k} u_{{\rm c},k-i} + \sum_{i=1}^{l_{\rm c}} Q_{i,k} z_{k-i}, \tag{4.16}$$

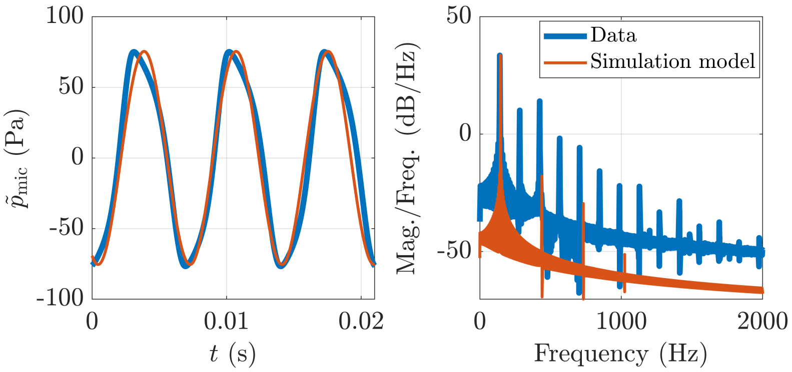

Figure 4.7: Comparison of the time responses and amplitude spectra of the open-loop experiment and the rudimentary simulation model. Note that the amplitude spectra of the data and simulation model match only at the first peak. The parameters used for the simulation model are given in Table 4.1.

where $k \geq 0$ is the current discrete time step, $u_k \in \mathbb{R}^{l_u}$ is the controller output and thus the control input, $u_{\mathrm{c},k} \in \mathbb{R}^{l_u}$ is the constrained control input, $z_k \in \mathbb{R}^{l_z}$ is the measured performance variable, l_{c} is the controller-window length, and, for all $i \in \{1, \ldots, l_{\mathrm{c}}\}$, $P_{i,k} \in \mathbb{R}^{l_u \times l_u}$ and $Q_{i,k} \in \mathbb{R}^{l_u \times l_z}$ are the controller coefficient matrices. In particular, $u_{\mathrm{c},k}$ results from applying system constraints to u_k, which depends on the studied system. The controller (4.16) can be written as

$$u_k = \phi_k \theta_k, \tag{4.17}$$

where

$$\phi_k \triangleq \begin{bmatrix} u_{\mathrm{c},k-1}^{\mathsf{T}} & \cdots & u_{\mathrm{c},k-l_{\mathrm{c}}}^{\mathsf{T}} & z_{k-1}^{\mathsf{T}} & \cdots & z_{k-l_{\mathrm{c}}}^{\mathsf{T}} \end{bmatrix} \otimes I_{l_u} \in \mathbb{R}^{l_u \times l_\theta}, \tag{4.18}$$

$$\theta_k \triangleq \mathrm{vec} \begin{bmatrix} P_{1,k} & \cdots & P_{l_{\mathrm{c}},k} & Q_{1,k} & \cdots & Q_{l_{\mathrm{c}},k} \end{bmatrix} \in \mathbb{R}^{l_\theta}, \tag{4.19}$$

$l_\theta \triangleq l_{\mathrm{c}} l_u (l_u + l_z)$, θ_k is the vector of controller coefficients, which are updated at each time step k, and $\otimes$ is the Kroenecker product.

If z_k and u_k are scalar, then the SISO transfer function of (4.16) from z_k to u_k is given by

$$G_{\mathrm{c},k}(\mathbf{q}) = \frac{Q_{1,k}\mathbf{q}^{l_{\mathrm{c}}-1} + \cdots + Q_{l_{\mathrm{c}},k}}{\mathbf{q}^{l_{\mathrm{c}}} - P_{1,k}\mathbf{q}^{l_{\mathrm{c}}-1} - \cdots - P_{l_{\mathrm{c}},k}}, \tag{4.20}$$

where $\mathbf{q}$ is the forward-shift operator.

Next, define the retrospective cost variable

$$\hat{z}_k(\hat{\theta}) \triangleq z_k - G_{\mathrm{f}}(\mathbf{q})(u_k - \phi_k \hat{\theta}), \tag{4.21}$$

where G_f is an $l_z \times l_u$ asymptotically stable, strictly proper transfer function, and $\hat{\theta} \in \mathbb{R}^{l_\theta}$ is the controller coefficient vector determined by optimization below. The rationale underlying (4.21) is to replace the applied past control inputs with the re-optimized control input $\phi_k\hat{\theta}$ so that the closed-loop transfer function from $u_k - \phi_k\theta_{k+1}$ to z_k matches G_f [105, 106]. Consequently, G_f serves as a closed-loop target model for the adaptation process.

In this dissertation, G_f is chosen to be a finite-impulse-response transfer function of window length l_f of the form

$$G_\mathrm{f}(\mathbf{q}) \triangleq \sum_{i=1}^{l_\mathrm{f}} N_{i,k}\mathbf{q}^{-i}, \tag{4.22}$$

where $N_{1,k}, \ldots, N_{l_\mathrm{f},k} \in \mathbb{R}^{l_z \times l_u}$. We can thus rewrite (4.21) as

$$\hat{z}_k(\hat{\theta}) = z_k - N_k(U_{\mathrm{c},k} - \Phi_k\hat{\theta}), \tag{4.23}$$

where

$$\Phi_k \triangleq \begin{bmatrix} \phi_{k-1} \\ \vdots \\ \phi_{k-l_\mathrm{f}} \end{bmatrix} \in \mathbb{R}^{l_\mathrm{f}l_u \times l_\theta},\ U_{\mathrm{c},k} \triangleq \begin{bmatrix} u_{\mathrm{c},k-1} \\ \vdots \\ u_{\mathrm{c},k-l_\mathrm{f}} \end{bmatrix} \in \mathbb{R}^{l_\mathrm{f}l_u}, \tag{4.24}$$

$$N_k \triangleq \begin{bmatrix} N_{1,k} & \cdots & N_{l_\mathrm{f},k} \end{bmatrix} \in \mathbb{R}^{l_z \times l_\mathrm{f}l_u}. \tag{4.25}$$

The choice of N_k includes all required modeling information. When the plant is SISO, that is, $l_z = l_u = 1$, this information consists of the sign of the leading numerator coefficient, the relative degree of the sampled-data system, and all nonminimum-phase (NMP) zeros [105, 106]. Since zeros are invariant under feedback, omission of a NMP zero from G_f may entail unstable pole-zero cancellation. Cancellation can be prevented, however, by using the control weighting R_u introduced below, as discussed in [105, 112]. In most applications, N_k is constant and is determined by features of the system being controlled, as mentioned in [105]. Other applications may require N_k to be constructed and updated online using data, as mentioned in [106].

Using (4.21), we define the cumulative cost function

$$J_{\mathrm{R},k}(\hat{\theta}) \triangleq \sum_{i=0}^{k} [\hat{z}_i^\mathrm{T}(\hat{\theta})\hat{z}_i(\hat{\theta}) + (\phi_i\hat{\theta})^\mathrm{T}R_u\phi_i\hat{\theta}] + (\hat{\theta} - \theta_0)^\mathrm{T}P_0^{-1}(\hat{\theta} - \theta_0), \tag{4.26}$$

where $P_0 \in \mathbb{R}^{l_\theta \times l_\theta}$ is positive definite and $R_u \in \mathbb{R}^{l_u \times l_u}$ is positive semidefinite. As can be seen from (4.17), R_u serves as a control weighting, which prevents RCAC from cancelling unmodeled

NMP zeros, and the matrix P_0^{-1} defines the regularization term and initializes the recursion for P_k defined below.

The following result uses recursive least squares (RLS), as mentioned in [113] and [114], to minimize (4.26), where, at each step k, the minimizer of (4.26) provides the update θ_{k+1} of the controller coefficient vector θ_k.

Proposition. Let P_0 be positive definite, and R_u be positive semidefinite. Then, for all $k \geq 0$, (4.26) has the unique global minimizer θ_k given by

$$P_k = P_{k-1} - P_{k-1} \begin{bmatrix} N_{k-1}\Phi_{k-1} \\ \phi_{k-1} \end{bmatrix}^{\mathsf{T}} \Gamma_{k-1} \begin{bmatrix} N_{k-1}\Phi_{k-1} \\ \phi_{k-1} \end{bmatrix} P_{k-1}, \tag{4.27}$$

$$\theta_k = \theta_{k-1} - P_k \begin{bmatrix} N_{k-1}\Phi_{k-1} \\ \phi_{k-1} \end{bmatrix}^{\mathsf{T}} \bar{R} \begin{bmatrix} z_{k-1} - N_{k-1}(U_{\mathrm{c},k-1} - \Phi_{k-1}\theta_{k-1}) \\ \phi_{k-1}\theta_{k-1} \end{bmatrix}, \tag{4.28}$$

where

$$\Gamma_{k-1} \triangleq \bar{R} - \bar{R} \begin{bmatrix} N_{k-1}\Phi_{k-1} \\ \phi_{k-1} \end{bmatrix} \left(P_{k-1}^{-1} + \begin{bmatrix} N_{k-1}\Phi_{k-1} \\ \phi_{k-1} \end{bmatrix}^{\mathsf{T}} \bar{R} \begin{bmatrix} N_{k-1}\Phi_{k-1} \\ \phi_{k-1} \end{bmatrix} \right)^{-1} \begin{bmatrix} N_{k-1}\Phi_{k-1} \\ \phi_{k-1} \end{bmatrix}^{\mathsf{T}} \bar{R}$$

$$\in \mathbb{R}^{(l_z+l_u)\times(l_z+l_u)}, \tag{4.29}$$

$$\bar{R} \triangleq \mathrm{diag}(I_{l_z}, R_u) \in \mathbb{R}^{(l_z+l_u)\times(l_z+l_u)}. \tag{4.30}$$

For all of the numerical simulations and physical experiments in this paper, θ_k is initialized as $\theta_0 = 0_{l_\theta\times 1}$ to reflect the absence of additional prior modeling information. Aside from the selection of hyperparameters discussed above, no other modeling information is used by RCAC. For convenience, we set $P_0 = p_0 I_{l_\theta}$, where the scalar $p_0 > 0$ determines the initial rate of adaptation.

4.6 Sampled-Data Implementation of the Adaptive Control Law

For the Rijke-tube experiment, the adaptive controller is implemented as a sampled-data controller. Figure 4.8 shows a block diagram of the sampled-data closed-loop system, where $y \in \mathbb{R}$ is the output of the continuous-time system $\mathcal{M}$, y_k is the sampled output, $r_k \in \mathbb{R}$ is the discrete-time command, $e_k \triangleq r_k - y_k$ is the command-following error, $u \in \mathbb{R}$ is the input of $\mathcal{M}$, and $\tau_{\mathrm{s}} > 0$ is the sampling period. For all adaptive controller experiments in this chapter, $\tau_{\mathrm{s}} = 0.001$ s/step. Since the system is SISO, $l_y = l_u = \mathbb{R}$. The digital-to-analog (digital-to-analog (D/A)) and analog-to-digital (analog-to-digital (A/D)) interfaces, which are synchronous, are zero-order-hold (zero-order-hold (ZOH)) and sampler, respectively. For this work, $r \equiv 0$ reflects the desire to suppress oscillations in the measured signal. Finally, in this chapter, $\mathcal{M}$ represents a Rijke-tube model introduced in Section 4.3 for numerical simulations and the Rijke-tube experiment introduced in Section 4.1 for physical experiments.

For this application, for all $k \geq 0$, $u_{\mathrm{c},k} = u_k$. Furthermore, the measured performance variable $z_k \in \mathbb{R}$, which is used for adaptation, is the normalized error

$$z_k \triangleq \mathcal{N}(e_k) \triangleq \frac{e_k}{1 + \nu|e_k|}, \tag{4.31}$$

where $\nu \in [0, \infty)$. We fix $\nu = 0.2$ throughout this chapter. The adaptive controller $G_{\mathrm{c},k}$ operates on z_k to produce the discrete-time control $u_k \in \mathbb{R}$. Hence, $l_u = l_z = 1$. $G_{\mathrm{c},k}$ and u_k are updated at each sampling time $t_k \triangleq k\tau_{\mathrm{s}}$.

In numerical simulations and physical experiments, the controller and adaptation are enabled and disabled in various ways. In particular, for the experimental scenarios, we consider the following modes of operation starting at step $k_0 \geq 0$:

i) *Mode 1:* The controller and adaptation are disabled. For all $k \geq k_0$, $u_k = 0$, $\theta_{k+1} = \theta_k$, and $P_{k+1} = P_k$.

ii) *Mode 2:* The controller and adaptation are enabled. For all $k \geq k_0$, u_k, θ_{k+1}, and P_{k+1} are updated by (4.17), (4.27), and (4.28), respectively.

iii) *Mode 3:* The controller is enabled, but adaptation is disabled, yielding a fixed-gain controller. For all $k \geq k_0$, u_k is updated by (4.17), $\theta_{k+1} = \theta_k$, and $P_{k+1} = P_k$.

Mode 1 is employed when the user requires that the open-loop system reach a desired behavior before control is applied, such as fully developed thermoacoustic oscillations. Mode 2 corresponds to normal operation of the adaptive controller. Mode 3 is useful for probing the properties of the controller at a given time step; in effect, at step k, the gains of $G_{\mathrm{c},k}$ are frozen, and the controller operates as a fixed-gain controller, called the *frozen-gain adaptive controller*.

Implementation of the adaptive controller requires selection of the closed-loop target model G_{f}, which captures the properties mentioned in Section 4.5 [105]. In addition, the hyperparameters l_{c}, p_0, and R_u must be selected depending on the system and performance requirements. Note that R_u is scalar since $l_u = 1$. As mentioned in the Section 4.2, all of these quantities are selected for the Rijke-tube physical experiments after performing closed-loop numerical simulations with a simulation model.

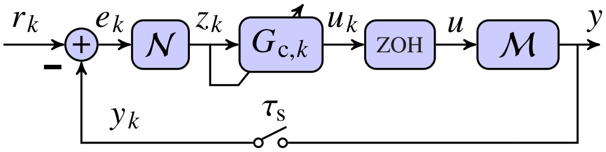

Figure 4.8: Adaptive control of a continuous-time system $\mathcal{M}$. For this work, $r \equiv 0$ reflects the desire to suppress oscillations in the measured signal, $\mathcal{N}$ is the normalization function (4.31), and $\mathcal{M}$ represents the Rijke-tube model introduced in Section 4.3 for numerical simulations and the Rijke-tube experiment introduced in Section 4.1 for physical experiments.

4.7 Numerical simulation of the Rijke-tube model for hyperparameter selection

In this section, the simulation model is used to select hyperparameters, such that the adaptive controller suppresses the self-excited response of the Rijke-tube simulation model in three cases, where the heating element is placed at three different positions along the tube by changing the positive values of x_{ds} and x_{us}, such that $x_{\mathrm{us}} \in \{0.3, 0.35, 0.4\}$ m and $x_{\mathrm{ds}} = L - x_{\mathrm{us}}$. Hence, the parameters used for the simulation model are given in Table 4.1, except for x_{us}, for which three different values are considered. For simplicity in controlling the Rijke tube, we fix N_k, such that, for all $k \geq 0$, $N_k = N = -1$, and thus $G_{\mathrm{f}}(\mathbf{q}) = -1/\mathbf{q}$, where the minus sign reflects sign information and the relative degree is set to 1. Hence, only l_{c}, p_0, and R_u need to be selected. As mentioned in the introduction to this chapter, the level of suppression of the thermoacoustic oscillations, referred to as oscillation suppression, is used to evaluate the performance of the controller, which is defined to be the ratio of the steady-state open-loop maximum time-domain pressure amplitude to the steady-state closed-loop maximum time-domain pressure amplitude in dB.

The controller initially operates in Mode 1, and the experiment transitions to Mode 2 at $t = 15$ s, which is sufficient time for the oscillatory response of the open-loop models to fully develop. Several simulations are performed, in which the hyperparameters l_{c}, p_0, and R_u are manually adjusted until at least 40 dB of oscillation suppression is obtained across all scenarios ($x_{\mathrm{us}} \in \{0.3, 0.35, 0.4\}$ m). The selected hyperparameters are given by $l_{\mathrm{c}} = 5$, $p_0 = 10^{-5}$, and $R_u = 1$.

The results of the numerical simulations using the selected hyperparameters are shown in Figures 4.9, 4.10, 4.11, and 4.12. Figure 4.9 shows that, in all cases, the adaptive controller suppresses the oscillations; in particular, for $x_{\mathrm{us}} \in \{0.4, 0.35, 0.3\}$ m, the adaptive controller suppresses the oscillations by 72.74 dB, 59.63 dB, and 54.70 dB, respectively. Figure 4.10 shows that, in all cases, the adaptive controller suppresses the highest magnitude peak of the amplitude spectra corresponding to the open-loop response of the simulation model. Figure 4.11 shows that the poles of the adaptive controller evolve in a similar manner in all cases. In contrast, the zeros evolve differently in different cases, which shows that the response of the adaptive controller depends on the operating conditions. Note that none of the poles lie close to the unit circle, which shows that, in contrast to the standard approach for harmonic disturbance rejection in linear systems, the adaptive controller does not exploit an internal-model strategy for oscillation suppression [115]. Furthermore, Figure 4.12 shows that the magnitude of the adaptive controller indicates high gain near $\pi/4$ rad/sample, which is equivalent to 125 Hz given τ_s. The high-gain response of the adaptive controller thus corresponds to the first harmonic of the open-loop amplitude spectra, which occurs near 140 Hz, as shown in Figure 4.10. The hyperparameters used in these examples are initially used in the physical experiments.

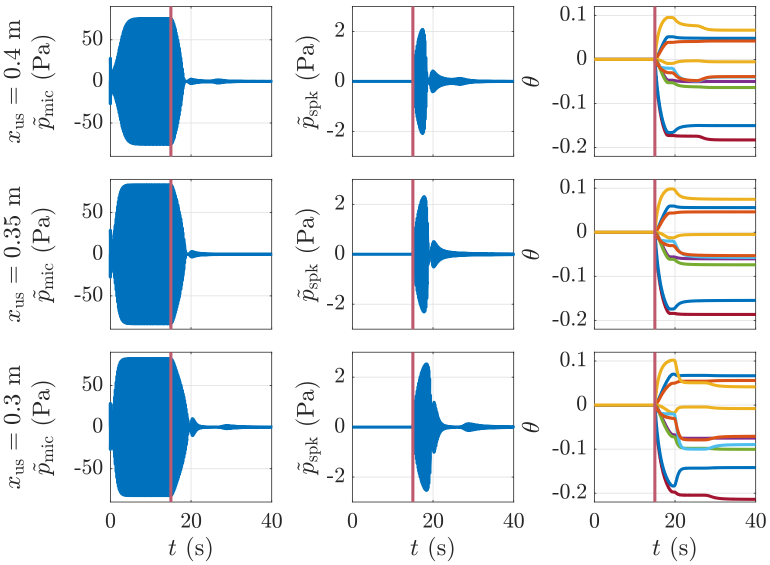

Figure 4.9: Adaptive control of the simulated Rijke-tube model. The experiment transitions from Mode 1 to Mode 2 at $t = 15$ s, as indicated by the vertical red lines. Each row shows the responses for $x_{us} \in \{0.3, 0.35, 0.4\}$ m, for $t \in [0, 40]$ s. The first, second, and third columns show the pressure measurements $\tilde{p}_{mic}$, the requested speaker pressure $\tilde{p}_{spk}$, and the adaptive controller coefficients θ, respectively.

4.8 Physical Adaptive Control Experiments

The closed-loop Rijke-tube physical experiment shown in Figure 4.13 is used in the following subsections to perform physical adaptive control experiments. The hyperparameters determined in Section 4.7 are initially used for the adaptive controller. In particular, Subsection 4.8.1 shows experiments in which the Rijke-tube setup parameters are kept constant, Subsection 4.8.2 shows the effects of hyperparameter perturbation on the RCAC rate of adaptation and suppression performance, Subsection 4.8.3 evaluates the suppression performance of the frozen-gain adaptive

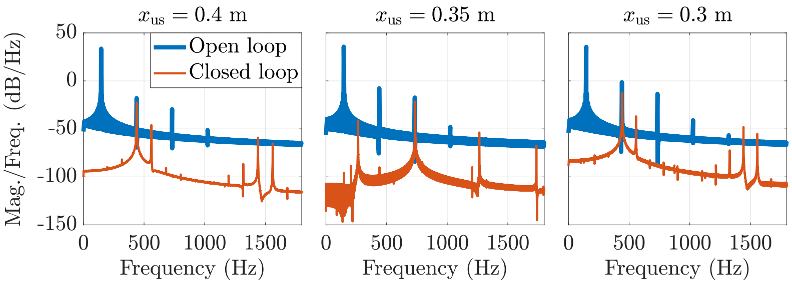

Figure 4.10: Amplitude spectra of the simulated Rijke-tube model. The amplitude spectra of the pressure measurements obtained from the open-loop simulations and the closed-loop simulations using the adaptive controller are shown for $x_{\mathrm{us}} \in \{0.3, 0.35, 0.4\}$ m.

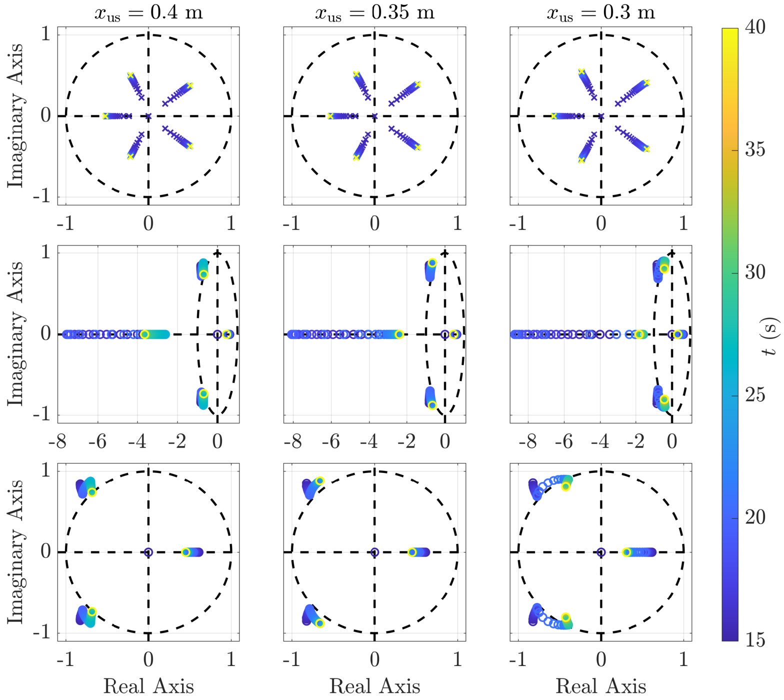

Figure 4.11: Evolution of the poles and zeros of the adaptive controller during the simulation of the closed-loop system with the Rijke-tube model. Each column shows the poles and zeros for $x_{\mathrm{us}} \in \{0.3, 0.35, 0.4\}$ m and $t \in [15, 40]$ s. The top row displays the poles as crosses, the middle row displays the zeros as circles, and the bottom row shows zoomed-in versions of the plots in the middle row.

controller resulting from an initial implementation of RCAC, Subsection 4.8.4 shows experiments in which the parameters of the Rijke-tube setup are modified during closed-loop operation, and Subsections 4.8.5 and 4.8.6 provide experiment-based stability analyses of RCAC.

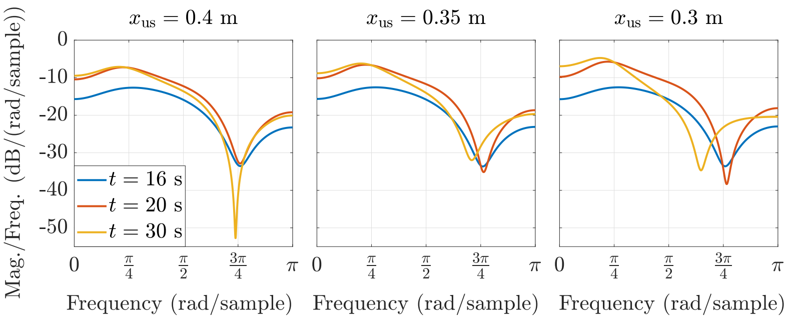

Figure 4.12: Evolution of the frequency response of the adaptive controller during the simulation of the closed-loop system with the Rijke-tube model. The magnitude responses of the adaptive controller are shown for $x_{\text{us}} \in \{0.3, 0.35, 0.4\}$ m and $t \in \{16, 20, 30\}$ s.

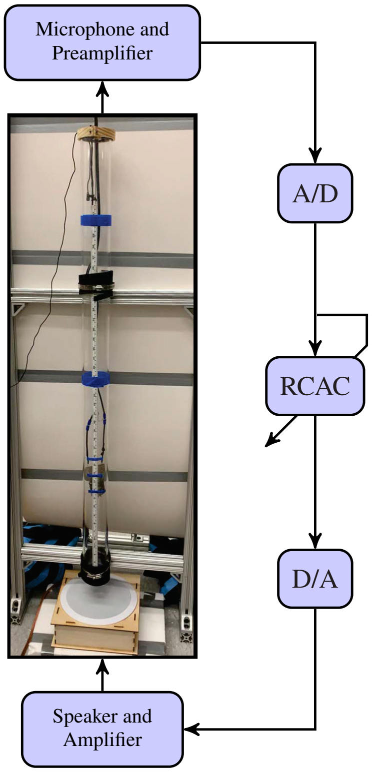

Figure 4.13: Closed-loop Rijke-tube physical experiment.

4.8.1 Rijke-tube fixed-parameter experiments

We now consider experimental scenarios where the coil position and supplied voltage are kept constant. In total, 9 combinations are considered, such that $x_{\text{us}} \in \{0.3, 0.35, 0.4\}$ m and $V_{\text{RMS}} \in \{70, 80, 90\}$ V, which are the cases shown in Figures 4.2 and 4.3. Through testing, it is determined that the oscillations are more difficult to suppress as x_{us} moves closer to 0.3 m (a quarter of the tube length from its bottom, as mentioned in Section 4.1) and V_{RMS} increases. The experiment begins in Mode 1 and transitions to Mode 2 after the oscillations are formed.

Since it is mentioned in [1] and [95] that a constant-gain proportional controller can be used to suppress the oscillations, the constant-gain proportional controller in Figure 4.14 is also implemented for comparison, where K is the constant proportional gain and the sampling rate is $\tau_{\rm s}/20$ s/step. A small sampling rate is chosen to allow the digital computer to better approximate the continuous-time implementations considered in [1] and [95]. For all $k \geq 0$, $u_k = 0$ in the case where the constant-gain proportional controller is disabled and $u_k = Ke_k$ in the case where the constant-gain proportional controller is enabled. The constant-gain proportional controller is used in the 4 corner cases of the 9 cases considered, using 4 different values of K. The results of the suppression experiments with the constant-gain proportional controller in Figure 4.14 for $x_{\rm us} \in \{0.3, 0.4\}$ m, $V_{\rm RMS} \in \{70, 90\}$ V, and $K \in \{0.025, 0.05, 0.075, 0.01\}$ are shown in Figure 4.15. In all of these experiments, the oscillation suppression is at most 45.73 dB, and no suppression is achieved in 9 cases.

For the adaptive controller implementation, the hyperparameters are the same as the ones determined from the numerical simulations using the simulation model, that is, $l_{\rm c} = 5$, $p_0 = 10^{-5}$, $R_u = 1$, and $G_{\rm f}(\mathbf{q}) = -1/\mathbf{q}$. The results of the adaptive suppression experiments for $x_{\rm us} \in \{0.3, 0.35, 0.4\}$ m and $V_{\rm RMS} \in \{70, 80, 90\}$ V are shown in Figures 4.16, 4.17, 4.18, 4.19, and 4.20. In all of these experiments, the oscillation suppression is at least 45.85 dB. Hence, as in Section 4.7, oscillation suppression greater than 45 dB is achieved using the same hyperparameters in all tests. Furthermore, Figure 4.20 shows that the magnitude of the adaptive controller indicates high gain near $\pi/4$ rad/sample, which is equivalent to 125 Hz given $\tau_{\rm s}$. The high-gain response of the adaptive controller thus corresponds to the first harmonic of the open-loop amplitude spectra, which occurs near 140 Hz, as shown in Figure 4.17 and similarly to Section 4.7.

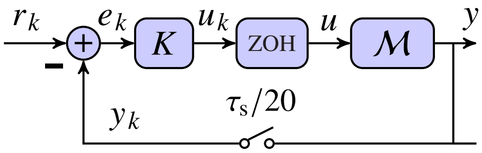

Figure 4.14: Constant-gain proportional control of the continuous-time system $\mathcal{M}$. For this work, $r \equiv 0$ reflects the desire to suppress oscillations in the measured signal. $\mathcal{M}$ represents the Rijke-tube physical experiment.

4.8.2 Hyperparameter perturbation experiments

We now consider experimental scenarios where the hyperparameters p_0 and R_u are modified, starting from the values determined in Section 4.7. In particular, the adaptive controller is implemented in the case where $x_{\rm us} = 0.3$ m and $V_{\rm RMS} = 90$ V for $p_0 \in \{10^{-5}, 10^{-4}, 10^{-3}\}$ and $R_u \in \{0.5, 0.75, 1\}$.

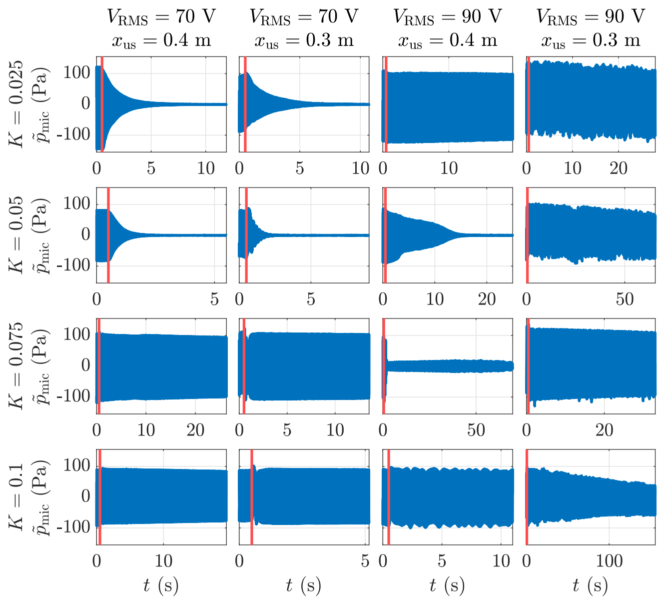

Figure 4.15: *Rijke-tube fixed-parameter experiments.* Pressure measurements $\tilde{p}_{\rm mic}$ from the closed-loop experiments using the constant-gain proportional controller in Figure 4.14 are shown for $x_{\rm us} \in \{0.3, 0.4\}$ m, $V_{\rm RMS} \in \{70, 90\}$ V, and $K \in \{0.025, 0.05, 0.075, 0.01\}$. The constant-gain proportional controller is initially disabled and is enabled at the time indicated by the vertical red lines. In order to render the details discernible, different time windows are used in each plot.

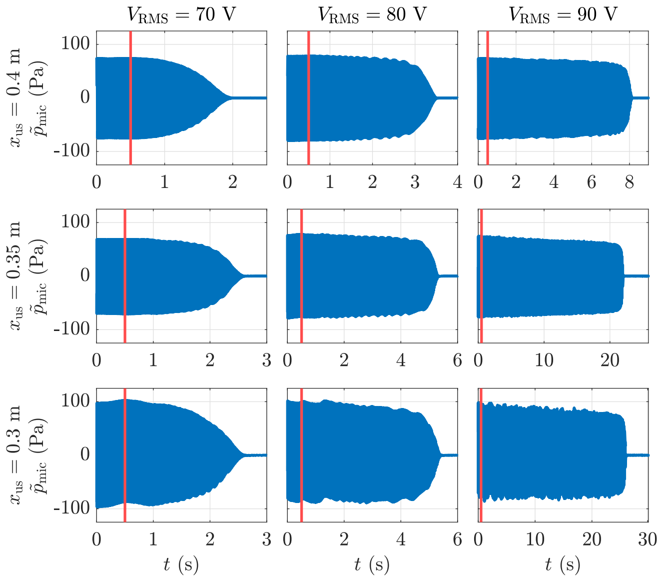

Figure 4.16: *Rijke-tube fixed-parameter experiments.* Pressure measurements $\tilde{p}_{\rm mic}$ from the closed-loop experiments using the adaptive controller are shown for $x_{\rm us} \in \{0.3, 0.35, 0.4\}$ m and $V_{\rm RMS} \in \{70, 80, 90\}$ V. Each experiment transitions from Mode 1 to Mode 2 at the time indicated by the vertical red line. The same hyperparameters are used in all tests.

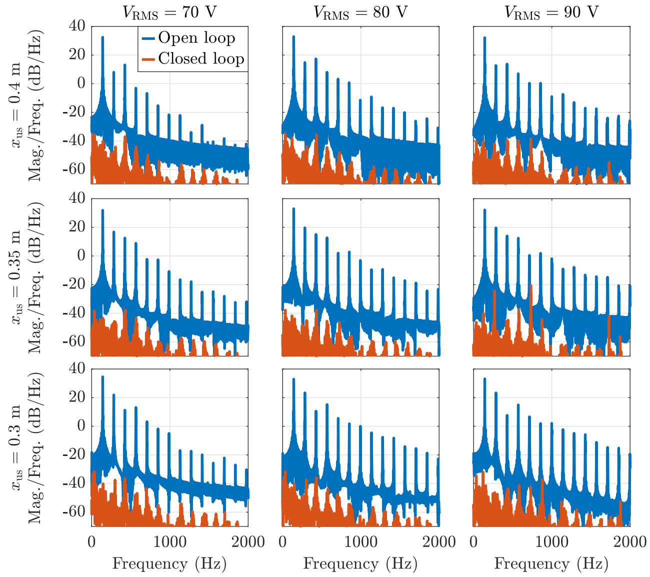

Figure 4.17: *Rijke-tube fixed-parameter experiments.* Amplitude spectra of the Rijke-tube physical experiment. The amplitude spectra of the pressure measurements obtained from the open-loop experiments and the closed-loop experiments using the adaptive controller are shown for $x_{\mathrm{us}} \in \{0.3, 0.35, 0.4\}$ m and $V_{\mathrm{RMS}} \in \{70, 80, 90\}$ V. The same hyperparameters are used in all closed-loop tests.

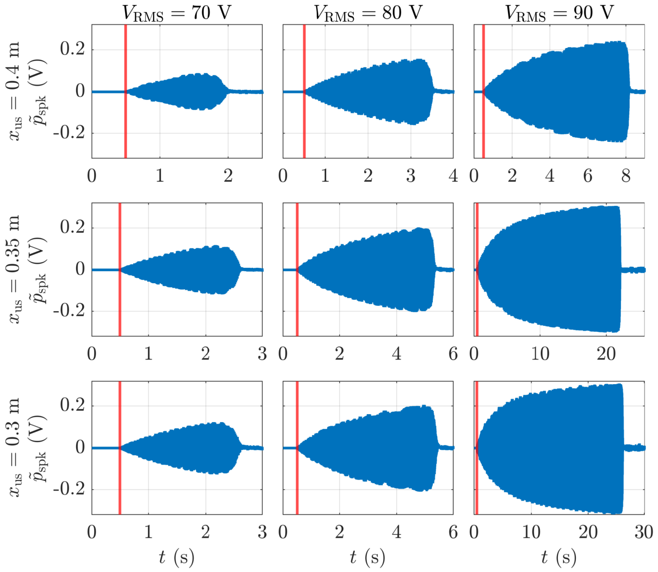

Figure 4.18: *Rijke-tube fixed-parameter experiments.* The requested speaker voltage $\tilde{p}_{\mathrm{spk}}$ from the closed-loop experiments using the adaptive controller is shown for $x_{\mathrm{us}} \in \{0.3, 0.35, 0.4\}$ m and $V_{\mathrm{RMS}} \in \{70, 80, 90\}$ V. Each experiment transitions from Mode 1 to Mode 2 at the time indicated by the vertical red line. The same hyperparameters are used in all tests.

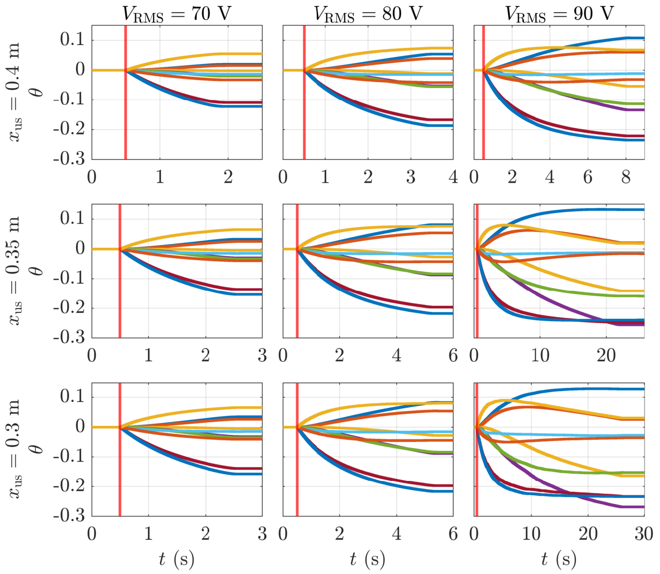

Figure 4.19: *Rijke-tube fixed-parameter experiments.* The controller coefficients θ from the closed-loop experiments using the adaptive controller are shown for $x_{\mathrm{us}} \in \{0.3, 0.35, 0.4\}$ m and $V_{\mathrm{RMS}} \in \{70, 80, 90\}$ V. Each experiment transitions from Mode 1 to Mode 2 at the time indicated by the vertical red line. The same hyperparameters are used in all tests.

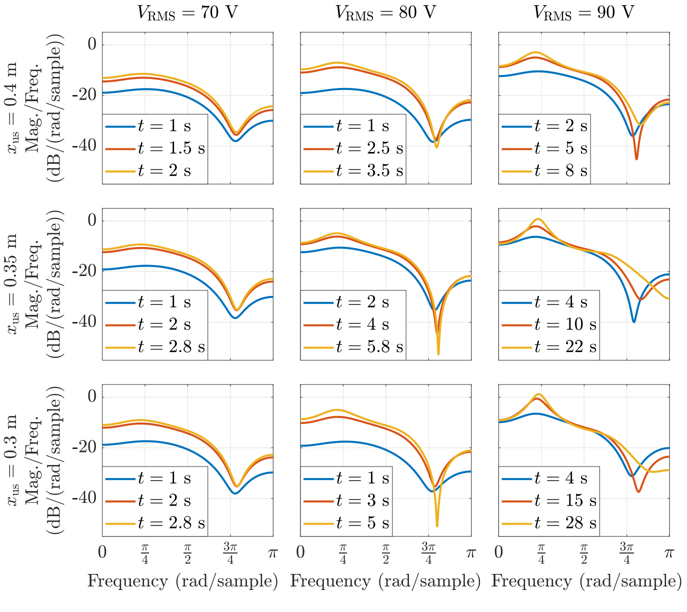

Figure 4.20: *Rijke-tube fixed-parameter experiments.* The magnitude responses of the adaptive controller from the closed-loop experiments are shown for $x_{\mathrm{us}} \in \{0.3, 0.35, 0.4\}$ m, $V_{\mathrm{RMS}} \in \{70, 80, 90\}$ V, and the times indicated in each legend. The same hyperparameters are used in all tests.

As in Subsection 4.8.1, $l_c = 5$ and $G_f(\mathbf{q}) = -1/\mathbf{q}$. The experiment begins in Mode 1 and transitions to Mode 2 after the oscillations are established.

The results for all hyperparameter combinations are shown in Figures 4.21, 4.22, 4.23, and 4.24. In all of these experiments, the oscillation suppression is at least 31.13 dB. Furthermore, Figure 4.24 shows that, for all hyperparameter combinations, the magnitude of the adaptive controller indicates a gain higher than 0 dB near $\pi/4$ rad/sample. Note that increasing p_0 and decreasing R_u results in faster suppression, as shown in Figure 4.21, which requires larger speaker signal amplitudes, as shown in Figure 4.22.

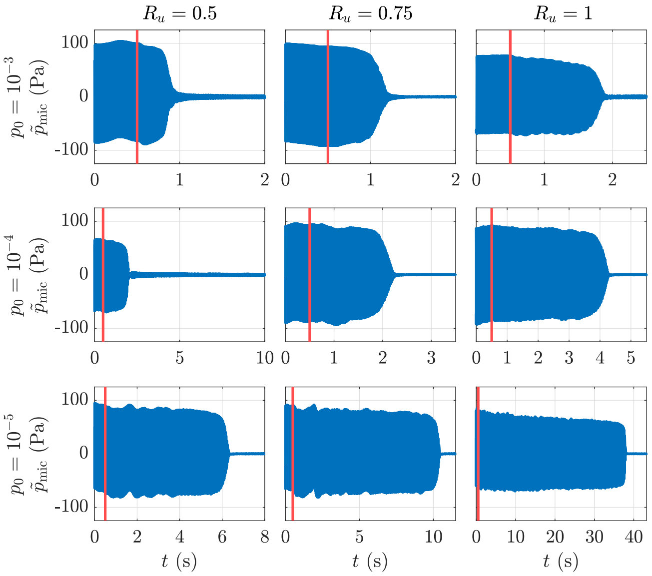

Figure 4.21: *Hyperparameter perturbation experiments.* Pressure measurements $\tilde{p}_{\rm mic}$ from the closed-loop experiments using the adaptive controller are shown for $x_{\rm us} = 0.3$ m, $V_{\rm RMS} = 90$ V, $p_0 \in \{10^{-5}, 10^{-4}, 10^{-3}\}$, and $R_u \in \{0.5, 0.75, 1\}$. Each experiment transitions from Mode 1 to Mode 2 at the time indicated by the vertical red line.

4.8.3 Performance evaluation of the frozen-gain adaptive controller

We now consider experimental scenarios where the adaptive controller coefficients are saved and used to implement a frozen-gain adaptive controller in subsequent experiments. This experiment is conducted for $x_{\rm us} = 0.3$ m and $V_{\rm RMS} = 90$ V. The following procedure consisting of five phases is followed:

- *Phase 1:* The experiment begins in Mode 1.
- *Phase 2:* The experiment transitions to Mode 2 after the oscillations are formed.

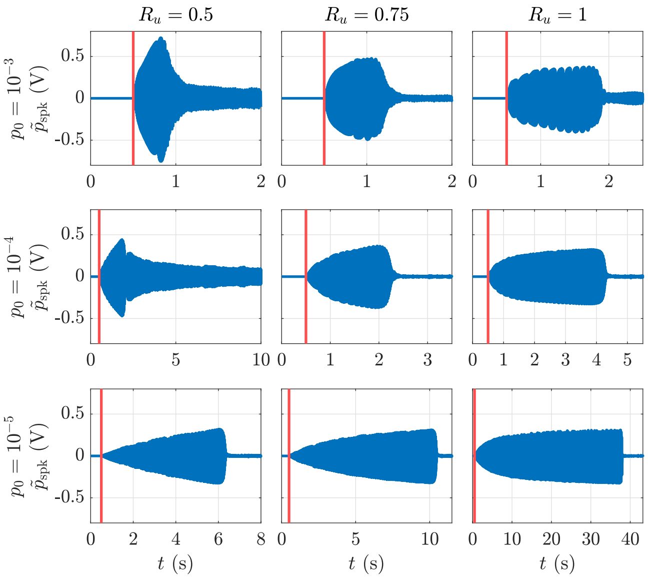

Figure 4.22: *Hyperparameter perturbation experiments.* Requested speaker voltage $\tilde{p}_{\rm spk}$ from the closed-loop experiments using the adaptive controller is shown for $x_{\rm us} = 0.3$ m, $V_{\rm RMS} = 90$ V, $p_0 \in \{10^{-5}, 10^{-4}, 10^{-3}\}$, and $R_u \in \{0.5, 0.75, 1\}$. Each experiment transitions from Mode 1 to Mode 2 at the time indicated by the vertical red line.

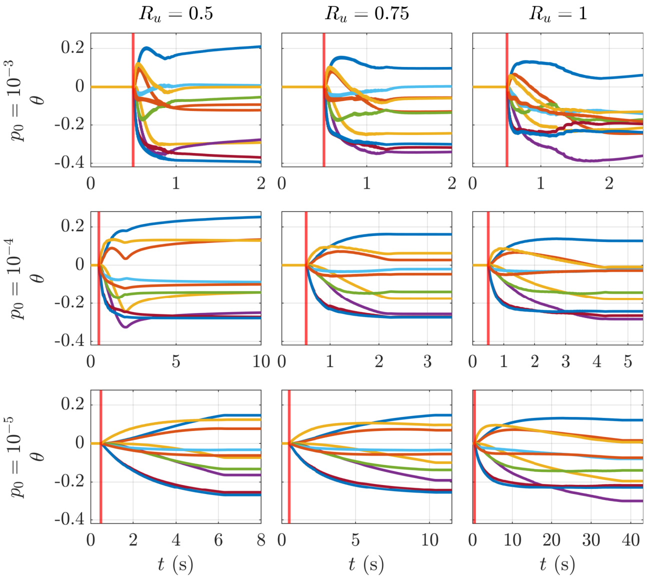

Figure 4.23: *Hyperparameter perturbation experiments.* The controller coefficients θ from the closed-loop experiments using the adaptive controller are shown for $x_{\rm us} = 0.3$ m, $V_{\rm RMS} = 90$ V, $p_0 \in \{10^{-5}, 10^{-4}, 10^{-3}\}$, and $R_u \in \{0.5, 0.75, 1\}$. Each experiment transitions from Mode 1 to Mode 2 at the time indicated by the vertical red line.

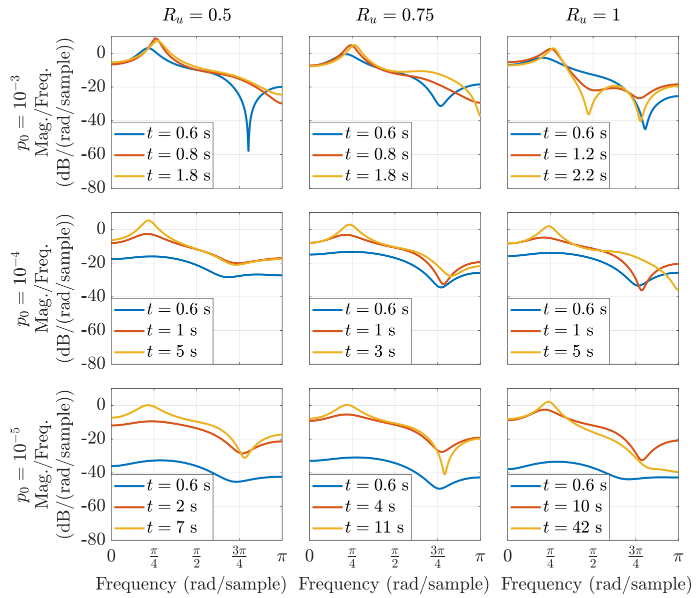

Figure 4.24: *Hyperparameter perturbation experiments.* The magnitude responses of the adaptive controller from the closed-loop experiments are shown for $x_{\text{us}} = 0.3$ m, $V_{\text{RMS}} = 90$ V, $p_0 \in \{10^{-5}, 10^{-4}, 10^{-3}\}$, $R_u \in \{0.5, 0.75, 1\}$, and the times indicated in the legends.

- *Phase 3:* After no further oscillation suppression is achieved, the experiment transitions to Mode 3.

- *Phase 4:* After some time, the experiment transitions to Mode 1, which allows the oscillations to recover their open-loop amplitude.

- *Phase 5:* After the oscillations recover their open-loop amplitude, the experiment transitions to Mode 3.

For this test, $l_{\text{c}} = 5$, $p_0 = 10^{-4}$, $R_u = 0.75$, and $G_{\text{f}}(\mathbf{q}) = -1/\mathbf{q}$ are used. Note that the values of p_0 and R_u are changed from those determined in Section 4.7 since the results of Subsection 4.8.2 showed that these hyperparameters yield faster suppression.

The experimental results are shown in Figure 4.25. At the end of Phase 2, the adaptive controller suppresses oscillations by 43.75 dB. At the end of Phase 5, the frozen-gain adaptive controller suppresses the oscillations by 45.31 dB.

4.8.4 Rijke-tube time-varying parameter experiments

We now consider experimental scenarios where the experimental Rijke-tube setup is modified during closed-loop operation. In particular, the coil position and Variac voltage are changed during the experiments. The following procedure consisting of seven phases is followed:

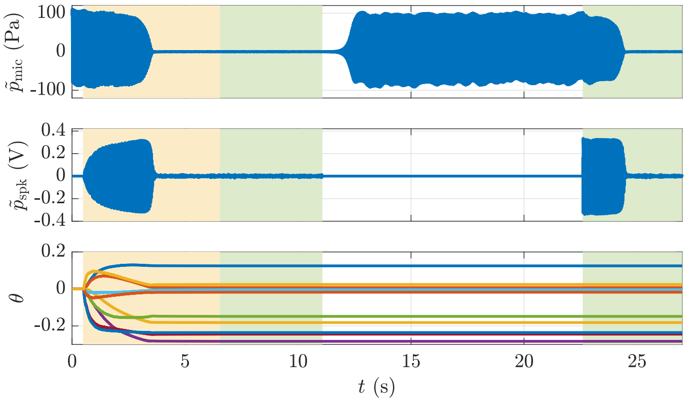

Figure 4.25: *Performance evaluation of the frozen-gain adaptive controller.* Results from the closed-loop experiment using the frozen-gain adaptive controller. The pressure measurements $\tilde{p}_{\rm mic}$, requested speaker voltage $\tilde{p}_{\rm spk}$, and controller coefficients θ are shown. The white, yellow, and green shading corresponds to Modes 1, 2, and 3, respectively.

- *Phase 1:* The experiment begins in Mode 1.
- *Phase 2:* The experiment transitions to Mode 2 after the oscillations are formed.
- *Phase 3:* After no further oscillation suppression is achieved, the experiment transitions to Mode 3.
- *Phase 4:* Either the coil position is decreased or the Variac voltage is increased.
- *Phase 5:* After some time, the experiment transitions to Mode 1, which allows oscillations to recover their open-loop amplitude.
- *Phase 6:* The experiment transitions to Mode 3 (frozen-gain adaptive controller is implemented) after the oscillations recover their open-loop amplitude.
- *Phase 7:* After approximately 30 s, the experiment transitions to Mode 2.

For the experiment where the coil voltage is changed, the voltage is changed from $V_{\rm RMS} = 70$ V to $V_{\rm RMS} = 90$ V with the coil position maintained at $x_{\rm us} = 0.3$ m. For the experiment where the coil position is changed, the position is changed from $x_{\rm us} = 0.4$ m to $x_{\rm us} = 0.3$ m with the coil voltage maintained at $V_{\rm RMS} = 90$ V. Figure 4.3 shows that the magnitudes of the peaks of the amplitude spectra increase after each transition.

For comparison, the constant-gain proportional controller introduced in Subsection 4.8.1 and shown in Figure 4.14 with $K = 0.05$ is implemented in the same experimental scenarios. The results are shown in Figures 4.26 and 4.27. In both experimental scenarios, the oscillation suppression achieved by the constant-gain proportional controller before either the coil position or the Variac voltage is changed is at least 38.69 dB. After either the coil position or the Variac voltage is changed, the oscillations recover their open-loop amplitude, and the constant-gain proportional controller yields no suppression.

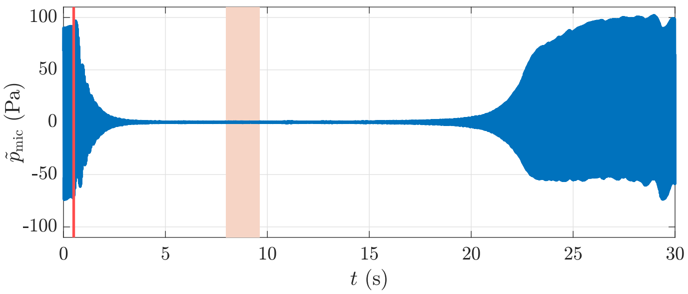

Figure 4.26: *Rijke-tube time-varying parameter experiments.* Pressure measurements $\tilde{p}_{\rm mic}$ from a closed-loop experiment using the constant-gain proportional controller in Figure 4.14 are shown for $K = 0.05$. In this experiment, the coil voltage transitions from $V_{\rm RMS} = 70$ V to $V_{\rm RMS} = 90$ V with the coil position maintained at $x_{\rm us} = 0.3$ m. The constant-gain proportional controller is initially disabled and is enabled at the time indicated by the vertical red line. The red shading denotes the time interval during which the coil voltage transitions from $V_{\rm RMS} = 70$ V to $V_{\rm RMS} = 90$ V.

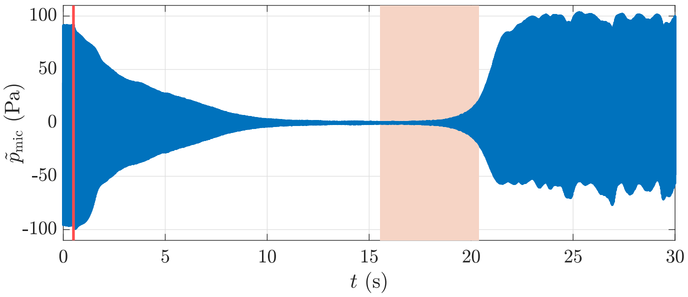

Figure 4.27: *Rijke-tube time-varying parameter experiments.* Pressure measurements $\tilde{p}_{\rm mic}$ from a closed-loop experiment using the constant-gain proportional controller in Figure 4.14 are shown for $K = 0.05$. In this experiment, the coil position transitions from $x_{\rm us} = 0.4$ m to $x_{\rm us} = 0.3$ m with the coil voltage maintained at $V_{\rm RMS} = 90$ V. The constant-gain proportional controller is initially disabled and is enabled at the time indicated by the vertical red line. The red shading denotes the time interval during which the coil location transitions from $x_{\rm us} = 0.4$ m to $x_{\rm us} = 0.3$ m.

For the adaptive suppression experiments, $l_{\rm c} = 5$, $p_0 = 10^{-4}$, $R_u = 0.75$, and $G_{\rm f}(\mathbf{q}) = -1/\mathbf{q}$ are used, as in Subsection 4.8.3. The adaptive controller suppression results are shown in Figures 4.28, 4.29, 4.30, and 4.31. At the end of Phase 2, the oscillation suppression achieved by the adaptive controller is at least 43.83 dB in both experimental scenarios. Throughout Phases 3 and 4, the frozen-gain adaptive controller maintains the oscillation suppression obtained at the end of the previous phase. At the end of Phase 6, the oscillation suppression achieved by the frozen-gain adaptive controller is at least 1.73 dB. At the end of Phase 7, the oscillation suppression achieved by the adaptive controller is at least 51.91 dB. Hence, after Phase 6, further adaptation suppresses the oscillations. Furthermore, Figures 4.29 and 4.31 show that, in both scenarios, the peak of the magnitude response of the adaptive controller near $\pi/4$ rad/sample at the end of Phase 3 subsequently increases in magnitude during Phase 7.

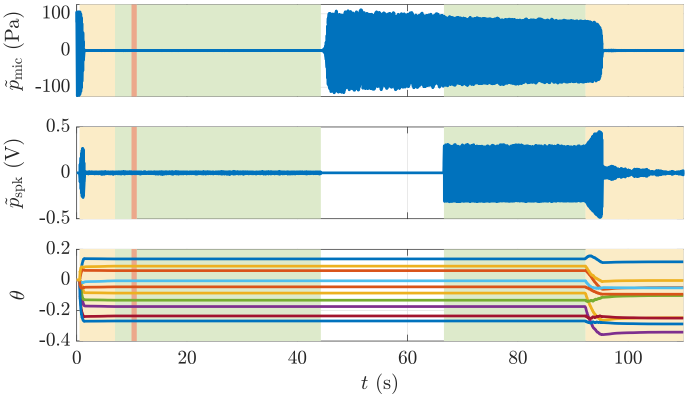

Figure 4.28: *Rijke-tube time-varying parameter experiments.* Results from the closed-loop experiment using the adaptive controller where the coil voltage transitions from $V_{\rm RMS} = 70$ V to $V_{\rm RMS} = 90$ V with the coil position maintained at $x_{\rm us} = 0.3$ m. The pressure measurements $\tilde{p}_{\rm mic}$, requested speaker voltage $\tilde{p}_{\rm spk}$, and controller coefficients θ are shown. The white, yellow, and green shading corresponds to modes 1, 2, and 3, respectively. The red shading denotes the time interval during which the coil voltage transitions from $V_{\rm RMS} = 70$ V to $V_{\rm RMS} = 90$ V.

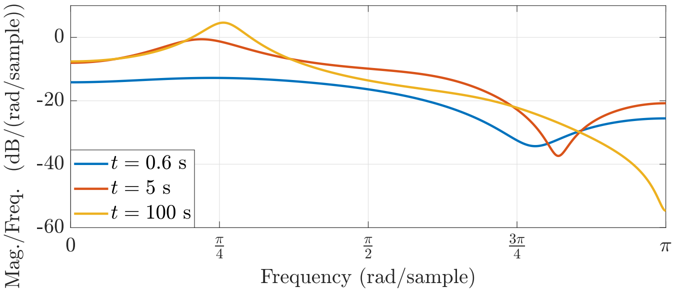

Figure 4.29: *Rijke-tube time-varying parameter experiments.* The magnitude response of the adaptive controller for the closed-loop experiment where the coil voltage transitions from $V_{\rm RMS} = 70$ V to $V_{\rm RMS} = 90$ V with the coil position maintained at $x_{\rm us} = 0.3$ m is shown for $t \in \{0.6, 5, 100\}$ s.

4.8.5 Gain-Margin Experiments

We now consider experimental scenarios where the gain of the adaptive controller is modified. These scenarios are conducted for $x_{\rm us} = 0.3$ m and $V_{\rm RMS} = 90$ V. The controller output is multiplied by α, as shown in Figure 4.32, which is initially set to $\alpha = 1$. Each scenario begins in Mode 1 and transitions to Mode 2 after the oscillations are formed. After no further oscillation suppresion is achieved, two experimental scenarios are considered:

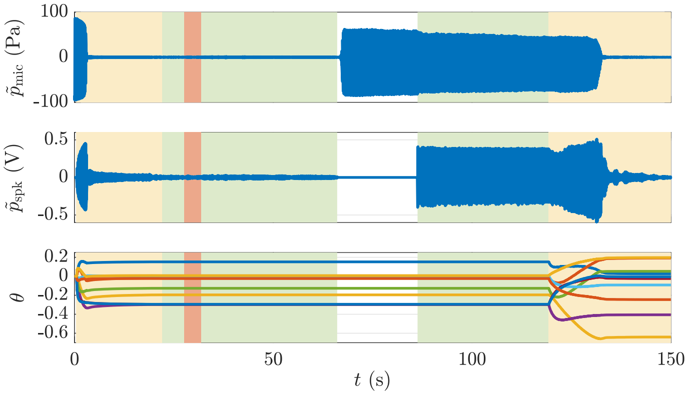

Figure 4.30: *Rijke-tube time-varying parameter experiments.* Results from the closed-loop experiment using the adaptive controller where the coil position transitions from $x_{\rm us} = 0.4$ m to $x_{\rm us} = 0.3$ m with the coil voltage maintained at $V_{\rm RMS} = 90$ V. The pressure measurements $\tilde{p}_{\rm mic}$, requested speaker voltage $\tilde{p}_{\rm spk}$, and controller coefficients θ are shown. The white, yellow, and green shading corresponds to modes 1, 2, and 3, respectively. The red shading denotes the time interval during which the coil location transitions from $x_{\rm us} = 0.4$ m to $x_{\rm us} = 0.3$ m.

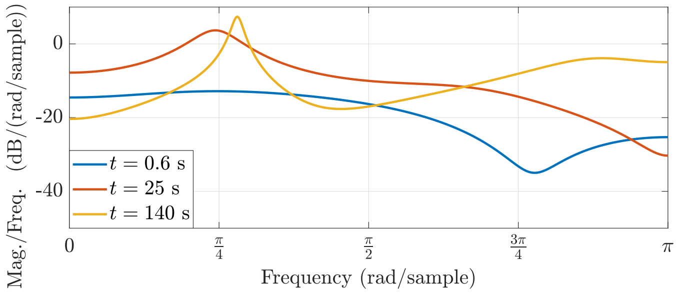

Figure 4.31: *Rijke-tube time-varying parameter experiments.* The magnitude response of the adaptive controller for the closed-loop experiment where the coil position transitions from $x_{\rm us} = 0.4$ m to $x_{\rm us} = 0.3$ m with the coil voltage maintained at $V_{\rm RMS} = 90$ V is shown for $t \in \{0.6, 25, 140\}$ s.

- *Scenario 1:* The experiment continues to operate in Mode 2.
- *Scenario 2:* The experiment transitions to Mode 3.

After this, in each scenario, the value of α is changed when no further suppression is achieved. For the these experiments, $l_{\rm c} = 5$, $p_0 = 10^{-4}$, $R_u = 0.75$, and $G_{\rm f}(\mathbf{q}) = -1/\mathbf{q}$ are used, as in Subsection 4.8.3.

Experimental results are shown in Figure 4.33. In Scenario 1, increases in α yield a slight decrease in oscillation suppression, while decreases in α yield oscillation suppression similar to the case where $\alpha = 1$. In Scenario 2, increases in α yield a slight decrease in oscillation suppression, while decreases in α yield a noticeable decrease in oscillation suppression. Hence, the adaptive controller maintains oscillation suppression under changes in its gain.

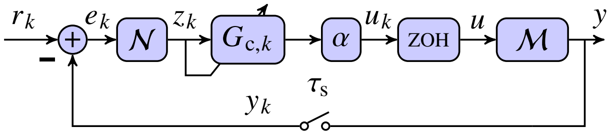

Figure 4.32: Adaptive control of $\mathcal{M}$ with controller gain α.

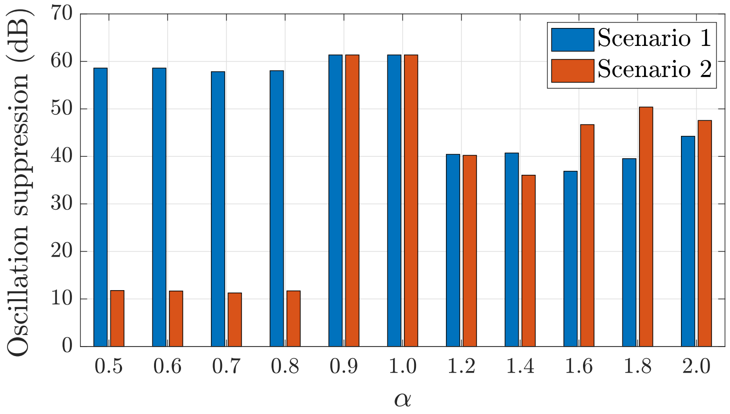

Figure 4.33: *Gain-Margin Tests.* Oscillation suppression using the controller architecture in Figure 4.32 is shown for varying values of α. After no further oscillation suppresion is achieved in the case where $\alpha = 1$, two experimental scenarios are considered. In Scenario 1, the experiment continues to operate in Mode 2. In Scenario 2, the experiment transitions to Mode 3. After this, in each scenario, the value of α is changed when no further suppression is achieved.

4.8.6 G_f relative-degree experiments

We now consider experimental scenarios involving input delay and changes in the relative degree of G_f. These experiments are conducted for $x_\mathrm{us} = 0.3$ m and $V_\mathrm{RMS} = 90$ V. For these experiments, an input delay of d steps is added to the control architecture, as shown in Figure 4.34. The experiment begins in Mode 1 and transitions to Mode 2 after the oscillations are formed. Afterwards, the experiment continues to operate in Mode 2. For this test, the hyperparameters are given by $l_\mathrm{c} = 5$, $p_0 = 10^{-4}$, and $R_u = 0.75$, as in Subsection 4.8.3. Furthermore, $G_\mathrm{f}(\mathbf{q}) = -\mathbf{q}^{-d_\mathrm{zu}}$, where d_zu determines the relative degree of G_f. Note that $d_\mathrm{zu} = 1$ in Subsections 4.8.1 to 4.8.5.

Experimental results are shown in Figure 4.35. For all $d \in \{0, 1, 2, 3, 4\}$, the values of d_zu that yield the greatest oscillation suppression lie within $\{d - 1, d, d + 1\}$.

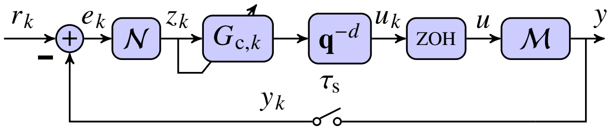

Figure 4.34: Adaptive control of $\mathcal{M}$ with controller delay of d steps.

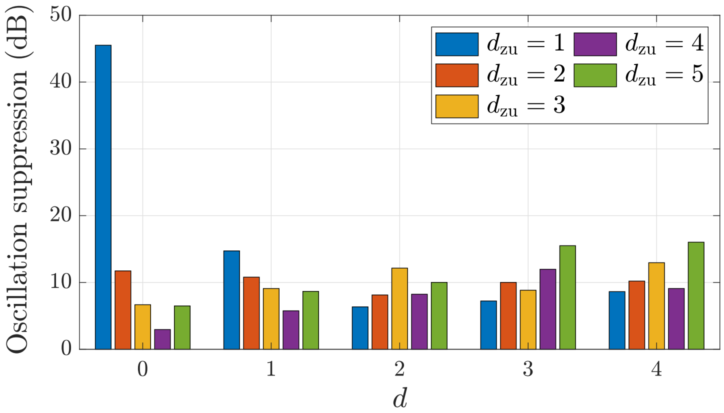

Figure 4.35: *G_{f} relative-degree experiments.* G_{f} relative-degree experimental results using the controller architecture in Figure 4.34 are shown for various values of the input delay d and the relative degree d_{zu} of G_{f}.

4.9 Conclusions

This chapter described a Rijke-tube physical experiment and its open-loop response under various system parameters. For adaptive control, a hyperparameter selection procedure was proposed. This procedure consists of tuning a Rijke-tube model to emulate the first modal peak of the open-loop response of the Rijke-tube physical experiment under a single choice of system parameters, applying the adaptive controller to the simulation model, and running numerical simulations to determine hyperparameters that suppress the model oscillations. The selected hyperparameters were then used by the adaptive controller to suppress the oscillatory response of the Rijke-tube physical experiment under various system parameters. Further experiments showed the effect of modified hyperparameters on the time it takes for the adaptive controller to suppress oscillations, the performance and robustness of the frozen-gain adaptive controller, the ability of the adaptive controller to readapt under changes in working conditions, the stability of the adaptive controller under changes in its gain, and the effect of the relative degree of the closed-loop target model on the level of suppression. In Chapter 5, the hyperparameter selection methodology developed in this chapter will be used to select the hyperparameters of a quasi-static version of the RCAC algorithm introduced in this chapter to minimize the thermoacoustic oscillations in the DISCo facility.

CHAPTER 5

Quasi-Static Adaptive Controller Application to Dual Independent Swirl Combustor

Various methodologies have been proposed for mitigating thermoacoustic oscillations in gas-turbine combustors. Passive control techniques seek to prevent or reduce these oscillations by redesigning the hardware of the combustor, such as the fuel and air injectors or the combustor geometry, and placing acoustic dampers [34–37]. However, since operating-point changes for meeting load demand and fuel-property variations may induce thermoacoustic oscillations, and since design modifications entail high costs and time-consuming activities, passive control methods tend to work effectively only within a limited range of operation [38].

In contrast to passive control methods, active feedback control techniques seek to suppress thermoacoustic oscillations by modulating actuators, such as fuel and air injectors, using data from sensors, such as pressure and chemiluminescence measurements, thereby stabilizing the desired operating point as it changes [39–44]. Since thermoacoustic oscillations typically occur at high frequency, active feedback controllers typically require actuators with high bandwidth [13, 45]. This requirement can be prohibitive, however, due to the engineering challenges of designing and implementing such devices within a harsh environment. While open-loop control approaches can be implemented with low-bandwidth actuators [116–118], these techniques have a limited operational range, similarly to passive control.

Another approach to low-bandwidth feedback control is operating point control ([119]), in which sensor measurements are used to search an operating point that optimizes a metric ([120–123]). As mentioned in [124], this approach to feedback control is similar to real-time optimization techniques since, under slow actuator modulation, the plant dynamics can be represented as a static map. Henceforth, we'll refer to these techniques as *quasi-static control*. Extremum-seeking control (ESC) falls under this category, in which a gradient estimate is used to search for a local minimum of a static map [125–132]. Applications of ESC for combustion instability suppression are studied in [14, 133–137].

The contribution of the present work is the application of a novel quasi-static adaptive controller to a laboratory gas-turbine combustor; this technique, called quasi-static RCAC (quasi-static RCAC (QSRCAC)), is an extension of retrospective cost adaptive control (RCAC) [105, 106]. QSRCAC is applied in a laboratory-scale experiment to minimize thermoacoustic oscillations in a combustor while reaching and maintaining a desired thermal power at the exit of the combustor. A preliminary version of QSRCAC was considered in [138]; the current work extends QSRCAC to use nonnegative performance variables and estimates of the cost gradient to minimize the performance variables. As shown in Figure 5.1, implementing RCAC with static G_f to the combustor studied in this chapter does not yield satisfactory results since a MIMO problem requires an online estimate of G_f. This response motivates the development of QSRCAC.

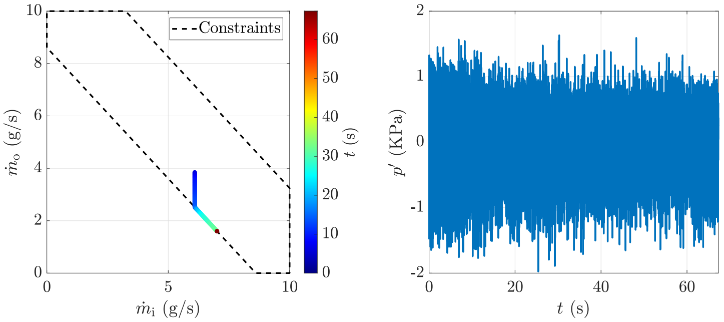

Figure 5.1: Results of implementing RCAC with static G_f to the combustor studied in this chapter.

The contents of the chapter are as follows. Section 5.1 provides an overview of the combustor, namely, the Dual Independent Swirl Combustor (DISCo). Section 5.2 specifies the control problem and describes the experimental configuration of DISCo for the laboratory experiments. Section 5.3 presents the hyperparameter selection procedure developed in Chapter 4 applied to DISCo. Section 5.4 presents a simulation model for DISCo. Section 5.5 describes an online gradient estimator based on the extended Kalman filter. Section 5.6 expands RCAC presented in Section 4.5 to include gradient estimates obtained via the technique presented in Section 5.5, resulting in QSRCAC. Section 5.7 considers the approach under which the discrete-time quasi-static adaptive controller interacts with the continuous-time DISCo simulation model. Section 5.8 presents the results of numerical closed-loop simulations with the DISCo simulation model. Section 5.9 describes how QSRCAC interacts with DISCo. Section 5.10 presents the results of closed-loop experiments in which QSRCAC is applied to DISCo. Finally, Section 5.11 presents conclusions to this chapter.

5.1 Overview of DISCo

A brief description of the Dual Independent Swirl Combustor (DISCo) facility is provided in this section. A more in-depth description of the facility, the swirler, and verification of its thermoacoustic response is provided in [139]. The single-element model combustor considered in this work consists of a dual-swirl stabilized burner design that allows for full control of operation of the swirl parameters, such as the split ratio between inner and outer swirler as well as the strength of the swirling flow. DISCo is a laboratory scale gas turbine combustor model designed to naturally exhibit low-frequency thermoacoustic oscillation near the 300 Hz range. DISCo can operate at atmospheric pressure and at elevated pressures up to 15 atm by adding a custom designed pressure vessel around the combustion chamber to simulate realistic aircraft combustor scenarios. A 3D rendering of DISCo and the commissioned DISCo facility are shown in Figure 5.2.

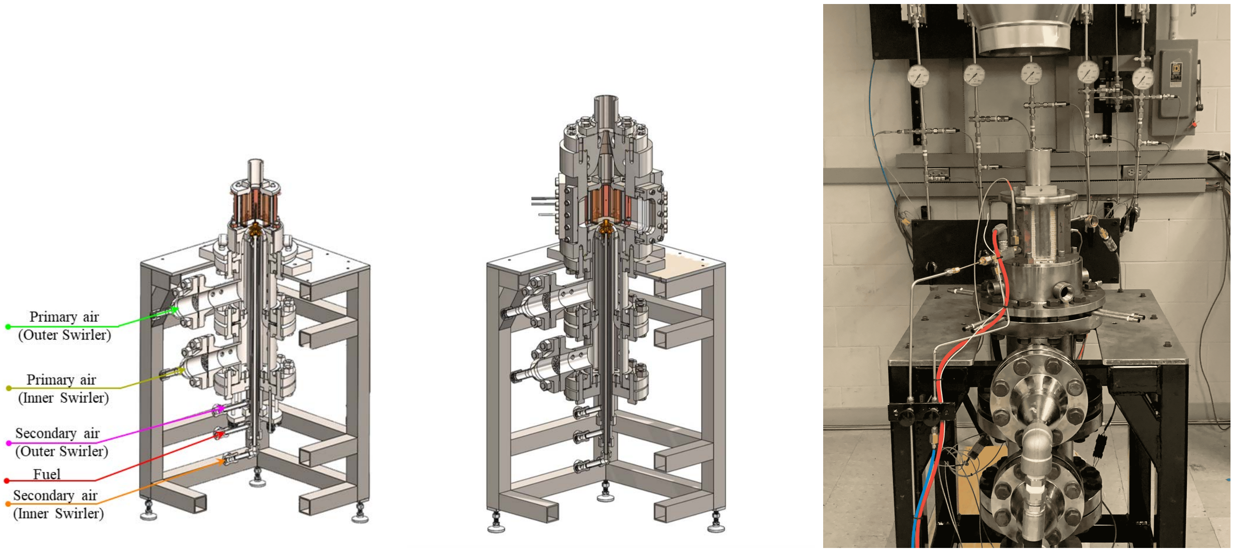

(a) (b) (c)

Figure 5.2: DISCo model facility. (a) 3D rendering of DISCo in atmospheric pressure operation configuration. (b) 3D rendering of DISCo in elevated pressure operation configuration. (c) Commissioned DISCo facility in atmospheric conditions.

DISCo allows for the independent manipulation of the mass-flow rate through each of the five flow paths labelled in Figure 5.3 (a). The outer swirler (A) and inner swirler (B) are the primary air feeds. Furthermore, there exist secondary air feeds that sidestep the swirl vanes and contain only axial components for the inner swirler (C) and the outer swirler (D). The fuel is supplied through a single feed (E), delivering a partially premixed mixture into the combustion chamber. Manipulation of these mass-flow rates allows us to independently vary the total air mass-flow rate, equivalence ratio, inner-to-outer swirler split ratio, and the swirl number of the inner and outer swirlers.

The regulation of the mass-flow rates through each of the flow paths is performed through five independent TESCOM pressure regulators coupled with ER 3000 pressure controllers, which are metered by choked orifices positioned downstream of these pressure regulators. Although the sensor update rate of the ER 3000 controllers is around 25 ms, the response of the entire system to a change in commanded mass-flow rates is relatively slow due to the inertia of the fluid systems involved in the process. This is illustrated in Figure 5.4, which shows that the response of a DISCo pressure regulator 0.5 g/s step command change of in the air lines has a rise time of 0.2 s.

Figure 5.3 (b) shows the position of the high-speed pressure sensors. The outer plenum is instrumented at positions S_5 and S_6 with two high-speed differential pressure transducers, which are Kulite XCS-190L with a maximum differential pressure of 1 atm. Both the inner plenum and combustion chamber are instrumented with a more sensitive microphone Kulite MIC-190L in positions S_8 and S_1, respectively.

Figure 5.3 (c) shows the position of the holes used to place the thermocouples at the combustor exit. The thermocouples are all bare wire, type B and have a diameter of 0.25 mm. The exit temperature is computed as the average of the temperatures measured by the three thermocouples.

To verify the frequency content of the thermoacoustic oscillations in DISCo, a Fast Fourier Transform of the time-resolved pressure data is performed. Figure 5.5 shows the pressure fluctuation measurements sampled at 15 kHz from the sensor positioned at S_1 and its corresponding frequency domain response for a total air mass-flow rate of 8 g/s, an equivalence ratio of 0.85, and a inner-to-outer swirler split ratio of 1.6. The theoretical thermal power for this experiment is 21.8 kW. Figure 5.5 (b) shows two sharp peaks at 274 Hz and 548 Hz, which can be attributed to the quarter wave mode of the inner swirl plenum and the longitudinal mode of the outer swirl plenum. Note that the peak at 274 Hz validates the design specifications of DISCo.

The pressure regulators operate slowly relative to the combustion dynamics, as shown in Figures 5.4 and 5.5 (b). Obtaining and incorporating actuators with higher bandwidth would be expensive and may entail hardware redesign. This motivates the development of control strategies for low-bandwidth actuators.

5.2 Overview of the control objective and experimental configuration

The objective of this work is to develop a quasi-static adaptive controller that yields an operating point under which the thermoacoustic oscillations within the combustion chamber are reduced and a desired combustor exit temperature is reached. For the quasi-static adaptive control tests in this

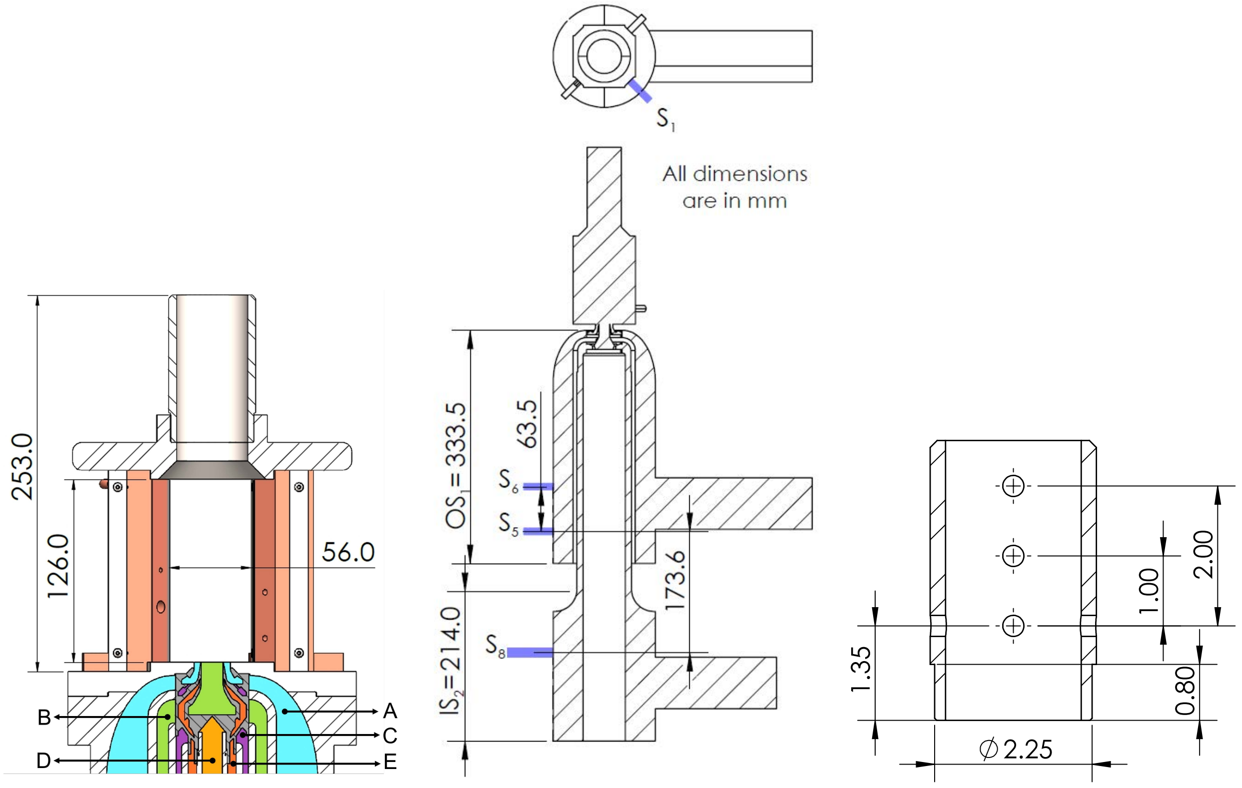

(a) (b) (c)

Figure 5.3: Cross-sectional views of DISCo. (a) shows various flowpaths through the dual swirler that modulate the operation of DISCo. (b) shows the position of the pressure sensors with respect to the fluid volume. (c) shows the position of the thermocouples at the combustor exit.

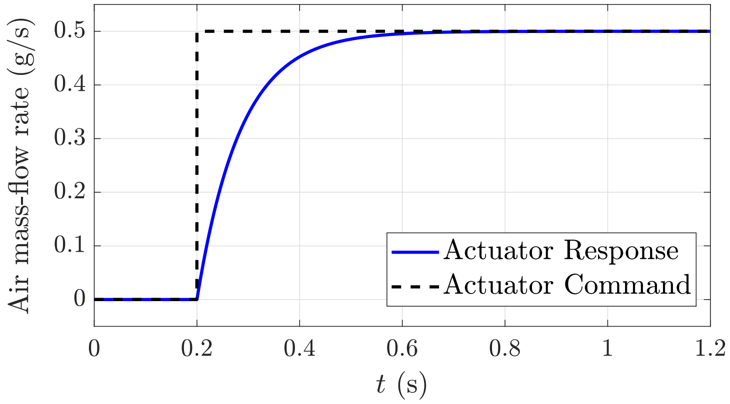

Figure 5.4: Air mass-flow rate response of DISCo pressure regulator to a step change command of 0.5 g/s.

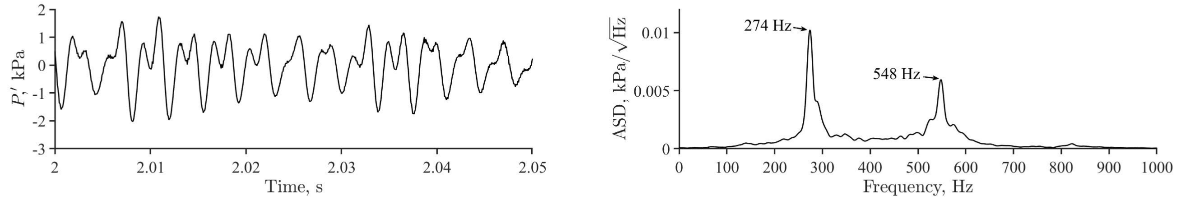

(a)

(b)

Figure 5.5: Frequency content verification of DISCo for a total air mass-flow rate of 8 g/s, an equivalence ratio of 0.85, and a inner-to-outer swirler split ratio of 1.6. (a) shows the pressure fluctuation measurements obtained from the pressure sensor positioned at S1. (b) shows the amplitude spectral density plot corresponding to the measurements shown in (a).

work, the mass-flow rate through the secondary air feeds are kept at zero and the fuel mass-flow rate are kept constant after the initial conditions is reached. Hence, only the outer swirler and the inner swirler air mass-flow rates will be modulated by the controller.

A supervisory control system modulates the pressure regulators to ignite the combustor and reach the initial operating point. Control of the pressure regulators is subsequently given to the dSpace Scalexio digital computer, which implements the quasi-static adaptive controller for physical closed-loop experiments.

Two types of tests of increasing complexity are performed in this work:

- *Two-input, single-output (TISO) test:* The controller yields outer swirler and the inner swirler air mass-flow rates (two system inputs), which reduce the root mean square (RMS) of the pressure fluctuation measurements (one measured output).
- *Two-input, Two-output (TITO) test:* The controller yields outer swirler and the inner swirler air mass-flow rates (two system inputs), which reduce the RMS of the pressure fluctuation measurements and reach a desired combustor exit temperature (two measured outputs).

The TISO test is used as a preliminary performance assessment of the proposed quasi-static adaptive controller at reducing the amplitude of thermoacoustic instabilities within DISCo. The TITO test presents a problem of more practical relevance, that is, reducing the amplitude of thermoacoustic instabilities and maintaining a constant thermal power at the combustor exit to achieve a desired flame length. In both tests, the pressure fluctuation measurements from the sensor at S_1 are used to compute the RMS of the thermoacoustic oscillations. In the TITO test, the averaged temperature measurement from the thermocouples at the exit of the combustor is subtracted from the desired combustor exit temperature to compute the temperature error.

Table 5.1 shows the operating conditions of DISCo used for both tests. The air mass-flow rate per swirler and total air mass-flow rate ranges impose a convex constraint on the inner and outer swirler mass-flow rates. Note that the air mass-flow rate per swirler range is derived from actuator constraints, equivalence ratio range is chosen to prevent flameout, and the total air mass-flow rate range is derived from the chosen fuel mass-flow rate and the equivalence ratio range.

Table 5.1: Operating conditions of DISCo for the physical experiments.

Parameter	**Value or range**
Operating pressure (atm)	1
Fuel mass-flow rate (g/s)	0.4
Air mass-flow rate per swirler (g/s)	[0.75, 9]
Total air mass-flow rate (g/s)	[7, 11.3]
Equivalence ratio	[0.6, 1.1]

5.3 Overview of the methodology

The hyperparameter selection methodology based on closed-loop numerical simulation developed in Chapter 4 is applied in this chapter and is shown in Figure 5.6.

The methodology as applied to DISCo is described next. First, physical experiments are conducted in an open-loop configuration (no feedback control) to obtain pressure fluctuation and temperature measurements from the combustor model facility. Then, a fit procedure is applied, where the parameters of a rudimentary simulation model are chosen to emulate the amplitude of the pressure fluctuation measurements and the temperature measurements at given input mass-flow rates. This procedure yields a simulation model, which is used for quasi-static adaptive closed-loop numerical simulations to select hyperparameters based on achieved controller performance. The selected hyperparameters are then used in physical closed-loop experiments.

For these experiments, the quasi-static adaptive controller is implemented on a dSpace Scalexio system to minimize the oscillations within the combustion chamber and maintain a desired temperature at the exit of the combustor. Note that the simulation model is used only to select hyperparameters for the controller, and is otherwise not used or needed for feedback control. Furthermore, the simulation model need not be high-fidelity, as is shown in the experimental results in Section 5.10.

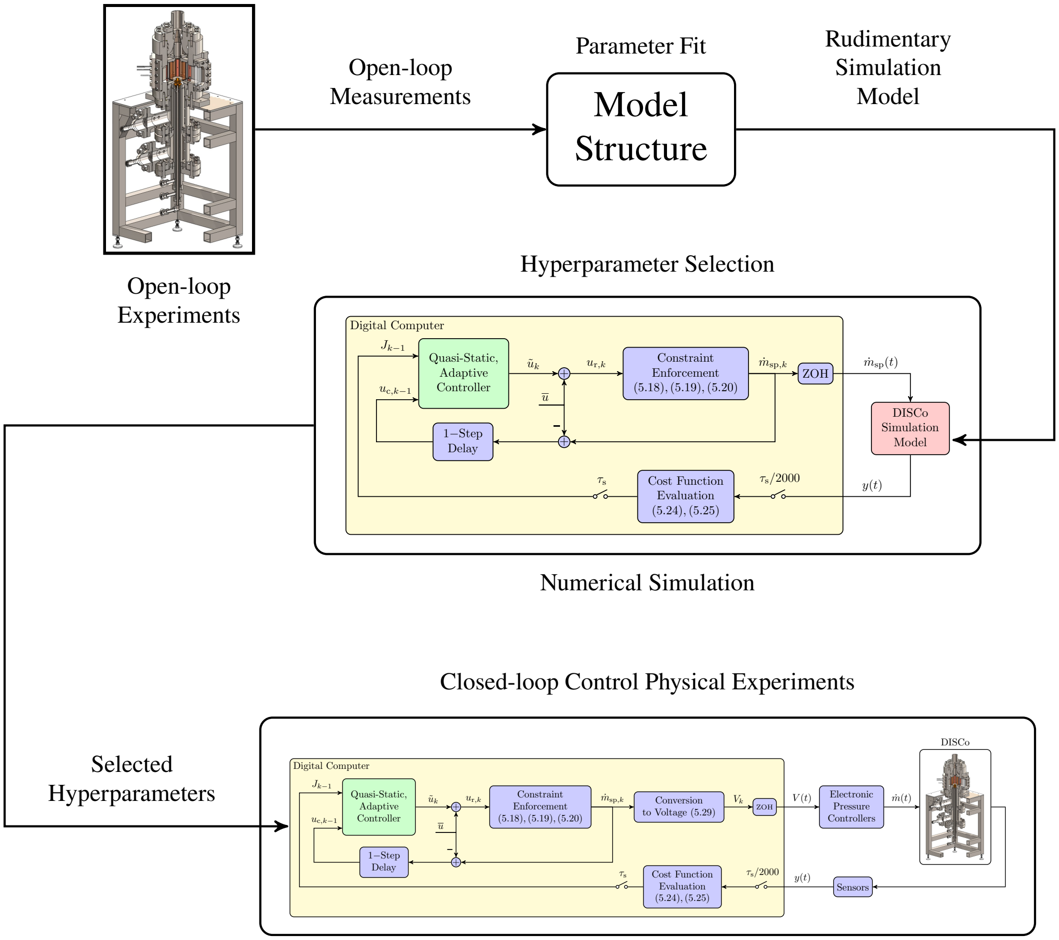

Figure 5.6: Hyperparameter selection methodology. The objective is to select hyperparameters by applying the quasi-static adaptive controller to a simulation model of DISCo. The selected hyperparameters are then used in DISCo laboratory experiments.

5.4 DISCo simulation model

An overview of the dynamics of the DISCo simulation model is given in this section. The block diagram in Figure 5.7 summarizes these dynamics.

Let $\dot{m}_{\rm sp}(t) \overset{\triangle}{=} \left[\dot{m}_{\rm sp,i}(t) \;\; \dot{m}_{\rm sp,o}(t)\right]^{\mathsf{T}} \in \mathbb{R}^2$ be the specified air mass-flow rate vector and the model input, where $\dot{m}_{\rm sp,i}, \dot{m}_{\rm sp,o} \in \mathbb{R}$ are the specified inner and outer swirl air mass-flow rates, respectively. Then, the dynamics of the pressure regulators are modeled by

$$\ddot{m}(t) = -a\dot{m}(t) + b\dot{m}_{\rm sp}(t), \tag{5.1}$$

where $\dot{m}(t) \overset{\triangle}{=} [\dot{m}_{\rm i}(t) \;\; \dot{m}_{\rm o}(t)]^{\mathsf{T}} \in \mathbb{R}^2$ is the air mass-flow rate vector, $\dot{m}_{\rm i}, \dot{m}_{\rm o} \in \mathbb{R}$ are the inner and outer swirl air mass-flow rates, respectively, and $a, b > 0$. Next, let $\mathcal{F}, \mathcal{G} \colon \mathbb{R}^2 \to \mathbb{R}$ be the static maps defined as

$$\mathcal{F}(\dot{m}) \triangleq -0.132\dot{m}_{\mathrm{i}}^2 + 0.269\dot{m}_{\mathrm{o}}^2 + 0.361 \cdot 10^{-2}\dot{m}_{\mathrm{i}}\dot{m}_{\mathrm{o}}$$
$$- 0.278\dot{m}_{\mathrm{i}} - 3.7496\dot{m}_{\mathrm{o}} + 14.16, \tag{5.2}$$
$$\mathcal{G}(\dot{m}) \triangleq \frac{1}{32}\left(\dot{m}_{\mathrm{i}} - \dot{m}_{\mathrm{o}}\right)^2 - \frac{1}{32}\left[\dot{m}_{\mathrm{i}} + \dot{m}_{\mathrm{o}} - (\dot{m}_{\mathrm{min}} + \dot{m}_{\mathrm{max}})\right]^2 + 3, \tag{5.3}$$

where $\dot{m}_{\mathrm{min}}, \dot{m}_{\mathrm{max}} > 0$ are the minimum and maximum air mass-flow rates allowed per swirler, respectively. $\mathcal{F}$ is obtained by sampling the RMS of the pressure fluctuation voltage measurements for 1 s for several values of $\dot{m}_{\mathrm{i}}$ and $\dot{m}_{\mathrm{o}}$ and using these to perform multivariate polynomial regression. The structure of $\mathcal{G}$ is chosen to fit the data using approximate coefficients rounded to integer values. The output values of $\mathcal{F}$ and $\mathcal{G}$ for all $\dot{m}_{\mathrm{i}}, \dot{m}_{\mathrm{o}} \in [1, 9]$ g/s are shown in Figure 5.8.

Next, define the model output $y(t) \triangleq \left[\hat{p}'(t) \;\; \hat{T}(t)\right]^{\mathsf{T}}$, where $\hat{p}'(t) \in \mathbb{R}$ is the normalized combustor pressure fluctuations and $\hat{T}(t) > 0$ is the normalized combustor exit temperature. The values of $\hat{p}'(t)$ and $\hat{T}(t)$ are normalized such that they follow the voltage measurements obtained from the pressure and temperature sensors in open-loop experiments. Then, $\hat{p}'(t)$ and $\hat{T}(t)$ are given by

$$\hat{p}'(t) = \mathcal{F}(\dot{m}(t)) \sin\left(\frac{2\pi}{f_0}t\right) + w_1(t), \tag{5.4}$$
$$\hat{T}(t) = \mathcal{G}(\dot{m}(t)) + w_2(t), \tag{5.5}$$

where $f_0 > 0$, and $w_1(t)$ and $w_2(t)$ are noise signals. In particular, for all $k \geq 0$ and all $t \in [k\tau_{\mathrm{sim}}, (k+1)\tau_{\mathrm{sim}})$, where $\tau_{\mathrm{sim}} > 0$ is the simulation time step, $w_1(t)$ and $w_2(t)$ are given by

$$w_1(t) = \omega_{1,k}, \tag{5.6}$$
$$w_2(t) = \omega_{2,k}, \tag{5.7}$$

where $\omega_{1,k}$ is a Gaussian random variable with mean 0 and standard deviation σ_1, and $\omega_{2,k}$ is a Gaussian random variable with mean 0 and standard deviation σ_2.

Table 5.2 shows the DISCo simulation model parameters, where a and b are chosen to match the response of the pressure regulators, and the frequency f_0 corresponds to the second highest peak shown in Figure 5.5 (b), σ_1 and σ_2 are chosen to match the signal-to-noise ratio of the pressure fluctuation and temperature measurements, and τ_{sim} is the sampling rate of the sensors.

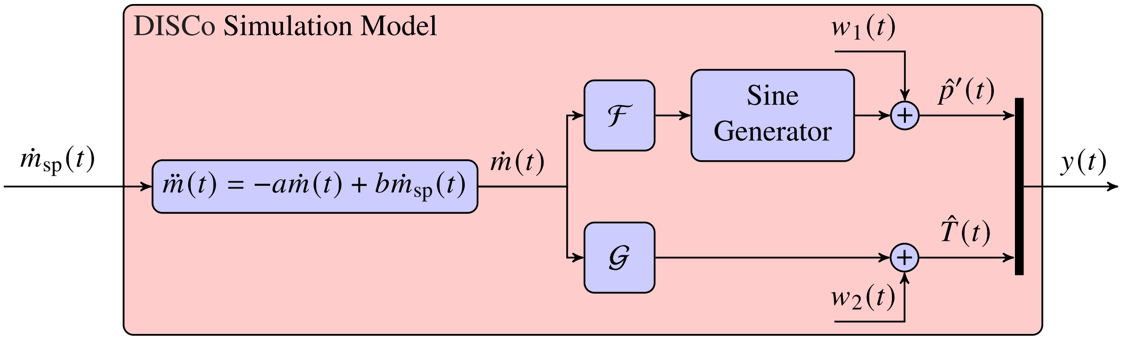

Figure 5.7: DISCo simulation model block diagram.

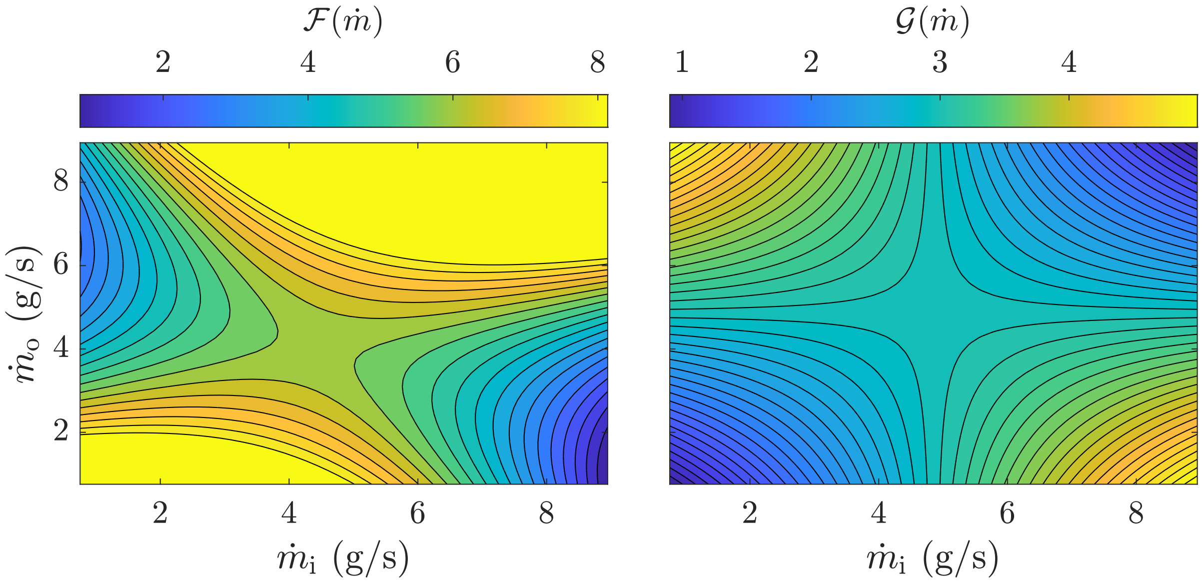

Figure 5.8: $\mathcal{F}(\dot m)$ and $\mathcal{G}(\dot m)$ output values where $\dot m = [\dot m_{\mathrm{i}} \;\; \dot m_{\mathrm{o}}]^{\mathsf{T}} \in [1,9] \times [1,9]$ g/s. The values corresponding to $\mathcal{F}(\dot m) > 8.2$ have been saturated at 8.2 for visualization purposes.

Table 5.2: Parameters of the DISCo simulation model.

Parameter	a	b	f_0	σ_1	σ_2	τ_{sim}
Value	110	110	500	0.1	0.05	10^{-4}

5.5 Online gradient estimator using an Extended Kalman Filter

For all $k \geq 0$, let $J_k \overset{\triangle}{=} [J_{1,k} \;\; \cdots \;\; J_{l_J,k}]^{\mathsf{T}} \in \mathbb{R}^{l_J}$ be a cost function vector computed from system measurements, where, for all $i \in \{1,\ldots,l_J\}$, $J_{i,k} \geq 0$ is the ith component of J_k, let $u_{\mathrm{c},k}$ be the constrained control input defined in Section 4.5, and let $\nabla J_k \overset{\triangle}{=} [\nabla J_{1,k} \;\; \cdots \;\; \nabla J_{l_J,k}]^{\mathsf{T}} \in \mathbb{R}^{l_J \times l_u}$ be the gradient of J_k over $u_{\mathrm{c},k}$, where, for all $i \in \{1,\ldots,l_J\}$, the transpose of $\nabla J_{i,k} \in \mathbb{R}^{l_u}$ corresponds to the ith row of ∇J_k.

Next, let $i \in \{1, \ldots, l_J\}$. Then, the measurement model for $J_{i,k}$ is given by

$$J_{i,k} = J_{\mathrm{b},i} + \nabla J_{i,k}^{\mathsf{T}} u_{\mathrm{c},k}, \tag{5.8}$$

where $J_{\mathrm{b},i} \in \mathbb{R}$ is a bias variable. Note that (5.8) is an extension of Equation (17) from [125]. Furthermore, let $\nabla \hat{J}_{i,k} \in \mathbb{R}^{l_u}$ be an estimate of $\nabla J_{i,k}$, let $\hat{J}_{\mathrm{b},i} \in \mathbb{R}$ be an estimate of $J_{\mathrm{b},i}$, let $\hat{x}_{i,k} \triangleq \begin{bmatrix} \nabla \hat{J}_{i,k}^{\mathsf{T}} & \hat{J}_{\mathrm{b},i} \end{bmatrix}^{\mathsf{T}} \in \mathbb{R}^{l_u+1}$ be an estimate of $x_{i,k} \triangleq \begin{bmatrix} \nabla J_{i,k}^{\mathsf{T}} & J_{\mathrm{b},i} \end{bmatrix}^{\mathsf{T}}$, and let $P_{i,k} \in \mathbb{R}^{(l_u+1)\times(l_u+1)}$ be the covariance of the estimate $\hat{x}_{i,k}$ of $x_{i,k}$. Then, as indicated by (5.8) and Section 3.1 of [125], the estimate $\nabla \hat{J}_{i,k}$ is given by the recursive update of the Extended Kalman Filter (extended Kalman filter (EKF)), whose prediction and update equations are given, for $i \in \{1, \ldots, l_J\}$, by

$$\hat{x}_{i,k} = \hat{x}_{i,k-1} + K_{i,k-1}\left(G_{i,k-1} - H_{k-1}\hat{x}_{i,k-1}\right), \tag{5.9}$$

$$P_{i,k} = (I_{l_u+1} - K_{i,k-1}H_{k-1})(P_{i,k-1} + Q_i), \tag{5.10}$$

$$\nabla \hat{J}_{i,k} = \begin{bmatrix} I_{l_u} & 0_{l_u\times 1} \end{bmatrix} \hat{x}_{i,k}, \tag{5.11}$$

where

$$G_{i,k-1} \triangleq \begin{bmatrix} J_{i,k-1} \\ J_{i,k-1-k_1} \\ \vdots \\ J_{i,k-1-k_{l_u}} \end{bmatrix} \in \mathbb{R}^{l_u+1}, \; H_{k-1} \triangleq \begin{bmatrix} u_{\mathrm{c},k-1}^{\mathsf{T}} & 1 \\ u_{\mathrm{c},k-1-k_1}^{\mathsf{T}} & 1 \\ \vdots & \vdots \\ u_{\mathrm{c},k-1-k_{l_u}}^{\mathsf{T}} & 1 \end{bmatrix} \in \mathbb{R}^{(l_u+1)\times(l_u+1)},$$

$$K_{i,k-1} \triangleq [(P_{i,k-1} + Q_i)H_{k-1}^{\mathsf{T}})(H_{k-1}(P_{i,k-1} + Q_i)H_{k-1}^{\mathsf{T}} + R_i]^{-1} \in \mathbb{R}^{(l_u+1)\times(l_u+1)},$$

$Q_i, R_i \in \mathbb{R}^{(l_u+1)\times(l_u+1)}$ are the constant weighting matrices, and $0 < k_1 < \cdots < k_{l_u}$ are indices. The matrices Q_i and R_i determine the rate of estimation, and $k_1, \ldots, k_{l_u}$ are chosen to enhance the accuracy of the estimate $\hat{x}_{i,k}$. Finally, the estimate $\nabla \hat{J}_k$ is given by

$$\nabla \hat{J}_k \triangleq \begin{bmatrix} \nabla \hat{J}_{1,k} & \cdots & \nabla \hat{J}_{l_J,k} \end{bmatrix}^{\mathsf{T}} \in \mathbb{R}^{l_J \times l_u}. \tag{5.12}$$

For all of the numerical simulations and physical experiments in this chapter, $\hat{x}_{i,k}$ is initialized as $\hat{x}_{i,0} = 0_{l_u\times 1}$. The matrices $P_{i,0}$, Q_i, and R_i have the form $P_{i,0} = p_{i,0}I_{l_u+1}$, $Q_i = q_i I_{l_u+1}$, and $R_i = r_i I_{l_u+1}$, where the positive scalars $p_{i,0}$, q_i, and r_i determine the rate of estimation.

5.6 Quasi-static, adaptive control using RCAC

The block diagram for quasi-static RCAC (QSRCAC) shown in Figure 5.9, which includes RCAC introduced in Section 4.5, the EKF gradient estimator introduced in Section 5.5, a normalization function, and a gradient conversion function. In this application, $l_J = l_z$ and $l_\mathrm{f} = l_u$. QSRCAC operates on the previous time step cost function vector $J_{k-1} \in \mathbb{R}^{l_z}$ and $u_{\mathrm{c},k-1} \in \mathbb{R}^{l_u}$, to produce the QSRCAC output vector $\tilde{u}_k \in \mathbb{R}^{l_u}$. As mentioned in Section 5.5, for all $i \in \{1, \ldots, l_z\}$, $J_{i,k-1} > 0$. Hence, the objective of QSRCAC is to minimize each of the components of J_k by modulating $\tilde{u}_k$, that is,

$$\min_{(\tilde{u}_n)_{n=0}^{\infty}} \limsup_{k\to\infty} \sum_{i=1}^{l_z} J_{i,k}. \tag{5.13}$$

In order to obtain the performance variable z_{k-1} used by RCAC, we normalize the cost function using

$$z_{k-1} \overset{\triangle}{=} [I_{l_z} + \nu \operatorname{diag}(J_{k-1})]^{-1} J_{k-1}, \tag{5.14}$$

where $\nu \in [0, \infty)$. We fix $\nu = 0.2$ throughout this work. Next, the gradient estimator block operates on J_{k-1} and u_{k-1} to produce $\nabla\hat{J}_k$ by using the EKF-based estimator described in Section 5.5. Furthermore, the gradient conversion block yields $N_{k-1} = \begin{bmatrix} N_{1,k-1} & \cdots & N_{l_u,k-1} \end{bmatrix}$, such that, for all $i \in \{1, \ldots, l_u\}$,

$$N_{i,k-1} = \begin{bmatrix} & \overline{\nabla}\hat{J}_{1,i,k} & \\ 0_{l_z\times(i-1)} & \vdots & 0_{l_z\times(l_u-i)} \\ & \overline{\nabla}\hat{J}_{l_z,i,k} & \end{bmatrix}, \tag{5.15}$$

where, for all $j \in \{1, \ldots, l_z\}$,

$$\overline{\nabla}\hat{J}_{j,i,k} \overset{\triangle}{=} \begin{cases} \nabla\hat{J}_{j,i,k}/\|\nabla\hat{J}_{j,k}\|, & \|\nabla\hat{J}_{j,k}\| \geq \varepsilon \\ \nabla\hat{J}_{j,i,k}/\varepsilon, & \text{otherwise}, \end{cases} \tag{5.16}$$

$\nabla\hat{J}_{j,i,k}$ is the ith component of $\nabla\hat{J}_{j,k}$, and $\varepsilon > 0$. We fix $\varepsilon = 10^{-4}$ throughout this work. Then, the RCAC block uses z_{k-1}, N_{k-1}, and u_{k-1} to produce $u_k \in \mathbb{R}^{l_u}$ by using the operations shown in Section 4.5.

Finally, define $\tilde{u}_k \overset{\triangle}{=} u_k + \Delta u_k$, where $\Delta u_k \in \mathbb{R}^{l_u}$ is a perturbation signal, which is defined in Section 5.7. Note that $u_{\mathrm{c},k-1}$ is shown as an input to QSRCAC since the output $\tilde{u}_k$ may be subject to constraints. Hence, $u_{\mathrm{c},k-1}$ is obtained from $\tilde{u}_k$ after constraints and a 1-step delay is applied. Note that, while [125] only uses $\nabla\hat{J}_k$, QSRCAC uses J_{k-1} and $\nabla\hat{J}_k$.

In numerical simulations and physical experiments, the EKF and RCAC are enabled and disabled in various ways. We consider the following modes of operation starting at step $k_0 \geq 0$:

i) *Mode 1: EKF and RCAC are disabled.* For all $k \geq k_0$, $\theta_k = \theta_{k-1}$, $P_k = P_{k-1}$, $u_k = 0$, $\Delta u_k = 0$, and, for all $i \in l_z$, $\hat{x}_{i,k} = \hat{x}_{i,k-1}$, $P_{i,k} = P_{i,k-1}$, and $\nabla \hat{J}_{i,k} = 0$.

ii) *Mode 2: EKF is enabled and RCAC is disabled.* For all $k \geq k_0$, $\theta_k = \theta_{k-1}$, $P_k = P_{k-1}$, $u_k = 0$, $\Delta u_k = \mathcal{H}(k)$, where $\mathcal{H}\colon \{0, 1, \ldots\} \to \mathbb{R}^{l_u}$ is a nonzero, periodic vector function, and, for all $i \in l_z$, $\hat{x}_{i,k}$, $P_{i,k}$, and $\nabla \hat{J}_{i,k}$, are updated by (5.9), (5.10) and (5.11), respectively.

iii) *Mode 3: EKF and RCAC are enabled.* For all $k \geq k_0$, θ_k, P_k, and u_k are updated by (4.27), (4.28), and (4.17), respectively, $\Delta u_k = 0$, and, for all $i \in l_z$, $\hat{x}_{i,k}$, $P_{i,k}$, and $\nabla \hat{J}_{i,k}$, are updated by (5.9), (5.10) and (5.11), respectively.

Note that Δu_k is nonzero only in Mode 2, unlike in [125], in which the perturbation signal is never zero over any period of time. Hence, Δu_k is only used to initialize the EKF and it does not affect the adaptation of RCAC.

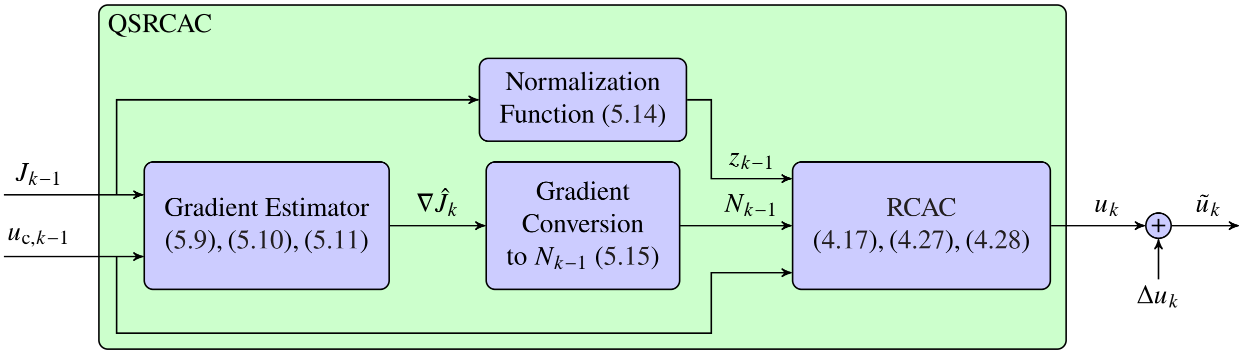

Figure 5.9: QSRCAC block diagram.

5.7 Sampled-data implementation of QSRCAC for DISCo numerical simulations

QSRCAC presented in Section 5.6 is implemented as a sampled-data controller to control the response of the DISCo simulation model introduced in Section 5.4. For the current control problem, $l_u = 2$ since both the inner and outer swirl mass-flow rates are modulated. As mentioned in Section 5.2, the value of l_z depends on the test being performed; $l_z = 1$ for the TISO tests and $l_z = 2$ for the TITO tests. Figure 5.10 shows the block diagram of the sampled-data closed-loop system considered for numerical simulations, where $\overline{u} \in \mathbb{R}^2$ is the command bias and $\tau_s > 0$ is the adaptive controller sampling period. The command bias $\overline{u}$ encodes the initial operating point set by the supervisory control system, as mentioned in Section 5.2. The DISCo simulation model output measurements are sampled every $\tau_{\rm s}/2000$ s. For all numerical simulations, $\tau_{\rm s} = 0.2$ s/step, such that $\tau_{\rm s} = 2000\ \tau_{\rm sim}$. The digital-to-analog (D/A) and analog-to-digital (A/D) interfaces, which are synchronous, are zero-order-hold (ZOH) and sampler, respectively.

Let the requested command $u_{{\rm r},k}$ be given by

$$u_{{\rm r},k} \triangleq \tilde{u}_k + \overline{u}. \tag{5.17}$$

Then, the constraints mentioned in Section 5.2 are applied to $u_{{\rm r},k}$ to obtain $\dot{m}_{{\rm sp},k}$, which is given by

$$\dot{m}_{{\rm sp},k} \triangleq \begin{bmatrix}\dot{m}_{{\rm sp,i},k} & \dot{m}_{{\rm sp,o},k}\end{bmatrix}^{\sf T} \triangleq \underset{v \triangleq [v_{\rm i}\ v_{\rm o}]^{\sf T} \in \mathbb{R}^2}{\operatorname{argmin}} \quad ||u_{{\rm r},k} - v||_2, \tag{5.18}$$

subject to

$$v_{\rm i}, v_{\rm o} \in [\dot{m}_{\rm min}, \dot{m}_{\rm max}], \quad v_{\rm i} + v_{\rm o} \in [\dot{m}_{\rm t,min}, \dot{m}_{\rm t,max}], \tag{5.19}$$

$$|v_{\rm i} - \dot{m}_{{\rm sp,i},k-1}| \le \Delta\dot{m}_{\rm max}, \quad |v_{\rm o} - \dot{m}_{{\rm sp,o},k-1}| \le \Delta\dot{m}_{\rm max}, \tag{5.20}$$

where $\dot{m}_{\rm min}, \dot{m}_{\rm max} > 0$ denote the minimum and maximum air mass-flow rates allowed per swirler, $\dot{m}_{\rm t,min}, \dot{m}_{\rm t,max} > 0$ denote the minimum and maximum total air mass-flow rates allowed, and $\Delta\dot{m}_{\rm max} > 0$ denotes the maximum magnitude change air of mass-flow rate per swirler between steps. At each adaptive controller step, a convex optimization solver is used to solve (5.18)–(5.20). Then, the constrained input of QSRCAC is given by

$$u_{{\rm c},k-1} \triangleq \dot{m}_{{\rm sp},k-1} - \overline{u}. \tag{5.21}$$

For all $t \in [k\tau_{\rm s}, (k+1)\tau_{\rm s})$, the DISCo simulation model input is given by

$$\dot{m}_{\rm sp}(t) = \dot{m}_{{\rm sp},k}. \tag{5.22}$$

The Cost Function Evaluation block computes J_{k-1} from the sensor measurements. Let $\hat{p}'_{\rm rms} > 0$ be the RMS obtained from $\hat{p}'$ and let $l_{\rm rms} > 0$ be the number of samples used to compute the RMS, such that, for all $t \ge l_{\rm rms}\tau_{\rm s}/2000$,

$$\hat{p}'_{\rm rms}(t) \triangleq \sqrt{\frac{1}{l_{\rm rms}} \sum_{\kappa=0}^{l_{\rm rms}} \left[\hat{p}'\left(t - \kappa\frac{\tau_{\rm s}}{2000}\right)\right]^2}, \tag{5.23}$$

Hence, for the TISO tests ($l_z = 1$),

$$J_{k-1} = K_1 p'_{\rm rms}(k\tau_{\rm s}), \tag{5.24}$$

and, for the TITO tests ($l_z = 2$),

$$J_{k-1} = \begin{bmatrix} K_1 \; p'_{\rm rms}(k\tau_{\rm s}) \\ K_2 \; (\hat{T}(k\tau_{\rm s}) - \hat{T}_{\rm ref})^2 \end{bmatrix}, \tag{5.25}$$

where $K_1, K_2 > 0$, and $\hat{T}_{\rm ref} > 0$ is the normalized temperature reference value that determines the desired combustor exit temperature in the TITO tests.

Table 5.3 shows the parameters chosen for numerical simulations. Note that $\tau_{\rm s}$ is chosen to approximately match the rise time corresponding to the actuator step response, $\overline{u}$ is chosen arbitrarily, and $\hat{T}_{\rm ref}$ is chosen to reflect the thermocouple voltage measurement equivalent to a desired combustor exit temperature of approximately 1500 K. Furthermore, $\dot{m}_{\rm min}, \dot{m}_{\rm max}, \dot{m}_{\rm t,min}, \dot{m}_{\rm t,max}$ are determined from the constraints in Table 5.1, and $\Delta\dot{m}_{\rm max}$ is determined from experimental results to prevent flameout. Figure 5.11 shows the output values of $\mathcal{F}$, $\mathcal{G}$, and $\overline{\mathcal{G}}$, where $\overline{\mathcal{G}}(\dot{m}) \triangleq |\mathcal{G}(\dot{m}) - \hat{T}_{\rm ref}|$, $\hat{T}_{\rm ref} = 3.7$, for all $\dot{m}_{\rm i}, \dot{m}_{\rm o} \in [1, 9]$ g/s and the convex constraints given by Table 5.1. For the TISO test, the objective is to reach values of $\dot{m}_{\rm i}$ and $\dot{m}_{\rm o}$ that minimize $\mathcal{F}$ within the mass-flow rate constraints. For the TITO test, the objective is to reach values of $\dot{m}_{\rm i}$ and $\dot{m}_{\rm o}$ that minimize $\mathcal{F}$ and $\overline{G}$ within the mass-flow rate constraints. Finally, let the perturbation signal function $\mathcal{H}$ used in Mode 2 of QSRCAC be given by

$$\mathcal{H}(k) = [\mathrm{Tr}(k+2) \;\; \mathrm{Tr}(k)]^{\mathsf{T}}, \tag{5.26}$$

where $\mathrm{Tr}\colon [0, \ldots, \infty) \to \mathbb{R}$ is a triangular function such that, for all $k \geq 0$,

$$\mathrm{Tr}(k) \triangleq \frac{4a}{p} \left| \left(\left(k\tau_{\rm s} - \frac{p}{4} \right) \bmod p \right) - \frac{p}{2} \right| - a, \tag{5.27}$$

in which $p = 1.6$ and $a = 0.25$ are the period and amplitude of the triangular function, respectively, and mod is the Euclidean modulo operator, as described in [140]. While most extremum seeking control (ESC) implementations use a sinusoidal function for perturbation signals, the triangular function is chosen in this work since this allows equally-spaced mass-flow rate steps, as shown in Figure 5.12.

Table 5.3: Parameters for sampled-data implementation of QSRCAC.

	Sampling Period	**Command Bias**	**Temperature Reference**	**Constraint Enforcement**				
Parameter	$\tau_{\rm s}$	$\overline{u}$	$\hat{T}_{\rm ref}$	$\dot{m}_{\rm min}$	$\dot{m}_{\rm max}$	$\dot{m}_{\rm t,min}$	$\dot{m}_{\rm t,max}$	$\Delta\dot{m}_{\rm max}$
Unit	s/step	g/s	–	g/s	g/s	g/s	g/s	g/s/step
Value	0.2	$[3,\ 5]^{\mathsf{T}}$	3.7	0.75	9	7	11.3	0.5

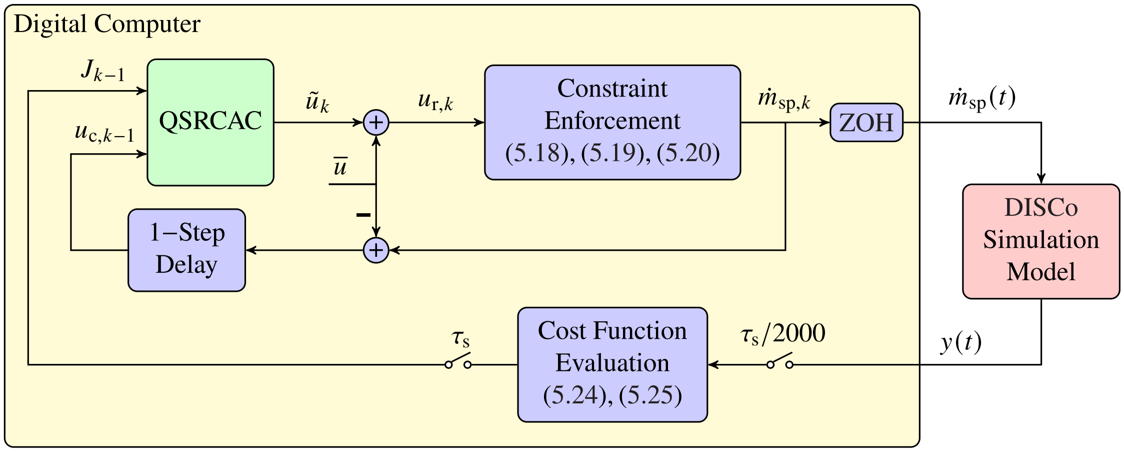

Figure 5.10: Sampled-data implementation of QSRCAC for DISCo simulation.

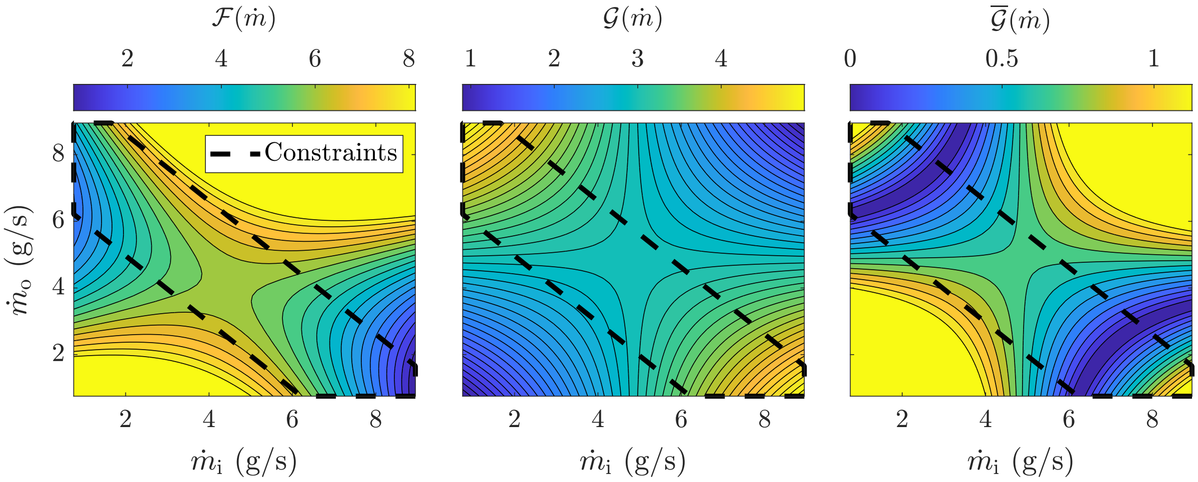

Figure 5.11: $\mathcal{F}(\dot{m})$, $\mathcal{G}(\dot{m})$, and $\overline{\mathcal{G}}(\dot{m}) \triangleq |\mathcal{G}(\dot{m}) - \hat{T}_{\rm ref}|$ output values where $\hat{T}_{\rm ref} = 3.7$ and $\dot{m} = [\dot{m}_{\rm i}\ \ \dot{m}_{\rm o}]^{\rm T} \in [1,9] \times [1,9]$ g/s. The black, dashed line segments represent the constraints on $\dot{m}_{\rm i}$ and $\dot{m}_{\rm o}$. The values corresponding to $\mathcal{F}(\dot{m}) > 8.2$ and $\overline{\mathcal{G}}(\dot{m}) > 1.2$ have been saturated at 8.2 and 1.2, respectively, for visualization purposes.

5.8 Numerical simulation of the DISCo model for hyperparameter selection

In this section, the DISCo simulation model introduced in Section 5.4 is used to select hyperparameters. The controller initially operates in Mode 1. Then, the controller transitions to Mode 2 at $t = 2$ s. Finally, the controller transitions to Mode 3 at $t = 12$ s. Hence, the EKF is initialized near the initial operating point $\overline{u}$ for 10 s. Several simulations are performed , in which the hyperparameters are manually adjusted until QSRCAC yields a value of $\dot{m}$ such that $\mathcal{F}$ is minimized in the TISO test

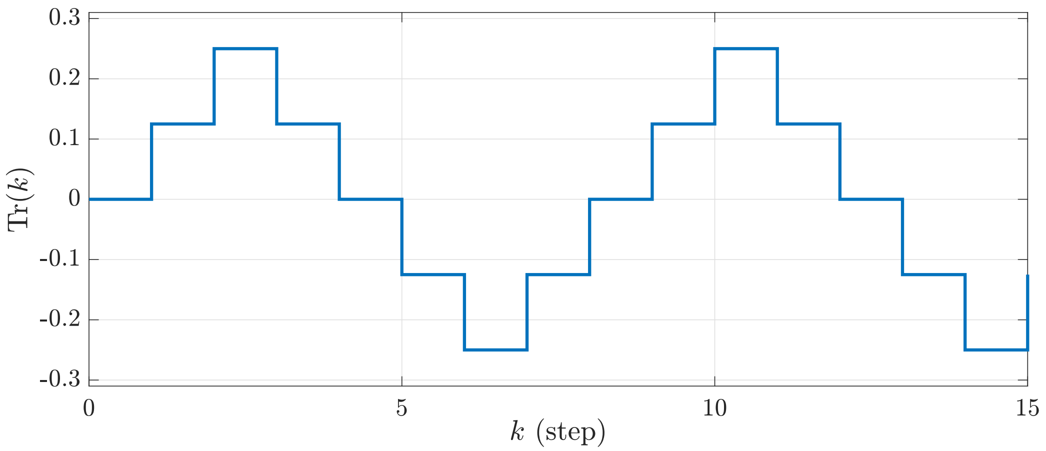

Figure 5.12: Plot of $\mathrm{Tr}(k)$ for all $k \in [0, 15]$.

and $\overline{G}$ is also minimized in the TITO test. The selected hyperparameters are shown in Table 5.4.

The results of the numerical simulations are shown in Figures 5.13, 5.14, and 5.15 for the TISO test and in Figures 5.16, 5.17, and 5.18 for the TITO test. As shown in Figures 5.13 and 5.16, QSRCAC yields air mass-flow rates $\dot{m}$ that locally minimize $\mathcal{F}$ and $\overline{G}$ in both the TISO and the TITO tests. Hence, the hyperparameters used in these numerical simulations will be used in the physical experiments.

Table 5.4: Selected hyperparameters for QSRCAC based on simulation results.

	RCAC			**EKF**					**Cost Function**		
Parameter	l_c	r_u	p_0	$p_{1,0}, p_{2,0}$	q_1, q_2	r_1, r_2	k_1	k_2	l_{rms}	K_1	K_2
Value	1	0.35	10^{-2}	10^{-3}	10^{-1}	10^{2}	2	6	100	2000	5000

5.9 Sampled-data implementation of QSRCAC for DISCo physical experiments

QSRCAC presented in Section 5.6 is implemented as a sampled-data controller to control the response of the DISCo physical facility introduced in Section 5.1. Figure 5.19 shows the block diagram of the sampled-data, closed-loop system considered for physical experiments. The implementation is similar to the one introduced in Section 5.7 and shown in Figure 5.10. The main difference is the output of the Digital Computer block, which is the analog voltage signal vector $V \in \mathbb{R}^{l_u}$ used to modulate the Electronic Pressure Controllers, such that in steady state, $f(V) = \dot{m}$, where $f\colon \mathbb{R}^{l_{\mathrm{u}}} \to \mathbb{R}^{l_{\mathrm{u}}}$ is an invertible function that can be determined by calibration. Then, for all

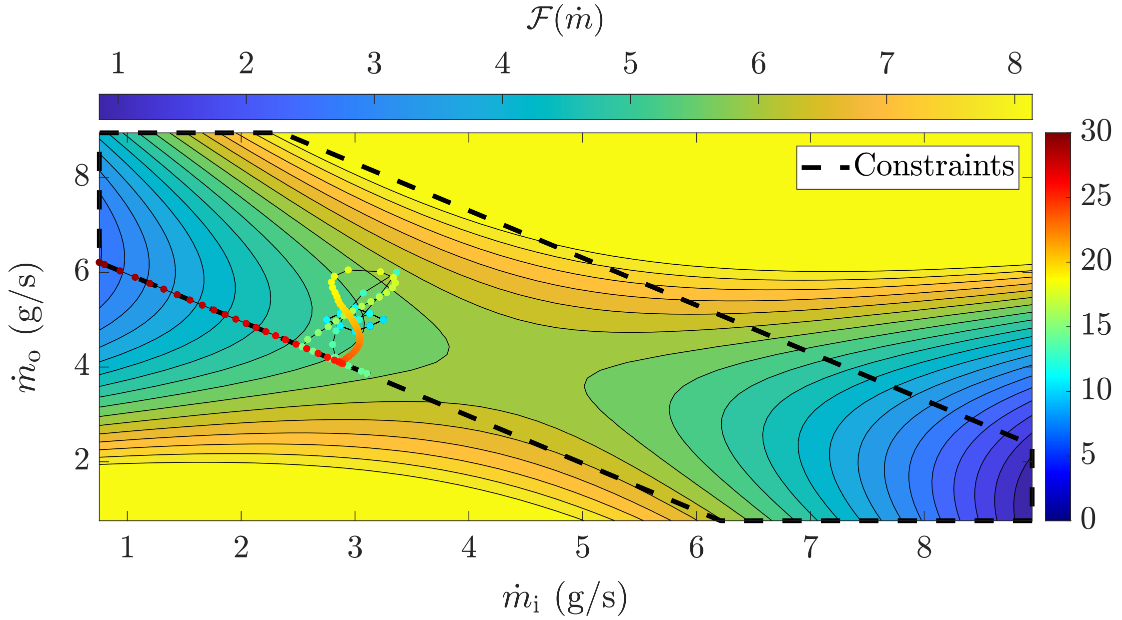

Figure 5.13: *TISO test:* Evolution of $\dot{m}_\mathrm{sp}$ during the closed-loop numerical simulation for $t \in [0, 30]$ s. The output values of $\mathcal{F}(\dot{m})$ for all $\dot{m} = [\dot{m}_\mathrm{i} \;\; \dot{m}_\mathrm{o}]^\mathsf{T} \in [1, 9] \times [1, 9]$ g/s are shown in the background. The black, dashed line segments represent the constraints on $\dot{m}_\mathrm{i}$ and $\dot{m}_\mathrm{o}$.

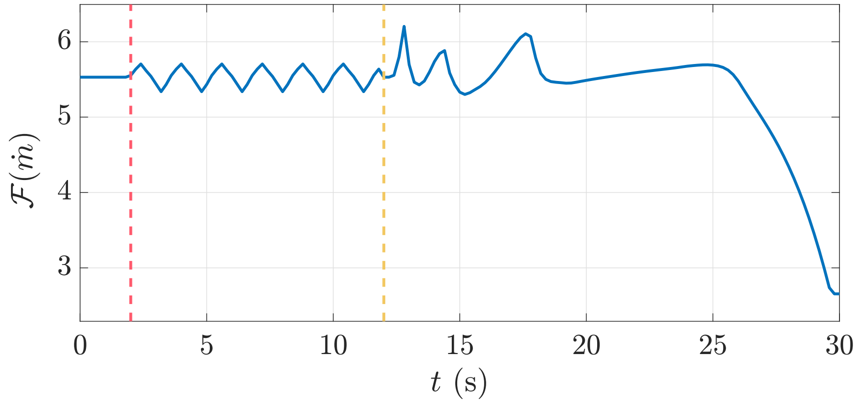

Figure 5.14: *TISO test:* $\mathcal{F}(\dot{m})$ versus time for the the closed-loop numerical simulation. The transitions from Mode 1 to Mode 2 and from Mode 2 to Mode 3 are indicated by the dashed, vertical red and yellow lines, respectively.

$t \in [k\tau_\mathrm{s}, (k+1)\tau_\mathrm{s})$,

$$V(t) = V_k, \tag{5.28}$$

where $V_k \in \mathbb{R}^{l_u}$ is given by

$$V_k = f^{-1}(\dot{m}_{\mathrm{sp},k}). \tag{5.29}$$

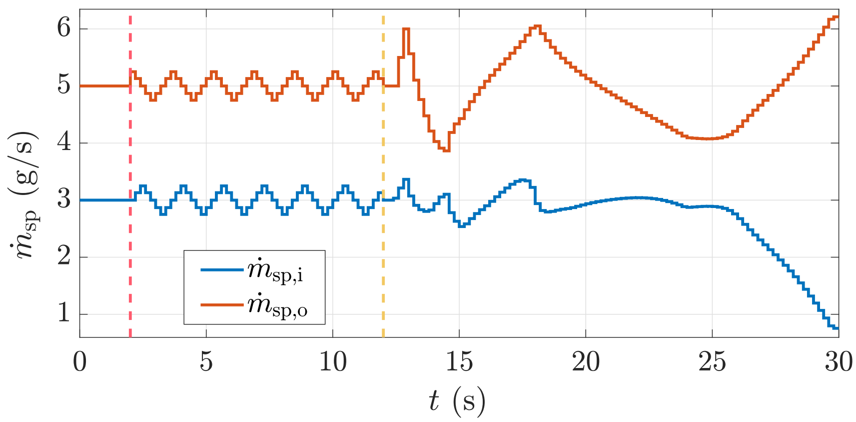

Figure 5.15: *TISO test:* $\dot{m}_{\mathrm{sp}}$ versus time for the the closed-loop numerical simulation. The transitions from Mode 1 to Mode 2 and from Mode 2 to Mode 3 are indicated by the dashed, vertical red and yellow lines, respectively.

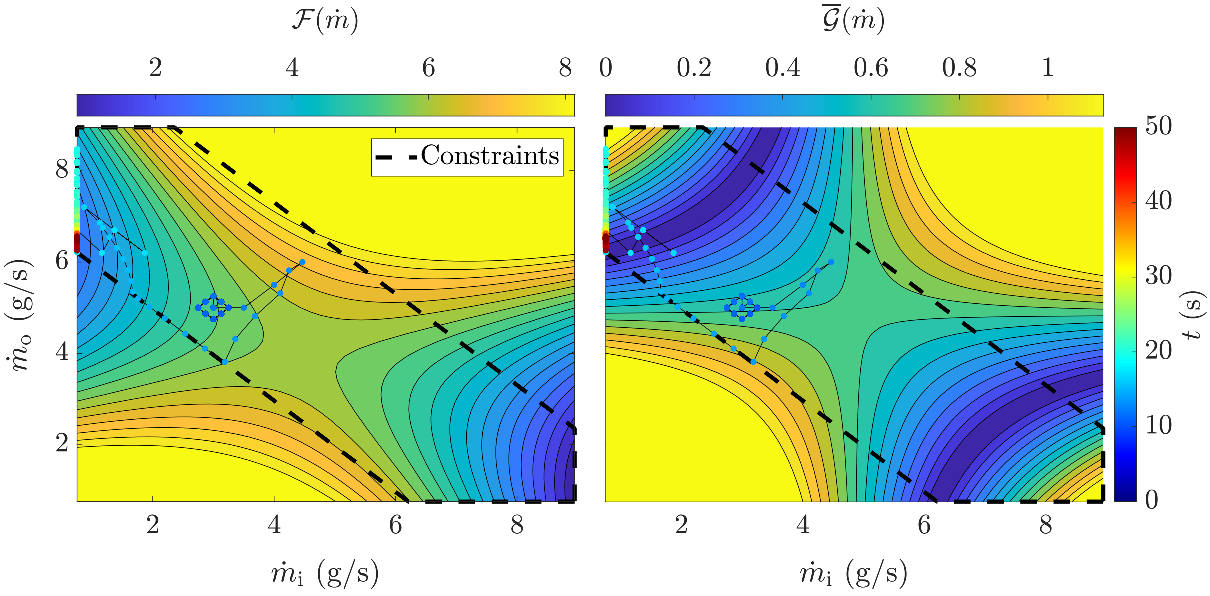

Figure 5.16: *TITO test:* Evolution of $\dot{m}_{\mathrm{sp}}$ during the closed-loop numerical simulation for $t \in [0, 50]$ s. The output values of $\mathcal{F}(\dot{m})$ and $\overline{\mathcal{G}}(\dot{m})$ with $\hat{T}_{\mathrm{ref}} = 3.7$ and for all $\dot{m} = [\dot{m}_{\mathrm{i}} \ \ \dot{m}_{\mathrm{o}}]^{\mathsf{T}} \in [1, 9] \times [1, 9]$ g/s are shown in the background. The black, dashed line segments represent the constraints on $\dot{m}_{\mathrm{i}}$ and $\dot{m}_{\mathrm{o}}$.

The rest of the parameters are the same as the ones shown in Section 5.7 and Tables 5.3 and 5.4. As in Chapter 4, the level of suppression of the thermoacoustic oscillations, referred to as oscillation suppression, is used to evaluate the performance of the controller, which is defined to be the ratio of the steady-state open-loop maximum time-domain pressure amplitude to the steady-state

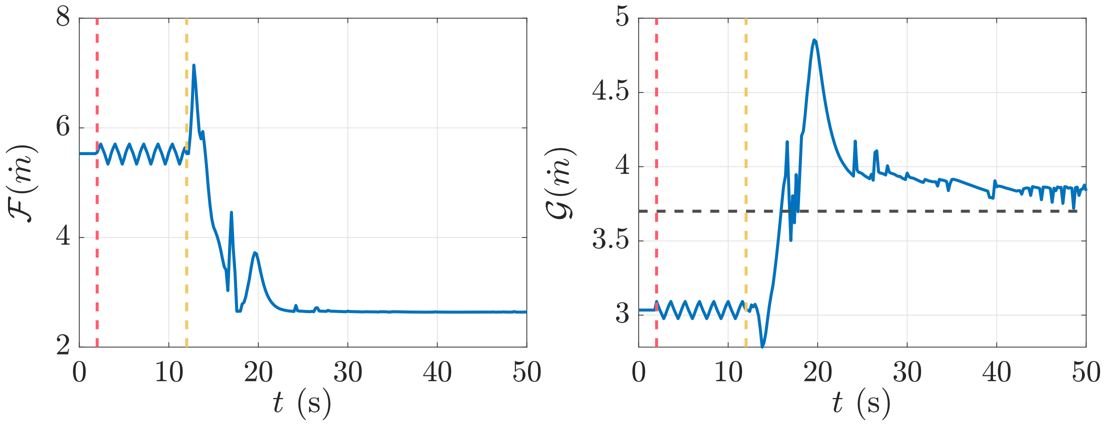

Figure 5.17: *TITO test:* $\mathcal{F}(\dot{m})$ and $\mathcal{G}(\dot{m})$ versus time for the the closed-loop numerical simulation. The transitions from Mode 1 to Mode 2 and from Mode 2 to Mode 3 are indicated by the dashed, vertical red and yellow lines, respectively. In plot of $\mathcal{G}(\dot{m})$, the value of $\hat{T}_{\text{ref}}$ is indicated by the dashed, horizontal black line

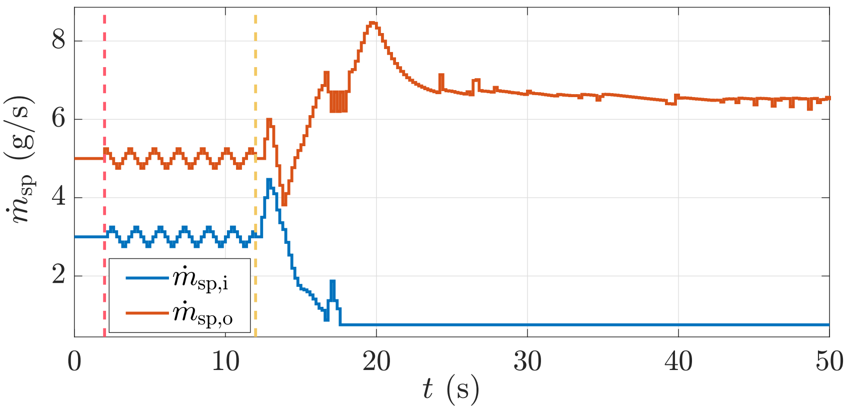

Figure 5.18: *TITO test:* $\dot{m}_{\text{sp}}$ versus time for the the closed-loop numerical simulation. The transitions from Mode 1 to Mode 2 and from Mode 2 to Mode 3 are indicated by the dashed, vertical red and yellow lines, respectively.

closed-loop maximum time-domain pressure amplitude in dB.

5.10 Physical quasi-static adaptive control experimental results

In this section, the quasi-static adaptive controller is used to modulate the dynamics of the DISCo facility introduced in Section 5.1 with the objective of minimizing the RMS of the pressure fluctuation measurements in the TISO test and also reaching a desired combustor exit temperature in the TITO test. The controller initially operates in Mode 1. Then, the controller transitions to

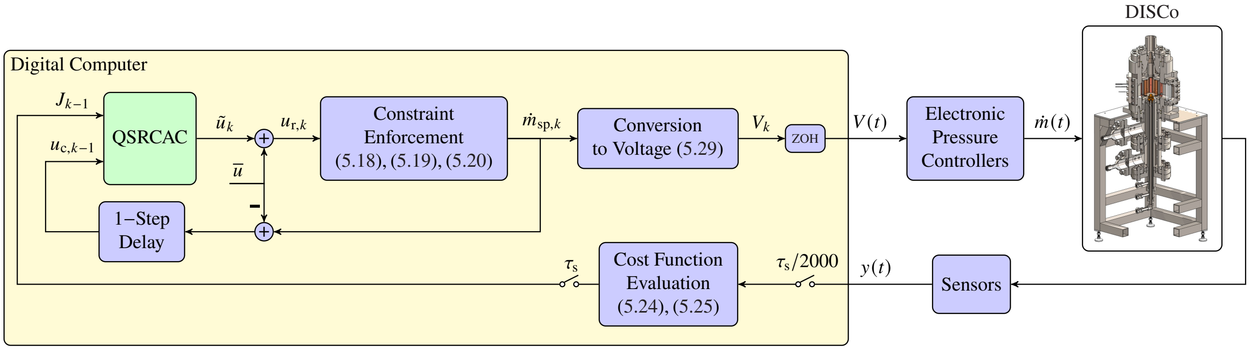

Figure 5.19: Quasi-static, adaptive control of DISCo facility.

Mode 2 and, after 10 s, the controller transitions to Mode 3. Hence, the EKF is initialized around the initial operating point for 10 s, as in the numerical simulations. The same hyperparameters used in Section 5.8 and shown in Tables 5.3 and 5.4 are used in these physical experiments. Let $p' \in \mathbb{R}$ be the measured pressure fluctuations in kPA, $T \in \mathbb{R}$ be the measured combustor exit temperature in K, $T_{\mathrm{ref}} \in \mathbb{R}$ be the reference combustor exit temperature in K, and define

$$p'_{\mathrm{rms}}(t) \triangleq \sqrt{\frac{1}{l_{\mathrm{rms}}} \sum_{\kappa=0}^{l_{\mathrm{rms}}} \left[p'\left(t - \kappa \frac{\tau_{\mathrm{s}}}{2000}\right)\right]^2}. \tag{5.30}$$

While their equivalent normalized versions $\hat{p}', \hat{T}, \hat{T}_{\mathrm{ref}}$, and $\hat{p}'_{\mathrm{rms}}$ are used by the controller, p', T, T, and p'_{rms} are used in this section to assess the performance of the quasi-static adaptive controller in a physically significant manner.

The results of the physical experiments are shown in Figures 5.20, 5.21, 5.22, and 5.23 for the TISO test and in Figures 5.24, 5.25, 5.26, and 5.27 for the TITO test. As shown in Figures 5.20 and 5.24, QSRCAC yields air mass-flow rates $\dot{m}$ that achieves an oscillation suppression of 28 dB in both the TISO and the TITO tests and reduces $T - T_{\mathrm{ref}}$ by a factor of approximately 5 in the TITO test. Furthermore, Figures 5.22 and 5.26 show that QSRCAC manages to suppress the main frequency peaks of the open-loop response.

5.11 Conclusions

This chapter proposed a quasi-static adaptive controller to modulate the a model combustor facility in the case where the feedback control law operates with a low bandwidth relative to the open-loop dynamics of the combustor. The hyperparameter selection methodology developed in Chapter 4 was presented was used to determine hyperparameters that reduce the RMS of the thermoacoustic oscillations and the error between the exit combustor temperature and a reference value. The selected

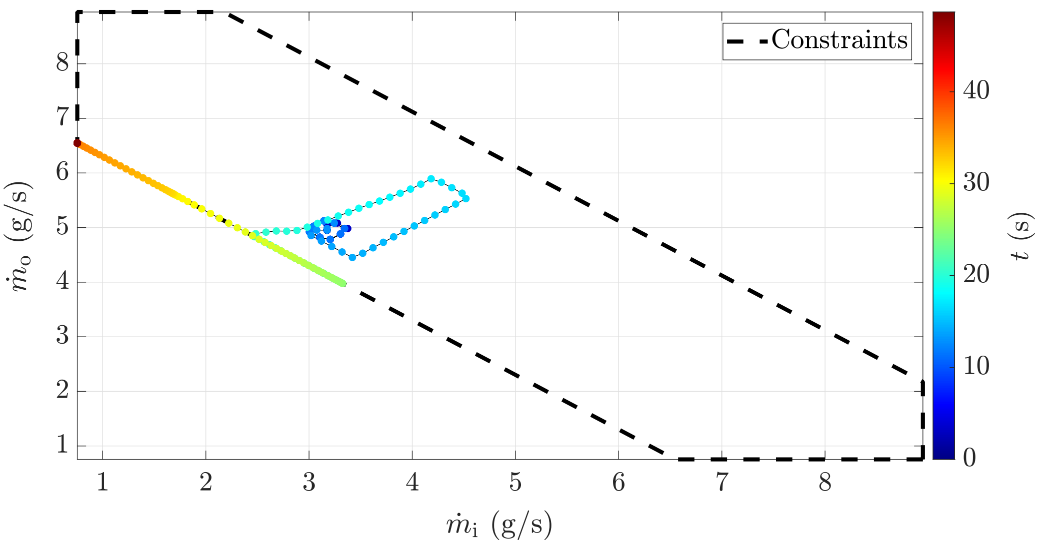

Figure 5.20: *TISO Test:* Evolution of $\dot{m}_\mathrm{sp}$ during the closed-loop physical experiment for $t \in [0, 48]$ s. The black, dashed line segments represent the constraints on $\dot{m}_\mathrm{i}$ and $\dot{m}_\mathrm{o}$.

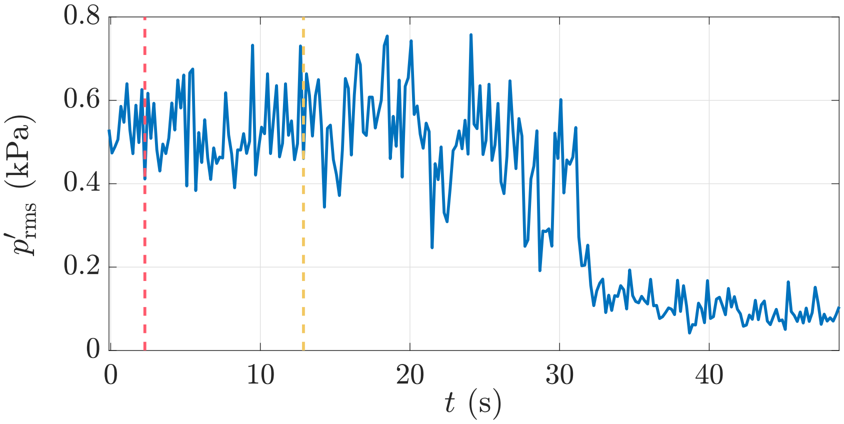

Figure 5.21: *TISO Test:* p'_rms versus time for the the closed-loop physical experiment. The transitions from Mode 1 to Mode 2 and from Mode 2 to Mode 3 are indicated by the dashed, vertical red and yellow lines, respectively.

hyperparameters were then used by the quasi-static adaptive controller in physical experiments with the DISCo facility to achieve results similar to those in the numerical simulations.

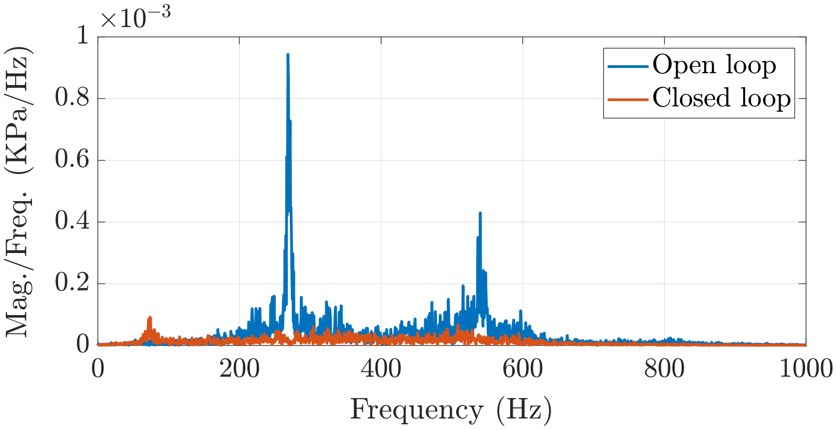

Figure 5.22: *TISO Test:* Amplitude spectra of the combustor pressure measurements obtained from the open-loop experiments and the closed-loop experiments using the quasi-static adaptive controller.

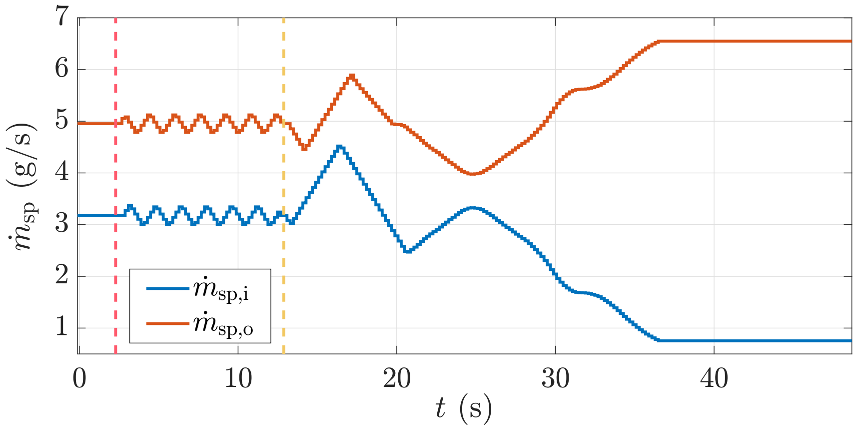

Figure 5.23: *TISO Test:* $\dot{m}_{\mathrm{sp}}$ versus time for the the closed-loop physical experiment The transitions from Mode 1 to Mode 2 and from Mode 2 to Mode 3 are indicated by the dashed, vertical red and yellow lines, respectively.

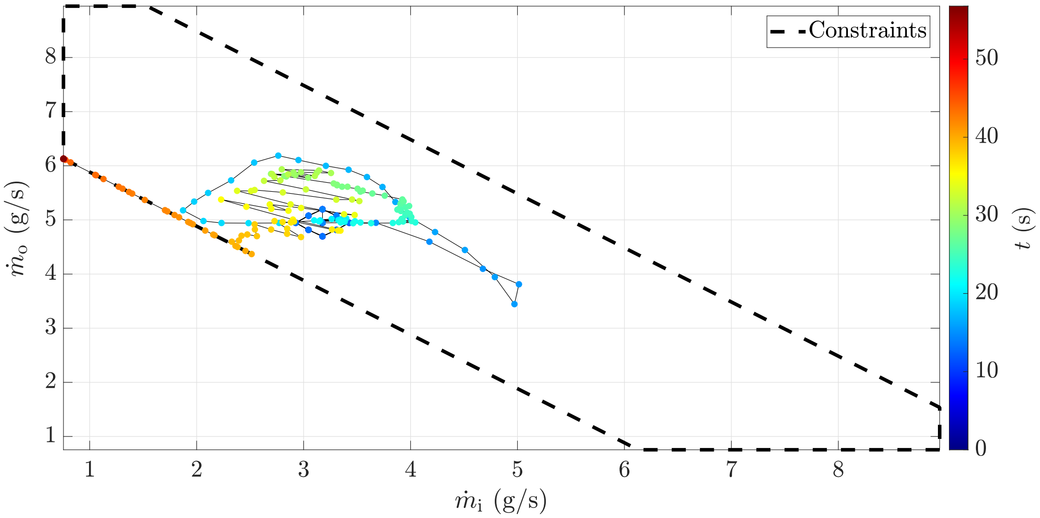

Figure 5.24: *TITO Test:* Evolution of $\dot{m}_{\mathrm{sp}}$ during the closed-loop physical experiment for $t \in [0, 56]$ s. The black, dashed line segments represent the constraints on $\dot{m}_{\mathrm{i}}$ and $\dot{m}_{\mathrm{o}}$.

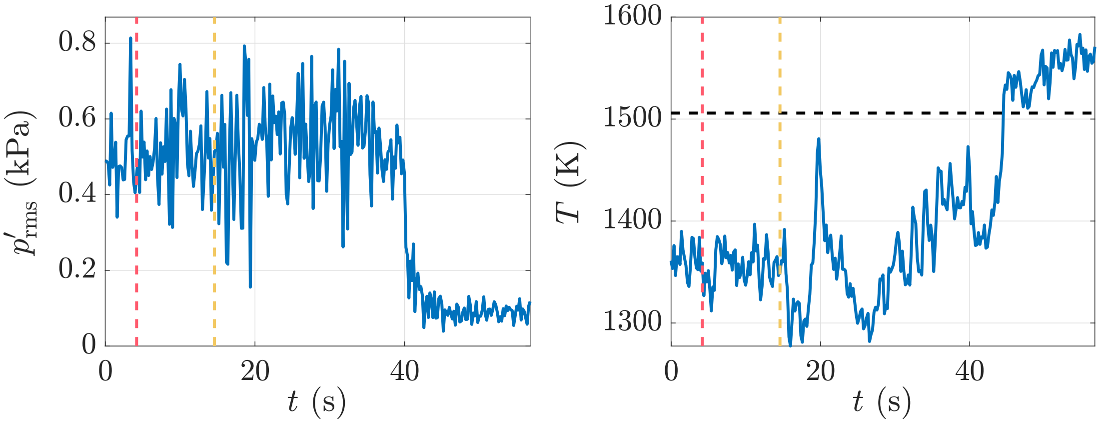

Figure 5.25: *TITO Test:* p'_{rms} and T versus time for the the closed-loop physical experiment. The transitions from Mode 1 to Mode 2 and from Mode 2 to Mode 3 are indicated by the dashed, vertical red and yellow lines, respectively. In the plot of T, the value of T_{ref} is indicated by the dashed, horizontal black line

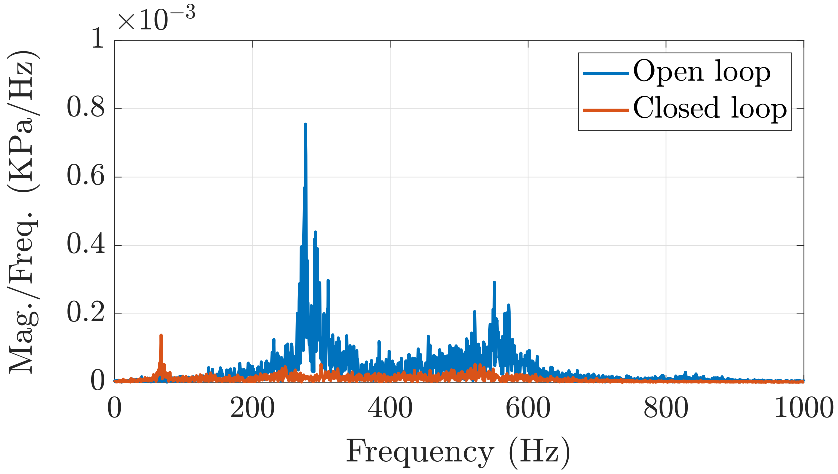

Figure 5.26: *TITO Test:* Amplitude spectra of the combustor pressure measurements obtained from the open-loop experiments and the closed-loop experiments using the quasi-static adaptive controller.

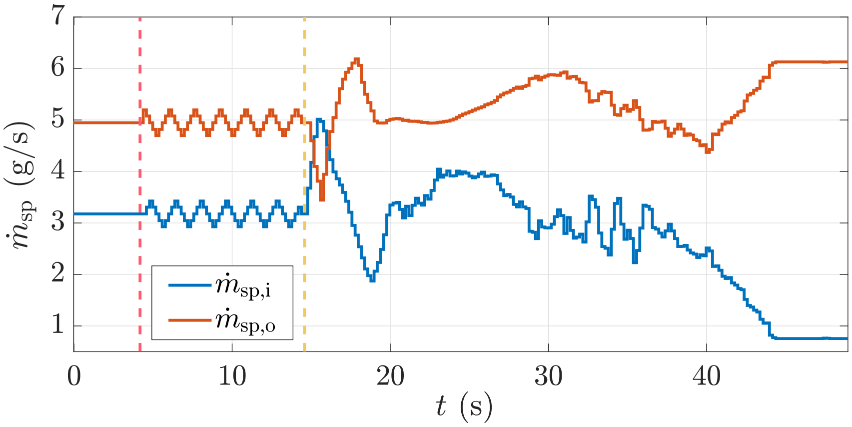

Figure 5.27: *TITO Test:* $\dot{m}_{\mathrm{sp}}$ versus time for the the closed-loop physical experiment. The transitions from Mode 1 to Mode 2 and from Mode 2 to Mode 3 are indicated by the dashed, vertical red and yellow lines, respectively.

CHAPTER 6

Conclusions and Future Work

This dissertation developed a methodology for the implementation of adaptive control for suppression of self-excited oscillations in self-excited systems, which was applied to a gas turbine combustor. Chapter 2 considered discrete-time Lur'e models that involve asymptotically stable linear dynamics with a washout filter connected in feedback with a piecewise-C^1 affinely constrained nonlinearity, and whose response is self-excited in the sense that it is 1) bounded for all initial conditions, and 2) nonconvergent for almost all initial conditions; sufficient conditions involving the growth rate of the nonlinearity were given under which the system is self-excited. Chapter 3 presented a mixed integer optimization framework for identifying SES's based on a DTL model structure with a CPA nonlinearity constructed using the insight gained in Chapter 2; MIO-ID was applied to numerical and experimental data, which resulted DTLI models that closely reproduced the oscillatory behavior displayed by the studied systems, thus validating the abstractions derived in Chapter 2. Chapter 4 developed a hyperparameter selection procedure for implementing a digital adaptive controller based on RCAC to a Rijke-tube physical experiment; the methodology required the construction of a simulation model using the results derived in Chapters 2 and 3, which resulted in the suppression of the oscillatory response of the Rijke-tube physical experiment under various system parameters. Finally, Chapter 5 implemented the RCAC algorithm in a quasi-static setup and applied the hyperparameter selection methodology developed in Chapter 4 to a gas turbine combustor to reduce the RMS of the thermoacoustic oscillations and the error between the exit combustor temperature and a reference value to yield a desired flame length.

Future work will focus on extending the results obtained in each of the chapters. For the self-excited dynamics of discrete-time Lur'e models, future work will focus on obtaining conditions for self-oscillation to accommodate a broader type of nonlinearities and deriving analogous results for continuous-time Lur'e models. For the SES identification methodology, future research will focus on adapting this approach to the case where the nonlinearity is a hysteresis to obtain DTLI models with lower order linear dynamics. For the hyperparameter selection methodology, future research will focus in applying this to adaptive stabilization of self-excited systems other than the Rijke-tube and gas-turbine combustors. Finally, for the quasi-static adaptive controller, future work will focus on studying the effect of the hyperparameters, and comparing the performance of this methodology to that of similar control algorithms, such as extremum seeking control.

BIBLIOGRAPHY

[1] J. P. Epperlein, B. Bamieh, and K. J. Astrom, “Thermoacoustics and the Rijke tube: Experiments, identification, and modeling,” *IEEE Contr. Sys. Mag.*, vol. 35, no. 2, pp. 57–77, 2015.

[2] P. Gray and S. K. Scott, *Chemical Oscillations and Instabilities: Non-linear Chemical Kinetics*. Oxford, 1990.

[3] A. Goldbeter and M. J. Berridge, *Biochemical Oscillations and Cellular Rhythms: The Molecular Bases of Periodic and Chaotic Behaviour*. Cambridge, 1996.

[4] R. D. Blevins, *Flow-Induced Vibration*. Van Nostrand Reinhold, 1990.

[5] E. Jonsson, C. Risoa, C. A. Luppa, C. E. S. Cesnik, J. R. R. A. Martins, and B. I. Epureanu, “Flutter and post-flutter constraints in aircraft design optimization,” *Prog. Aerosp. Sci.*, vol. 109, 2019, article 100537, 28 pages.

[6] Z. Gianikos, B. Kirschmeier, A. Gopalarathnam, and M. Bryant, “Limit cycle characterization of an aeroelastic wing in a bluff body wake,” *J. Fluids Struct.*, vol. 95, p. 102986, 05 2020.

[7] A. P. Dowling, “Nonlinear self-excited oscillations of a ducted flame,” *J. Fluid Mech.*, vol. 346, pp. 271–291, 1997.

[8] Y. Chen and J. F. Driscoll, “A multi-chamber model of combustion instabilities and its assessment using kilohertz laser diagnostics in a gas turbine model combustor,” *Combust. Flame*, vol. 174, pp. 120–137, 2016.

[9] A. Jenkins, “Self-oscillation,” *Phys. Rep.*, vol. 525, no. 2, pp. 167–222, 2013.

[10] W. Ding, *Self-Excited Vibration: Theory, Paradigms, and Research Methods*. Springer, 2010.

[11] D. Green and W. G. Unruh, “The failure of the Tacoma Bridge: A physical model,” *Amer. J. P.*, vol. 74, no. 8, pp. 706–716, 2006.

[12] A. P. Dowling and A. S. Morgans, “Feedback control of combustion oscillations,” *Ann. Rev. Fluid Mech.*, vol. 37, pp. 151–182, 2005.

[13] T. Yi and E. J. Gutmark, “Dynamics of a high-frequency fuel actuator and its applications for combustion instability control,” *J. Eng. Gas. Turbine Power*, vol. 129, p. 649, 2007.

[14] A. Banaszuk, Y. Zhang, and C. A. Jacobson, “Adaptive control of combustion instability using extremum-seeking,” in *Proc. Amer. Contr. Conf.*, vol. 1, no. 6. IEEE, 2000, pp. 416–422.

[15] S. Evesque and A. Dowling, “Adaptive control of combustion oscillations,” in *4th AIAA/CEAS Aeroacoustics Conf.*, 1998, p. 2351.

[16] S. Koshigoe, T. Komatsuzaki, and V. Yang, “Adaptive control of combustion instability with on-line system identification,” *J. Prop. Power*, vol. 15, no. 3, pp. 383–389, 1999.

[17] G. Billoud, M. Galland, C. Huynh Huu, and S. Cancel E, “Adaptive active control of combustion instabilities,” *Comb. Sci. Tech.*, vol. 81, no. 4-6, pp. 257–283, 1992.

[18] P. L. Rijke, “LXXI. Notice of a new method of causing a vibration of the air contained in a tube open at both ends,” *Lond. Edinb. Dubl. Phil. Mag*, vol. 17, no. 116, pp. 419–422, 1859.

[19] J. W. S. Rayleigh, “The explanation of certain acoustical phenomena,” *Nature*, vol. 18, no. 455, pp. 319–321, 1878.

[20] N. Olgac, U. Zalluhoglu, and A. S. Kammer, “Predicting thermoacoustic instability: a novel analytical approach and its experimental validation,” *J. Prop. Power*, vol. 30, no. 4, pp. 1005–1015, 2014.

[21] M. A. Heckl, “Non-linear acoustic effects in the Rijke tube,” *Acta Acustica*, vol. 72, no. 1, pp. 63–71, 1990.

[22] S. Bittanti, A. De Marco, G. Poncia, and W. Prandoni, “Identification of a model for thermoacoustic instabilities in a Rijke tube,” *IEEE Trans. Contr. Sys. Tech.*, vol. 10, no. 4, pp. 490–502, 2002.

[23] K. Matveev, “Energy consideration of the nonlinear effects in a Rijke tube,” *J. Fluids Struct.*, vol. 18, no. 6, pp. 783–794, 2003.

[24] K. Balasubramanian and R. Sujith, “Thermoacoustic instability in a Rijke tube: Non-normality and nonlinearity,” *Phys. Fluids*, vol. 20, no. 4, 2008.

[25] J. Rubio-Hervas, M. Reyhanoglu, and W. MacKunis, “Observer-based sliding mode control of Rijke-type combustion instability,” *J. Low Freq. Noise, Vibr. Active Contr.*, vol. 34, no. 2, pp. 201–217, 2015.

[26] G. A. de Andrade, R. Vazquez, and D. J. Pagano, “Backstepping-based estimation of thermoacoustic oscillations in a Rijke tube with experimental validation,” *IEEE Trans. Autom. Contr.*, vol. 65, no. 12, pp. 5336–5343, 2020.

[27] A. S. Feitelberg and M. A. Lacey, “The GE rich-quench-lean gas turbine combustor,” *J. Eng. Gas Turbines Power*, vol. 120, no. 3, p. 502, 1998.

[28] S. Samuelsen, *Rich burn, quick-mix, lean burn (RQL) combustor*. US Department of Energy, Office of Fossil Energy, National Energy Technology Laboratory, 2006, ch. 3.2.1.3, pp. 227–233.

[29] A. K. Gupta, “Gas turbine combustion: prospects and challenges,” *Energy Convers. Manag.*, vol. 38, no. 10-13, pp. 1311–1318, 1997.

[30] J. J. Keller, “Thermoacoustic oscillations in combustion chambers of gas turbines,” *AIAA J.*, vol. 33, no. 12, pp. 2280–2287, 1995.

[31] T. C. Lieuwen, “Modeling Premixed Combustion-Acoustic Wave Interactions: A Review,” *J. Propulsion Power*, vol. 19, pp. 765–781, 2003.

[32] B. T. Zinn and T. C. Lieuwen, *Combustion Instabilities: Basic Concepts*. AIAA, 2005, ch. 1, pp. 3–26.

[33] T. C. Lieuwen, *Unsteady Combustor Physics*. Cambridge, 2012.

[34] K. C. Schadow and E. Gutmark, “Combustion instability related to vortex shedding in dump combustors and their passive control,” *Prog. Energy Combust. Sci.*, vol. 18, no. 2, pp. 117–132, 1992.

[35] G. A. Richards, D. L. Straub, and E. H. Robey, “Passive control of combustion dynamics in stationary gas turbines,” *J. Prop. Power*, vol. 19, no. 5, pp. 795–810, 2003.

[36] D. Zhao, C. A’barrow, A. S. Morgans, and J. Carrotte, “Acoustic damping of a helmholtz resonator with an oscillating volume,” *AIAA J.*, vol. 47, no. 7, pp. 1672–1679, 2009.

[37] D. Zhao and X. Y. Li, “A review of acoustic dampers applied to combustion chambers in aerospace industry,” *Prog. Aerosp. Sci.*, vol. 74, pp. 114–130, 2015.

[38] A. P. Dowling and A. S. Morgans, “Feedback Control of Combustion Oscillations,” *Ann. Rev. Fluid Mech.*, vol. 37, pp. 151–182, 2005.

[39] A. Gulati and R. Mani, “Active control of unsteady combustion-induced oscillations,” *J. Prop. Power*, vol. 8, no. 5, pp. 1109–1115, 1992.

[40] K. R. McManus, T. Poinsot, and S. M. Candel, “A review of active control of combustion instabilities,” *Prog. Energy Combust. Sci.*, vol. 19, no. 1, pp. 1–29, 1993.

[41] A. M. Annaswamy and A. F. Ghoniem, “Active control in combustion systems,” *IEEE Contr. Syst. Mag.*, vol. 15, no. 6, pp. 49–63, 1995.

[42] H. C. Mongia, T. J. Held, G. C. Hsiao, and R. P. Pandalai, “Challenges and progress in controlling dynamics in gas turbine combustors,” *J. Prop. Power*, vol. 19, no. 5, pp. 822–829, 2003.

[43] J. Hermann and S. Hoffman, “Implementation of active control in a full-scale gas-turbine combustor,” in *Combustion Instabilities In Gas Turbine Engines: Operational Experience, Fundamental Mechanisms, and Modeling*. AIAA, 2005, pp. 611–634.

[44] S. L. Brunton and B. R. Noack, “Closed-loop turbulence control: Progress and challenges,” *Appl. Mech. Rev.*, vol. 67, no. 5, 2015.

[45] D. Zhao, Z. Lu, H. Zhao, X. Y. Li, B. Wang, and P. Liu, “A review of active control approaches in stabilizing combustion systems in aerospace industry,” *Prog. Aerosp. Sci.*, vol. 97, pp. 35–60, 2018.

[46] D. J. Toal, N. Bressloff, A. Keane, and C. Holden, “The development of a hybridized particle swarm for kriging hyperparameter tuning,” *Eng. Opt.*, vol. 43, no. 6, pp. 675–699, 2011.

[47] K. Weiss, T. M. Khoshgoftaar, and D. Wang, “A survey of transfer learning,” *J. Big Data*, vol. 3, no. 1, pp. 1–40, 2016.

[48] P. Schratz, J. Muenchow, E. Iturritxa, J. Richter, and A. Brenning, “Hyperparameter tuning and performance assessment of statistical and machine-learning algorithms using spatial data,” *Ecol. Modell.*, vol. 406, pp. 109–120, 2019.

[49] S. Niu, Y. Liu, J. Wang, and H. Song, “A decade survey of transfer learning (2010–2020),” *IEEE Trans.Artif. Intell.*, vol. 1, no. 2, pp. 151–166, 2020.

[50] D. S. Bernstein, “Facing future challenges in feedback control of aerospace systems through scientific experimentation,” *J. Guid. Contr. Dyn.*, vol. 45, no. 12, pp. 2202–2210, 2022.

[51] J. Paredes, S. A. U. Islam, and D. S. Bernstein, “A time-delayed Lur’e model with biased self-excited oscillations,” in *Proc. Amer. Contr. Conf.*, 2020, pp. 2699–2704.

[52] J. A. Paredes, O. Kouba, and D. S. Bernstein, “Self-excited dynamics of discrete-time lur’e models with affinely constrained, piecewise-c1 feedback nonlinearities,” *IEEE Trans. Autom. Contr.*, 2023, [Submitted].

[53] J. Paredes and D. S. Bernstein, “Identification of self-excited systems using discrete-time, time-delayed Lur’e models,” in *Proc. Amer. Contr. Conf.*, 2021, pp. 3939–3944.

[54] J. A. Paredes, Y. Yang, and D. S. Bernstein, “Output-only identification of self-excited systems using discrete-time Lur’e models with application to a gas-turbine combustor,” *Int. J. Contr.*, pp. 1–26, 2022, available online.

[55] J. Paredes, S. A. U. Islam, and D. S. Bernstein, “Adaptive stabilization of thermoacoustic oscillations in a Rijke Tube,” in *Proc. Amer. Contr. Conf.* IEEE, 2022, pp. 28–33.

[56] J. A. Paredes and D. S. Bernstein, “Experimental implementation of retrospective cost adaptive control for suppressing thermoacoustic oscillations in a Rijke tube,” *IEEE Trans. Contr. Sys. Tech*, 2023, [Accepted].

[57] J. Paredes, R. Ramesh, S. Obidov, M. Gamba, and D. Bernstein, “Experimental investigation of adaptive feedback control on a dual-swirl-stabilized gas turbine model combustor,” in *AIAA Prop. Energy Forum*, 2022, p. 2058.

[58] J. A. Paredes, R. Ramesh, M. Gamba, and D. S. Bernstein, “Experimental implementation of a quasi-static adaptive controller to a dual independent swirl combustor,” *Comb. Sci. Tech.*, 2023, [To be submitted].

[59] H. K. Khalil, *Nonlinear Systems*, 3rd ed. Prentice Hall, 2002.

[60] D. H. Zanette, “Self-sustained oscillations with delayed velocity feedback,” *Papers in Physics*, vol. 9, pp. 090 003–1–090 003–7, March 2017.

[61] S. Chatterjee, “Self-excited oscillation under nonlinear feedback with time-delay,” *J. Sound Vibr.*, vol. 330, no. 9, pp. 1860–1876, 2011.

[62] G. Stan and R. Sepulchre, “Analysis of interconnected oscillators by dissipativity theory,” *IEEE Trans. Autom. Contr.*, vol. 52, no. 2, pp. 256–270, 2007.

[63] A. Mees and L. Chua, “The hopf bifurcation theorem and its applications to nonlinear oscillations in circuits and systems,” *IEEE Trans. Circ. Sys.*, vol. 26, no. 4, pp. 235–254, 1979.

[64] L. T. Aguilar, I. Boiko, L. Fridman, and R. Iriarte, “Generating self-excited oscillations via two-relay controller,” *IEEE Trans. Autom. Contr.*, vol. 54, no. 2, pp. 416–420, 2009.

[65] S. Risau-Gusman, “Effects of time-delayed feedback on the properties of self-sustained oscillators,” *Phys. Rev. E*, vol. 94, p. 042212, October 2016.

[66] V. Yakubovich, “Frequency-domain criteria for oscillation in nonlinear systems with one stationary nonlinear component,” *Sib. Math. J.*, vol. 14, no. 5, pp. 768–788, 1973.

[67] E. A. Tomberg and V. A. Yakubovich, “Conditions for auto-oscillations in nonlinear systems,” *Sib. Math. J.*, vol. 30, no. 4, pp. 641–653, 1989.

[68] M. Arcak, M. Larsen, and P. Kokotović, “Boundedness without absolute stability in systems with stiffening nonlinearities,” *Eur. J. Contr.*, vol. 8, no. 3, pp. 243–250, 2002.

[69] R. Sepulchre and G.-B. Stan, “Feedback mechanisms for global oscillations in Lur’e systems,” *Sys. Contr. Lett.*, vol. 54, no. 8, pp. 809–818, 2005.

[70] D. V. Efimov and A. L. Fradkov, “Oscillatority of nonlinear systems with static feedback,” *SIAM J. Contr. Optim.*, vol. 48, no. 2, pp. 618–640, 2009.

[71] E. Sarkans and H. Logemann, “Input-to-state stability of discrete-time Lur’e systems,” *SIAM J. Contr. Optim.*, vol. 54, no. 3, pp. 1739–1768, 2016.

[72] T. H. Van Pelt and D. S. Bernstein, “Non-linear system identification using Hammerstein and non-linear feedback models with piecewise linear static maps,” *Int. J. Contr.*, vol. 74, no. 18, pp. 1807–1823, 2001.

[73] G. Dolanc and S. Strmcnik, “Identification of nonlinear systems using a piecewise-linear Hammerstein model,” *Sys. Contr. Lett.*, vol. 54, no. 2, pp. 145–158, 2005.

[74] J. Voros, “Parameter identification of Wiener systems with multisegment piecewise-linear nonlinearities,” *Sys. Contr. Lett.*, vol. 56, no. 2, pp. 99–105, 2007.

[75] J. D. Lee, I. Panageas, G. Piliouras, M. Simchowitz, M. I. Jordan, and B. Recht, “First-order methods almost always avoid strict saddle points,” *Math. Prog.*, vol. 176, no. 1, pp. 311–337, 2019.

[76] Z.-P. Jiang and Y. Wang, “Input-to-state stability for discrete-time nonlinear systems,” *Automatica*, vol. 37, pp. 857–869, 2001.

[77] W. Rudin, *Principles of Mathematical Analysis*, 2nd ed. McGraw-Hill, 1964.

[78] G. J. O. Jameson, *Topology and Normed Spaces*. Wiley, 1974.

[79] M. Shub, *Global Stability of Dynamical Systems*. Springer, 1987.

[80] C. Floudas, *Nonlinear and mixed-integer optimization*. Oxford University Press, 1995.

[81] P. Belotti, C. Kirches, S. Leyffer, J. Linderoth, J. Luedtke, and A. Mahajan, “Mixed-integer nonlinear optimization,” *Acta Numer.*, vol. 22, p. 1–131, 2013.

[82] J. Roll, A. Bemporad, and L. Ljung, “Identification of piecewise affine systems via mixed-integer programming,” *Automatica*, vol. 40, no. 1, pp. 37–50, 2004.

[83] V. Dua, “A mixed-integer programming approach for optimal configuration of artificial neural networks,” *Chem. Eng. Res. Des.*, vol. 88, no. 1, pp. 55–60, 2010.

[84] D. Förster, R. B. Inderka, and F. Gauterin, “Data-driven identification of characteristic real-driving cycles based on k-means clustering and mixed-integer optimization,” *IEEE Trans. Vehicular Tech.*, vol. 69, no. 3, pp. 2398–2410, 2019.

[85] M. Mejari, V. V. Naik, D. Piga, and A. Bemporad, “Identification of hybrid and linear parameter-varying models via piecewise affine regression using mixed integer programming,” *Int. J. Robust Nonlinear Contr.*, vol. 30, no. 15, pp. 5802–5819, 2020.

[86] K. J. Åström and B. Wittenmark, *Adaptive Control*, 2nd ed. Addison-Wesley, 1995.

[87] D. S. Bernstein, *Scalar, Vector, and Matrix Mathematics: Theory, Facts, and Formulas—Revised and Expanded Edition*. Princeton University Press, 2018.

[88] R. Ramesh, S. Obidov, J. Paredes, D. S. Bernstein, and M. Gamba, “Design and characterization of the dual independent swirl combustor facility (DISCo),” in *AIAA Prop. Energy Forum*, 2021, p. 3479.

[89] A. P. Dowling, “The calculation of thermoacoustic oscillations,” *J. Sound Vibr.*, vol. 180, no. 4, pp. 557–581, 1995.

[90] L. Kabiraj and R. Sujith, “Nonlinear self-excited thermoacoustic oscillations: intermittency and flame blowout,” *J. Fluid Mech.*, vol. 713, no. 376-397, p. 13, 2012.

[91] T. C. Lieuwen and V. Yang, *Combustion Instabilities in Gas Turbine Engines: Operational Experience, Fundamental Mechanisms, and Modeling*. AIAA, 2005.

[92] A. M. Annaswamy and A. F. Ghoniem, “Active control of combustion instability: Theory and practice,” *IEEE Contr. Sys. Mag.*, vol. 22, no. 6, pp. 37–54, 2002.

[93] Y. Huang and V. Yang, “Dynamics and stability of lean-premixed swirl-stabilized combustion,” *Prog. Energy Comb. Sci.*, vol. 35, no. 4, pp. 293–364, 2009.

[94] M. A. Heckl, “Active control of the noise from a Rijke tube,” *J. Sound Vib.*, vol. 124, no. 1, pp. 117–133, 1988.

[95] U. Zalluhoglu, A. S. Kammer, and N. Olgac, “Delayed feedback control laws for Rijke tube thermoacoustic instability, synthesis, and experimental validation,” *IEEE Trans. Contr. Sys. Tech.*, vol. 24, no. 5, pp. 1861–1868, 2016.

[96] G. A. de Andrade, R. Vazquez, and D. J. Pagano, “Boundary control of a rijke tube using irrational transfer functions with experimental validation,” in *Proc. IFAC World Congress*, 2017, pp. 4528–4533.

[97] A. Kemal and C. T. Bowman, “Real-time adaptive feedback control of combustion instability,” in *Proc. Int. Symp. Combustion*, 1996, pp. 2803–2809.

[98] A. M. Annaswamy, M. Fleifil, J. W. Rumsey, R. Prasanth, J.-P. Hathout, and A. F. Ghoniem, “Thermoacoustic instability: Model-based optimal control designs and experimental validation,” *IEEE Trans. Contr. Sys. Tech.*, vol. 8, no. 6, pp. 905–918, 2000.

[99] A. S. Morgans and A. M. Annaswamy, “Adaptive control of combustion instabilities for combustion systems with right-half plane zeros,” *Comb. Sci. Tech.*, vol. 180, no. 9, pp. 1549–1571, 2008.

[100] M. A. Vaudrey, W. T. Baumann, and W. R. Saunders, “Time-averaged gradient control of thermoacoustic instabilities,” *J. Prop. Power*, vol. 19, no. 5, pp. 830–836, 2003.

[101] S. J. Illingworth and A. S. Morgans, “Advances in feedback control of the Rijke tube thermoacoustic instability,” *Int. J. Flow Contr.*, vol. 2, no. 4, 2010.

[102] W. Wei, J. Wang, D.-h. Li, M. Zhu, H.-j. Tang, and F.-l. Weng, “Dynamic compensation based adaptive control of thermo-acoustic instabilities in Rijke tube: An experimental validation,” *ISA Trans.*, vol. 52, no. 3, pp. 450–460, 2013.

[103] R. Blonbou, A. Laverdant, S. Zaleski, and P. Kuentzmann, “Active control of combustion instabilities on a Rijke tube using neural networks,” *Proc. Comb. Inst.*, vol. 28, no. 1, pp. 747–755, 2000.

[104] G. A. de Andrade, R. Vazquez, and D. J. Pagano, “Backstepping stabilization of a linearized ode–pde rijke tube model,” *Automatica*, vol. 96, pp. 98–109, 2018.

[105] Y. Rahman, A. Xie, and D. S. Bernstein, “Retrospective Cost Adaptive Control: Pole Placement, Frequency Response, and Connections with LQG Control,” *IEEE Contr. Sys. Mag.*, vol. 37, no. 5, pp. 28–69, 2017.

[106] S. A. U. Islam, T. Nguyen, I. Kolmanovsky, and D. S. Bernstein, “Data-Driven Retrospective Cost Adaptive Control for Flight Control Applications,” *J. Guid. Contr. Dyn.*, vol. 44, pp. 1732–1758, October 2021.

[107] J. B. Hoagg and D. S. Bernstein, “Retrospective Cost Model Reference Adaptive Control for Nonminimum-Phase Systems,” *J. Guid. Contr. Dyn.*, vol. 35, pp. 1767–1786, 2012.

[108] S. M. Sarpotdar, N. Ananthkrishnan, and S. Sharma, “The Rijke tube–A thermo-acoustic device,” *Resonance*, vol. 8, no. 1, pp. 59–71, 2003.

[109] R. Raun, M. Beckstead, J. Finlinson, and K. Brooks, “A review of Rijke tubes, Rijke burners and related devices,” *Prog. Energy Combustion Sci.*, vol. 19, no. 4, pp. 313–364, 1993.

[110] K. Manoj, S. A. Pawar, J. Kurths, and R. Sujith, “Rijke tube: A nonlinear oscillator,” *Chaos*, vol. 32, no. 7, p. 072101, 2022.

[111] J. W. S. Rayleigh, *The Theory of Sound.* Macmillan & Company, 1896, vol. 2.

[112] E. D. Sumer and D. S. Bernstein, “Retrospective cost adaptive control with error-dependent regularization for MIMO systems with uncertain nonminimum-phase transmission zeros,” in *Proc. AIAA Guid. Nav. Contr. Conf.*, 2012, AIAA-2012-4670-123.

[113] L. Ljung and T. Soderstrom, *Theory and Practice of Recursive Identification.* The MIT Press, 1983.

[114] S. A. U. Islam and D. S. Bernstein, “Recursive least squares for real-time implementation,” *IEEE Contr. Syst. Mag.*, vol. 39, no. 3, pp. 82–85, 2019.

[115] B. Francis and M. W. Wonham, “The internal model principle of control theory,” *Automatica*, vol. 12, pp. 457–465, 1976.

[116] J. P. Hathout, M. Fleifil, A. M. Annaswamy, and A. F. Ghoniem, “Combustion instability active control using periodic fuel injection,” *J. Prop. Power*, vol. 18, no. 2, pp. 390–399, 2002.

[117] J. H. Uhm and S. Acharya, “Low-bandwidth open-loop control of combustion instability,” *Comb. Flame*, vol. 142, no. 4, pp. 348–363, 2005.

[118] ——, “Role of low-bandwidth open-loop control of combustion instability using a high-momentum air jet—mechanistic details,” *Comb. Flame*, vol. 147, no. 1-2, pp. 22–31, 2006.

[119] N. Docquier and S. Candel, “Combustion control and sensors: a review,” *Prog. Energy Comb. Sci.*, vol. 28, no. 2, pp. 107–150, 2002.

[120] G. A. Richards, M. Janus, and E. H. Robey, “Control of flame oscillations with equivalence ratio modulation,” *J. Prop. Power*, vol. 15, no. 2, pp. 232–240, 1999.

[121] B. S. Hong, A. Ray, and V. Yang, “Wide-range robust control of combustion instability,” *Comb. Flame*, vol. 128, no. 3, pp. 242–258, 2002.

[122] J. Ballester and T. García-Armingol, "Diagnostic techniques for the monitoring and control of practical flames," *Prog. Energy Combust. Sci.*, vol. 36, no. 4, pp. 375–411, 2010.

[123] Y. Ding, D. Durox, N. Darabiha, and T. Schuller, "Chemiluminescence based operating point control of domestic gas boilers with variable natural gas composition," *Appl. Therm. Eng.*, vol. 149, pp. 1052–1060, 2019.

[124] D. Krishnamoorthy and S. Skogestad, "Real-time optimization as a feedback control problem-a review," *Comput. Chem. Eng.*, p. 107723, 2022.

[125] G. Gelbert, J. P. Moeck, C. O. Paschereit, and R. King, "Advanced algorithms for gradient estimation in one-and two-parameter extremum seeking controllers," *J. Proc. Contr.*, vol. 22, no. 4, pp. 700–709, 2012.

[126] J. P. Koeln and A. G. Alleyne, "Optimal subcooling in vapor compression systems via extremum seeking control: Theory and experiments," *Int. J. Refrig.*, vol. 43, pp. 14–25, 2014.

[127] N. Bizon, "Improving the PEMFC energy efficiency by optimizing the fueling rates based on extremum seeking algorithm," *Int. J. Hydrog. Energy*, vol. 39, no. 20, pp. 10 641–10 654, 2014.

[128] Z. Wu, C. W. Wong, L. Wang, Z. Lu, Y. Zhu, and Y. Zhou, "A rapidly settled closed-loop control for airfoil aerodynamics based on plasma actuation," *Exp. Fluids*, vol. 56, pp. 1–15, 2015.

[129] R. D. Brackston, A. Wynn, and J. F. Morrison, "Extremum seeking to control the amplitude and frequency of a pulsed jet for bluff body drag reduction," *Exp. Fluids*, vol. 57, pp. 1–14, 2016.

[130] Z. Wu, C. W. Wong, and Y. Zhou, "Dual-input/single-output extremum-seeking system for jet control," *AIAA J.*, vol. 56, no. 4, pp. 1463–1471, 2018.

[131] L. Hazeleger, M. Haring, and N. van de Wouw, "Extremum-seeking control for optimization of time-varying steady-state responses of nonlinear systems," *Automatica*, vol. 119, p. 109068, 2020.

[132] C. Feudjio, J. Zamudio, L. Dewasme, H. Hernández, and A. Vande, "Dual-input slope seeking control of continuous micro-algae cultures with experimental validation," *Appl. Sci.*, vol. 11, no. 16, p. 7451, 2021.

[133] K. B. Ariyur and M. Krstić, *Combustion Instabilities*. John Wiley & Sons, 2003, ch. 10, pp. 143–155.

[134] C. Johnson, Y. Neumeier, E. Lubarsky, J. Lee, M. Neumaier, and B. Zinn, "Suppression of combustion instabilities in a liquid fuel combustor using a fast adaptive control algorithm," in *AIAA Aerosp. Sci. Meet.*, 2000, p. 476.

[135] S. Murugappan, E. Gutmark, and S. Acharya, "Application of extremum seeking controller for suppression of combustion instabilities in spray combustion," in *AIAA Aerosp. Sci. Meet.*, 2000, p. 1025.

[136] A. Banaszuk, M. Ariyur, K. B .and Krstić, and C. A. Jacobson, "An adaptive algorithm for control of combustion instability," *Automatica*, vol. 40, no. 11, pp. 1965–1972, 2004.

[137] W. H. Moase, C. Manzie, and M. J. Brear, "Newton-like extremum-seeking for the control of thermoacoustic instability," *IEEE Trans. Autom. Contr.*, vol. 55, no. 9, pp. 2094–2105, 2010.

[138] A. L. Bruce, N. Mohseni, A. Goel, and D. S. Bernstein, "Adaptive quasi-static control of multistable systems," in *Proc. Amer. Contr. Conf.* IEEE, 2020, pp. 2055–2060.

[139] R. Ramesh, S. Obidov, J. Paredes, D. S. Bernstein, and M. Gamba, "Design and characterization of the dual independent swirl combustor facility (DISCo)," in *AIAA Prop. Energy Forum*, 2021, p. 3479.

[140] R. T. Boute, "The Euclidean definition of the functions div and mod," *Trans. Prog. Lang. Syst.*, vol. 14, no. 2, pp. 127–144, 1992.